APPLIED COMPUTATIONAL ELECTROMAGNETICS SOCIETY JOURNAL

July 2015
Vol. 30 No. 7
ISSN 1054-4887

The ACES Journal is abstracted in INSPEC, in Engineering Index, DTIC, Science Citation Index Expanded, the Research Alert, and to Current Contents/Engineering, Computing & Technology.

The illustrations on the front cover have been obtained from the research groups at the Department of Electrical Engineering, The University of Mississippi.

EMERITUS EDITORIAL ASSISTANTS

JULY 2015 REVIEWERS

THE APPLIED COMPUTATIONAL ELECTROMAGNETICS SOCIETY

JOURNAL

Vol. 30 No. 7 July 2015

TABLE OF CONTENTS

Questioning Degree of Accuracy Offered by the Spectral Element Method in Computational Electromagnetics

I. Mahariq [1,2], H. Kurt [2], and M. Kuzuoğlu [3]

[1] Department of Electrical and Electronics Engineering
University of Turkish Aeronautical Association, Ankara 06790, Turkey

[2] Department of Electrical and Electronics Engineering
TOBB University of Economics and Technology, Ankara 06560, Turkey

[3] Department of Electrical and Electronics Engineering
Middle East Technical University, Ankara 06531, Turkey
ibmahariq@gmail.com, hkurt@etu.edu.tr, kuzuoglu@metu.edu.tr

Abstract ─ In this paper, a comparison amongst the spectral element method (SEM), the finite difference method (FDM), and the first-order finite element method (FEM) is presented. For the sake of consistency, the comparison is carried out on one-dimensional and two-dimensional boundary value problems based on the same measure of error in order to emphasize on the high accuracy gained by the SEM. Then, the deterioration in the accuracy of the SEM due to the elemental deformation is demonstrated. Following this, we try to answer the question: Do we need the high accuracy offered by the SEM in computational electromagnetics? The answer is supported by solving a typical, unbounded electromagnetic scattering problem in the frequency domain by the SEM. Domain truncation is performed by the well-known perfectly matched layer (PML).

Index Terms ─ Deformation, electromagnetic scattering, finite difference, finite element, photonic nanojet, spectral element method.

I. INTRODUCTION

Spectral element method was first introduced by Patera [1] in 1984 for computational fluid dynamics. Patera proposed a spectral element method that combines the flexibility of the finite element method (FEM) with the accuracy of spectral methods (the case where *p*-type method is applied for a single-element domain). In the spectral element method, he utilized high-order Lagrangian polynomial interpolant over Chebyshev collocation points in order to represent the velocity in each element in the computational domain.

Generally speaking, spectral element methods are considered as a family of approximation schemes based on the Galerkin method. They share common characteristics with finite-element discretizations, and this provides the reason why they can be viewed as *h*- or *p*-versions of FEM. That is, when viewed as *h*-version (mesh refinement), a Lagrangian interpolation formula on the parent element exists in both, as well as the basis functions have local support. On the other hand, spectral element methods use high-degree polynomials on a fixed geometric mesh for the sake of enhanced accuracy, and this is the fact characterizing the *p*-version (order refinement) of FEMs [2].

Orthogonality of basis functions either in the *h*- or *p*-versions of the FEM is due to non-overlapping local functions. However, in spectral element methods orthogonality is related to both analytical nature and topological nature (local extension) of the basis functions. This fact tells us why spectral element method is different from the FEM of *h*-version or *p*-version [3].

There are mainly two implementations that have been proposed; one is based on the Chebyshev polynomials [1], and the other is based on the Legendre polynomials. In both cases, Gauss-Lobatto quadrature grid is utilized to perform Lagrangian interpolation. This implementation ensures the continuity of the solution and benefit from the associated numerical quadrature schemes. Patera [1] chose Chebyshev polynomials basically because of the possibility of using fast transform techniques. On the other side, the stiffness and mass matrices were evaluated by the quadratures that were performed analytically without utilizing the weighting factor associated with Chebyshev polynomials [2], (the weighting factor is $1/\sqrt{1-x^2}$, by which Chebyshev polynomials are orthogonal in contrast to Legendre polynomials whose orthogonality comes with unity weighting factor). In

Submitted On: January 12, 2015
Accepted On: June 18, 2015

this study, the implementation of SEM is based on Legendre polynomials and Gauss-Lobatto-Legendre quadrature grid is utilized to perform Lagrangian interpolation.

In computational electromagnetics, the first- or second-order FEM and the finite difference method are extensively used in numerical modeling of electromagnetic radiation and/or scattering problems, both in frequency and time domains. On the other hand, although it is known for its high accuracy [4-7], the spectral element method is not familiar to the community of electromagnetics. However, to attract the attention of the community, a consistent comparison illustrating the accuracy of these numerical methods will have a remarkable value.

In this paper, domain truncation is performed by the perfectly matched layer (PML) [8], namely the systematic formulation provided by Kuzuoglu and Mittra [9]. Based on that formulation, Mahariq, et al. [10], provided the values of the attenuation factors for the PML when SEM is utilized in modeling of frequency-domain electromagnetic problems while persevering the high accuracy of SEM.

There are three main goals of the current study. The first is to demonstrate the accuracy of the SEM, the 3-node-stencil FDM and the first-order FEM. For this purpose, a comparison is carried out by solving some boundary value problems in one dimension and two dimensions based on the same measure of error. After emphasizing on the accuracy of SEM, we illustrate the deterioration in the accuracy of SEM due to the irregularity in the elemental shapes (deformed elements). The third goal of this paper is to demonstrate a typical electromagnetic scattering problem which best provides an unusual answer to the title of the current study, i.e., does an electromagnetic problem requires the high accuracy gained by using the SEM?

The paper is arranged as follows: in Section II, a comparison amongst SEM, FDM and FEM is provided. In Section III, the deterioration in the SEM accuracy due to the elemental deformation is demonstrated. Section IV provides a typical electromagnetic scattering problem solved by the SEM, and finally some conclusions are presented in Section V.

II. ON THE ACCURACY OF SEM, FDM AND FEM

To get an insight about the accuracy gained from SEM, when compared to other numerical methods, demonstrations are performed using numerical examples. For this purpose, a comparison is first carried out between SEM and FDM with a stencil composed of 3 nodes in one dimension. We considered the following one-dimensional boundary-value problem:

$$\frac{d^2u}{dx^2}+k^2u=0,\ \text{in the interval}\,[0,1.1], \tag{1}$$

with $u(0)=1,\ u(1.1)=\exp(-jk1.1)$, where $k=2\pi$. We define an error measure as follows:

$$Err=\max_i \frac{\left|u_{i,exact}-u_{i,numerical}\right|}{\left|u_{i,exact}\right|}, \tag{2}$$

where $u_{i,exact}$ is the exact solution (for this problem, it is $\exp(-jkx)$), and $u_{i,numerical}$ is the numerical solution obtained by the specified numerical method at the ith node in the computational domain. This definition of the error measure is used throughout this paper.

In Table 1, the maximum relative errors for both FDM and SEM are presented as the number of nodes (N) increases in both methods. Obviously, it can be observed that the errors of FDM are slowly decaying although the number of nodes is chosen in the order of 10. On the other hand, SEM shows high accuracy with much fewer number of nodes. That is, the accuracy obtained by FDM at 100 nodes can be achieved by 8 nodes with SEM.

Table 1: Maximum relative errors of FDM and SEM for the problem defined in Eq. 1

FDM		SEM	
N	*Err*	N	*Err*
10	0.1840	7	0.0103
20	0.0524	8	0.0012
30	0.0238	9	1.455e-04
40	0.0135	10	1.608e-05
50	0.0087	11	2.074e-06
60	0.0060	12	2.308e-07
70	0.0044	13	2.570e-08
80	0.0034	14	2.624e-09
90	0.0027	15	2.613e-10
100	0.0022	16	2.420e-11
110	0.0020	17	2.318e-12

To compare SEM with the first-order FEM, we consider the following 1D problem:

$$\begin{aligned}&\frac{d^2u}{dx^2}+u=0,\ \text{in}\,[-1,0],\ \text{and}\\ &\frac{d^2u}{dx^2}+4^2u=0,\ \text{in}\,[0,1]\\ &\text{with}\ u(-1)=\sin(-1),\ u(1)=\sin(4).\end{aligned} \tag{3}$$

In fact, the solution of (3) is $u(x)=\sin(\mathrm{c}\,x)$, with $\mathrm{c}=1$ in $[-1,0]$, and $\mathrm{c}=4$ in $[0,1]$. However, for error calculations, to avoid division by zero, we compute the error (only for this problem) as the maximum difference between the exact solution and the numerical solution.

The comparison is shown in Table 2, in which N represents the number nodes in each sub-domain. Again, it can be seen that SEM accuracy is much higher than that of FEM. Figure 1 shows the plot of the solution obtained by SEM for 15 nodes in each subdomain.

Table 2: Maximum errors of FEM and SEM for the problem defined in Eq. 3

FEM		SEM	
N	*Err*	N	*Err*
10	0.0546	7	7.033e-05
20	0.0252	8	3.340e-06
30	0.0164	9	4.697e-07
40	0.0121	10	1.876e-08
50	0.0096	11	2.593e-09
60	0.0080	12	9.092e-11
70	0.0068	13	1.132e-11
80	0.0059	14	3.481e-13
90	0.0053	15	3.941e-14
100	0.0047	16	1.587e-14

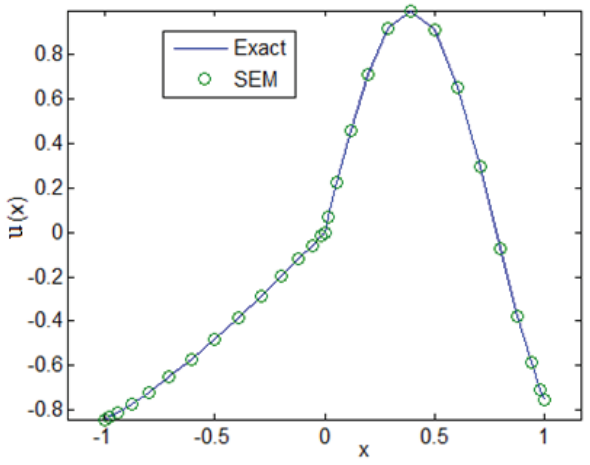

Fig. 1. Exact and SEM solutions of the problem defined in Eq. 3.

It is worth also to compare FEM and SEM in a two dimensional boundary value problem. For this purpose, the point source problem (2D Green's function) is considered. This problem is governed by the Helmholtz equation:

$$\nabla^2 u + k^2 u = -\delta(\vec{r}), \tag{4}$$

where $k = 2\pi / \lambda$, and λ is the wavelength. To avoid the singularity at the origin, the homogenous Helmholtz equation is solved inside a square element (Ω) of dimensions $\lambda \times \lambda$ and $\lambda = 1$, and Ω is defined in the xy-plane so that the point (0,0) does not belong to this element. On the boundary $\partial\Omega$, the exact to (4), which is expressed in terms of Hankel function of the second kind zero order is as follows: $(u(\vec{r}) = (j/4)H_0^{(2)}(k\,|\,\vec{\mathrm{r}}\,|)$, is applied as boundary conditions, where $|\,\vec{\mathrm{r}}\,|$ is the euclidean distance from the origin to a point $\vec{\mathrm{r}}$ on the boundary $\partial\Omega$. Right-triangle elements are utilized in meshing the problem. Figure 2 shows the solution obtained by FEM at a grid of 20×20 nodes. As observed from Table 3, the error profile in 2D does not differ from that of 1D case.

It can be clearly observed from the demonstrated numerical problems that the accuracy of SEM is much higher than that of FDM or FEM. However, it is important to study the deterioration in the accuracy of SEM when deformed elements are used to discretize a given problem. This aspect is discussed in the next section.

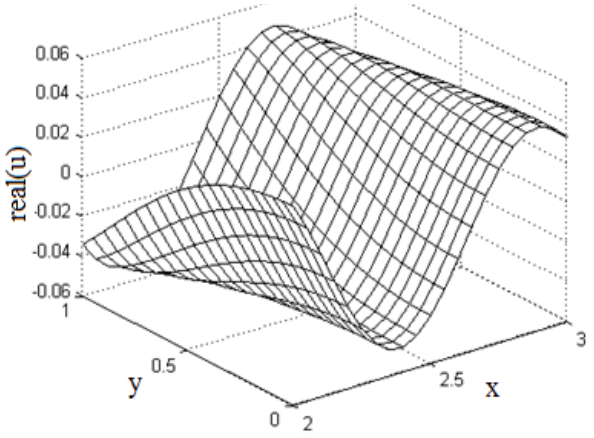

Fig. 2. FEM solution of the 2D point source problem defined in Eq. 4.

Table 3: Maximum relative errors of FEM and SEM for the problem defined in Eq. 4

FEM		SEM	
N	*Err*	N	*Err*
10	0.5554	7	0.00091
15	0.3229	8	1.30E-04
20	0.2018	9	1.25E-05
25	0.1356	10	1.14E-06
30	0.0967	11	1.13E-07
35	0.0724	12	1.26E-08
40	0.0562	13	1.51E-09
45	0.0447	14	2.23E-10
50	0.0364	15	2.57E-11
55	0.0302	16	3.23E-12
60	0.0255	17	2.86E-13
80	0.0145		
100	0.0103		

III. ELEMENTAL DEFORMATION

Most of practical engineering problems encounter

complex geometries; hence, the computational domain requires to be discretized into irregular elements. Meshing a problem in the case of FEM has been intensively investigated in the literature. For instance, if triangular elements are used to mesh a problem, it is recommended that the smallest angle in the element should not be lower than 15° in order not to deteriorate the accuracy. Hence, it is important to study the effect of elemental deformation on the accuracy in the case of SEM. In this section, we demonstrate the accuracy of spectral element method for a single-element domain of quadrilateral deformed elements.

In SEM, mapping an irregular element to the standard element (see Fig. 3) is required in order to perform the differential and integration operations involved in the process of approximating the partial differential equations by SEM. As mentioned above, the nodal basis for the standard element is usually built by Lagrangian basis polynomials associated with a tensor product grid of Gauss-Legendre-Lobatto (GLL) nodes. Figure 4 shows such a grid for a ninth-order polynomial space. As seen from Fig. 3, the flexibility in the shapes of elements can be utilized in meshing complex geometries where different scattering objects of arbitrary shapes are involved.

In this work, to differentiate between a reference square element and an irregular element, the following definition for the elemental aspect ratio (AR) is considered:

$$AR = \frac{\max(d_i)}{\min(d_i)}, \tag{5}$$

where d_i $(1 \le i \le 4)$ stands for side length of a quadrilateral element and $i = 1,2,3,4$. To make use of this definition, one needs to study the accuracy of SEM for a single-element domain having a reference area with equal dimensions (1×1). We call such an element as a reference element. Then, by changing the dimensions and the shape of the element while having the same area as that of the reference element, a comparison can be performed. With this approach, the effect of AR on the accuracy can be realized. It is also worth to note that all sides of the element have equal nodes as GLL is utilized.

The point source problem introduced in (4) is considered for this purpose. The maximum relative errors are presented in Table 4 as N increases for the reference square element and for a quadrilateral element of unit area for the aspect ratios: 1.33, 1.88, and 2.87. The real part of the solution in the straight-sided quadrilateral element is shown in Fig. 5 for AR=2.87. As seen from Table 4, the effect of the aspect ratio on the accuracy can be clearly observed. However, even at large deformation (i.e., at AR=2.87), SEM still provides much higher accuracy than its counterparts (FDM and FEM) at much coarser grids.

In terms of the presented accuracy of SEM, one may wonder whether such a high accuracy is required in order to successfully model an electromagnetic problem or not. In the next section, we try to answer such questioning.

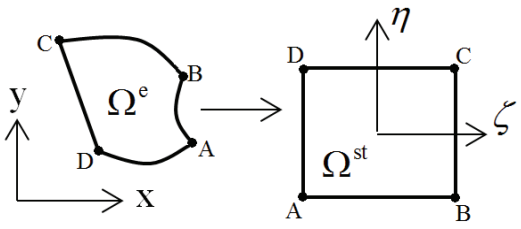

Fig. 3. Mapping an element Ω^e to the standard element Ω^{st}.

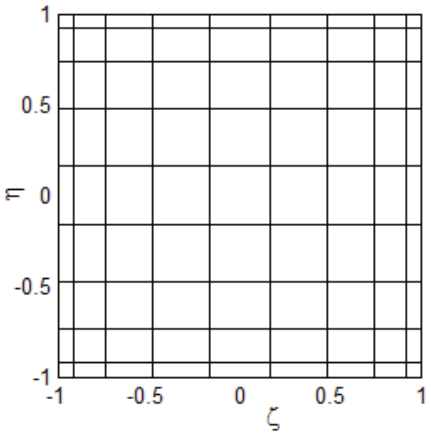

Fig. 4. GLL grid nodes on the standard element for a ninth-order polynomial space (nodes are represented by the intersections of horizontal and vertical lines).

Table 4: Maximum relative errors of SEM for the reference element and the straight-sided quadrilateral element having unit area

N	Ref. Elmt.	Straight-Sided Element		
		AR = 1.33	AR = 1.88	AR = 2.87
	Err	*Err*	*Err*	*Err*
7	9e-4	1e-3	3e-3	6e-2
8	1e-4	2e-4	6e-4	1e-2
9	1e-5	2e-5	1e-4	4e-3
10	1e-6	2e-6	3e-5	1e-3
11	1e-7	2e-7	5e-6	3e-4
12	1e-8	2e-8	8e-7	6e-5
13	1e-9	2e-9	1e-7	2e-5
14	2e-10	3e-10	2e-8	3e-6
15	3e-11	3e-11	4e-9	7e-7
16	3e-12	4e-12	6e-10	2e-7
17	3e-13	4e-13	8e-11	3 e-8

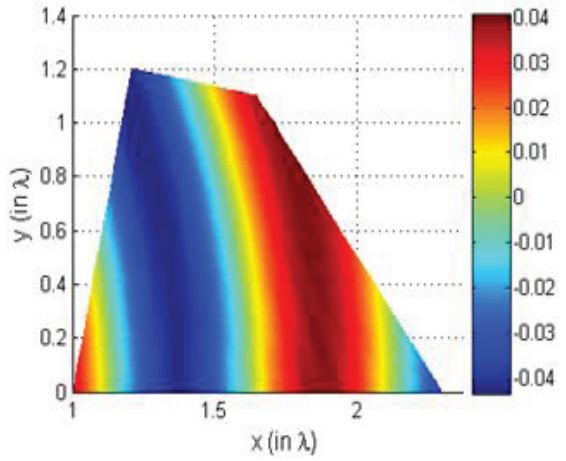

Fig. 5. SEM solution for the straight-sided quadrilateral element at AR=2.87.

IV. SCATTERING PROBLEM IN RESONANCE ELEMENTS

Accuracy of numerical approach is crucial in order to capture the intrinsic property of resonances of optical cavities. We specifically take two-dimensional dielectric micro-cylinder in this section of the study to emphasize the importance of fine discretization of the computational domain.

When an electromagnetic plane wave is incident perpendicularly to a dielectric cylinder or to a dielectric sphere, instead of having a shadow region behind the dielectric material, a photonic nanojet is obtained at some specific choices of material dimensions and a corresponding refractive index. In order to obtain a photonic nanojet, the dielectric microspheres or micro cylinders must be lossless dielectric materials and of diameters greater than the illuminating wavelength [11-15]. The phenomenon is named as photonic nanojet, due to the unique nature of the light distribution at the focal area. In Ref. 17, we provided detailed formulation of SEM and applied the method for investigating plane wave interaction with dielectric micro-cylinder.

In the case of photonic nanojet where the scatterer is assumed to be an infinitely-long dielectric cylinder, the problem can be considered as a two-dimensional one when an incident plane wave propagating in a direction perpendicular to the cylinder axis is assumed. We consider an incident plane wave propagating in the x-direction and the electric field is polarized in the z-direction (i.e., in a transverse magnetic mode, TM_z):

$$E_z^{inc} = \hat{a}_z \exp(-jkx). \tag{6}$$

To solve the problem numerically, one must truncate the unbounded domain. In this work, domain truncation is performed by the perfectly matched layer, namely using the formulation presented in [10]. Figure 6 shows in the xy-plane, a dielectric cylinder represented by Ω_C, free space region represented by Ω_{FS}, and the PML region denoted by Ω_{PML}, which represents the region surrounding Ω_{FS}.

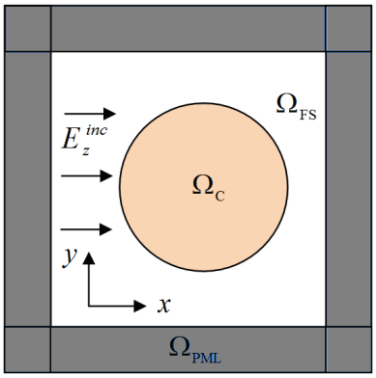

Fig. 6. Definition of the computational domain composed of a dielectric micro-cylinder (Ω_C) embedded in the free space (Ω_{FS}) and truncated by PML [17].

The set of the partial differential equations governing this electromagnetic scattering problem can be written as follows:

$$\nabla.\Lambda\nabla \mathrm{u} + \mathrm{a}\,\varepsilon_r k^2\,\mathrm{u} = k^2\left(1-\varepsilon_r\right)E_z^{inc}, \tag{7}$$

in which Λ is a tensor defined as:

$$\Lambda = \begin{bmatrix} \Lambda_{11} & 0 \\ 0 & \Lambda_{22} \end{bmatrix}, \tag{8}$$

where ε_r is the relative permittivity of the cylinder, $\mathrm{a} = 1 + \dfrac{\alpha}{\mathrm{jk}}$, α is the attenuation factor,

$\begin{bmatrix}\Lambda_{11} & \Lambda_{22}\end{bmatrix} = \begin{bmatrix}\dfrac{1}{\mathrm{a}} & \mathrm{a}\end{bmatrix}$ for x-decay in the PML region,

$\begin{bmatrix}\Lambda_{11} & \Lambda_{22}\end{bmatrix} = \begin{bmatrix}\mathrm{a} & \dfrac{1}{\mathrm{a}}\end{bmatrix}$ for y-decay in the PML region,

$\begin{bmatrix}\Lambda_{11} & \Lambda_{22}\end{bmatrix} = \begin{bmatrix}\dfrac{1}{\mathrm{a}} & \dfrac{1}{\mathrm{a}}\end{bmatrix}$ for a corner (xy-decay) in the PML region with $\mathrm{a}=1$ in Ω_{FS}, and ε_r being greater than 1 in Ω_{SC} only, and 1 elsewhere. If n denotes the refractive index of the cylinder, then $n^2 = \varepsilon_r$.

It is worth to mention that, after obtaining the solution by spectral element method, which represents the scattered field, the incident plane wave is added to the scattered field in the subdomains Ω_C and Ω_{FS} only. One can produce the same spatial light distribution for the case where FDTD method is used. We have performed FDTD study and verified the exact photonic nanojet generation. With the application of SEM in the frequency domain, it is easy to decompose

the total field into incident and scattered field components. Figure 7 shows the visualization of photonic nanojet when the cylinder radius is $R = 5.0\lambda$ and dielectric constant is $n = 1.30$.

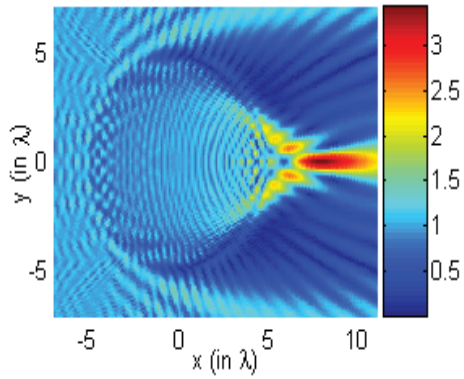

Fig. 7. Visualization by the SEM of photonic nanojet at $R = 5.0\lambda$ and $n = 1.30$.

Figure 8 shows one of the captured resonance mode supported by a dielectric micro cylinder with $R = 3.5\lambda$ and $n = 1.70$. The light focusing action with small amplitude can be observed at the interior part of the dielectric cylinder. On the other hand, strong electric field localization at around the small cylinder appears with a highly symmetric light distribution in the form of two rings. Light is trapped at the circumference of the cylinder by the total internal reflection mechanism.

The special case corresponding to specific radius and refractive index values in Fig. 8 can be attributed to whispering gallery mode (WGM). In the representation of WGM, m indicates the azimuthal mode number, and l represents the radial mode number. Using this notation we can express Fig. 8 in terms of WGM resonances. By means of spectral element method, we captured resonance modes as well as photonic nano jets cases as the details are reported in Ref. [17].

Photonic nanojet analysis can also be performed analytically. The well-known Mie theory was intensively utilized in electromagnetic scattering problems. However, when the characteristic dimensions of the scattering object becomes much larger than the wavelength, improper algorithms may lead to considerable numerical errors [16]. In the examples presented in the previous section, where resonance behavior takes places, the diameter of the micro-cylinder is larger than the wavelength but not too much. It is very important to check whether the analysis that Mie theory provides produces such resonance cases or not. Itagi and Challener [16] provided the solution of the scattered light by a dielectric cylinder using Mie theory. This analytical solution is used to verify the existence of WGM in scattering by dielectric microcylinders. Figure 9 presents the scattered field inside the cylinder at $R = 3.5\lambda$. The good match between Fig. 8 and Fig. 9 can be observed clearly.

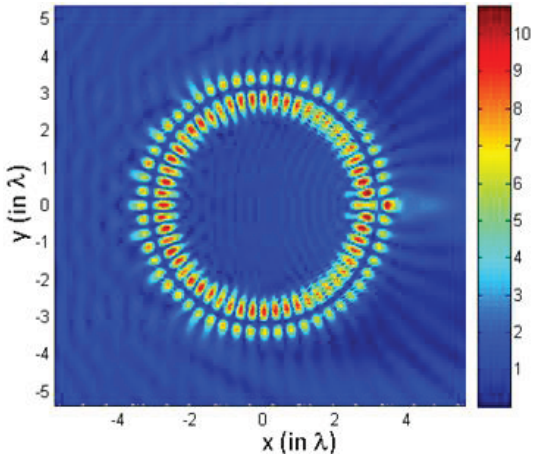

Fig. 8. Visualization of the evolution of a photonic nano-jet for $R = 3.5\lambda$ and $n = 1.70$. Whispering gallery mode representation gives $l = 2$ and $m = 28$ [17].

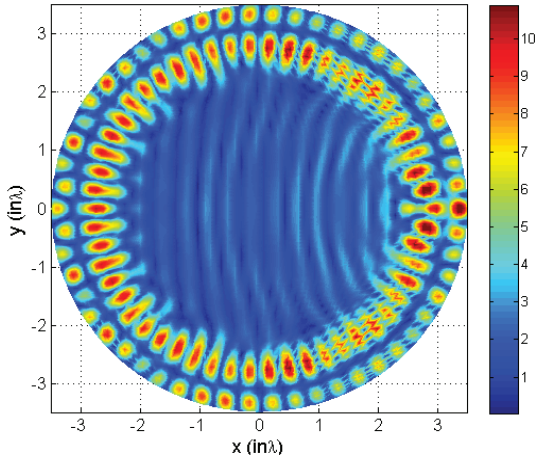

Fig. 9. The analytical solution in Ω_C visualizes the WGM ($l = 2$ and $m = 28$) for the case shown in Fig. 8.

With the use of SEM, we could accurately perform field analysis of photonic nanojets in dielectric lossless micro cylinders. Strong light focusing at the shadow side of the micro-cylinder is reported. Advantageous features of SEM allow the observation of commonly reported nanojet scenarios as well as the least pointed out transition region where resonance mode appears under certain conditions. The creation of whispering gallery mode types is plainly observed.

Two dimensional dielectric cylinders may act either as resonant or focusing element depending on the stimulating conditions. One cannot observe and capture resonance frequencies if the discretization of the

computational domain is not properly performed. As an example, we provide field distribution of the dielectric cylinder under the same parameters ($n=1.70$ and $R=3.5\lambda$) except the case that low resolution (16×16 nodes are assigned for each element) is introduced. Compared to Fig. 8, we see that the resonance is lost as shown in Fig. 10.

Depending on the nature of the resonance mode (spectrally how sharp or broad the mode) one should utilize even finer or coarse discretization in the computational method as in SEM. Consequently, capturing of resonance requires fine discretization of the computational domain.

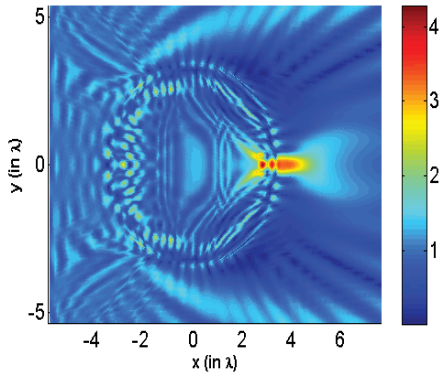

Fig. 10. Visualization of the evolution of a photonic nanojet for $R=3.5\lambda$ and $n=1.70$ at 16×16 nodes per element. WGM behavior is destroyed due to low resolution.

V. CONCLUSION

To realize and appreciate the accuracy of spectral element method, we carried out a comparison between this method and its well-known counter parts such as FDM and FEM. For this purpose, we applied these numerical methods to solve specific problems and the corresponding error calculations are subjected to a specific error measure. From the illustrated examples, it is clear that the accuracy of spectral element method is much higher than that of its counter parts.

In most of practical engineering problems, the geometry of the region of interest is irregular. This means that discretization of the problem into elements of regular shapes is impossible. Spectral element method gives the capability of using deformed elements; and hence, a freedom in modeling irregular problems. For this reason, we illustrated the accuracy of this numerical method for single-deformed element case in order to check the deterioration of the elemental deformation on the accuracy of SEM. The aspect ratio of the element is considered as a measure of the deformation with fixed area. Based on the illustrations, we conclude that the accuracy of SEM even with large elemental deformation (which should be avoided while meshing an electromagnetic problem) still dominates the accuracy achieved by FDM or FEM.

The accuracy of the spectral element method is very high as it can be observed from the presented numerical demonstrations. Here, it is important to ask the following interesting question: What would be the order of the error while solving a computational problem? One may seek an accuracy at around 10^{-2} or 10^{-3} while designing a system to capture the general behavior of the device. Hence, low-order FEM or FDM are very suitable and do meet some engineering purposes. However, based on the electromagnetic scattering problem discussed in Section IV, the answer to the above question has to be modified: we do indeed need high accuracy in some cases, especially resonance characteristics require fine resolution. That is, when low-order numerical methods are used to study electromagnetic scattering by dielectric microspheres or micro cylinders, whispering gallery mode will be missed. So, if the engineer design the material based on the numerical solution from a low-order method, and if whispering gallery mode takes place in the final implementation, the whole design will be in jeopardy.

ACKNOWLEDGMENT

The first author acknowledges the financial support from Technical Research Council of Turkey (TUBITAK). Kurt acknowledges partial support from the Turkish Academy of Sciences.

REFERENCES

[1] A. T. Patera, “A spectral element method for fluid dynamics: Laminar flow in a channel expansion,” *Journal of Computional Physics*, vol. 54, pp. 468-488, 1984.

[2] M. O. Deville, P. F. Fischer, and E. H. Mund, *High-Order Methods for Incompressible Fluid Flow*, Cambridge University Press, vol. 9, 2002.

[3] G. Karniadakis and S. Sherwin, *Spectral/hp Element Methods for Computational Fluid Dynamics*, Oxford University Press, 2013.

[4] J. Lee, T. Xiao, and Q. H. Liu, “A 3-D spectral-element method using mixed-order curl conforming vector basis functions for electromagnetic fields,” *IEEE Trans. on Microwave Theory and Techniques*, vol. 54-1, pp. 437-444, Jan. 2006.

[5] J. Lee and Q. H. Liu, “A 3-D spectral-element time-domain method for electromagnetic simulation,” *IEEE Trans. on Microwave Theory and Technique*, vol. 55-5, pp. 983-991, May 2007.

[6] O. Z. Mehdizadeh and M. Paraschivoiu, “Investigation of a two-dimensional spectral element method for Helmholtz’s equation,” *Journal of Computational Physics*, vol. 189, pp. 111-129, 2003.

[7] S. J. Hesthaven, S. Gottlieb, and D. Gottlieb, *Spectral Methods for Time-Dependent Problems*, Cambridge University Press, 2007.
[8] J. P. Berenger, "A perfectly matched layer for the absorption of electromagnetic waves," *Journal of Computational Physics*, vol. 114, pp. 185-200, 1994.
[9] M. Kuzuoglu and R. Mittra, *A Systematic Study of Perfectly Matched Absorbers*, Frontiers in Electromagnetics, IEEE Press, 2000.
[10] I. Mahariq, M. Kuzuoglu, and I. H. Tarman, "On the attenuation of the perfectly matched layer in electromagnetic scattering problems with the spectral element method," *Applied Computational Electromagnetics Society Journal*, vol. 29.9, pp. 701-710, 2014.
[11] Z. Chen, A. Taflove, and V. Backman, "Photonic nanojet enhancement of backscattering of light by nanoparticles: a potential novel visible-light ultramicroscopy technique," *Optics Express*, vol. 12, pp. 1214-1220, 2004.
[12] S. Lecler, Y. Takakura, and P. Meyrueis, "Properties of a three-dimensional photonic jet," *Optics Lett*., vol. 30 (19), pp. 2641-2643, 2005.
[13] A. Devilez, B. Stout, N. Bonod, and E. Popov, "Spectral analysis of three-dimensional photonic jets," *Optics Express*, vol. 16, pp. 14200-14212, 2008.
[14] P. Ferrand, J. Wenger, A. Devilez, M. Pianta, B. Stout, N. Bonod, E. Popov, and H. Rigneault, "Direct imaging of photonic nanojets," *Optics Express*, vol. 16, pp. 6930-6940, 2008.
[15] M.-S. Kim, T. Scharf, S. Mühlig, C. Rockstuhl, and H. P. Herzig, "Engineering photonic nanojets," *Optics Express*, vol. 19, pp. 10206-10220, 2011.
[16] A. V. Itagi and W. A. Challener, "Optics of photonic nanojets," *Journal of Optics Society*, vol. 22, no. 12, 2005.
[17] I. Mahariq, M. Kuzuoglu, I. H. Tarman, and H. Kurt, "Photonic nanojet analysis by spectral element method," *IEEE Photonics Journal*, 6, 6802714 (2014).

Ibrahim Mahariq took his B.Sc. degree from the department of Electrical and Computer Engineering/ Palestine Polytechnic University in 2003. He worked there as Teaching Assistant during 2003-2005. He received the M.Sc. in Design of Electrical Machines, and his Ph.D. in Computational Electromagnetics from Middle East Technical University, Ankara, Turkey. Mahariq was granted TUBITAK scholarship for his Ph.D. studies in 2010. Mahariq is currently working on Photonics to earn his second Ph.D. in the department of Electrical and Electronics Engineering at TOBB University of Economics and Technology, Ankara, Turkey. Mahariq is currently serving as an Assistant Professor at the University of Turkish Aeronautical Association, Department of Electrical and Electronics Engineering.

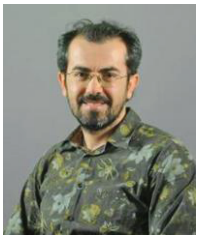

Hamza Kurt received the B.S. degree from Middle East Technical University, Ankara, Turkey, in 2000, the M.S. degree from the University of Southern California, Los Angeles, CA, USA, in 2002, and the Ph.D. degree from the Georgia Institute of Technology (Georgia Tech), Atlanta, GA, USA, in 2006, all in Electrical and Electronics Engineering. He was a Research Fellow with the Cedars-Sinai Medical Center, Bio-photonics Research Lab, Los Angeles, from 2001 to 2002. He spent a year with the Institut d'Optique Graduate School, Paris, France, as a Post-Doctoral Scientist. Since December 2007, he has been with the TOBB University of Economics and Technology, Ankara, as an Associate Professor with the Electrical and Electronics Engineering Department. He has authored more than 50 research papers in refereed international journals.

His current research interests include nanophotonics including the design and analysis of nanophotonic materials and media for the realization of wavelength-scale optical elements, slow light structures, graded index optics, high-resolution imaging, polarization insensitive devices, optical cavities/waveguides, and optical biosensors. Kurt is a Member of the Optical Society of America and IEEE Photonics Society.

Mustafa Kuzuoglu received the B.Sc., M.Sc., and Ph.D. degrees in Electrical Engineering from Middle East Technical University (METU), Ankara, Turkey, in 1979, 1981, and 1986, respectively. He is currently a Professor with METU. His research interests include computational electromagnetics, inverse problems, and radars.

Interaction Between 3-T MRI Systems and Patients with an Implanted Pacemaker

S. Pisa and E. Piuzzi

Department of Information Engineering, Electronics and Telecommunications
Sapienza University of Rome, Rome, 00184, Italy
pisa@diet.uniroma1.it, piuzzi@diet.uniroma1.it

Abstract ─ In this paper, a transverse electro-magnetic (TEM) coil operating at 128 MHz in a 3-T magnetic resonance imaging system has been studied in terms of the interaction with patients with or without an implanted pacemaker. The pacemaker has been simulated as a copper box with a catheter constituted by an insulated copper wire with an uncapped tip and it has been placed inside either box or anatomical models of the thorax. Electromagnetic and thermal simulations have been performed by using finite difference time domain codes. The obtained results show that in the absence of the pacemaker, and for a radiated power producing in the box a whole body specific absorption rate (SAR) of 1 W/kg, that is a typical value for MRI examinations, the coil produces in the anatomical models peak temperature values lower than the limits issued by the International Electrotechnical Commission (IEC). In the presence of the pacemaker, temperature increments at the catheter tip in excess of those issued by the IEC standard are obtained when the MRI scanned area involves the pacemaker region. The 3-T coil produces lower SAR and temperature increments with respect to a 64-MHz (1.5-T system) birdcage antenna in patients with implanted pacemaker.

Index Terms ─ Cardiac pacemakers, dosimetry, magnetic resonance imaging (MRI), temperature.

I. INTRODUCTION

Magnetic resonance imaging (MRI) is the primary tool for the diagnosis of a wide number of diseases. However, MRI is contraindicated for patients implanted with pacemakers and implantable cardioverter defibrillators [1-3]. The most adverse effect seems to be the heating of the heart tissue around the catheter tip produced by the high currents induced on the catheter by the RF field used in the MRI technique [4-6].

The International Electrotechnical Commission (IEC) [7] considers that, to prevent tissue damage in the body, the radiofrequency field should induce temperature increases in the body core lower than 0.5 °C for normal operating mode and 1 °C for first level controlled operating mode, where medical supervision of the patient is required. Moreover, local tissue temperature should not exceed 39 °C and 40 °C for normal and first level controlled operating modes, respectively. Consequently, in [7] limitations have been reported with reference to the specific absorption rate (SAR). In particular, the whole body SAR (SAR_{WB}) should not exceed 2 W/kg and 4 W/kg in normal and first level controlled operating modes, respectively.

Most of MRI systems in use operate at 1.5 T (corresponding to a Larmor frequency of about 64 MHz). For typical RF sequences used in MRI the IEC limits are usually satisfied in terms of SAR and temperature [8-11]. However, if a subject with an implanted pacemaker is exposed to MRI radiofrequency (RF) fields, temperatures well above the IEC limits are reached at the catheter tip [12-17].

The last generation of MRI apparatus works with 3-T static magnetic field (Larmor frequency of about 128 MHz) [18-20]. To the Authors' knowledge, only few studies have been performed to investigate possible effects, on patients with metallic implants, due to 128 MHz MRI apparatus [21-23]. In [21], sixteen patients with pacemakers underwent 3-T MRI scanning of a region far from the one interested by the pacemaker, with a whole body system and with SAR limitation to 2 W/kg, without significant effects. In [22], a box phantom containing a vagus nerve stimulation catheter was exposed within a 3-T whole body coil with a 3 W/kg SAR. Temperature increments up to 14.7 °C were obtained after 15 minutes of exposure. Also in this case, the highest temperature increments were obtained when the scanned region was involving the catheter leads. Finally, a numerical study was performed in [23] to investigate possible effects due to 128 MHz apparatus on a realistic torso model obtaining temperature increments lower than 0.128 °C. In this case, vagus a very simplified pacemaker and coil model was used and no information on the radiated power was given.

In this paper, the interaction between the 128 MHz field of MRI apparatus and pacemakers will be studied

Submitted On: July 1, 2014
Accepted On: February 23, 2015

by using a numerical technique with realistic antenna, body and pacemaker models. Moreover, a comparison between SAR and temperature increments produced by 128 MHz and 64 MHz coils will be performed.

II. ELECTROMAGNETIC AND THERMAL MODELS

The radiofrequency antenna used in this work to generate the electromagnetic (EM) field needed for MRI examinations is a shielded transverse electromagnetic (TEM) coil [18,19]. The coil external diameter is 78 cm, and the height 80 cm (see Fig. 1 (a)). The TEM coil is constituted by 16 cylindrical copper legs with a diameter of 2 cm and a height of 65 cm (see Fig. 1 (b)). The legs are equidistant on a cylindrical surface with a diameter of 70 cm. The legs are connected, by tuning capacitances (C_T in Fig. 1 (c)), to two rings (with a 2 cm × 4 cm cross-section) that are in contact with the external shield. The capacitances are tuned to achieve the desired resonant frequency. Four 50 Ω generators (V_G in Fig. 1 (c)), sinusoidal in time, spaced apart by 90° and with 90° phase shift, are connected between the legs and the upper ring and are used for exciting the antenna at the frequency of 128 MHz. In correspondence of the generators, two tuning capacitances are used, one in series (C_S) and the other in parallel (C_P) to the generator ($C_T = C_S + C_P$) (see Fig. 1 (c)). This excitation simulates the one usually adopted in real coils [18,19], and produces a magnetic field with a circular clockwise polarization, with respect to the positive z-axis, necessary for maximum coupling with nuclear proton spin. A single generator with Gaussian time behavior is used for studying the frequency behavior of the reflection coefficient, from which the TEM resonance frequencies can be evaluated [18,19].

For sake of comparison, a 64 MHz low-pass birdcage coil has been also considered. The birdcage is identical to the TEM coil but the end rings are not in contact with the external shield. As a consequence, while in TEM coils the current paths close along the shield, in birdcages they close through the legs [24].

A box model (30×20×60 cm) and three 5-mm resolution anatomical models, derived from the Virtual Family (Duke) data set [25], have been considered.

The Duke anatomical model is a highly detailed and realistic model of the human body directly derived from MRI scans of a healthy volunteer. In particular, the three considered anatomical models are partial body models and are used for studying MRI exams targeting the thoracic, abdominal and head regions of the body. Figure 2 shows these models with their positioning inside the TEM coil without the shield. All the anatomical models have been obtained by positioning the Duke data set (110×58×360 cells and 78 different tissues) inside the TEM coil and removing body portions far from the coil where the RF power deposition is expected to be negligible. The use of the reduced models gives rise to consistent savings of memory occupation and execution times, in both EM and thermal simulations, without reducing the accuracy of the computed results [17].

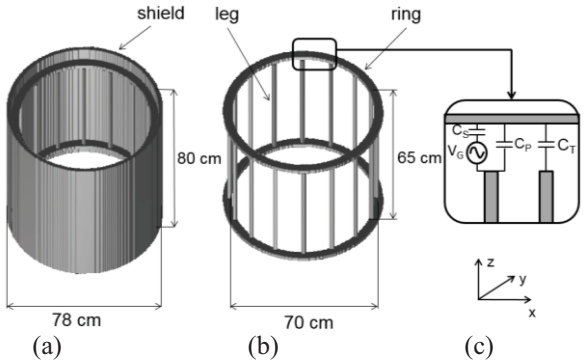

Fig. 1. (a) Shielded TEM coil, (b) TEM coil without the shield, and (c) zoom on the leg-ring connection region.

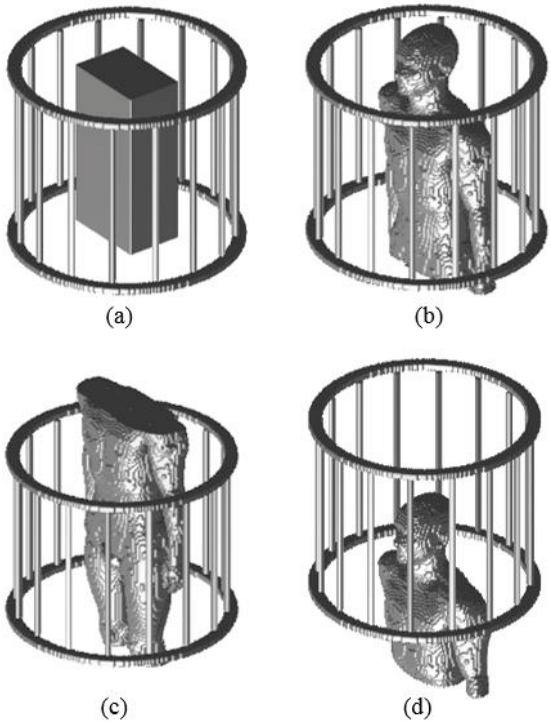

Fig. 2. (a) Box model, and three anatomical models corresponding to MRI exams targeting the: (b) thoracic, (c) abdominal, and (d) head regions of the body with their positioning inside the TEM antenna with removed shield.

The considered pacemaker is constituted by a copper box (4×1×5 cm) equipped with a catheter (see

Fig. 3 (a)). The catheter consists of a cylindrical copper wire with a diameter of 0.8 mm. The copper wire is covered by an insulating material with an external diameter of 2 mm from which the last 2 mm before the catheter tip have been removed (uncapped catheter – UC). The UC geometry represents a good model of commercially available monopolar catheters [17].

In the human box model, the copper box is placed 1 cm below the box surface and the catheter is placed on the same plane as in a typical experimental set-up (see Fig. 3 (b)) [26].

In the anatomical models the pacemaker is inserted in the subcutaneous fat layers in the left part of the thorax with a placement, based on computed tomography (CT) scans of patients with pacemaker, approximating the clinical one (see Fig. 4) [27]. In the body placement, the catheter roughly follows the vein path to the heart cavities of the anatomical model and is inserted a few millimeters in the right ventricle internal wall. In order to avoid unrealistic crossing of the catheter through different tissues, the vein path has been slightly modified at some points by adding cylindrical blood vessels of 3 mm diameter. This ensures that the catheter is always inserted into the vessels.

Electromagnetic simulations have been performed using a code based on a conformal FDTD scheme with graded-mesh [28]. The FDTD domain has been closed applying a 4-layer uniaxial perfectly matched layer (UPML) boundary condition with parabolic profile and 1% nominal reflection coefficient [29]. The investigated region has been divided in cells of variable side, from 0.5 mm (around the catheter) to 5 mm. For the permittivity, conductivity, and density data of the 78 Duke tissues, the values in [30] have been considered. At 128 MHz the wavelength in the tissue with the highest permittivity is about 28 cm. Hence, the maximum cell size (5 mm) corresponds to about 1/50 of the wavelength, resulting in a phase-spread ratio better than 0.999 for all propagation angles.

In all the simulations performed for the evaluation of the SAR distributions, a 128 MHz harmonic excitation has been applied. Once steady state conditions are reached, the amplitude of the three electric field components is determined, in the center of each cell, and the SAR distribution is calculated [17]. The evaluated SAR values are the peak SAR averaged over the mass of 1 FDTD cell (0.125 g - $SAR_{0.125g}$ or 0.125 mg - $SAR_{0.125mg}$ depending on the used mesh), the peak SAR averaged over 10 g (SAR_{10g}), and the SAR averaged over the whole body (SAR_{WB}), which is the quantity to be evaluated for assessing the compliance with IEC standard [7].

The temperature distribution T = T(r,t), inside the considered body models, has been computed by using the bioheat equation (BHE) [31,32]. To obtain a finite-difference formulation of the BHE, the body model is divided in cells of variable side, equal to those used in the FDTD computations, and the temperature is evaluated in a grid of points defined at the center of the cells. The BHE has been solved by using an alternate direction implicit finite difference (ADI-FD) formulation [17,33].

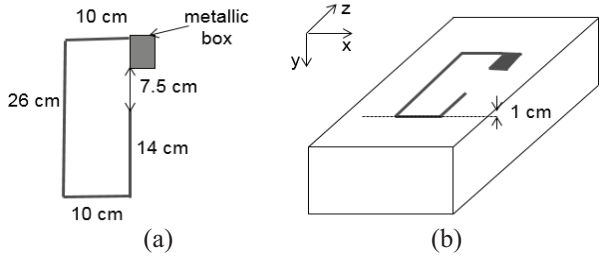

Fig. 3. (a) Pacemaker model, and (b) pacemaker positioning inside the box.

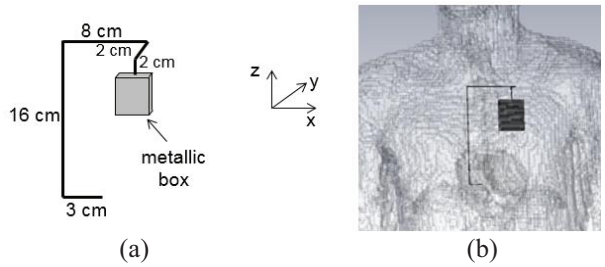

Fig. 4. (a) Pacemaker model, and (b) pacemaker positioning inside the thorax.

The numerical codes used in this paper for the solution of the EM and thermal problems in patients exposed to the field emitted by MRI antennas have been previously validated [16]. In particular, in [16] the SAR_{WB} values, computed by using the FDTD code in a box model of the human body exposed to a birdcage antenna, showed a very good agreement with measurements performed by means of a calorimetric set-up. Similarly, temperature time behaviors at the tip of a pacemaker placed inside a box model of the thorax, measured with a fluoroptic thermometer (Luxtron 3100), were in good agreement with thermal simulations performed with the ADI-FD code.

III. RESULS AND DISCUSSION

In all the simulations, the TEM coil has been tuned so that the mode with highest field homogeneity occurs at 128 MHz. This is accomplished by setting C_T = 9.34 pF, C_S = 4.67 pF, and C_P = 4.67 pF.

A. Box model without the pacemaker

The first considered thorax model is a parallelepiped box (30 cm × 20 cm × 60 cm) whose

electrical properties mimic those of an average human tissue at the considered frequency. Permittivity (ε), conductivity values (σ) and density (ρ) of the model are equal to 69.0, 0.62 S/m and 1006 kg/m^3, respectively. SAR values have been obtained for an antenna radiated power producing a SAR_{WB} of 1 W/kg (P_{RAD} = 40.8 W) that is a typical value for MRI examinations [10,16]. For the considered coil, the induced $SAR_{0.125g}$, and SAR_{10g} are 4.3, and 3.4 W/kg, respectively. Figure 5 (a) shows the SAR distribution on a coronal section passing 1 cm below the box surface (where the pacemaker will be placed). While Fig. 5 (b) shows the SAR distribution on the central axial section. Figure 5 (b) outlines that the highest local SAR values are achieved close to the external surface of the box and, in particular, for a circular left polarized EM field, they are close to the bottom-right and upper-left corners. It is worth noting that the SAR distribution does not show horizontal symmetry. In fact, while the structure is symmetric, the field excitation presents an azimuthal phase shift.

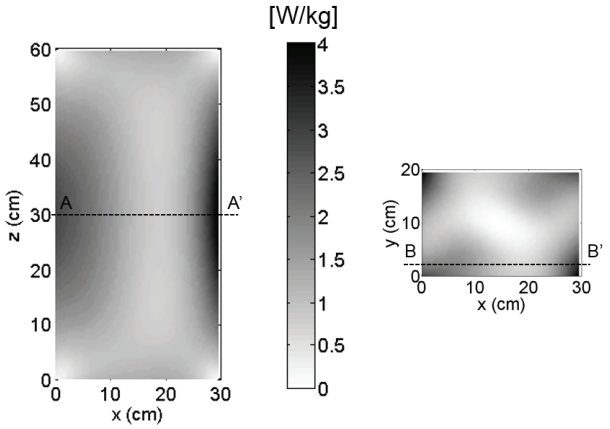

Fig. 5. (a) SAR distributions for the TEM coil on a coronal section 1 cm below the box surface, and (b) on the central axial section. (a) Corresponds to section B-B' in (b), and (b) corresponds to section A-A' in (a).

Thermal simulations have been performed by using the ADI-FD code with a box thermal conductivity (K) equal to 0.2 W/(m·°C), specific heat capacity (C) of 4178 J/(kg·°C) and neglecting the blood perfusion (B = 0). A convection coefficient equal to 10 W/(m^2·°C) has been also assumed at the air-box interface. Figure 6 shows the temperature distribution over the same coronal section of Fig. 5 (a). A maximum temperature increase of about 2.3 °C after 60 minutes of exposure has been observed. It is interesting to note that the highest temperature increments are achieved at the point where the peak SAR_{10g} is located (x = 28 cm, z = 30 cm). This is due to the fact that the point of the peak $SAR_{0.125g}$ (x = 30 cm, z = 30 cm) is close to the air-tissue interface where the thermal convection reduces the temperature increments.

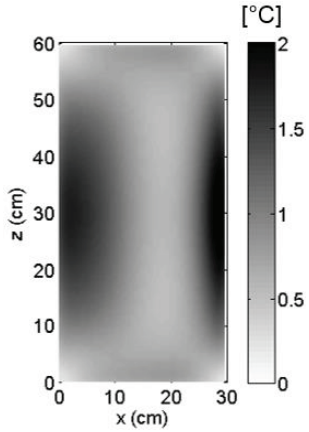

Fig. 6. Temperature distribution on a coronal section 1 cm below the box surface.

B. Anatomical models without the pacemaker

The first considered anatomical model is the one suitable for simulating an MRI examination at the level of the thorax (see Fig. 2 (b)). For a radiated power of 40.8 W (equal to that used for the box model of the thorax) about 35.5 W are absorbed in the reduced Duke.

Since the absorption in the remaining part of the body can be considered negligible, a SAR_{WB} of 0.49 W/kg can be extrapolated.

Figure 7 (a) shows the computed SAR distribution in a central coronal section. The peak $SAR_{0.125g}$ is 10.7 W/kg and has been obtained in the skin in the neck-shoulder region while the peak SAR_{10g} is 4.7 W/kg and has been obtained in the neck muscle.

Then, the second position (abdominal region examination) has been considered (see Fig. 2 (c)). The obtained results in terms of SAR are: 0.46, 6.2, 28.3 W/kg for the SAR_{WB}, SAR_{10g} and $SAR_{0.125g}$, respectively. Figure 7 (b) shows the SAR map in the central coronal section for this exposure. In this case, the peak $SAR_{0.125g}$ is located in the skin of the inguinal region and the peak SAR_{10g} in the leg muscle.

Finally, considering the head region examination (see Fig. 2 (d)), the obtained SAR_{WB}, SAR_{10g} and $SAR_{0.125g}$ have been 0.35, 8.2 and 26.2 W/kg, respectively. Figure 7 (c) shows the SAR map in the central coronal section. Similarly to the thorax examination, the peak $SAR_{0.125g}$ is located in the skin of the neck-shoulder region and the peak SAR_{10g} in the neck muscle.

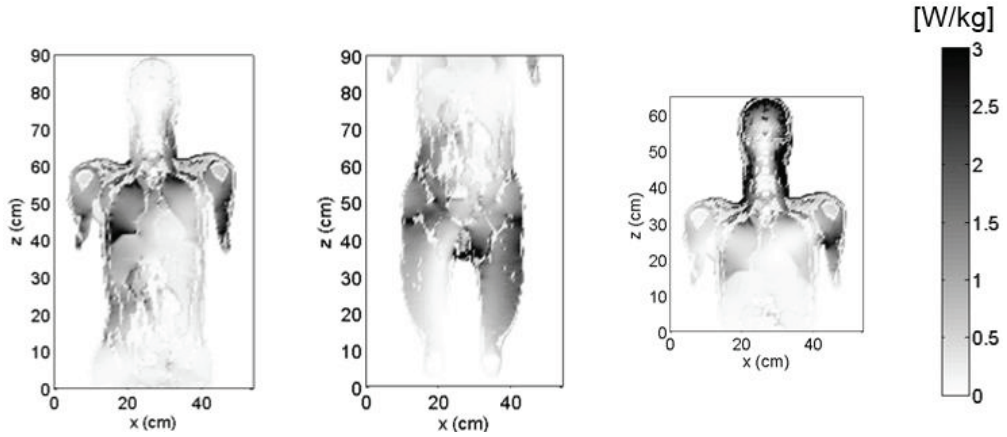

Fig. 7. SAR distributions on a central coronal section for the three models corresponding to MRI exams targeting the: (a) thoracic, (b) abdominal, and (c) head regions.

Starting from the obtained SAR results, temperature distributions have been computed in the absence and in the presence of perfusion by using the tissue thermal parameters available from [34]. The time behavior of temperature increment during a 1 hour MRI investigation has been computed at the points where the peak SAR are located. The considered exposure times are longer than those of a typical MRI examination, but have been considered in order to better evaluate the heating time constants. With reference to the thorax examination, Fig. 8 shows temperature increments as a function of time. The figure shows the strong limiting effect on temperature elevation of the blood perfusion. In fact the maximum temperature increment is 2.8 °C in the absence of perfusion and reduces to 1.1 °C when the blood perfusion is taken into account. The ratio between the maximum temperature increment in the absence and in the presence of perfusion is 2.5, very similar to that found in [35] by comparing measured temperature increases in a phantom model and in the human forearm. Moreover, both in the absence and in the presence of blood perfusion the highest temperature increments are obtained around the point where the SAR_{10g} is located.

Concerning the other two body positions, in the presence of blood perfusion, the T_{MAX} after one hour exposure is 1.1 °C and 1.8 °C for the abdomen and head examinations, respectively. It is important to note that the IEC SAR_{WB} limits for the normal and first level controlled operating modes are 2 W/kg and 4 W/kg, respectively. Due to the linearity of BHE, if these values are reached, temperature increments about 4 times and 8 times higher, with respect to those above reported, will be obtained. Under these conditions local tissue temperature limits issued by IEC for normal and first level controlled operating modes are overcome.

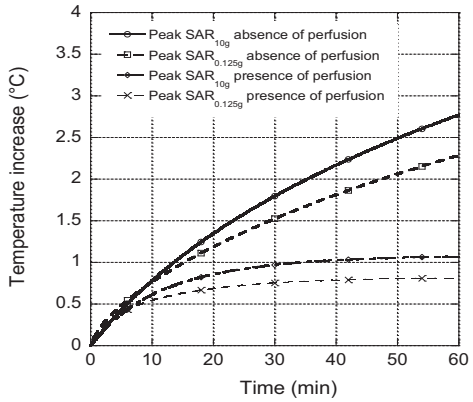

Fig. 8. Temperature time behaviour in the absence and in the presence of blood perfusion for the thorax examination.

C. Box model with the pacemaker

To study the exposure of a patient with an implanted pacemaker to a 3-T system, a pacemaker equipped with a unipolar catheter has been inserted inside the box model of the thorax in a typical operating position with the catheter tip 7.5 cm far from the pacemaker (see Fig. 3). The exposure has been studied exciting the coil with a power of 40.8 W that is the one producing a SAR_{WB} of 1 W/kg in the box in the absence of the pacemaker.

The current flowing along the catheter has been computed as the circulation of the magnetic field around the catheter axis. Figure 9 (a) shows the obtained current distribution. The distance along the wire from the point in which the catheter is inserted in the pacemaker is reported on the horizontal axis (the catheter length is 60 cm). The obtained current distribution can be explained observing that the current

inside the catheter wire is mainly produced by the electric field component, found in the absence of the wire (unperturbed field), parallel to the wire axis [13-17]. Moreover, for the considered 128 MHz field, the wavelength in the box tissue is about 28 cm, and hence, about half of the total wire length; this results in resonance phenomena along the wire. Finally, the maximum on the current behavior along the catheter, at distance equal to zero, can be explained as a short circuit effect of the pacemaker box, and the minimum at the catheter tip as an open end effect.

Figure 9 (b) shows the SAR distributions in a coronal section passing through the catheter. The figure outlines that the highest SAR values are obtained at the catheter tip. SAR_{WB}, peak $SAR_{0.125mg}$, and SAR_{10g} are 1.0, 7800, and 16.6 W/kg, respectively. In the presence of the pacemaker, the SAR_{WB} remains equal to the value without the pacemaker. To complete the dosimetry investigation, a thermal study has been then performed. In these simulations the tissue parameters used in the absence of the pacemaker have been employed. For the plastic insulation (p) and wire (w), instead, the values in [16] have been considered [$Cp = 1500$ J/(kg°C), $K_p = 0.2$ W/(m°C), $\rho_p = 1000$ kg/m^3; $C_w = 385$ J/(kg°C), $K_w = 401$ W/(m°C), $\rho_w = 8960$ kg/m^3]. The previously computed SAR distribution has been assumed as thermal source and a thermal transient analysis has been launched in the ADI-FD thermal solver for a duration of 15 minutes, that is the typical duration of an MRI examination [22].

Figure 10 (a) shows the time behavior of the simulated temperature along the catheter axis. After 15 minutes of exposure, a temperature increment of about 50 °C at a point just above the catheter tip has been obtained. The figure also outlines the reduction in temperature increase at points far from the tip.

Figure 10 (b) shows a map of the temperature distribution, after 15 minutes of exposure, on a coronal section passing through the pacemaker plane. The figure outlines a high temperature hot spot at the catheter tip and some lower hot spots in correspondence of the catheter bends.

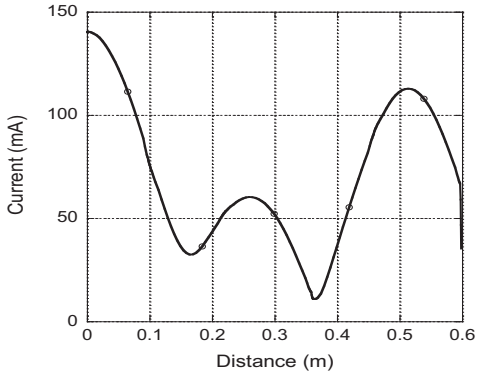

(a)

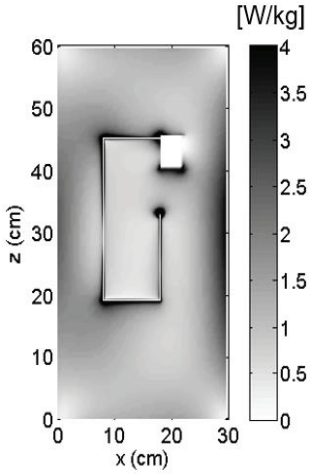

(b)

Fig. 9. (a) Current distribution along the catheter, and (b) SAR distribution on a coronal section 1 cm below the box surface.

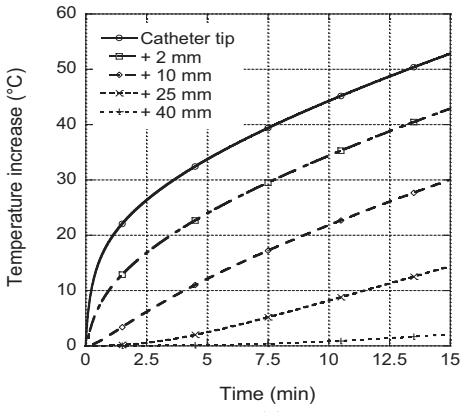

(a)

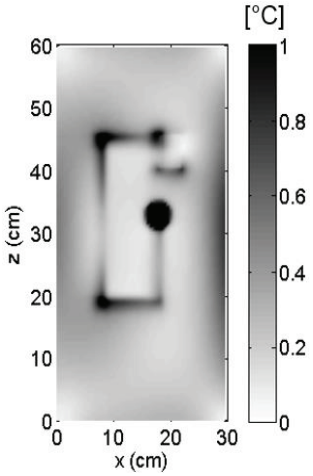

(b)

Fig. 10. (a) Temperature time behavior along the catheter axis, and (b) temperature distribution on a coronal section 1 cm below the box surface.

D. Anatomical models with the pacemaker

In order to achieve realistic SAR and temperature evaluations for a patient with an implanted pacemaker exposed to MRI fields, the pacemaker has been inserted inside the left part of the thorax of the Duke model, that in turn has been inserted inside the TEM coil and exposed to a 128 MHz left polarized field with a radiated power of 40.8 W (as for the box model). In particular, two configurations have been considered. In the first case (connected), the PM case is connected to the catheter as in Fig. 4 (a), while in the second case (disconnected), the first 2 cm of the catheter have been removed simulating the condition of a patient with the pulse generator not attached [36].

Figure 11 shows the current along the catheter, as a function of the distance from the point in which the catheter is inserted in the metallic box. In the considered cases the catheter length (31 cm) is comparable with the field wavelength in the body and only one resonance is present in the spatial current distribution. Moreover, a strong reduction in the current is observed in correspondence of the tip where the catheter is uncapped. The main difference between the two considered cases is the higher current along the catheter (78 mA versus 64 mA peak values) and at the catheter tip (20.9 mA versus 17.8 mA) of the disconnected case with respect to the connected one. Moreover, the short circuit effect of the PM case and the open end effect of the catheter tip, already evidenced in the previous section, are confirmed.

The computed $SAR_{0.125mg}$ at the catheter tip are 2670 W/kg and 3680 W/kg, while the SAR_{10g} are 5.5 W/kg and 7.5 W/kg for the connected and disconnected cases, respectively. These results confirm those in [36] where it was evidenced that the heating produced by MRI in patients with the pacemaker pulse generator disconnected was higher than that achieved when the pulse generator was attached. Similarly to the box exposure, the presence of the pacemaker does not affect significantly the SAR_{WB}. Moreover, the SAR distribution is similar to that in the absence of the pacemaker except for a strong hot spot at the catheter tip resulting from the high current densities induced in tissues around the tip.

Concerning the exposure of a patient with pacemaker when performing an examination at the level of the abdomen, a peak $SAR_{0.125mg}$ at the catheter tip of 510 W/kg has been computed. The peak SAR_{10g} is 6.2 W/kg, as in the absence of the pacemaker, while the SAR_{10g} at the catheter tip in the heart is 1.0 W/kg. Eventually, the SAR_{WB} is still 0.46 W/kg.

The exposure of a patient with pacemaker when performing an examination at the level of the head gives rise to SAR_{WB} and SAR_{10g} of 0.35 and 11.6 W/kg, as in the exposure without the pacemaker. The $SAR_{0.125mg}$ and SAR_{10g} at the catheter tip are 990 and 2.0 W/kg, respectively.

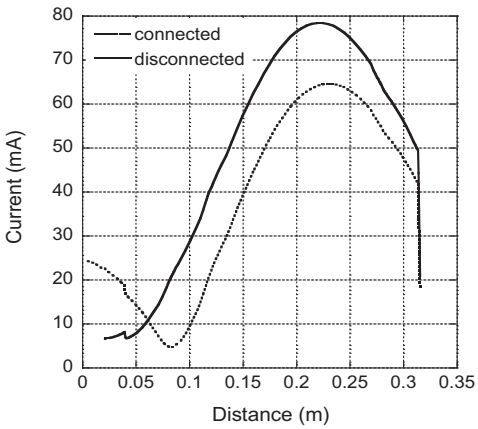

Fig. 11. Current distribution along the catheter inserted inside the left part of the thorax of the Duke model.

In order to assess the thermal risk associated with the computed SAR values, the graded mesh ADI solution of the bioheat equation has been applied. In this case, the heart-blood convection coefficient (HB) has been assumed equal to 1000 W/(m^2·°C) [37].

Figure 12 shows temperature versus time at the catheter tip, for the connected case, computed by neglecting the perfusion and in the presence of perfusion. In the first case, temperature increments of about 12 °C after 15 minutes exposure are obtained and the time behavior indicates an exponentially growing trend with a time constant of the order of hours. The presence of blood perfusion reduces temperature increments to about 3.0 °C and, in this case, the steady state is reached in a few minutes. In both considered cases, the temperature increments are higher than those indicated as safe in the IEC Standard [7].

Concerning the other two body positions, in the presence of blood perfusion, the T_{MAX} at the catheter tip after one hour exposure are 0.75 °C and 1.8 °C in the abdomen and head examinations, respectively.

These results indicate that only if the pacemaker is far from the coil center (as in the abdomen and head examinations) temperature increments, produced by the interaction of the RF field with the pacemaker, are compliant with the IEC limits. This result is in agreement with experimental findings [21,22] suggesting the possibility, for patients bearing a pacemaker, to perform MRI examinations when the region to scan is far from the pacemaker.

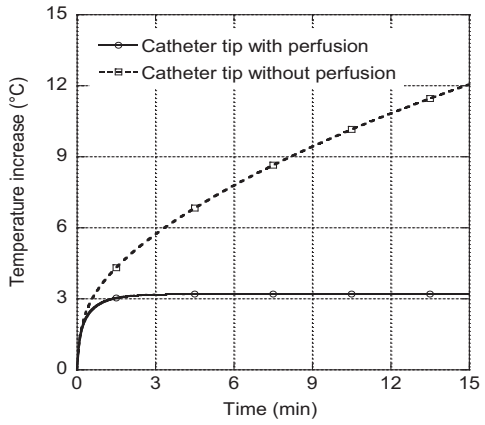

Fig. 12. Temperature time behavior at the catheter tip.

E. Comparison between TEM and birdcage coils

In order to compare the 3-T system with 1.5-T ones, some of the previously reported simulations have been repeated by using the 64 MHz birdcage coil previously described (see Section II).

In these simulations, the birdcage has been tuned to 64 MHz by using capacitances of 11.4 pF. Concerning the box simulations, permittivity and conductivity values of 78.2 and 0.6 S/m have been considered, respectively, while for the simulations with the Duke model the tissue permittivity and conductivity values in [30] have been used.

The results for the 128 MHz coil are reported in Table 1, 3rd column, while those for the 64 MHz coil in Table 1, 4th column. The table shows that in the absence of the pacemaker, SAR and temperature increments obtained at 128 MHz are slightly higher than those achieved at 64 MHz.

It is worth noting that, the reported SAR values have been obtained for an antenna-radiated power producing a SAR_{WB} of 1 W/kg in the box model. This radiated power gives rise in the box central region to magnetic fields of about 1.2 A/m and 1.6 A/m at 128 MHz and 64 MHz, respectively. TEM and birdcage coils can be compared considering the same RF magnetic field in the investigated sample. To this end, a value of 2.4 A/m has been chosen. This value is close to the typical mean field value necessary in MRI to produce a 90° flip angle in the sample [10]. Under these conditions, SAR_{WB} of 4 W/kg and 2.25 W/kg are obtained at 128 MHz and 64 MHz, respectively, with a SAR_{WB} ratio of 1.78, very similar to that found in [38] for a doubling of the frequency.

The presence of the pacemaker gives rise to higher SAR_{10g} and T_{MAX} in the birdcage coil with respect to the TEM one. This result can be explained comparing the SAR distributions of the box and of the anatomical model at 64 MHz reported in Fig. 13 (a) and (b) with the corresponding distributions at 128 MHz (see Fig. 5 (a) and 7 (a)). From the figures, the higher penetration depth of the 64 MHz field with respect to the 128 MHz one is evident. This, in turn, gives rise to higher currents at the catheter tip of the pacemaker exposed in the birdcage with respect to the TEM coil (22.4 mA versus 17.8 mA) and consequently to the higher SAR_{10g} and T_{MAX} at 64 MHz with respect to 128 MHz.

The superficial absorption of the 128 MHz field is also the responsible for the higher SAR and temperature increments in the TEM coil in the absence of the pacemaker.

Table 1: Comparison between TEM coils operating at 128 MHz and birdcage coils operating at 64 MHz

		3 T (128 MHz) TEM coil	1.5 T (64 MHz) Birdcage Coil
BOX	SAR_{WB}	1.0 W/kg	1.0 W/kg
//	SAR_{10g}	3.4 W/kg	2.9 W/kg
//	T_{MAX}	0.7 °C	0.6 °C
DUKE THOR.	SAR_{WB}	0.49 W/kg	0.46 W/kg
//	SAR_{10g}	4.7 W/kg	4.4 W/kg
//	T_{MAX} (WP)	1.1 °C	0.9
BOX + PM	SAR_{WB}	1.0 W/kg	1.0 W/kg
//	SAR_{10g}	16.6 W/kg	17.1 W/kg
//	T_{MAX}	53 °C	55 °C
D. THOR + PM	SAR_{WB}	0.49 W/kg	0.46 W/kg
//	SAR_{10g}	5.5 W/kg	14.0 W/kg
//	T_{MAX} (WP)	3 °C	8.3 °C

WP = with perfusion. T_{MAX} are temperatures after 15 min exposure.

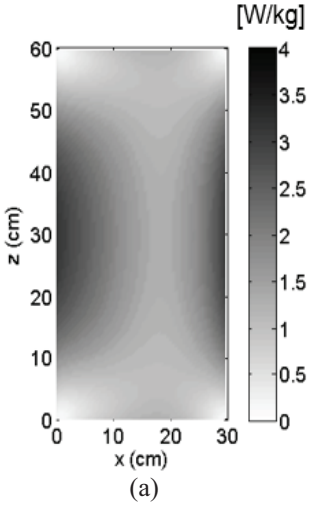

(a)

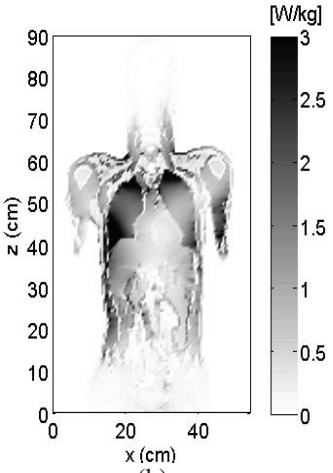

(b)

Fig. 13. (a) SAR distribution for the birdcage coil on a coronal section 1 cm below the box surface, and (b) on a central coronal section of the anatomical model (thoracic examination).

IV. CONCLUSION

In this paper, a TEM coil operating at 128 MHz in a 3-T MRI system has been studied in terms of the interaction with patients. A box model and an anatomical body model in different positions have been considered with or without the presence of an implanted monopolar pacemaker.

In the absence of the pacemaker, the power absorption in the box model is mainly concentrated in the external part of the box, while the region with highest temperature increments shows a slight shift towards the inner part of the box. The maximum temperature elevations in the box model are very similar to those obtained in the thorax model in the absence of blood perfusion. The highest SAR_{WB} have been obtained for the thorax examination and the lowest for the head one, while the opposite holds for the peak SAR_{10g} values.

The peak temperature increments computed inside the body in the presence of blood perfusion comply with IEC limits. However, if SAR_{WB} values are increased to the corresponding IEC limits for the normal and first level controlled operating modes, temperature limits would be overcome. Concerning the relation between maximum temperature increases and SAR_{10g}, the obtained results indicate a factor of about 0.2° C/(W/kg).

The insertion of a pacemaker inside the box model gives rise to very high peak $SAR_{0.125mg}$ and temperature increments in the absence of perfusion. The inclusion of the blood perfusion strongly reduces temperatures increments that, however, remain higher than IEC limits whenever the pacemaker is close to the coil center. In the presence of the pacemaker, high SAR values are achieved close to the catheter tip inside the heart. In this case, the factor linking the SAR_{10g} at the catheter tip to temperature increments is between 0.6 and 0.9 °C/(W/kg) depending on the SAR distribution.

A comparison between TEM coil and birdcage indicates that the 3-T TEM coil produces lower SAR and temperature increments with respect to a classic 64-MHz (1.5-T system) birdcage antenna for patients with implanted pacemaker.

REFERENCES

[1] ICNIRP Statement on: "Medical magnetic resonance (MR) procedures: protection of patients," *Health Phys*., vol. 87, pp. 197-216, 2004.

[2] J. R. Gimbel and E. Kanal, "Can patients with implantable pacemakers safely undergo magnetic resonance imaging?," *J. Am. Coll. Cardiol*., vol. 43, pp. 1325-1327, 2004.

[3] M. H. Schoenfeld, "Contemporary pacemaker and defibrillator device therapy: challenges confronting the general cardiologist," *Circulation*, vol. 115, pp. 638-653, 2007.

[4] S. Achenbach, B. Moshage, W. Diem, T. Bieberle, V. Schibgilla, and K. Bachmann "Effects of magnetic resonance imaging on cardiac pacemakers and electrodes," *Am. Heart. J*., vol. 134, pp. 467-473, 1997.

[5] T. Sommer, C. Vahlhaus, G. Lauck, A. von Smekal, M. Reinke, U. Hofer, W. Bloch, F. Traber, C. Schneider, J. Gieseke, W. Jung, and H. Schild, "MR imaging and cardiac pacemaker: in-vitro evaluation and in-vivo studies in 51 patients at 0.5 T," *Radiology*, vol. 215, pp. 869-879, 2000.

[6] A. Roguin, M. M. Zviman, G. R. Meininger, E. R. Rodrigues, T. M. Dickfeld, D. A. Bluemke, A. Lardo, R. D. Berger, H. Calkins, and H. R. Halperin, "Modern pacemaker and implantable cardioverter/defibrillator systems can be magnetic resonance imaging safe, in vitro and in vivo assessment of safety and function at 1.5 T," *Circulation*, vol. 110, pp. 475-482, 2004.

[7] International Electrotechnical Commission, International Standard, Medical Electrical Equipment–IEC 60601-2-33, *Particular Requirements for the Basic Safety and Essential Performance of Magnetic Resonance Equipment for Medical Diagnosis*, 3rd edition, Geneva: IEC, 2010.

[8] U. D. Nguyen, S. Brown, I. A. Chang, J. K. Krycia, and M. S. Mirotznik, "Numerical evaluation of heating of the human head due to magnetic resonance imaging," *IEEE Trans. Biomed. Eng*., vol. 51, pp. 1301-1309, 2004.

[9] W. Liu, C. M. Collins, and M. B. Smith, "Calculations of B1 distribution, specific energy

absorption rate, and intrinsic signal-to-noise ratio for a body-size birdcage coil loaded with different human subjects at 64 and 128 MHz," *Appl. Magn. Reson*., vol. 29, pp. 5-18, 2005.

[10] C. M. Collins, S. Li, and M. B. Smith, "SAR and B1 field distributions in a heterogeneous human head model within a birdcage coil," *Magnetic Resonance in Medicine*, vol. 40, pp. 847-856, 1998.

[11] Z. Wang and J. C. Lin, "SAR calculations in MRI scanning systems," *IEEE Microwave Magazine*, vol. 13, pp. 22-29, 2012.

[12] H. S. Ho, "Safety of metallic implants in magnetic resonance imaging," *J. Magn. Reson. Imaging*, vol. 14, pp. 472-477, 2001.

[13] J. A. Nyenhuis, S. M. Park, and R. Kamondetdacha, "MRI and implanted medical devices: basic interactions with an emphasis on heating," *IEEE Trans. Dev. Mat. Reliab*., vol. 5, pp. 467-480, 2005.

[14] S. M. Park, R. Kamondetdacha, A. Amjad, and J. A. Nyenhuis, "MRI safety: RF induced heating on straight wires," *IEEE Trans. Magn*., vol. 41, pp. 4197-4199, 2005.

[15] M. A. Stuchly, H. Abrishamkar, and M. L. Strydom, "Numerical evaluation of radio frequency power deposition in human models during MRI," *Proc. IEEE EMBS Int. Conf*., New York City, USA, pp. 272-275, 2006.

[16] S. Pisa, G. Calcagnini, M. Cavagnaro, E. Piuzzi, E. Mattei, and P. Bernardi, "A study of the interaction between implanted pacemakers and the radio frequency field produced by magnetic resonance imaging apparatus," *IEEE Trans. Electromag. Compat*., vol. 50, pp. 35-42, 2008.

[17] S. Pisa, P. Bernardi, M. Cavagnaro, and E. Piuzzi, "Power absorption and temperature elevation produced by magnetic resonance apparatus in the thorax of patients with implanted pacemakers," *IEEE Trans. Electromag. Compat*., vol. 52, pp. 32-40, 2010.

[18] J. T. Vaughan, G. Adriany, M. Garwood, E. Yacoub, T. Duong, L. Dela Barre, P. Andersen, and K. Ugurbil, "Detunable transverse electromagnetic (TEM) volume coil for high-field NMR," *Magnetic Resonance in Medicine*, vol. 47, pp. 990-1000, 2002.

[19] G. Bodganov and R. Ludwing, "Coupled microstrip line transverse electromagnetic resonator model for high-field magnetic resonance imaging," *Magnetic Resonance in Medicine*, vol. 47, pp. 579-593, 2002.

[20] M. Alecci, C. M. Collins, M. B. Smith, and P. Jezzard, "Radio frequency magnetic field mapping of a 3 tesla birdcage coil: experimental and theoretical dependence on sample properties," *Magnetic Resonance in Medicine*, vol. 46, pp. 379-385, 2001.

[21] J. R. Gimbel, "Magnetic resonance imaging of implantable cardiac rhythm devices at 3.0 tesla," *Pacing Clin. Electrophysiol*, vol. 31, pp. 795-801, 2008.

[22] F. G. Shellock, J. Begnaud, and D. M. Inman, "Vagus nerve stimulation therapy system: in vitro evaluation of magnetic resonance imaging-related heating and function at 1.5 and 3 tesla," *Neuromodulation*, vol. 9, pp. 204-213, 2006.

[23] M-A. Golombeck and O. Dossel, "MR-tomography on patients with heart pacemakers – a numerical study," *Proc. IEEE EMBS Int. Conf*., San Francisco, USA, pp. 1076-1079, 2004.

[24] J. C. Lin, P. Bernardi, S. Pisa, M. Cavagnaro, and E. Piuzzi, "Antennas for medical therapy and diagnostics," *in Modern Antenna Handbook*, ed. C. Balanis, Wiley, pp. 1377-1428, 2008.

[25] A. Christ, W. Kainz, E. G. Hahn, K. Honegger, M. Zefferer, E. Neufeld, W. Rascher, R. Janka, W. Bautz, J. Chen, B. Kiefer, P. Schmitt, H-P. Hollenbach, J. Shen, M. Oberle, D. Szczerba, A. Kam, J. W. Guag, and N. Kuster, "The virtual family development of surface-based anatomical models of two adults and two children for dosimetric simulations," *Phys. Med. Biol*., vol. 55, pp. 23-38, 2010.

[26] E. Mattei, M. Triventi, G. Calcagnini, F. Censi, W. Kainz, G. Mendoza, H. I. Bassen, and P. Bartolini, "Complexity of MRI induced heating on metallic leads: experimental measurements of 374 configurations," *Biomedical Engineering OnLine*, 7: 11, 2008.

[27] A. L. Aguilera, Y. V. Volokhina, and K. L. Fisher, "Radiography of cardiac conduction devices: a comprehensive review," *RadioGraphics*, vol. 31, pp. 1669-1682, 2011.

[28] S. Pisa, M. Cavagnaro, E. Piuzzin, and V. Lopresto, "Numerical-experimental validation of a GM-FDTD code for the study of cellular phones," *Microwave Opt. Technol. Lett*., vol. 47, pp. 396-400, 2005.

[29] A. Taflove and S. C. Hagness, *Computational Electrodynamics: The Finite-Difference Time-Domain Method*, Boston, MA: Artech House, 2000.

[30] D. Andreuccetti, R. Fossi, and C. Petrucci, "An internet resource for the calculation of the dielectric properties of body tissues in the frequency range 10 Hz - 100 GHz," *Internet document; URL:http://niremf.ifac.cnr.it/tissprop/*.

[31] H. H. Pennes, "Analysis of tissue and arterial blood temperatures in resting forearm," *J. Appl. Physiol*., vol. 1, pp. 93-122, 1948.

[32] P. Bernardi, M. Cavagnaro, S. Pisa, and E. Piuzzi,

"Specific absorption rate and temperature elevation in a subject exposed in the far-field of radio-frequency sources operating in the 10-900 MHz range," *IEEE Trans. Biomed. Eng*., vol. 50, pp. 295-304, 2003.

[33] S. Pisa, M. Cavagnaro, E. Piuzzi, P. Bernardi, and J. C. Lin, "Power density and temperature distributions produced by interstitial arrays of sleeved-slot antennas for hyperthermic cancer therapy," *IEEE Trans. Microwave Theory Tech*., vol. 51, pp. 2418-2426, 2003.

[34] URL: http://www.itis.ethz.ch/itis-for-health/tissue-properties/database/.

[35] S. Oh, Y-C. Ryu, G. Carluccio, C. T. Sica, and C. M. Collins, "Measurement of SAR-induced temperature increase in a phantom and in vivo with comparison to numerical simulation," *Magnetic Resonance in Medicine*, vol. 71, pp. 1923-1931, 2014.

[36] F. G. Shellock, S. Valencerina, and L. Fischer, "MRI-related heating of pacemaker at 1.5- and 3-tesla: evaluation with and without pulse generator attached to leads," *Circulation*, vol. 112: Supplement II, pp. 561, 2005.

[37] S. Tungjitkusolmun, V. R. Vorperian, N. Bhavaraju, H. Cao, J. Z. Tsai, and J. G. Webster, "Guidelines for predicting lesion size at common endocardial locations during radio-frequency ablation," *IEEE Trans. Biomed. Eng*., vol. 48, pp. 194-201, 2001.

[38] Z. Cao, J. Park, Z-H. Cho, and C. M. Collins, "Numerical evaluation of image homogeneity, signal-to-noise ratio, and specific absorption rate for human brain imaging at 1.5, 3, 7, 10.5, and 14 T in an 8-channel transmit/receive array," *J. Magn. Reson. Imaging*, DOI 10.1002/jmri.24689, pp. 1-7, 2014.

Stefano Pisa received the Electronic Engineering and Ph.D. degrees from the University of Rome "La Sapienza," Rome, Italy, in 1985 and 1988, respectively. In 1989, he joined the Department of Electronic Engineering, University of Rome "La Sapienza," as a Researcher. Since 2001, he has been an Associate Professor with the same university. His research interests are the interaction between electromagnetic fields and biological systems, therapeutic and diagnostic applications of electromagnetic fields, and the modeling and design of MW circuits. He has authored over 150 scientific papers and numerous invited presentations at international workshops and conferences. He serves as a Reviewer for different international journals. He is currently "Consulting Member" of the "Scientific Committee on Physics and Engineering" of the "International Commission on Non-Ionizing Radiation Protection" and a Member of the Advisory Group of the Dutch project "Electromagnetic Fields and Health".

Emanuele Piuzzi received the M.S. (cum laude) and Ph.D. degrees in Electronic Engineering from Sapienza University of Rome, Rome, Italy, in 1997 and 2001, respectively. He is currently an Assistant Professor in Electrical and Electronic Measurements with the Department of Information Engineering, Electronics and Telecommunications (DIET), Sapienza University of Rome. He is the co-author of over 100 publications.

His current research activities include the measurement of complex permittivity of materials, time domain reflectometry applications, biomedical instrumentation design, evaluation of human exposure to electromagnetic fields. Piuzzi is a Member of the Italian Group of Electrical and Electronic Measurements (GMEE) and of the Italian Electrotechnical Committee (CEI). He serves as a Reviewer for several international journals, mainly in the field of instrumentation and measurement.

Fast Design of Jerusalem-Cross Parameters by Equivalent Circuit Model and Least-Square Curve Fitting Technique

Hsing-Yi Chen, Tsung-Han Lin, and Pei-Kuen Li

Department of Communications Engineering
Yuan Ze University, Chung-Li, Taoyuan, 32003, Taiwan
eehychen@saturn.yzu.edu.tw, s1014846@mail.yzu.edu.tw, s1004835@mail.yzu.edu.tw

Abstract ─ Based on an equivalent circuit model, the least-square curve fitting technique is proposed to quickly design optimum values of geometrical parameters of a dual-band Jerusalem-cross element for arbitrarily specifying any dual resonant frequencies. The validity of the least-square curve fitting technique is checked by comparing geometrical parameters and dual resonant frequencies of six Jerusalem-cross grids obtained by the proposed technique with those obtained by the improved empirical model and measurement method. Design of dual-band Jerusalem-cross slots is also conducted by the proposed technique. Simulation results of reflection and dual resonant frequencies of Jerusalem-cross slots designed by the proposed technique are also validated by measurement data.

Index Terms ─ Dual-band Jerusalem-cross element, least-square curve fitting, reflection, transmission.

I. INTRODUCTION

Frequency selective surface (FSS) has been extensively studied for many decades [1-32]. It has many applications in polarizers [1], antenna designs [2-10], transmission improvement for signals through energy-saving glass [11-14], artificial magnetic conductor (AMC) designs [15-17], spatial microwave and optical filters [18-25], absorbers [26-31], and planar metamaterials [32]. The FSS is usually formed by periodic arrays of metallic patches or slots of arbitrary geometries. A FSS with periodic arrays of metallic patches or slots exhibits total reflection or total transmission in the neighborhood of the geometric resonant frequency, respectively. Typical FSS geometries are designed by dipoles, rings, square loops, fractal shapes, etc. Most of these FSSs are used to deal with reflection and transmission problems at a single resonant frequency. It is rather difficult to design FSS elements that offer dual-band responses.

Several numerical methods have been used to design FSS parameters such as method of moments (MoM) [18], finite-difference time-domain (FDTD) method [33-35], and finite-element method (FEM) [36]. These methods have a tedious computation procedure which involves many electromagnetic equations governing FSS theory. In recent years, many electromagnetic simulation commercial software packages are available for the design of FSS parameters, such as Ansoft's HFSS, Ansoft's Designer, and CST Microwave Studio. These commercial software packages are easily used to design FSS parameters. However, the design process of a FSS element using the commercial software package can be divided into preliminary and fine tune steps. In the preliminary design steps, various critical geometrical dimensions of a FSS element are well investigated through parametric study using a full-wave model simulation. Based on preliminary study, the final design can be achieved through fine tuning the critical geometrical parameters to obtain the desired resonant frequencies. This is a non-efficient and labor intensive process due to trial-and-error tests and heavy computational works. Alternatively, the equivalent circuit method [37-39] is much simpler than numerical methods for the design of FSS parameters. In this method, the segments of the FSS structure are modeled as capacitive and inductive components in a transmission line [37-38]. Limitation of the equivalent circuit method is that it can be used only for normal incidence and without substrates.

In this paper, we propose the least-square curve fitting technique [40] to quickly obtain optimum values of geometrical parameters of a dual-band Jerusalem-cross element for arbitrarily specifying any dual resonant frequencies. In the design process, an equivalent circuit model of the frequency characteristic for normal wave incidence [38] is introduced to facilitate the optimum design of a Jerusalem-cross element. In simulations, the transmission and reflection of Jerusalem-cross elements are obtained by using the Ansoft high-frequency structure simulator (HFSS, Ansoft, Pittsburgh, PA). Simulation results of geometrical parameters and dual resonant frequencies of Jerusalem-cross grids obtained by the proposed technique are compared with those

Submitted On: September 20, 2013
Accepted On: May 25, 2015

obtained by the improved empirical model and measurement method presented in the literature [38]. Dual-band Jerusalem-cross slots designed by the proposed technique are also presented. Simulation results of reflection and dual resonant frequencies of Jerusalem-cross slots are validated by measurement data.

II. EQUIVALENT CIRCUIT MODEL OF JERUSALEM-CROSS GRIDS

The equivalent circuit model of Jerusalem-cross grids is a very useful technique to quickly predict the resonant frequencies of their structures. Figure 1 shows a FSS element constructed with Jerusalem-cross grids and its geometrical parameters p, w, s, h, and d. Where p is the periodicity of a unit cell, w is the width of the conductive strip, s is the separation distance between adjacent units, h is the width of the end caps of the Jerusalem-cross, and d is the length of the end caps of the Jerusalem-cross. Based on Langley and Drinkwater's studies [38], for any array of thin, continuous, infinitely long, perfectly conducting Jerusalem-cross FSS for normal incidence EM waves, the equivalent circuit model can be presented as shown in Fig. 2. The series resonant circuit L_1C_1 is used to generate the lower resonant frequency f_1 (in reflection band), the series resonant circuit L_2C_2 is used to produce the higher resonant frequency f_2, and the capacitor C_t is used to create the transmission band frequency f_t. The normalized (with respect to the free-space impedance and admittance, respectively) inductive reactance X_{L1} and capacitive susceptance B_{C1} of the equivalent circuit model are given as follows:

$$X_{L_1} = \omega_1 L_1 = F(p,w,\lambda_1) = \frac{p}{\lambda_1}[-\ell n(\beta_w) + G(p,w,\lambda_1)], \quad (1)$$

where λ_1 and ω_1 are the wavelength and angular frequency of the first resonant frequency f_1, respectively:

$$G(p,w,\lambda_1) = \frac{1}{2}\times\frac{(1-\beta_w^2)^2[(1-\frac{\beta_w^4}{4})(A_{1+}+A_{1-})+4\beta_w^2 A_{1+}A_{1-}]}{(1-\frac{\beta_w^2}{4})+(\beta_w^2+\frac{\beta_w^4}{2}-\frac{\beta_w^6}{8})(A_{1+}+A_{1-})+2\beta_w^6 A_{1+}A_{1-}}, \quad (2)$$

$$A_{1+} = A_{1-} = \frac{1}{\sqrt{1-(\frac{p}{\lambda_1})^2}} - 1, \quad (3)$$

$$\beta_w = \sin(\frac{\pi w}{2p}), \quad (4)$$

$$B_{c_1} = \omega_1 C_1 = \frac{4d}{p}F(p,s,\lambda_1) + \frac{4(2h+s)}{p}F(p,p-d,\lambda_1) = \frac{4d}{\lambda_1}[-\ell n(\beta_s) + G(p,s,\lambda_1)] + \frac{4(2h+s)}{\lambda_1}[-\ell n(\beta_{pd}) + G(p,p-d,\lambda_1)], \quad (5)$$

where

$$G(p,s,\lambda_1) = \frac{1}{2}\times\frac{(1-\beta_s^2)^2[(1-\frac{\beta_s^4}{4})(A_{1+}+A_{1-})+4\beta_s^2 A_{1+}A_{1-}]}{(1-\frac{\beta_s^2}{4})+(\beta_s^2+\frac{\beta_s^4}{2}-\frac{\beta_s^6}{8})(A_{1+}+A_{1-})+2\beta_s^6 A_{1+}A_{1-}}, \quad (6)$$

$$G(p,p-d,\lambda_1) = \frac{1}{2}\times\frac{(1-\beta_{pd}^2)^2[(1-\frac{\beta_{pd}^4}{4})(A_{1+}+A_{1-})+4\beta_{pd}^2 A_{1+}A_{1-}]}{(1-\frac{\beta_{pd}^2}{4})+(\beta_{pd}^2+\frac{\beta_{pd}^4}{2}-\frac{\beta_{pd}^6}{8})(A_{1+}+A_{1-})+2\beta_{pd}^6 A_{1+}A_{1-}}, \quad (7)$$

$$\beta_s = \sin(\frac{\pi s}{2p}), \quad (8)$$

$$\beta_{pd} = \sin[\frac{\pi\ (\text{p-d})}{2p}]. \quad (9)$$

The first resonant frequency f_1 can be obtained from L_1 and C_1 expressed by:

$$f_1 = \frac{1}{2\pi\sqrt{L_1C_1}}. \quad (10)$$

The normalized inductive reactance X_{L2} of the equivalent circuit model is given as following:

$$X_{L_2} = \omega_2 L_2 = \frac{d}{2p}F(p,\ 2h+s,\lambda_2) + \frac{1}{2}F(\frac{p}{2},\ w,\lambda_2) = \frac{d}{2\lambda_2}[-\ell n(\beta_{hs}) + G(p,\ 2h+s,\lambda_2)] + \frac{p}{4\lambda_2}[-\ell n(\beta_{p/2}) + G(\frac{p}{2},w,\lambda_2)], \quad (11)$$

where λ_2 and ω_2 are the wavelength and angular frequency of the second resonant frequency f_2, respectively:

$$G(p,\ 2h+s,\lambda_2) = \frac{1}{2}\times\frac{(1-\beta_{hs}^2)^2[(1-\frac{\beta_{hs}^4}{4})(A_{2+}+A_{2-})+4\beta_{hs}^2 A_{2+}A_{2-}]}{(1-\frac{\beta_{hs}^2}{4})+(\beta_{hs}^2+\frac{\beta_{hs}^4}{2}-\frac{\beta_{hs}^6}{8})(A_{2+}+A_{2-})+2\beta_{hs}^6 A_{2+}A_{2-}}, \quad (12)$$

$$G(\frac{p}{2},\ w,\lambda_2) = \frac{1}{2}\times\frac{(1-\beta_{p2}^2)^2[(1-\frac{\beta_{p2}^4}{4})(A_{3+}+A_{3-})+4\beta_{p2}^2 A_{3+}A_{3-}]}{(1-\frac{\beta_{p2}^2}{4})+(\beta_{p2}^2+\frac{\beta_{p2}^4}{2}-\frac{\beta_{p2}^6}{8})(A_{3+}+A_{3-})+2\beta_{p2}^6 A_{3+}A_{3-}}, \quad (13)$$

$$A_{2+} = A_{2-} = \frac{1}{\sqrt{1-(\frac{p}{\lambda_2})^2}} - 1, \quad (14)$$

$$A_{3+} = A_{3-} = \frac{1}{\sqrt{1-(\frac{p}{2\lambda_2})^2}} - 1, \quad (15)$$

$$\beta_{hs} = \sin[\frac{\pi\ (2h+s)}{2p}], \tag{16}$$

$$\beta_{p2} = \sin(\frac{\pi\ \mathrm{w}}{p}). \tag{17}$$

The normalized capacitive susceptance B_{C2} of the equivalent circuit model is given as following:

$$\begin{aligned} B_{c_2} = \omega_2 C_2 &= \frac{8(2h+s)}{p} F(p, p-d, \lambda_2) \\ &= \frac{8(2h+s)}{\lambda_2}[-\ell n(\beta_{pd}) + G(p, p-d, \lambda_2)], \end{aligned} \tag{18}$$

where

$$G(p, p-d, \lambda_2)$$

$$= \frac{1}{2} \times \frac{(1-\beta_{pd}^2)^2[(1-\frac{\beta_{pd}^4}{4})(A_{2+}+A_{2-}) + 4\beta_{pd}^2 A_{2+}A_{2-}]}{(1-\frac{\beta_{pd}^2}{4}) + (\beta_{pd}^2 + \frac{\beta_{pd}^4}{2} - \frac{\beta_{pd}^6}{8})(A_{2+}+A_{2-}) + 2\beta_{pd}^6 A_{2+}A_{2-}}, \tag{19}$$

β_{pd}, A_{2+}, and A_{2-} are given in (9) and (14), respectively. The second resonant frequency f_2 can be obtained from L_2 and C_2 expressed by:

$$f_2 = \frac{1}{2\pi\sqrt{L_2 C_2}}. \tag{20}$$

Equations (1)-(20) are valid when $p<\lambda_2$ and $p>d$, where λ_2 is the wavelength of the second resonant frequency f_2. In band-stop electromagnetic shielding applications, the resonant frequencies f_1 and f_2 are specified first and then all parameters of the unit should be determined. However, to simultaneously determine all parameters of one Jerusalem-cross unit for arbitrarily given resonant frequencies f_1 and f_2 is not an easy job. In the following section, the least-square curve fitting technique will be applied to calculate all parameters of any Jerusalem-cross element for arbitrarily given dual resonant (rejection) frequencies f_1 and f_2.

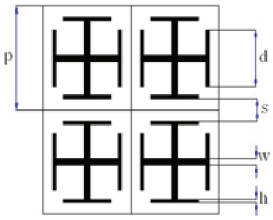

Fig. 1. Geometrical parameters of a FSS constructed with Jerusalem-cross grids.

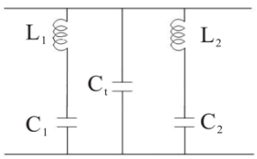

Fig. 2. An equivalent circuit model for Jerusalem-cross grids.

III. LEAST-SQUARE CURVE FITTING TECHNIQUE

The equivalent circuit model of a thin, continuous, and infinitely long array of Jerusalem-cross grids is presented in Fig. 2. In the band-stop electromagnetic shielding design, critical geometrical parameters of Jerusalem-cross grids p, w, s, h, and d should be solved for arbitrarily given dual resonant frequencies f_1 and f_2. Basically, resonant frequencies f_1 and f_2 are two nonlinear functions expressed by (10) and (20) in terms of geometrical parameters p, w, s, h, and d. The method of differential corrections, together with Newton's iterative method [40], can be used to fit the nonlinear functions f_1 and f_2. The differential corrections method approximates the nonlinear functions with a linear form that is more convenient to use for an iterative solution. By estimating approximate values of the unknown coefficients $A_1^{(0)}$, $A_2^{(0)}$, $A_3^{(0)}$, $A_4^{(0)}$, and $A_5^{(0)}$, and expanding (10) and (20) in a Taylor's series with only the first-order terms retained, we obtain:

$$\begin{aligned} f_1 &= f_1^{(0)} + \Delta A_1(\frac{\partial f_1}{\partial A_1})^{(0)} + \Delta A_2(\frac{\partial f_1}{\partial A_2})^{(0)} + \Delta A_3(\frac{\partial f_1}{\partial A_3})^{(0)} \\ &+ \Delta A_4(\frac{\partial f_1}{\partial A_4})^{(0)} + \Delta A_5(\frac{\partial f_1}{\partial A_5})^{(0)}, \end{aligned} \tag{21}$$

$$\begin{aligned} f_2 &= f_2^{(0)} + \Delta A_1(\frac{\partial f_2}{\partial A_1})^{(0)} + \Delta A_2(\frac{\partial f_2}{\partial A_2})^{(0)} + \Delta A_3(\frac{\partial f_2}{\partial A_3})^{(0)} \\ &+ \Delta A_4(\frac{\partial f_2}{\partial A_4})^{(0)} + \Delta A_5(\frac{\partial f_2}{\partial A_5})^{(0)}, \end{aligned} \tag{22}$$

where A_1=p, A_2=w, A_3=s, A_4=h, and A_5=d. The superscript (0) is used to indicate values obtained after substituting the first guess ($A_1^{(0)}$, $A_2^{(0)}$, $A_3^{(0)}$, $A_4^{(0)}$, and $A_5^{(0)}$), for the unknown parameters in (10) and (20). Equations (21) and (22) are two linear functions of the correction terms ΔA_1, ΔA_2, ΔA_3, ΔA_4, and ΔA_5, and hence the least-square curve fitting method can be used directly to determine these correction terms. The correction terms, when added to the first guess, give an improved approximation of the unknown coefficients, i.e., $A_1^{(1)} = A_1^{(0)} + \Delta A_1$, $A_2^{(1)} = A_2^{(0)} + \Delta A_2$, $A_3^{(1)} = A_3^{(0)} + \Delta A_3$, $A_4^{(1)} = A_4^{(0)} + \Delta A_4$, and $A_5^{(1)} = A_5^{(0)} + \Delta A_5$. When the improved estimates $A_1^{(1)}$, $A_2^{(1)}$, $A_3^{(1)}$, $A_4^{(1)}$, and $A_5^{(1)}$ are subsequently substituted as new estimates of the unknown coefficients, the Taylor's series reduces to:

$$\begin{aligned} f_1 &= f_1^{(1)} + \Delta A_1(\frac{\partial f_1}{\partial A_1})^{(1)} + \Delta A_2(\frac{\partial f_1}{\partial A_2})^{(1)} + \Delta A_3(\frac{\partial f_1}{\partial A_3})^{(1)} \\ &+ \Delta A_4(\frac{\partial f_1}{\partial A_4})^{(1)} + \Delta A_5(\frac{\partial f_1}{\partial A_5})^{(1)}, \end{aligned} \tag{23}$$

$$\begin{aligned} f_2 &= f_2^{(1)} + \Delta A_1(\frac{\partial f_2}{\partial A_1})^{(1)} + \Delta A_2(\frac{\partial f_2}{\partial A_2})^{(1)} + \Delta A_3(\frac{\partial f_2}{\partial A_3})^{(1)} \\ &+ \Delta A_4(\frac{\partial f_2}{\partial A_4})^{(1)} + \Delta A_5(\frac{\partial f_2}{\partial A_5})^{(1)}, \end{aligned} \tag{24}$$

where $f_1^{(1)}$ and $f_2^{(1)}$ as well as their derivatives are obtained by substituting the values of $A_1^{(1)}$, $A_2^{(1)}$, $A_3^{(1)}$, $A_4^{(1)}$, and $A_5^{(1)}$ in (10) and (20), respectively. Again, the correction terms ΔA_1, ΔA_2, ΔA_3, ΔA_4, and ΔA_5 are determined using the least-square curve fitting method. The procedure is continued until the solution converges to within a specified accuracy. The criterion of best fit of the technique of least-square curve fitting is that the sum of the squares of the errors be a minimum expressed by:

$$S = \sum_{i=1}^{N} \varepsilon_{i1}^2 + \sum_{i=1}^{N} \varepsilon_{i2}^2 = \text{minimum}, \tag{25}$$

where the term errors ε_{i1}^2 and ε_{i2}^2 mean the difference between the measured (observed) values of the first and second resonant frequencies $f_{1M}(i)$ and $f_{2M}(i)$ and computed values from (23) and (24) for the ith case, respectively. N is the total number of cases. Substituting (23) and (24) into (25), the result yields:

$$S = \sum_{i=1}^{N} [f_{1M}(i) - f_1(i)]^2 + \sum_{i=1}^{N} [f_{2M}(i) - f_2(i)]^2. \tag{26}$$

A necessary condition that a minimum for the error function S exists is that the partial derivatives with respect to each of the correction terms ΔA_1, ΔA_2, ΔA_3, ΔA_4, and ΔA_5 be zero. For example, in the first iteration:

$$\begin{aligned}
\frac{\partial S}{\partial(\Delta A_j)} = &-2\sum_{i=1}^{N} \left(\frac{\partial f_1}{\partial A_j}\right)^{(0)} \left[f_{1M}(i) - f_1^{(0)} - \Delta A_1 \left(\frac{\partial f_1}{\partial A_1}\right)^{(0)}\right. \\
&- \Delta A_2 \left(\frac{\partial f_1}{\partial A_2}\right)^{(0)} - \Delta A_3 \left(\frac{\partial f_1}{\partial A_3}\right)^{(0)} - \Delta A_4 \left(\frac{\partial f_1}{\partial A_4}\right)^{(0)} \\
&\left. - \Delta A_5 \left(\frac{\partial f_1}{\partial A_5}\right)^{(0)}\right] - 2\sum_{i=1}^{N} \left(\frac{\partial f_2}{\partial A_j}\right)^{(0)} \left[f_{2M}(i) - f_2^{(0)}\right. \\
&- \Delta A_1 \left(\frac{\partial f_2}{\partial A_1}\right)^{(0)} - \Delta A_2 \left(\frac{\partial f_2}{\partial A_2}\right)^{(0)} - \Delta A_3 \left(\frac{\partial f_2}{\partial A_3}\right)^{(0)} \\
&\left. - \Delta A_4 \left(\frac{\partial f_2}{\partial A_4}\right)^{(0)} - \Delta A_5 \left(\frac{\partial f_2}{\partial A_5}\right)^{(0)}\right] \\
&= 0,
\end{aligned} \tag{27}$$

where j= 1, 2, 3, 4, and 5. Equation (27) can be expressed as a matrix equation. One can easily solve for the correction terms ΔA_1, ΔA_2, ΔA_3, ΔA_4, and ΔA_5 in (28) by Gaussian elimination method.

Equation (28) is a very sensitive equation because the partial derivatives of resonant frequencies f_1 and f_2 with respect to each of the parameters A_1=p, A_2=w, A_3=s, A_4=h, and A_5=d still can generate nonlinear functions such as square root, natural logarithm, sine, and cosine. Therefore, the values of parameters p, w, s, h, and d should be limited to an acceptable range in the Newton's iterative process. In order to obtain a stable iterative process, the parameters p, w, s, h, and d are automatically checked and set to $0.75\lambda_2 < p < \lambda_2$, $0.1\lambda_2 < w < 0.2\lambda_2$, $0.03\lambda_2 < s < 0.1\lambda_2$, $0.03\lambda_2 < h < 0.1\lambda_2$, and $0.4\lambda_2 < d < 0.7\lambda_2$ in each iteration, respectively:

$$\begin{bmatrix}
\sum_{i=1}^{N} \left[\left(\frac{\partial f_1}{\partial A_1}\right)^{(0)}\right]^2 + \sum_{i=1}^{N} \left[\left(\frac{\partial f_2}{\partial A_1}\right)^{(0)}\right]^2 & \cdots & \sum_{i=1}^{N} \left(\frac{\partial f_1}{\partial A_1}\right)^{(0)} \left(\frac{\partial f_1}{\partial A_5}\right)^{(0)} + \sum_{i=1}^{N} \left(\frac{\partial f_2}{\partial A_1}\right)^{(0)} \left(\frac{\partial f_2}{\partial A_5}\right)^{(0)} \\
\sum_{i=1}^{N} \left(\frac{\partial f_1}{\partial A_2}\right)^{(0)} \left(\frac{\partial f_1}{\partial A_1}\right)^{(0)} + \sum_{i=1}^{N} \left(\frac{\partial f_2}{\partial A_2}\right)^{(0)} \left(\frac{\partial f_2}{\partial A_1}\right)^{(0)} & \cdots & \sum_{i=1}^{N} \left(\frac{\partial f_1}{\partial A_2}\right)^{(0)} \left(\frac{\partial f_1}{\partial A_5}\right)^{(0)} + \sum_{i=1}^{N} \left(\frac{\partial f_2}{\partial A_2}\right)^{(0)} \left(\frac{\partial f_2}{\partial A_5}\right)^{(0)} \\
\vdots & \vdots & \vdots \\
\sum_{i=1}^{N} \left(\frac{\partial f_1}{\partial A_5}\right)^{(0)} \left(\frac{\partial f_1}{\partial A_1}\right)^{(0)} + \sum_{i=1}^{N} \left(\frac{\partial f_2}{\partial A_5}\right)^{(0)} \left(\frac{\partial f_2}{\partial A_1}\right)^{(0)} & \cdots & \sum_{i=1}^{N} \left[\left(\frac{\partial f_1}{\partial A_5}\right)^{(0)}\right]^2 + \sum_{i=1}^{N} \left[\left(\frac{\partial f_2}{\partial A_5}\right)^{(0)}\right]^2
\end{bmatrix}
\times \begin{bmatrix} \Delta A_1 \\ \Delta A_2 \\ \Delta A_3 \\ \Delta A_4 \\ \Delta A_5 \end{bmatrix} = \begin{bmatrix}
\sum_{i=1}^{N} \left(\frac{\partial f_1}{\partial A_1}\right)^{(0)} \left[f_{1M}(i) - f_1^{(0)}\right] + \sum_{i=1}^{N} \left(\frac{\partial f_2}{\partial A_1}\right)^{(0)} \left[f_{2M}(i) - f_2^{(0)}\right] \\
\sum_{i=1}^{N} \left(\frac{\partial f_1}{\partial A_2}\right)^{(0)} \left[f_{1M}(i) - f_1^{(0)}\right] + \sum_{i=1}^{N} \left(\frac{\partial f_2}{\partial A_2}\right)^{(0)} \left[f_{2M}(i) - f_2^{(0)}\right] \\
\sum_{i=1}^{N} \left(\frac{\partial f_1}{\partial A_3}\right)^{(0)} \left[f_{1M}(i) - f_1^{(0)}\right] + \sum_{i=1}^{N} \left(\frac{\partial f_2}{\partial A_3}\right)^{(0)} \left[f_{2M}(i) - f_2^{(0)}\right] \\
\sum_{i=1}^{N} \left(\frac{\partial f_1}{\partial A_4}\right)^{(0)} \left[f_{1M}(i) - f_1^{(0)}\right] + \sum_{i=1}^{N} \left(\frac{\partial f_2}{\partial A_4}\right)^{(0)} \left[f_{2M}(i) - f_2^{(0)}\right] \\
\sum_{i=1}^{N} \left(\frac{\partial f_1}{\partial A_5}\right)^{(0)} \left[f_{1M}(i) - f_1^{(0)}\right] + \sum_{i=1}^{N} \left(\frac{\partial f_2}{\partial A_5}\right)^{(0)} \left[f_{2M}(i) - f_2^{(0)}\right]
\end{bmatrix}. \tag{28}$$

The partial derivatives of resonant frequencies f_1 and f_2 with respect to each of the parameters can be obtained by the following two equations:

$$\frac{\partial f_1}{\partial A_i} = -\frac{1}{4\pi}(L_1C_1)^{-\frac{3}{2}}(L_1\frac{\partial C_1}{\partial A_i} + C_1\frac{\partial L_1}{\partial A_i}), \quad (29)$$

$$\frac{\partial f_2}{\partial A_i} = -\frac{1}{4\pi}(L_2C_2)^{-\frac{3}{2}}(L_2\frac{\partial C_2}{\partial A_i} + C_2\frac{\partial L_2}{\partial A_i}), \quad (30)$$

where A_1=p, A_2=w, A_3=s, A_4=h, and A_5=d. The partial derivatives of inductances and capacitances L_1, L_2, C_1, and C_2 are with respect to each of the parameters p, w, s, h, and d as shown in APPENDIX.

IV. VALIDATION OF LEAST-SQUARE CURVE FITTING

In order to validate the least-square curve fitting technique, dimensions of six Jerusalem-cross grids with thin, infinitely long, and perfectly conducting strips listed in the literature [38] are checked by the proposed technique. Simulation results of transmission for six Jerusalem-cross grids generated by the least-square curve fitting technique are studied by the commercial software package HFSS. Comparisons of two specific resonant frequencies f_1 and f_2 obtained by the least-square curve fitting technique, improved empirical model [38], and measurement [38] are listed in Table 1. Obviously, the six sets of dimensions obtained by the improved empirical model are different from those obtained by the least-square curve fitting technique. But it is found that simulation results of the resonant frequencies f_1 and f_2 for the six sets of parameters generated by the least-square curve fitting technique make a good agreement with those obtained by the empirical model and measurement available in the literature [38]. Table 1 illustrates that the set of dimensions of a Jerusalem-cross grid for any specific dual resonant frequencies f_1 and f_2 is not unique. Table 2 shows the comparison of computational time obtained by the least-square (LS) curve fitting technique and HFSS implemented with genetic algorithm (GA) [41] for design of Jerusalem-cross parameters in a personal computer. It is illustrated that the proposed method provides a fast solution for design of Jerusalem-cross parameters. The frequency responses of transmission of the six Jerusalem-cross grids, their dimensions obtained by the least-square curve fitting technique, are also shown in Figs. 3-8. These Jerusalem-cross grids have a transmission of more than -30 dB at resonant frequencies f_1 and f_2. The average bandwidths obtained at resonant frequencies f_1 and f_2 are more than 12% with a transmission of -10 dB.

Table 1: Comparisons of resonant frequencies f_1 and f_2 obtained by the least-square (LS) curve fitting technique (Figs. 3-8), improved empirical model (IEM) [38], and measurement (M) [38] for different Jerusalem-cross grids for normal wave incidence

No.	Dimensions (mm) [38]					Dimensions (mm) (LS)					f_1 (GHz)			f_2 (GHz)		
	p	w	d	h	s	p	w	d	h	s	M [38]	IEM [38]	LS	M [38]	IEM [38]	LS
1	5.82	0.8	4.05	0.4	0.3	7.05	1.06	3.63	0.23	0.24	14.1	14.0	14.9 (Fig. 3)	41.5	42.7	40.5 (Fig. 3)
2	5.82	0.8	4.6	0.42	0.27	7.11	0.82	3.9	0.73	0.28	12.8	12.8	12.6 (Fig. 4)	38.3	38.0	37.6 (Fig. 4)
3	6.5	0.9	4.95	0.3	0.21	7.86	0.92	4.5	0.86	0.3	11.6	11.3	10.9 (Fig. 5)	33.7	34.2	33.6 (Fig. 5)
4	5.84	1.42	4.5	0.32	0.38	5.96	0.82	3.70	0.39	0.53	17.3	17.0	17.0 (Fig. 6)	43.0	41.8	41.9 (Fig. 6)
5	6.3	1.18	4.8	0.39	0.41	6.7	0.94	4.15	0.41	0.40	14.3	14.2	14.5 (Fig. 7)	38.3	38.2	37.4 (Fig. 7)
6	5.98	1.18	4.6	0.42	0.38	7.00	1.0	3.75	0.35	0.34	14.9	15.0	14.8 (Fig. 8)	40.1	40.0	40.1 (Fig. 8)

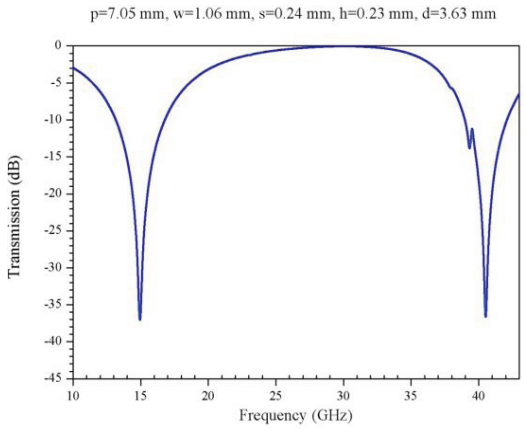

Fig. 3. The frequency response of transmission of the sample No. 1 listed in Table 1.

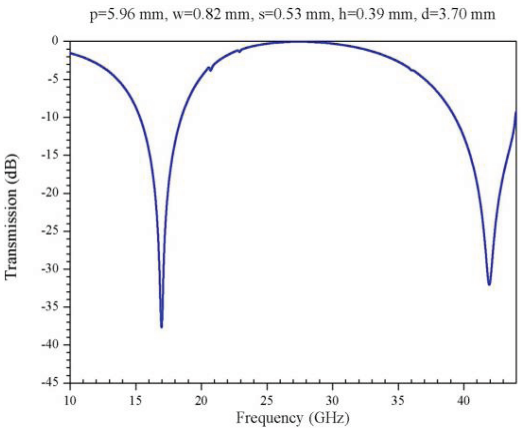

Fig. 6. The frequency response of transmission of the sample No. 4 listed in Table 1.

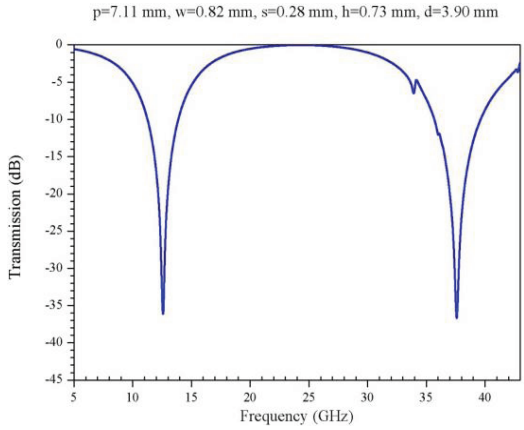

Fig. 4. The frequency response of transmission of the sample No. 2 listed in Table 1.

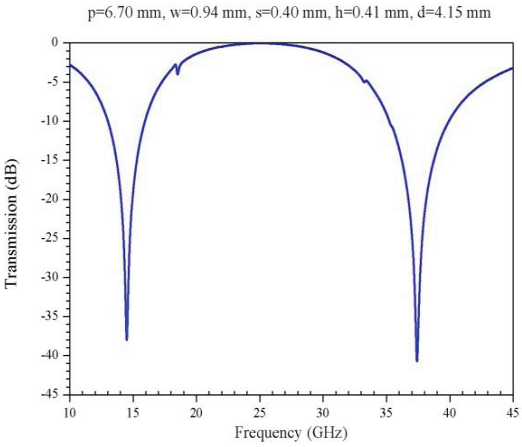

Fig. 7. The frequency response of transmission of the sample No. 5 listed in Table 1.

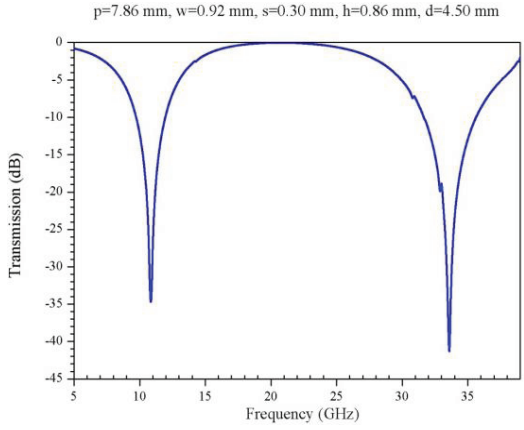

Fig. 5. The frequency response of transmission of the sample No. 3 listed in Table 1.

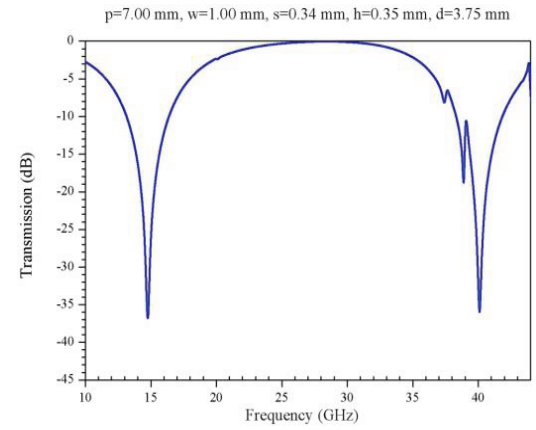

Fig. 8. The frequency response of transmission of the sample No. 6 listed in Table 1.

Table 2: Comparison of computational time obtained by the least-square (LS) curve fitting technique and HFSS implemented with genetic algorithm (GA) for design of Jerusalem-cross parameters

No.	LS	HFSS with GA
1	3 s	1 day 7 hr 27 m 21 s
2	8 s	2 day 18 hr 28 m 13 s
3	6 s	3 day 16 hr 45 m 17 s
4	13 s	4 day 13 hr 24 m 49 s
5	4 s	1 day 19 hr 14 m 29 s
6	9 s	3 day 23 hr 58 m 38 s

V. JERUSALEM-CROSS SLOTS

In order to improve EM transmission, aperture types of FSSs may be used to provide a better signal transmission at specific frequencies while also providing an isolation capability for unwanted EM noises. With all conducting and non-conducting areas interchanged, a Jerusalem-cross slot (a complementary Jerusalem-cross grid) can be used to reverse the transmission and reflection coefficients of the Jerusalem-cross grid [38]. We arbitrarily specify two pairs of dual resonant frequencies of (2.45, 5.8) and (3.96, 7.92) GHz to design two Jerusalem-cross slots by the least-square curve fitting technique. The Jerusalem-cross slots are constructed on a copper foil with a thickness of 0.05 mm. The specific frequencies of (2.45, 5.8) and (3.96, 7.92) GHz are in the Bluetooth (2.4-2.48 GHz), wireless local area network (IEEE802. 11a, upper band 5.725-5.825 GHz), and ultra-wideband (low-frequency band 3.168-4.752 GHz and high-frequency band 6.336-9.504 GHz) applications. Simulation results of reflection at frequencies (2.45, 5.8) and (3.96, 7.92) GHz will be investigated by checking the reflection with better than 10 dB return loss for the two Jerusalem-cross slots. The simulation results of frequency response of reflection will also be checked by measurement data. Measurement data of reflection of the two Jerusalem-cross slots are obtained by using an Anritsz37369C Vector Network Analyzer and a pair of horn antennas operating at frequencies of 1-18 GHz as shown in Fig. 9. The frequency responses of reflection of the first and second Jerusalem-cross slots with parameters (p=40.0 mm, w=5.4 mm, s=4.5 mm, h=2.1 mm, d=29.0 mm) and (p=28.5 mm, w=5.6 mm, s=3.8 mm, h=1.2 mm, d=21.6 mm) are shown in Figs. 10 and 11, respectively. From Figs. 10 and 11, it is shown that simulation results of frequency responses of reflection make a good agreement with those obtained by measurements. Figure 10 shows that the first Jerusalem-cross slot has a reflection of more than -30 dB at frequencies of 2.45 and 5.8 GHz. Simulation and measurement results of bandwidths at frequencies of 2.45 and 5.8 GHz have an average value of 15% with a reflection of -10 dB. From Fig. 11, the second Jerusalem-cross slot has a reflection of more than -40 dB at frequencies of 3.96 and 7.92 GHz. Simulation and measurement of bandwidths at frequencies of 3.96 and 7.92 GHz have an average value of 14.5% with a reflection of -10 dB. These bandwidths are enough to effectively transmit the Bluetooth, wireless local area network, and ultra-wideband signals.

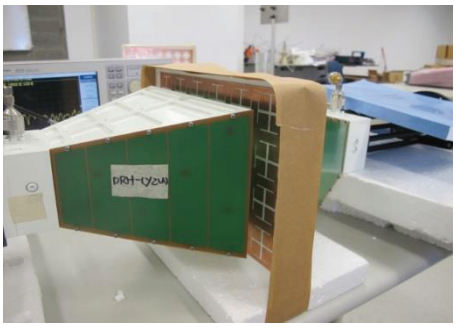

Fig. 9. Measurement setup.

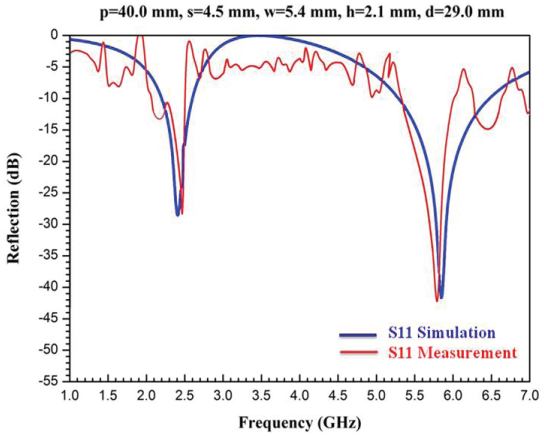

Fig. 10/ The frequency response of reflection of the first Jerusalem-cross slot.

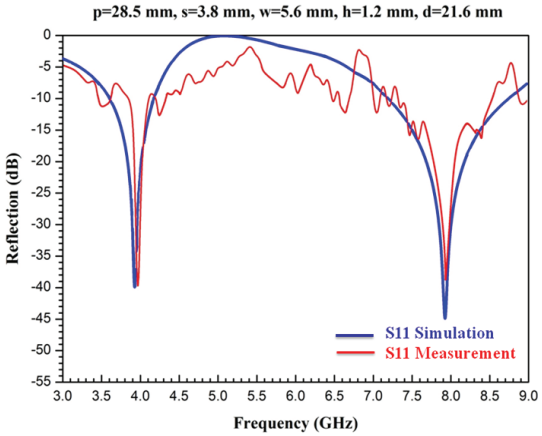

Fig. 11. The frequency response of reflection of the second Jerusalem-cross slot.

VI. CONCLUSION

In this paper, we propose the least-square curve fitting technique to quickly obtain optimum values of geometrical parameters of a dual-band Jerusalem-cross grid with thin, infinitely long, and perfectly conducting strips. Based on circuit model, the least-square curve fitting technique can provide a quick and accurate design of a dual-band Jerusalem-cross grid for arbitrarily specifying any dual resonant frequencies. The validity of the proposed technique has been checked by comparing two specific resonant frequencies f_1 and f_2 with those obtained by the improved empirical model and measurement method. The proposed method provides a fast solution for design of Jerusalem-cross parameters. The proposed technique can also be used to optimally design a dual-band Jerusalem-cross slot for arbitrarily specifying any two resonant frequencies. However, the proposed technique presented in this paper does not include the substrate. It is expected that the presence of the dielectric substrate will shift the resonant frequencies downwards. In the future works, the shifting factor will be further studied on the transmission and reflection of an energy-saving glass coated with a metallic oxide layer on one side of ordinary float glass which is widely used in modern building.

APPENDIX

This Appendix illustrates the partial derivatives of inductances and capacitances L_1, L_2, C_1, and C_2 with respect to each of the parameters p, w, s, h, and d as following:

$$\frac{\partial L_1}{\partial A_1}=\frac{\partial L_1}{\partial p}=\frac{1}{\omega_1\lambda_1}[-\ell n(\beta_w+G(p,w,\lambda_1)] + \frac{p}{\omega_1\lambda_1}[-\frac{1}{\beta_w}\frac{\partial\beta_w}{\partial p}+\frac{\partial G(p,w,\lambda_1)}{\partial p}], \tag{31}$$

where

$$\frac{\partial\beta_w}{\partial p}=-\frac{\pi w}{2p^2}\cos(\frac{\pi w}{2p}), \tag{32}$$

$$\frac{\partial G(p,w,\lambda_1)}{\partial p}=\frac{1}{2}\frac{G_d\frac{\partial G_n}{\partial p}-G_n\frac{\partial G_d}{\partial p}}{G_d^2}, \tag{33}$$

$$G_n=(1-\beta_w^2)^2[(1-\frac{\beta_w^4}{4})(A_{1+}+A_{1-})+4\beta_w^2A_{1+}A_{1-}], \tag{34}$$

$$G_d=(1-\frac{\beta_w^2}{4})+(\beta_w^2+\frac{\beta_w^4}{2}-\frac{\beta_w^6}{8})(A_{1+}+A_{1-})+2\beta_w^6A_{1+}A_{1-}, \tag{35}$$

$$\begin{aligned}\frac{\partial G_n}{\partial p}&=2(1-\beta_w^2)(-2\beta_w\frac{\partial\beta_w}{\partial p})[(1-\frac{\beta_w^4}{4})(A_{1+}+A_{1-})\\&+4\beta_w^2A_{1+}A_{1-}]+(1-\beta_w^2)^2[-\beta_w^3\frac{\partial\beta_w}{\partial p}(A_{1+}+A_{1-})\\&+(1-\frac{\beta_w^4}{4})(\frac{\partial A_{1+}}{\partial p}+\frac{\partial A_{1-}}{\partial p})+4\beta_w^2A_{1+}\frac{\partial A_{1-}}{\partial p}\\&+4\beta_w^2A_{1-}\frac{\partial A_{1+}}{\partial p}+8\beta_wA_{1+}A_{1-}\frac{\partial\beta_w}{\partial p}],\end{aligned} \tag{36}$$

$$\begin{aligned}\frac{\partial G_d}{\partial p}&=-\frac{1}{2}\beta_w\frac{\partial\beta_w}{\partial p}+(2\beta_w+2\beta_w^3-\frac{3}{4}\beta_w^5)\frac{\partial\beta_w}{\partial p}(A_{1+}+A_{1-})\\&+(\beta_w^2+\frac{\beta_w^4}{2}-\frac{\beta_w^6}{8})(\frac{\partial A_{1+}}{\partial p}+\frac{\partial A_{1-}}{\partial p})\\&+2\beta_w^6A_{1+}\frac{\partial A_{1-}}{\partial p}+2\beta_w^6A_{1-}\frac{\partial A_{1+}}{\partial p}\\&+12\beta_w^5A_{1+}A_{1-}\frac{\partial\beta_w}{\partial p},\end{aligned} \tag{37}$$

$$\frac{\partial A_{1+}}{\partial p}=\frac{\partial A_{1-}}{\partial p}=-\frac{1}{2}[1-(\frac{p}{\lambda_1})^2]^{-\frac{3}{2}}(\frac{2p}{\lambda_1^2}), \tag{38}$$

$$\frac{\partial L_1}{\partial A_2}=\frac{\partial L_1}{\partial w}=\frac{p}{\omega_1\lambda_1}[-\frac{1}{\beta_w}\frac{\partial\beta_w}{\partial w}+\frac{\partial G(p,w,\lambda_1)}{\partial w}], \tag{39}$$

where

$$\frac{\partial\beta_w}{\partial w}=\frac{\pi}{2p}\cos(\frac{\pi w}{2p}), \tag{40}$$

$$\frac{\partial G(p,w,\lambda_1)}{\partial w}=\frac{1}{2}\frac{G_d\frac{\partial G_n}{\partial w}-G_n\frac{\partial G_d}{\partial w}}{G_d^2}, \tag{41}$$

$$\begin{aligned}\frac{\partial G_n}{\partial w}&=2(1-\beta_w^2)(-2\beta_w\frac{\partial\beta_w}{\partial w})[(1-\frac{\beta_w^4}{4})(A_{1+}+A_{1-})\\&+4\beta_w^2A_{1+}A_{1-}]+(1-\beta_w^2)^2[-\beta_w^3\frac{\partial\beta_w}{\partial w}(A_{1+}+A_{1-})\\&+8\beta_wA_{1+}A_{1-}\frac{\partial\beta_w}{\partial w}],\end{aligned} \tag{42}$$

$$\begin{aligned}\frac{\partial G_d}{\partial w}&=-\frac{1}{2}\beta_w\frac{\partial\beta_w}{\partial w}\\&+(2\beta_w+2\beta_w^3-\frac{3}{4}\beta_w^5)\frac{\partial\beta_w}{\partial w}(A_{1+}+A_{1-})\\&+12\beta_w^5A_{1+}A_{1-}\frac{\partial\beta_w}{\partial w},\end{aligned} \tag{43}$$

$$\frac{\partial L_1}{\partial A_3}=\frac{\partial L_1}{\partial s}=0, \tag{44}$$

$$\frac{\partial L_1}{\partial A_4}=\frac{\partial L_1}{\partial h}=0, \tag{45}$$

$$\frac{\partial L_1}{\partial A_5}=\frac{\partial L_1}{\partial d}=0, \tag{46}$$

$$\begin{aligned}\frac{\partial C_1}{\partial A_1}=\frac{\partial C_1}{\partial p}=\frac{4d}{\omega_1\lambda_1}&[-\frac{1}{\beta_s}\frac{\partial\beta_s}{\partial p}+\frac{\partial G(p,s,\lambda_1)}{\partial p}\\&+\frac{4(2h+s)}{\omega_1\lambda_1}[-\frac{1}{\beta_{pd}}\frac{\partial\beta_{pd}}{\partial p}\\&+\frac{\partial G(p,p-d,\lambda_1)}{\partial p}],\end{aligned} \tag{47}$$

where

$$\frac{\partial\beta_s}{\partial p}=-\frac{\pi s}{2p^2}\cos(\frac{\pi s}{2p}), \tag{48}$$

$$\frac{\partial\beta_{pd}}{\partial p}=\frac{\pi d}{2p^2}\cos[\frac{\pi(p-d)}{2p}], \tag{49}$$

$$\frac{\partial G(p,s,\lambda_1)}{\partial p}=\frac{1}{2}\frac{G_{sd}\dfrac{\partial G_{sn}}{\partial p}-G_{sn}\dfrac{\partial G_{sd}}{\partial p}}{G_{sd}^2}, \tag{50}$$

$$G_{sn}=(1-\beta_s^2)^2[(1-\frac{\beta_s^4}{4})(A_{1+}+A_{1-})+4\beta_s^2A_{1+}A_{1-}], \tag{51}$$

$$\begin{aligned}G_{sd}&=(1-\frac{\beta_s^2}{4})+(\beta_s^2+\frac{\beta_s^4}{2}-\frac{\beta_s^6}{8})(A_{1+}+A_{1-})\\&\quad+2\beta_s^6A_{1+}A_{1-},\end{aligned} \tag{52}$$

$$\begin{aligned}\frac{\partial G_{sn}}{\partial p}&=2(1-\beta_s^2)(-2\beta_s\frac{\partial\beta_s}{\partial p})[(1-\frac{\beta_s^4}{4})(A_{1+}+A_{1-})\\&\quad+4\beta_s^2A_{1+}A_{1-}]+(1-\beta_s^2)^2[-\beta_s^3\frac{\partial\beta_s}{\partial p}(A_{1+}+A_{1-})\\&\quad+(1-\frac{\beta_s^4}{4})(\frac{\partial A_{1+}}{\partial p}+\frac{\partial A_{1-}}{\partial p})+4\beta_s^2A_{1+}\frac{\partial A_{1-}}{\partial p}\\&\quad+4\beta_s^2A_{1-}\frac{\partial A_{1+}}{\partial p}+8\beta_sA_{1+}A_{1-}\frac{\partial\beta_s}{\partial p}],\end{aligned} \tag{53}$$

$$\begin{aligned}\frac{\partial G_{sd}}{\partial p}&=-\frac{1}{2}\beta_s\frac{\partial\beta_s}{\partial p}\\&\quad+(2\beta_s+2\beta_s^3-\frac{3}{4}\beta_s^5)\frac{\partial\beta_s}{\partial p}(A_{1+}+A_{1-})\\&\quad+(\beta_s^2+\frac{\beta_s^4}{2}-\frac{\beta_s^6}{8})(\frac{\partial A_{1+}}{\partial p}+\frac{\partial A_{1-}}{\partial p})\\&\quad+2\beta_s^6A_{1+}\frac{\partial A_{1-}}{\partial p}+2\beta_s^6A_{1-}\frac{\partial A_{1+}}{\partial p}\\&\quad+12\beta_s^5A_{1+}A_{1-}\frac{\partial\beta_s}{\partial p},\end{aligned} \tag{54}$$

$$\frac{\partial G(p,p-d,\lambda_1)}{\partial p}=\frac{1}{2}\frac{G_{pdd}\dfrac{\partial G_{pdn}}{\partial p}-G_{pdn}\dfrac{\partial G_{pdd}}{\partial p}}{G_{pdd}^2}, \tag{55}$$

$$G_{pdn}=(1-\beta_{pd}^2)^2[(1-\frac{\beta_{pd}^4}{4})(A_{1+}+A_{1-})+4\beta_{pd}^2A_{1+}A_{1-}], \tag{56}$$

$$\begin{aligned}G_{pdd}&=(1-\frac{\beta_{pd}^2}{4})+(\beta_{pd}^2+\frac{\beta_{pd}^4}{2}-\frac{\beta_{pd}^6}{8})(A_{1+}+A_{1-})\\&\quad+2\beta_{pd}^6A_{1+}A_{1-},\end{aligned} \tag{57}$$

$$\begin{aligned}\frac{\partial G_{pdn}}{\partial p}&=2(1-\beta_{pd}^2)(-2\beta_{pd}\frac{\partial\beta_{pd}}{\partial p})[(1-\frac{\beta_{pd}^4}{4})(A_{1+}+A_{1-})\\&\quad+4\beta_{pd}^2A_{1+}A_{1-}]+(1-\beta_{pd}^2)^2[-\beta_{pd}^3\frac{\partial\beta_{pd}}{\partial p}(A_{1+}+A_{1-})\\&\quad+(1-\frac{\beta_{pd}^4}{4})(\frac{\partial A_{1+}}{\partial p}+\frac{\partial A_{1-}}{\partial p})+4\beta_{pd}^2A_{1+}\frac{\partial A_{1-}}{\partial p}\\&\quad+4\beta_{pd}^2A_{1-}\frac{\partial A_{1+}}{\partial p}+8\beta_{pd}A_{1+}A_{1-}\frac{\partial\beta_{pd}}{\partial p}],\end{aligned} \tag{58}$$

$$\begin{aligned}\frac{\partial G_{pdd}}{\partial p}&=-\frac{1}{2}\beta_{pd}\frac{\partial\beta_{pd}}{\partial p}\\&\quad+(2\beta_{pd}+2\beta_{pd}^3-\frac{3}{4}\beta_{pd}^5)\frac{\partial\beta_{pd}}{\partial p}(A_{1+}+A_{1-})\\&\quad+(\beta_{pd}^2+\frac{\beta_{pd}^4}{2}-\frac{\beta_{pd}^6}{8})(\frac{\partial A_{1+}}{\partial p}+\frac{\partial A_{1-}}{\partial p})\\&\quad+2\beta_{pd}^6A_{1+}\frac{\partial A_{1-}}{\partial p}+2\beta_{pd}^6A_{1-}\frac{\partial A_{1+}}{\partial p}\\&\quad+12\beta_{pd}^5A_{1+}A_{1-}\frac{\partial\beta_{pd}}{\partial p},\end{aligned} \tag{59}$$

$$\frac{\partial C_1}{\partial A_2}=\frac{\partial C_1}{\partial w}=0, \tag{60}$$

$$\begin{aligned}\frac{\partial C_1}{\partial A_3}&=\frac{\partial C_1}{\partial s}=\frac{4d}{\omega_1\lambda_1}[-\frac{1}{\beta_s}\frac{\partial\beta_s}{\partial s}+\frac{\partial G(p,s,\lambda_1)}{\partial s}\\&\quad+\frac{4}{\omega_1\lambda_1}[-\ell n(\beta_{pd})+G(p,p-d,\lambda_1)],\end{aligned} \tag{61}$$

where

$$\frac{\partial\beta_s}{\partial s}=\frac{\pi s}{2p}\cos(\frac{\pi s}{2p}), \tag{62}$$

$$\frac{\partial G(p,s,\lambda_1)}{\partial s}=\frac{1}{2}\frac{G_{sd}\dfrac{\partial G_{sn}}{\partial s}-G_{sn}\dfrac{\partial G_{sd}}{\partial s}}{G_{sd}^2}, \tag{63}$$

$$\begin{aligned}\frac{\partial G_{sn}}{\partial s}&=2(1-\beta_s^2)(-2\beta_s\frac{\partial\beta_s}{\partial s})[(1-\frac{\beta_s^4}{4})(A_{1+}+A_{1-})\\&\quad+4\beta_s^2A_{1+}A_{1-}]+(1-\beta_s^2)^2[-\beta_s^3\frac{\partial\beta_s}{\partial s}(A_{1+}+A_{1-})\\&\quad+8\beta_sA_{1+}A_{1-}\frac{\partial\beta_s}{\partial s}],\end{aligned} \tag{64}$$

$$\begin{aligned}\frac{\partial G_{sd}}{\partial s}&=-\frac{1}{2}\beta_s\frac{\partial\beta_s}{\partial s}\\&\quad+(2\beta_s+2\beta_s^3-\frac{3}{4}\beta_s^5)\frac{\partial\beta_s}{\partial s}(A_{1+}+A_{1-})\\&\quad+12\beta_s^5A_{1+}A_{1-}\frac{\partial\beta_s}{\partial s},\end{aligned} \tag{65}$$

$$\frac{\partial C_1}{\partial A_4}=\frac{\partial C_1}{\partial h}=\frac{8}{\omega_1\lambda_1}[-\ell n(\beta_{pd})+G(p,p-d,\lambda_1)], \tag{66}$$

$$\begin{aligned}\frac{\partial C_1}{\partial A_5}&=\frac{\partial C_1}{\partial d}\\&=\frac{4(2h+s)}{\omega_1\lambda_1}[-\frac{1}{\beta_{pd}}\frac{\partial\beta_{pd}}{\partial d}+\frac{\partial G(p,p-d,\lambda_1)}{\partial d}],\end{aligned} \tag{67}$$

where

$$\frac{\partial\beta_{pd}}{\partial d}=\frac{-\pi}{2p}\cos[\frac{\pi(p-d)}{2p}], \tag{68}$$

$$\frac{\partial G(p,p-d,\lambda_1)}{\partial d}=\frac{1}{2}\frac{G_{pdd}\dfrac{\partial G_{pdn}}{\partial d}-G_{pdn}\dfrac{\partial G_{pdd}}{\partial d}}{G_{pdd}^2}, \tag{69}$$

$$\begin{aligned}\frac{\partial G_{pdn}}{\partial d}&=2(1-\beta_{pd}^2)(-2\beta_{pd}\frac{\partial \beta_{pd}}{\partial d})[(1-\frac{\beta_{pd}^4}{4})(A_{1+}+A_{1-})\\&+4\beta_{pd}^2A_{1+}A_{1-}]+(1-\beta_{pd}^2)^2[-\beta_{pd}^3\frac{\partial\beta_{pd}}{\partial d}(A_{1+}+A_{1-})\\&+8\beta_{pd}A_{1+}A_{1-}\frac{\partial\beta_{pd}}{\partial d}],\end{aligned} \tag{70}$$

$$\begin{aligned}\frac{\partial G_{pdd}}{\partial d}&=-\frac{1}{2}\beta_{pd}\frac{\partial\beta_{pd}}{\partial d}\\&+(2\beta_{pd}+2\beta_{pd}^3-\frac{3}{4}\beta_{pd}^5)\frac{\partial\beta_{pd}}{\partial d}(A_{1+}+A_{1-})\\&+12\beta_{pd}^5A_{1+}A_{1-}\frac{\partial\beta_{pd}}{\partial d},\end{aligned} \tag{71}$$

$$\begin{aligned}\frac{\partial L_2}{\partial A_1}=\frac{\partial L_2}{\partial p}&=\frac{d}{2\omega_2\lambda_2}[-\frac{1}{\beta_{hs}}\frac{\partial\beta_{hs}}{\partial p}+\frac{\partial G(p,2h+s,\lambda_2)}{\partial p}]\\&+\frac{1}{4\omega_2\lambda_2}[-\ell n(\beta_{p2}+G(\frac{p}{2},w,\lambda_2)]\\&+\frac{p}{4\omega_2\lambda_2}[-\frac{1}{\beta_{p2}}\frac{\partial\beta_{p2}}{\partial p}+\frac{\partial G(\frac{p}{2},w,\lambda_2)}{\partial p}],\end{aligned} \tag{72}$$

where

$$\frac{\partial\beta_{hs}}{\partial p}=-\frac{\pi(2h+s)}{2p^2}\cos[\frac{\pi(2h+s)}{2p}], \tag{73}$$

$$\frac{\partial\beta_{p2}}{\partial p}=-\frac{\pi w}{p^2}\cos[\frac{\pi w}{p}], \tag{74}$$

$$\frac{\partial G(p,\ 2h+s,\lambda_2)}{\partial p}=\frac{1}{2}\frac{G_{hsd}\dfrac{\partial G_{hsn}}{\partial p}-G_{hsn}\dfrac{\partial G_{hsd}}{\partial p}}{G_{hsd}^2}, \tag{75}$$

$$\begin{aligned}G_{hsn}&=(1-\beta_{hs}^2)^2[(1-\frac{\beta_{hs}^4}{4})(A_{2+}+A_{2-})\\&+4\beta_{hs}^2A_{2+}A_{2-}],\end{aligned} \tag{76}$$

$$\begin{aligned}G_{hsd}&=(1-\frac{\beta_{hs}^2}{4})+(\beta_{hs}^2+\frac{\beta_{hs}^4}{2}-\frac{\beta_{hs}^6}{8})(A_{2+}+A_{2-})\\&+2\beta_{hs}^6A_{2+}A_{2-},\end{aligned} \tag{77}$$

$$\begin{aligned}\frac{\partial G_{hsn}}{\partial p}&=2(1-\beta_{hs}^2)(-2\beta_{hs}\frac{\partial\beta_{hs}}{\partial p})[(1-\frac{\beta_{hs}^4}{4})(A_{2+}+A_{2-})\\&+4\beta_{hs}^2A_{2+}A_{2-}]+(1-\beta_{hs}^2)^2[-\beta_{hs}^3\frac{\partial\beta_{hs}}{\partial p}(A_{2+}+A_{2-})\\&+(1-\frac{\beta_{hs}^4}{4})(\frac{\partial A_{2+}}{\partial p}+\frac{\partial A_{2-}}{\partial p})+4\beta_{hs}^2A_{2+}\frac{\partial A_{2-}}{\partial p}\\&+4\beta_{hs}^2A_{2-}\frac{\partial A_{2+}}{\partial p}+8\beta_{hs}A_{2+}A_{2-}\frac{\partial\beta_{hs}}{\partial p}],\end{aligned} \tag{78}$$

$$\begin{aligned}\frac{\partial G_{hsd}}{\partial p}&=-\frac{1}{2}\beta_{hs}\frac{\partial\beta_{hs}}{\partial p}\\&+(2\beta_{hs}+2\beta_{hs}^3-\frac{3}{4}\beta_{hs}^5)\frac{\partial\beta_{hs}}{\partial p}(A_{2+}+A_{2-})\\&+(\beta_{hs}^2+\frac{\beta_{hs}^4}{2}-\frac{\beta_{hs}^6}{8})(\frac{\partial A_{2+}}{\partial p}+\frac{\partial A_{2-}}{\partial p})\\&+2\beta_{hs}^6A_{2+}\frac{\partial A_{2-}}{\partial p}+2\beta_{hs}^6A_{2-}\frac{\partial A_{2+}}{\partial p}\\&+12\beta_{hs}^5A_{2+}A_{2-}\frac{\partial\beta_{hs}}{\partial p},\end{aligned} \tag{79}$$

$$\frac{\partial A_{2+}}{\partial p}=\frac{\partial A_{2-}}{\partial p}=-\frac{1}{2}[1-(\frac{p}{\lambda_2})^2]^{-\frac{3}{2}}(\frac{2p}{\lambda_2^2}), \tag{80}$$

$$\frac{\partial G(\frac{p}{2},w,\lambda_2)}{\partial p}=\frac{1}{2}\frac{G_{p2wd}\dfrac{\partial G_{p2wn}}{\partial p}-G_{p2wn}\dfrac{\partial G_{p2wd}}{\partial p}}{G_{p2wd}^2}, \tag{81}$$

$$\begin{aligned}G_{p2wn}&=(1-\beta_{p2}^2)^2[(1-\frac{\beta_{p2}^4}{4})(A_{3+}+A_{3-})\\&+4\beta_{p2}^2A_{3+}A_{3-}],\end{aligned} \tag{82}$$

$$\begin{aligned}G_{p2wd}&=(1-\frac{\beta_{p2}^2}{4})\\&+(\beta_{p2}^2+\frac{\beta_{p2}^4}{2}-\frac{\beta_{p2}^6}{8})(A_{3+}+A_{3-})\\&+2\beta_{p2}^6A_{3+}A_{3-},\end{aligned} \tag{83}$$

$$\begin{aligned}\frac{\partial G_{p2wn}}{\partial p}&=2(1-\beta_{p2}^2)(-2\beta_{p2}\frac{\partial\beta_{p2}}{\partial p})[(1-\frac{\beta_{p2}^4}{4})(A_{3+}+A_{3-})\\&+4\beta_{p2}^2A_{2+}A_{2-}]+(1-\beta_{p2}^2)^2[-\beta_{p2}^3\frac{\partial\beta_{p2}}{\partial p}(A_{3+}+A_{3-})\\&+(1-\frac{\beta_{p2}^4}{4})(\frac{\partial A_{3+}}{\partial p}+\frac{\partial A_{3-}}{\partial p})\\&+4\beta_{p2}^2A_{3+}\frac{\partial A_{3-}}{\partial p}+4\beta_{p2}^2A_{3-}\frac{\partial A_{3+}}{\partial p}\\&+8\beta_{p2}A_{3+}A_{3-}\frac{\partial\beta_{p2}}{\partial p}],\end{aligned} \tag{84}$$

$$\begin{aligned}\frac{\partial G_{p2wd}}{\partial p}&=-\frac{1}{2}\beta_{p2}\frac{\partial\beta_{p2}}{\partial p}\\&+(2\beta_{p2}+2\beta_{p2}^3-\frac{3}{4}\beta_{p2}^5)\frac{\partial\beta_{p2}}{\partial p}(A_{3+}+A_{3-})\\&+(\beta_{p2}^2+\frac{\beta_{p2}^4}{2}-\frac{\beta_{p2}^6}{8})(\frac{\partial A_{3+}}{\partial p}+\frac{\partial A_{3-}}{\partial p})\\&+2\beta_{p2}^6A_{3+}\frac{\partial A_{3-}}{\partial p}+2\beta_{p2}^6A_{3-}\frac{\partial A_{3+}}{\partial p}\\&+12\beta_{p2}^5A_{3+}A_{3-}\frac{\partial\beta_{p2}}{\partial p},\end{aligned} \tag{85}$$

$$\frac{\partial A_{3+}}{\partial p}=\frac{\partial A_{3-}}{\partial p}=-\frac{1}{2}[1-(\frac{p}{2\lambda_2})^2]^{-\frac{3}{2}}(\frac{p}{2\lambda_2^2}), \tag{86}$$

$$\frac{\partial L_2}{\partial A_2}=\frac{\partial L_2}{\partial w}=\frac{p}{4\omega_2\lambda_2}[-\frac{1}{\beta_{p2}}\frac{\partial\beta_{p2}}{\partial w}+\frac{\partial G(\frac{p}{2},w,\lambda_2)}{\partial w}], \tag{87}$$

where

$$\frac{\partial\beta_{p2}}{\partial w}=\frac{\pi w}{p}\cos[\frac{\pi w}{p}], \tag{88}$$

$$\frac{\partial G(\frac{p}{2},w,\lambda_2)}{\partial w}=\frac{1}{2}\frac{G_{p2wd}\frac{\partial G_{p2wn}}{\partial w}-G_{p2wn}\frac{\partial G_{p2wd}}{\partial w}}{G_{p2wd}^2}, \tag{89}$$

$$\begin{aligned}\frac{\partial G_{p2wn}}{\partial w}&=2(1-\beta_{p2}^2)(-2\beta_{p2}\frac{\partial\beta_{p2}}{\partial w})[(1-\frac{\beta_{p2}^4}{4})(A_{3+}+A_{3-})\\&+4\beta_{p2}^2A_{2+}A_{2-}]\\&+(1-\beta_{p2}^2)^2[-\beta_{p2}^3\frac{\partial\beta_{p2}}{\partial w}(A_{3+}+A_{3-})\\&+8\beta_{p2}A_{3+}A_{3-}\frac{\partial\beta_{p2}}{\partial w}],\end{aligned} \tag{90}$$

$$\begin{aligned}\frac{\partial G_{p2wd}}{\partial w}&=-\frac{1}{2}\beta_{p2}\frac{\partial\beta_{p2}}{\partial w}\\&+(2\beta_{p2}+2\beta_{p2}^3-\frac{3}{4}\beta_{p2}^5)\frac{\partial\beta_{p2}}{\partial w}(A_{3+}+A_{3-})\\&+12\beta_{p2}^5A_{3+}A_{3-}\frac{\partial\beta_{p2}}{\partial w},\end{aligned} \tag{91}$$

$$\frac{\partial L_2}{\partial A_3}=\frac{\partial L_2}{\partial s}=\frac{d}{2\omega_2\lambda_2}[-\frac{1}{\beta_{hs}}\frac{\partial\beta_{hs}}{\partial s}+\frac{\partial G(p,2h+s,\lambda_2)}{\partial s}], \tag{92}$$

where

$$\frac{\partial\beta_{hs}}{\partial s}=\frac{\pi}{2p}\cos[\frac{\pi(2h+s)}{p}], \tag{93}$$

$$\frac{\partial G(p,\ 2h+s,\lambda_2)}{\partial s}=\frac{1}{2}\frac{G_{hsd}\frac{\partial G_{hsn}}{\partial s}-G_{hsn}\frac{\partial G_{hsd}}{\partial s}}{G_{hsd}^2}, \tag{94}$$

$$\begin{aligned}\frac{\partial G_{hsn}}{\partial s}&=2(1-\beta_{hs}^2)(-2\beta_{hs}\frac{\partial\beta_{hs}}{\partial s})[(1-\frac{\beta_{hs}^4}{4})(A_{2+}+A_{2-})\\&+4\beta_{hs}^2A_{2+}A_{2-}]+(1-\beta_{hs}^2)^2[-\beta_{hs}^3\frac{\partial\beta_{hs}}{\partial s}(A_{2+}+A_{2-})\\&+8\beta_{hs}A_{2+}A_{2-}\frac{\partial\beta_{hs}}{\partial s}],\end{aligned} \tag{95}$$

$$\begin{aligned}\frac{\partial G_{hsd}}{\partial s}&=-\frac{1}{2}\beta_{hs}\frac{\partial\beta_{hs}}{\partial s}\\&+(2\beta_{hs}+2\beta_{hs}^3-\frac{3}{4}\beta_{hs}^5)\frac{\partial\beta_{hs}}{\partial s}(A_{2+}+A_{2-})\\&+12\beta_{hs}^5A_{2+}A_{2-}\frac{\partial\beta_{hs}}{\partial s},\end{aligned} \tag{96}$$

$$\begin{aligned}\frac{\partial L_2}{\partial A_4}&=\frac{\partial L_2}{\partial h}\\&=\frac{d}{2\omega_2\lambda_2}[-\frac{1}{\beta_{hs}}\frac{\partial\beta_{hs}}{\partial h}+\frac{\partial G(p,\ 2h+s,\lambda_2)}{\partial h}],\end{aligned} \tag{97}$$

where

$$\frac{\partial\beta_{hs}}{\partial h}=\frac{\pi}{p}\cos[\frac{\pi(2h+s)}{p}], \tag{98}$$

$$\frac{\partial G(p,\ 2h+s,\lambda_2)}{\partial h}=\frac{1}{2}\frac{G_{hsd}\frac{\partial G_{hsn}}{\partial h}-G_{hsn}\frac{\partial G_{hsd}}{\partial h}}{G_{hsd}^2}, \tag{99}$$

$$\begin{aligned}\frac{\partial G_{hsn}}{\partial h}&=2(1-\beta_{hs}^2)(-2\beta_{hs}\frac{\partial\beta_{hs}}{\partial h})[(1-\frac{\beta_{hs}^4}{4})(A_{2+}+A_{2-})\\&+4\beta_{hs}^2A_{2+}A_{2-}]+(1-\beta_{hs}^2)^2[-\beta_{hs}^3\frac{\partial\beta_{hs}}{\partial h}(A_{2+}+A_{2-})\\&+8\beta_{hs}A_{2+}A_{2-}\frac{\partial\beta_{hs}}{\partial h}]\end{aligned} \tag{100}$$

$$\begin{aligned}\frac{\partial G_{hsd}}{\partial h}&=-\frac{1}{2}\beta_{hs}\frac{\partial\beta_{hs}}{\partial h}\\&+(2\beta_{hs}+2\beta_{hs}^3-\frac{3}{4}\beta_{hs}^5)\frac{\partial\beta_{hs}}{\partial h}(A_{2+}+A_{2-})\\&+12\beta_{hs}^5A_{2+}A_{2-}\frac{\partial\beta_{hs}}{\partial h},\end{aligned} \tag{101}$$

$$\frac{\partial L_2}{\partial A_5}=\frac{\partial L_2}{\partial d}=\frac{d}{2\omega_2\lambda_2}[-\ell n(\beta_{hs})+G(p,\ 2h+s,\lambda_2)], \tag{102}$$

$$\begin{aligned}\frac{\partial C_2}{\partial A_1}&=\frac{\partial C_2}{\partial p}\\&=\frac{8(2h+s)}{\omega_2\lambda_2}[-\frac{1}{\beta_{pd}}\frac{\partial\beta_{pd}}{\partial p}+\frac{\partial G(p,p-d,\lambda_2)}{\partial p}],\end{aligned} \tag{103}$$

where

$$\frac{\partial G(p,p-d,\lambda_2)}{\partial p}=\frac{1}{2}\frac{G_{pdd2}\frac{\partial G_{pdn2}}{\partial p}-G_{pdn2}\frac{\partial G_{pdd2}}{\partial p}}{G_{pdd2}^2}, \tag{104}$$

$$\frac{\partial G_{pdn2}}{\partial p} = 2(1-\beta_{pd}^2)(-2\beta_{pd}\frac{\partial \beta_{pd}}{\partial p})[(1-\frac{\beta_{pd}^4}{4})(A_{2+}+A_{2-}) + 4\beta_{pd}^2 A_{2+}A_{2-}] + (1-\beta_{pd}^2)^2[-\beta_{pd}^3\frac{\partial \beta_{pd}}{\partial p}(A_{2+}+A_{2-}) + (1-\frac{\beta_{pd}^4}{4})(\frac{\partial A_{2+}}{\partial p}+\frac{\partial A_{2-}}{\partial p}) + 4\beta_{pd}^2 A_{2+}\frac{\partial A_{2-}}{\partial p} + 4\beta_{pd}^2 A_{2-}\frac{\partial A_{2+}}{\partial p} + 8\beta_{pd}A_{2+}A_{2-}\frac{\partial \beta_{pd}}{\partial p}], \quad (105)$$

$$\frac{\partial G_{pdd2}}{\partial p} = -\frac{1}{2}\beta_{pd}\frac{\partial \beta_{pd}}{\partial p} + (2\beta_{pd}+2\beta_{pd}^3-\frac{3}{4}\beta_{pd}^5)\frac{\partial \beta_{pd}}{\partial p}(A_{2+}+A_{2-}) + (\beta_{pd}^2+\frac{\beta_{pd}^4}{2}-\frac{\beta_{pd}^6}{8})(\frac{\partial A_{2+}}{\partial p}+\frac{\partial A_{2-}}{\partial p}) + 2\beta_{pd}^6 A_{2+}\frac{\partial A_{2-}}{\partial p} + 2\beta_{pd}^6 A_{2-}\frac{\partial A_{2+}}{\partial p} + 12\beta_{pd}^5 A_{2+}A_{2-}\frac{\partial \beta_{pd}}{\partial p}, \quad (106)$$

$$\frac{\partial C_2}{\partial A_2} = \frac{\partial C_2}{\partial w} = 0, \quad (107)$$

$$\frac{\partial C_2}{\partial A_3} = \frac{\partial C_2}{\partial s} = \frac{8}{\omega_2\lambda_2}[-\ell n(\beta_{pd}) + G(p, p-d, \lambda_2)], \quad (108)$$

$$\frac{\partial C_2}{\partial A_4} = \frac{\partial C_2}{\partial h} = \frac{16}{\omega_2\lambda_2}[-\ell n(\beta_{pd}) + G(p, p-d, \lambda_2)], \quad (109)$$

$$\frac{\partial C_2}{\partial A_5} = \frac{\partial C_2}{\partial d} = \frac{8(2h+s)}{\omega_2\lambda_2}[-\frac{1}{\beta_{pd}}\frac{\partial \beta_{pd}}{\partial d} + \frac{\partial G(p, p-d, \lambda_2)}{\partial d}], \quad (110)$$

where

$$\frac{\partial G(p, p-d, \lambda_2)}{\partial d} = \frac{1}{2}\frac{G_{pdd2}\dfrac{\partial G_{pdn2}}{\partial d} - G_{pdn2}\dfrac{\partial G_{pdd2}}{\partial d}}{G_{pdd2}^2}, \quad (111)$$

$$\frac{\partial G_{pdn2}}{\partial d} = 2(1-\beta_{pd}^2)(-2\beta_{pd}\frac{\partial \beta_{pd}}{\partial d})[(1-\frac{\beta_{pd}^4}{4})(A_{2+}+A_{2-}) + 4\beta_{pd}^2 A_{2+}A_{2-}] + (1-\beta_{pd}^2)^2[-\beta_{pd}^3\frac{\partial \beta_{pd}}{\partial d}(A_{2+}+A_{2-}) + 8\beta_{pd}A_{2+}A_{2-}\frac{\partial \beta_{pd}}{\partial d}], \quad (112)$$

$$\frac{\partial G_{pdd2}}{\partial d} = -\frac{1}{2}\beta_{pd}\frac{\partial \beta_{pd}}{\partial d} + (2\beta_{pd}+2\beta_{pd}^3-\frac{3}{4}\beta_{pd}^5)\frac{\partial \beta_{pd}}{\partial d}(A_{2+}+A_{2-}) + 12\beta_{pd}^5 A_{2+}A_{2-}\frac{\partial \beta_{pd}}{\partial d}. \quad (113)$$

ACKNOWLEDGMENT

The authors would like to thank the National Science Council of the Republic of China (ROC) for the financial support of this research under the contract of NSC 102-2221-E-155-019.

REFERENCES

[1] R. Ulrich, "Far-infrared properties of metallic mesh and its complementary structure," *Infrared Phys.*, vol. 7, no. 1, pp. 37-50, 1967.

[2] B. A. Munk, R. J. Luebbers, and R. D. Fulton, "Transmission through a 2-layer array of loaded slots," *IEEE Trans. Antennas Propag.*, vol. AP22, no. 6, pp. 804-809, Nov. 1974.

[3] F. Yang and Y. Rahmat-Samii, "Reflection phase characterizations of the EBG ground plane for low profile wire antenna applications," *IEEE Trans. Antennas Propag.*, vol. 51, no. 10, pp. 2691-2703, Oct. 2003.

[4] Y. Zhang, J. von Hagen, M. Younis, C. Fischer, and W. Wiesbeck, "Planar artificial magnetic conductors and patch antennas," *IEEE Trans. Antennas Propag.*, vol. 51, no. 10, pp. 2704-2712, Oct. 2003.

[5] X. L. Bao, G. Ruvio, M. J. Ammann, and M. John, "A novel GPS patch antenna on a fractal hi-impedance surface substrate," *IEEE Antennas Wireless Propag. Lett.*, vol. 5, pp. 323-326, 2006.

[6] H. Mosallaei and K. Sarabandi, "Antenna miniaturization and bandwidth enhancement using a reactive impedance substrate," *IEEE Trans. Antennas Propag.*, vol. 52, no. 9, pp. 2403-2414, Sep. 2004.

[7] R. F. J. Broas, D. F. Sievenpiper, and E. Yablonovitch, "A high-impedance ground plane applied to a cellphone handset geometry," *IEEE Trans. Microw. Theory Tech.*, vol. 49, no. 7, pp. 1262-1265, Jul. 2001.

[8] A. P. Feresidis, G. Goussetis, S. Wang, and J. C. Vardaxoglou, "Artificial magnetic conductor surfaces and their application to low-profile high-gain planar antennas," *IEEE Trans. Antennas Propag.*, vol. 53, no. 1, pp. 209-215, Jan. 2005.

[9] H. Y. Chen and Y. Tao, "Bandwidth enhancement

of a U-slot patch antenna using dual-band frequency selective surface with double rectangular ring elements," *Microw. Opt. Technol. Lett.*, vol. 53, no. 7, pp. 1547-1553, Jul. 2011.

[10] H. Y. Chen and Y. Tao, "Performance improvement of a U-slot patch antenna using a dual-band frequency selective surface with modified Jerusalem cross elements," *IEEE Trans. Antennas Propag.*, vol. 59, no. 9, pp. 3482-3486, Sep. 2011.

[11] M. Philippakis, C. Martel, D. Kemp, M. C. S. M. R. Allan, S. Appleton, W. Damerell, C. Burton, and E. A. Parker, *Application of FSS Structures to Selectively Control the Propagation of Signals into and out of Buildings*, ERA Technology, Leatherhead, Surrey, UK, Tech. Rep., 2004.

[12] M. Gustafsson, A. Karlsson, A. P. P. Rebelo, and B. Widenberg, "Design of frequency selective windows for improved indoor outdoor communication," *IEEE Trans. Antennas Propag.*, vol. 54, no. 6, pp. 1897-1900, Jun. 2006.

[13] G. I. Kiani, L. G. Osslon, A. Karlsson, and K. P. Esselle, "Transmission of infrared and visible wavelengths through energy-saving glass due to etching of frequency-selective surfaces," *IET Microw. Antennas Propag.*, vol. 4, pp. 955-961, 2010.

[14] G. I. Kiani, L. G. Osslon, A. Karlsson, K. P. Esselle, and M. Nilsson, "Cross-dipole bandpass frequency selective surface for energy-saving glass used in building," *IEEE Trans. Antennas Propag*., vol. 59, no. 2, pp. 520-525, Feb. 2011.

[15] D. J. Kern, D. H. Werner, A. Monorchio, L. Lanuzza, and M. J. Wilhelm, "The design synthesis of multiband artificial magnetic conductors using high impedance frequency selective surfaces," *IEEE Trans. Antennas Propag.*, vol. 53, no. 1, pp. 8-17, Jan. 2005.

[16] J. McVay, N. Engheta, and A. Hoorfar, "High impedance metamaterial surfaces using Hilbert-curve inclusions," *IEEE Microw. Wireless Compon. Lett.*, vol. 14, pp. 130-132, 2004.

[17] J. Bell and M. Iskander, "A low-profile archimedean spiral antenna using an EBG ground plane," *IEEE Antennas Wireless Propag. Lett*., vol. 3, pp. 223-226, 2004.

[18] R. Mittra, C. H Chan, and T. Cwik, "Techniques for analyzing frequency selective surfaces - a review," *Pro. IEEE*, vol. 76, no. 12, pp. 1593-1615, Dec. 1988.

[19] F. R. Yang, K. P. Ma, Y. Qian, and T. Itoh, "A uniplanar compact photonic-bandgap (UC-PBG) structure and its applications for microwave circuits," *IEEE Trans. Microw. Theory Tech.*, vol. 47, no. 8, pp. 1509-1514, Aug. 1999.

[20] K. Sarabandi and N. Behdad, "A frequency selective surface with miniaturized elements," *IEEE Trans. Antennas Propag*., vol. 55, no. 5, pp. 1239-1245, May 2007.

[21] T. Kamgaing and O. M. Ramahi, "Design and modeling of high-impedance electromagnetic surfaces for switching noise suppression in power planes," *IEEE Trans. Electromagn. Compat.*, vol. 47, no. 3, pp. 479-489, Aug. 2005.

[22] T. K. Wu, "Four-band frequency selective surface with double-square-loop patch elements," *IEEE Trans. Antennas Propag.*, vol. 42, no. 12, pp. 1659-1663, Dec. 1994.

[23] H. L. Liu, K. L. Ford, and R. J. Langley, "Design methodology for a miniaturized frequency selective surface using lumped reactive components," *IEEE Trans. Antennas Propag*., vol. 57, no. 9, pp. 2732-2738, Sep. 2009.

[24] R. R. Xu, H. C. Zhao, Z. Y. Zong, and W. Wu, "Dual-band capacitive loaded frequency selective surfaces with close band spacing," *IEEE Microw. Wireless Compon. Lett*., vol. 18, no. 12, Dec. 2008.

[25] G. I. Kiani, K. L. Ford, K. P. Esselle, A. R. Weily, C. Panagamuwa, and J. C. Batchelor, "Single-layer bandpass active frequency selective surface," *Microw. Opt. Technol. Lett.*, vol. 50, no. 8, pp. 2149-2151, Aug. 2008.

[26] G. I. Kiani, K. L. Ford, K. P. Esselle, A. R. Weily, and C. J. Panagamuwa, "Oblique incidence performance of a novel frequency selective surface absorber," *IEEE Trans. Antennas Propag.*, vol. 55, no. 10, pp. 2931-2934, Oct. 2007.

[27] B. A. Munk, P. Munk, and J. Pryor, "On designing Jaumann and circuit analog absorbers (CA absorbers) for oblique angle of incidence," *IEEE Trans. Antennas Propag.*, vol. 55, no. 1, pp. 186-193, Jan. 2007.

[28] A. K. Zadeh and A. Karlsson, "Capacitive circuit method for fast and efficient design of wideband radar absorbers," *IEEE Trans. Antennas Propag.*, vol. 57, no. 8, pp. 2307-2314, Aug. 2009.

[29] A. Itou, O. Hashimoto, H. Yokokawa, and K. Sumi, "A fundamental study of a thin wave absorber using FSS technology," *Electron. Commun. Jpn.*, vol. 87, pt. 1, pp. 77-86, 2004.

[30] A. Itou, H. Ebara, H. Nakajima, K. Wada, and O. Hashimoto, "An experimental study of a wave absorber using a frequency-selective surface," *Microw. Opt. Technol. Lett.*, vol. 28, pp. 321-323, 2001.

[31] G. I. Kiani, A. R. Weily, and K. P. Esselle, "A novel absorb/transmit FSS for secure indoor wireless networks with reduced multipath fading," *IEEE Microw. Wireless Compon. Lett.*, vol. 16, no. 6, pp. 378-380, 2006.

[32] N. Engheta and R. W. Ziolkowski, *Metamaterials: Physics and Engineering Explorations*, Hoboken/Piscataway, NJ, Wiley-IEEE Press, 2006.

[33] R. Baggen, M. Martinez-Vazquez, J. Leiss, and S. Holzwarth, "Comparison of EBG substrates with and without vias for GALILEO/GPS applications," In *Proc. EuCAP 2007, 2nd European Conf. Antennas Propag.*, Edinburgh, UK, 2007.

[34] Y. Fan, B. L. Ooi, H. D. Hriston, and M. S. Leong, "Compound diffractive lens consisting of Fresnel zone plate and frequency selective screen," *IEEE Trans. Antennas Propag.*, vol. 58, no. 6, pp. 1842-1847, Jun. 2010.

[35] P. Harms, R. Mittra, and W. Ko, "Implementation of the periodic boundary-condition in the finite-difference time-domain algorithm for FSS structures," *IEEE Trans. Antennas Propag.*, vol. 42, no. 9, pp. 1317-1324, Sep. 1994.

[36] J. L. Volakis, T. Ozdemir, and J. gong, "Hybrid finite-element methodologies for antennas and scattering," *IEEE Trans. Antennas Propag.*, vol. 45, no. 3, pp. 493-507, Mar. 1997.

[37] T. W. Leonard and J. W. Cofer, "A new equivalent circuit representation for the Jerusalem cross," in *Proc. IEE Int. Conf. Antennas and Propagation*, London, England, vol. 2, pp. 65-69, 1978.

[38] R. J. Langley and A. J. Drinkwater, "Improved empirical model for the Jersalem cross," *IEE Proc.*, vol. 129, Pt. H., no. 1, pp. 1-6, Feb. 1982.

[39] M. Hosseinipanah and Q Wu, "Equivalent circuit model for designing of Jerusalem cross-based artificial magnetic conductors," *Radioeng*., vol. 18, no. 4, pp. 544-550, Dec. 2009.

[40] L. H. Lafara, *Computer Method for Science and Engineering*, New York: Hayden, pp. 148-157, 1973.

[41] S. H. Sun and B. Z. Wang, "Parameter optimization based on GA and HFSS," *J. Electron. Sci. Technol. China*, vol. 3, no. 1, pp. 45-47, Mar. 2005.

Hsing-Yi Chen was born in Taiwan, in 1954. He received the B.S. and M.S. degrees in Electrical Engineering in 1978 and 1981 from Chung Yuan Christian University and National Tsing Hua University, respectively. He received the Ph.D. degree in Electrical Engineering from University of Utah, Salt Lake City, Utah in 1989. He joined the faculty of the Department of Electrical Engineering, Yuan Ze University, Taiwan, in September 1989. He was the Chairman of Electrical Engineering from 1996 to 2002, the Chairman of Communications Engineering from 2001 to 2002, the Dean of Engineering College from 2002 to 2006, the Dean of Electrical and Communication Engineering College from 2006 to 2012, and the Dean of Research and Development Office from 2012 to 2013. Currently, he is the Dean of General Affairs Office, Yuan Ze University. His current interests include electrostatic discharge, electromagnetic scattering and absorption, waveguide design, radar systems, electromagnetic compatibility and interference, bioelectromagnetics, electromagnetic radiation hazard protection, and applications of frequency selective surface.

He is a Member of Phi Tau Phi. He was also a Member of the editorial board of the *Journal of Occupational Safety and Health* from 1996 to 1997. He was elected an Outstanding Alumnus of the Tainan Second High School in 1995. He has been the recipient of numerous awards including the 1990 Distinguished Research, Service, and Teaching Award presented by the Yuan Ze University, the 1999 and 2002 YZU Outstanding Research Award, and the 2005 Y. Z. Hsu Outstanding Professor Award for Science, Technology & Humanity Category. He was awarded Chair Professor by Far Eastern Y. Z. Hsu Science and Technology Memorial Foundation in 2008. His name is listed in Who's Who in the World in 1998.

Tsung-Han Lin was born in Taiwan, in 1988. He received the B.S. degree in Electronic Engineering from Chung Yuan Christian University in 2010. He is currently working toward the M.S. degree in Communications Engineering at Yuan Ze University, Taiwan. His research interests include patch antenna design, frequency selective surfaces, and numerical computation of electromagnetics.

Pei-Kuen Li was born in Taiwan, in 1988. He received the B.S. and M.S. degrees in Communications Engineering from Yuan Ze University in 2011 and 2013, respectively. His research interests include electrostatic discharge, patch antenna design, electromagnetic compatibility and interference, wireless communications, and numerical computation of electromagnetics.

Pole Arc Skewing Analysis of Synchronous Reluctance Machine Using Discrete Method Combined with Winding Function Approach

P. Naderi and A. Shiri

Electrical Engineering Department
Shahid Rajaee Teacher Training University, Tehran, 1678815811, Iran
p.naderi@srttu.edu, abbas.shiri@srttu.edu

Abstract ─ The paper investigates the effect of pole arc skewing in synchronous reluctance machine on its torque ripple. To do this, the machine's reluctances are calculated by using winding function approach (WFA). A numerical-based method is proposed for modeling the machine's dynamic equations. The effect of rotor skewing and the winding type (single-layer or double layer) on the machine's behavior and torque ripple are investigated. The results show that skewing the rotor is significantly effective in double-layer winding case and it is not a proper idea for machine with single-layer winding. The proposed method is capable of studying the voltage-fed machine's behavior which is common in reality in comparison with current source-fed machine. Also, shorter calculation time and capability of studying parameter sensitivity are other advantages of the proposed method in comparison with finite element method (FEM).

Index Terms ─ Air-gap function, rotor skewing, slot opening, winding function.

I. INTRODUCTION

The synchronous reluctance machine (SynRM) has been widely employed in industry such as high speed applications and vehicular technology. Besides having high efficiency, these motors have working ability in variable frequency conditions. In many researches, the torque produced by the SynRM is supposed smooth; however, a real machine has some torque/current ripples due to some effects including slot opening and also limited slot numbers which make the winding function and magneto-motive force (MMF) non-sinusoidal. In this paper, by using winding function approach (WFA), rotor skewing, pole arc changing and also winding chording are analyzed in order to reduce the torque ripple. The WFA is a powerful tool for electrical machine modeling which has some advantages in comparison with FEM [1]-[4]. In [1], using WFA, the pole skewing is addressed for torque ripple reduction in SynRM. The machine performance is studied in both single and double-layer winding case. Lubin, et. al., have modeled a 4-pole SynRM using both FEM and WFA and the results have been compared [2]. In both mentioned references, the three-phase sinusoidal current source has been used as power supply which is not usual in reality. In [2], only a single-layer winding machine has been modeled by FEM and WFA, and the pole skewing is not considered in investigations. However, in [1], the pole skewing effect in double-layer winding machine has been presented. In the mentioned references, the machine performance has not been studied in voltage feed conditions. The synchronous machine has been also modeled in some researches for behavior studying and fault detection. In [3], using WFA, eccentricity fault effect has been addressed by Jocsimovich, et. al.; however, slot opening effect has not been considered in modeling. In another work, eccentricity fault have been studied by Faiz, et. al., for induction machine using WFA; however, only two simple windings have been considered and ideal air-gap function has been used [4]. In [5], WFA has been used for dynamic eccentricity fault diagnosis. In [6], the effect of slot and pole combination has been addressed for performance analysis of tooth-coil synchronous machine by winding harmonic spectrum analysis. In this reference, the slot opening effect has not been considered. In [7], by simplifying the model (which reduces the accuracy of the results) and considering some damper bars for the machine and using electromagnetic equations, fault detection has been discussed. By taking in to account suitable design modifications, such as multiple flux barriers, axially laminated anisotropic rotor instead of regular induction motor rotor, the poor power factor of the SynRM has been improved [8]-[11]. Although, ideal machines can be modeled by using classical approaches such as *dq* transformation, these kinds of modeling ignore all the space harmonics; therefore, they are not suitable for exact studying of the real machines [12]. In modeling of the real machine, the effects such as slot openings and distributed winding functions should be considered in the air-gap function. The latter is very important for eccentricity fault detection. Considering the above-mentioned facts, an advanced method should be used for

Submitted On: December 29, 2014
Accepted On: May 10, 2015

space harmonics analysis and eccentricity fault detection instead of the classical methods [13]-[16].

In this paper, a sample SynRM is modeled using WFA and inductance calculations in cases of skewed and un-skewed rotor are done. Then, to compute the currents, torque, etc., an iteration-based numerical method has been proposed for modeling of the machine's dynamical equation. The proposed method gives different results in comparison with those appeared in [1].

The results show that the skewing is an effective tool for torque ripple reduction in both single and double-layer windings; however, in single-layer winding, the reduction of torque ripple is not considerable. By applying a three phase sinusoidal current to the stator winding as done in [1], it is shown that the torque ripple is considerably reduced due to rotor skewing. Due to the fact that the motor is supplied by voltage source in reality, the latter is investigated in this paper which shows different results in comparison to [1], in which the machine has been fed by current source, especially in case of single-layer winding.

II. PROBLEM DEFINATION

Torque ripple calculation of a three-phase four-pole SynRM is considered in this research (Fig. 1) which has been studied in [1] with the same structure. Stator has 36 slots where three slots have been assigned for each pole per phase. As shown in Fig. 1, the stator reference ($\theta_s = 0$) is supposed in the center of the phase 'A' winding, while the rotor reference ($\theta_r = 0$) is set to the maximum air-gap length. Supposing the number of turns per pole per phase to be N_s, there exists the number of Ns/*3* turns in each slot in single-layer winding and the number of $N_s/6$ turns in each slot in double-layer case. Clearly, the multi-layer winding reduces space harmonics produced by distributed windings; however, it has not any effect on the harmonics produced by the number of the slots and also slot openings. In [1], pole skewing has been proposed for reduction of space harmonics which is reconsidered in this paper to obtain extended results. The pole skewing is shown in Fig. 2. Calculations will be done for different scenarios to obtain extended results and the latter will be compared with the results in [1]. The machine parameters are shown in Table 1. In the following section, some phenomena involved in the dynamic modeling of the machine, are discussed.

III. MODELING OF THE SLOT OPENING AND THE POLE SALIENCY

One of the non-ideal features of a real machine is slot opening geometry. The proper function should be defined for rotor poles and slot opening for accuracy of the modeling. Geometrical structure of rotor poles and stator slots are shown in Fig. 3.

A. Rotor's poles

Referring to geometric parameters shown in Fig. 3, the rotor pole saliency for one of the inter-polar-gap can be written as [2]:

$$g_r(\varphi)=\frac{r.(\pi/2 - |2\varphi+\beta|).[\mathrm{Sin}(|2\varphi+\beta|)-\mathrm{Sin}(\beta)]}{\mathrm{Cos}(2\varphi+\beta)} \quad (1)$$

$$\text{for } 0 \le \varphi \le \lambda,$$

where all angles are mechanical as shown in Fig. 3 and r is the inner radius of the stator. Since the rotor has 4 poles, the gap function of these poles can be mathematically modeled as:

$$f_{r1}(\theta_r) = g_r(\theta_r).[u(\theta_r) - u(\theta_r - {}^{\pi}/_{2} + \beta)], \quad (2)$$

$$f_r(\theta_r, x) = \sum_{k=-4}^{4} f_{r1}\Big(\theta_r - \alpha_{sk}\,{}^{x}/_{l} + (\pi - 2\beta)/4 - k\,{}^{\pi}/_{2}\Big). \quad (3)$$

In the above equations, $\theta_r = \theta_s - \theta_m$ and $0 < x < l$.

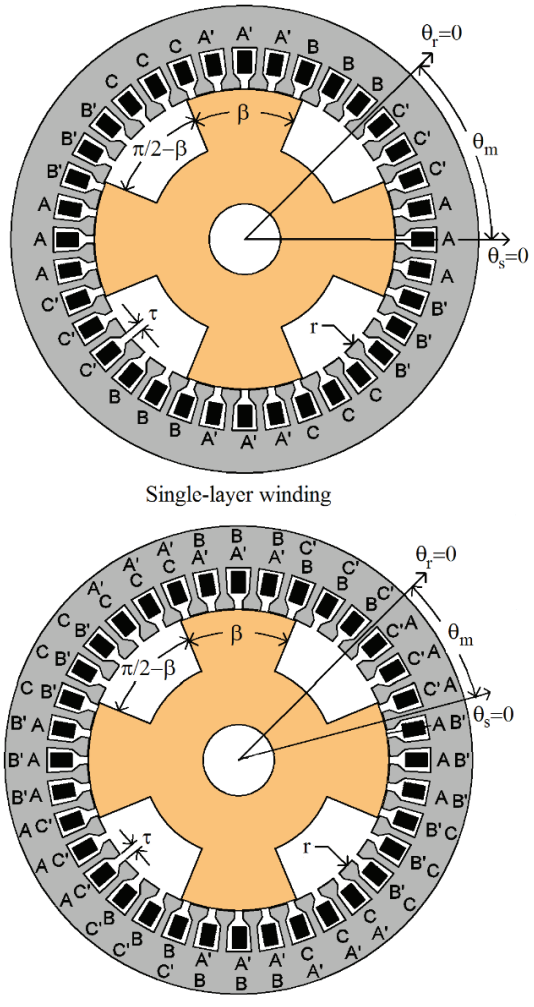

Fig. 1. The SynRM structure.

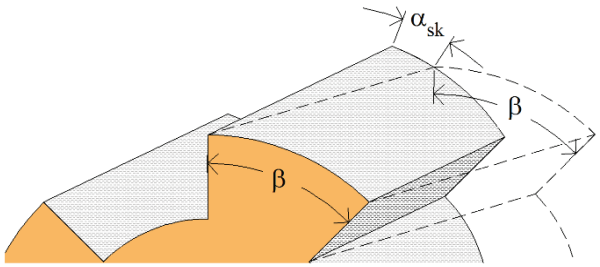

Fig. 2. Illustration of pole skewing.

Table 1: Geometrical and electrical specifications of the machine [1]

Symbol	Parameter	Value
N_s	Turns per pole	*90*
β	Pole saliency	*45° (un-skewed)*
R_s	Winding resistance	*2 Ω*
τ	Angle of slot opening	*3°*
g_o	Air-gap	*0.26 mm*
Yn	Windings connection	*Star grounded*
r	Stator radius	*4.5 cm*
l	Machine length	*15.5 cm*
l_{ls}	Leakage inductance	*1 mH*
b0,b1	Slot width properties	*2.97, 7.51 mm*
h0,h1	Slot depth properties	*3.71, 3.51 mm*
N_{slot}	Number of slots	*36*
P	Number of poles	*4*
γ	Slot pitch	*10°*

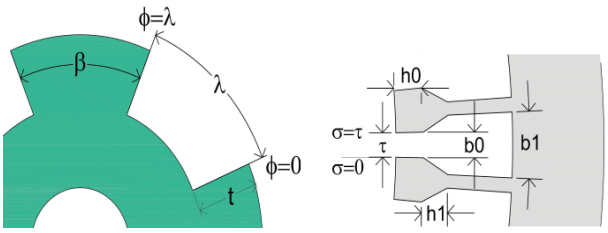

Fig. 3. Geometrical structure of rotor poles and stator slots.

B. Slot opening modeling

The slot opening for a half-gap can be written as follows [2]:

$$g_s(\sigma)= \begin{cases} \pi/2 . r.\sigma & 0 \le r.\sigma \le h0 \\ \pi/2 . r.\sigma + \varepsilon(r.\sigma - h0) & h0 \le r.\sigma \le \frac{\tau}{2} \end{cases}, \quad \text{for } 0 \le \sigma \le \tau/2 \tag{4}$$

$$\varepsilon = \pi/2 - \mathrm{Tan}^{-1}(2h1/(b1 - b0)). \tag{5}$$

The gap function for slot openings can be modeled as:

$$f_{s1}(\theta_s) = g_s(\theta_s).[u(\theta_s) - u(\theta_s - \tau/2)], \tag{6}$$

$$f_{s2}(\theta_s) = f_{s1}(\theta_s) + f_{s1}(-\theta_s + \tau). \tag{7}$$

Using the above equations and considering that the stator has 36 slots, we can wright:

For single-layer winding:

$$f_s(\theta_s) = \sum_{k=0}^{36} f_{s2}(\theta_s + \tau/2 - k\,(2\pi/36)), \tag{8-a}$$

For double-layer winding:

$$f_s(\theta_s) = \sum_{k=0}^{36} f_{s2}(\theta_s + \tau/2 + \pi/N_{slot} - k\,(2\pi/36)). \tag{8-b}$$

C. Total air gap function

The total air-gap function consists of three parts including slot openings, rotor saliency and conventional air-gap which can be written as follows:

$$f_g(\theta_s, \theta_m, x) = f_s(\theta_s) + f_r(\theta_s, \theta_m, x) + g_0\,, \tag{9}$$

where g_0 is the constant air-gap between the stator teeth and rotor saliency and also $\theta_r = \theta_s - \theta_m$. So, as it is seen in (2)-(9), the air-gap is a function of pole skewing (α_{sk}), mechanical rotor position (θ_m), and also mechanical angle of stator (θ_s). The air-gap function for stator slot and rotor saliency is plotted in Fig. 4 for a sample case with 22.5 degrees skewing.

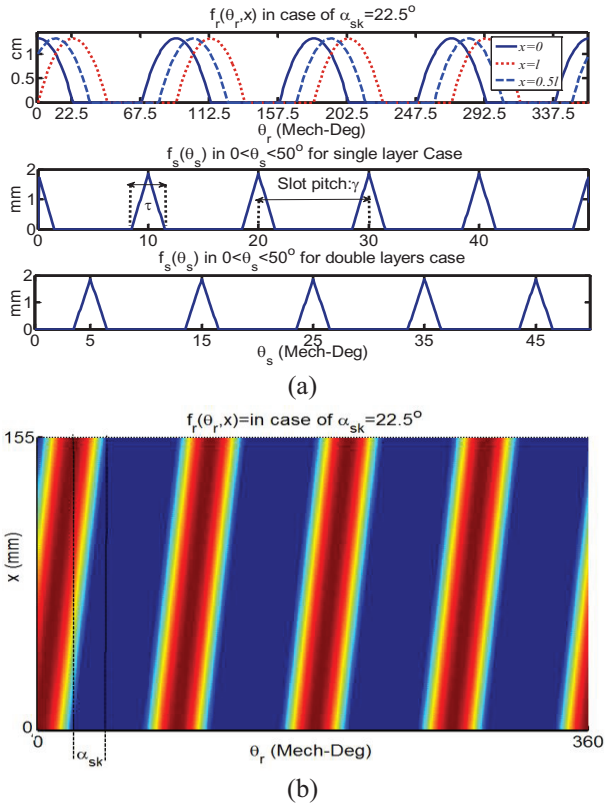

Fig. 4. Illustration of air-gap functions considering $\alpha_{sk} = 22.5^{\circ}$: (a) 2-D scheme of rotor saliency and slot opening, and (b) 3-D scheme of rotor poles saliency.

IV. WINDING FUNCTION

Sinusoidal winding function is an ideal feature of the machine that is not sufficient for exact modeling purposes. In fact, limited number of slots is one of the real factors that cause winding and MMF functions to be non-sinusoidal. It should be noted that a 4-pole machine with 36 slots and 90 turns per pole is equivalent to a machine with 30 turns per slot in single-layer and 15 turns per slot in double-layer winding. Now, the winding function for phase 'A' ($N_A(\theta_s)$), is shown in Fig. 5 (a), which is obtained by considering Fig. 6 (b). Clearly, the winding function for phases 'B' and 'C' are obtained similar to phase 'A' with 120 and 240 degrees phase shift, respectively. The winding function shown in Fig. 5 (a) will be used for modeling in next sections [1]-[5] and [17].

V. INDUCTANCE COMPUTATION BY WFA

Considering $\theta_r = \theta_s - \theta_m$, winding function approach is used to calculate the machine's inductances as written in (10) (the winding functions used for calculations are shown in Fig. 5 (a)):

$$L_{ij}(\theta_m) = \mu_0 r \int_0^l \int_0^{2\pi} N_i(\theta_s) N_j(\theta_s) f_g^{-1}(\theta_s, \theta_m, x).\, d\theta_s\,.\,dx. \quad (10)$$

Using the above equation for different θ_m values ($0 \le \theta_m \le \pi$), the inductance matrix is calculated as:

$$L(\theta_m) = \begin{bmatrix} L_{AA}(\theta_m) + l_{ls} & L_{AB}(\theta_m) & L_{AC}(\theta_m) \\ L_{AB}(\theta_m) & L_{BB}(\theta_m) + l_{ls} & L_{BC}(\theta_m) \\ L_{AC}(\theta_m) & L_{BC}(\theta_m) & L_{CC}(\theta_m) + l_{ls} \end{bmatrix}. \quad (11)$$

In (10), $f_g(\theta_s, \theta_s, x)$ is the air-gap function which consists of three parts including rotor poles (f_r), slot opening (f_s) and conventional air-gap (g_0), as written in (9). The instantaneous machine torque is calculated as follows:

$$\tau_e(\theta_m) = {}^1\!/_2\, i^T\, {}^{dL}\!/_{d\theta_m}\, i. \quad (12)$$

In which, L is the machine's inductance matrix as written in (11), superscript T denotes the transpose of the matrix and i is the currents vector of stator's windings which is given as follows:

$$i(\theta_m) = [i_A(\theta_m) \quad i_B(\theta_m) \quad i_C(\theta_m)]^T. \quad (13)$$

It is important to note that a proper procedure should be employed for modeling and computing of the machine's variables such as currents, fluxes, etc., when a three-phase power is applied. Using current source as input of the machine does not model the real behavior of the latter. So, the machine's performance will be different in comparison with the real performance. Thus, a proper dynamic model for machine to calculate the currents and torque is necessary.

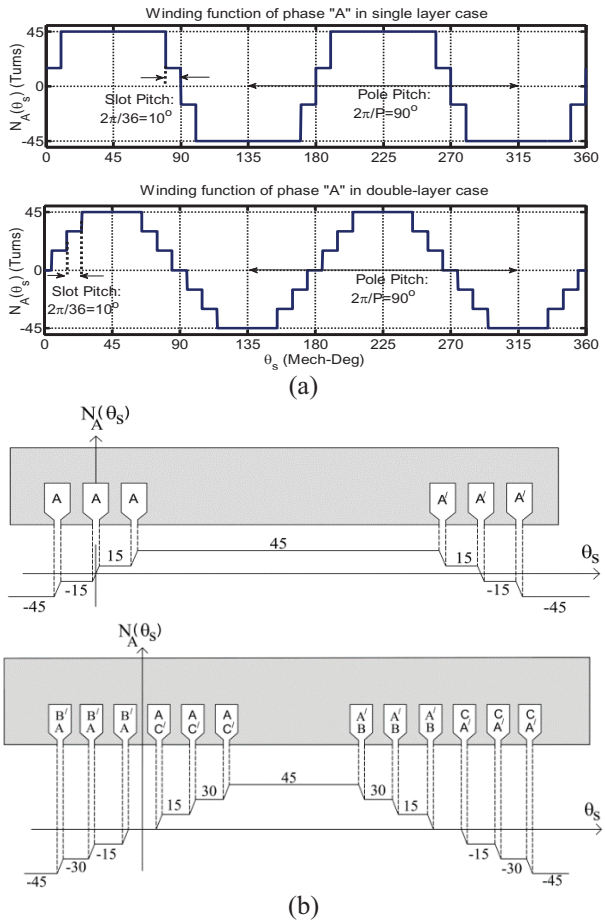

Fig. 5. (a) Winding function of phase 'A' in single and double-layer winding, and (b) slot-winding configurations.

VI. DISCRETE MODEL OF SynRM

To investigate the performance of the SynRM in steady state, we use the dynamic model of the machine. Neglecting the core losses, the motor's equations can be written as:

$$v(t) = R.\, i(t) + d\lambda(t)/dt, \quad (14)$$

$$\lambda(t) = L(t).\, i(t), \quad (15)$$

$$d\lambda(t)/dt = 1/\Delta t\, (L(t)i(t) - L(t-\Delta t)i(t-\Delta t)), \quad (16)$$

$$i(t) = (1/\Delta t\,.\,L(t) + R)^{-1}.[v(t) + 1/\Delta t\,.\,L(t-\Delta t)I(t-\Delta t)], \quad (17)$$

$$t = \theta_m/\omega_m \rightarrow \theta_m = \omega_m t \rightarrow x(\theta_m) = x(\omega_m t)\ for\ given\ x, \quad (18)$$

$$dL_{xy}(\theta_m)/d\theta_m = (L_{xy}(\theta_m + \Delta\theta_m) - L_{xy}(\theta_m))/\Delta\theta_m, \quad (19)$$

$$\Delta\theta_m = \omega_m \Delta t. \quad (20)$$

As Δt being step time, equations (16) and (19) can be used for derivation. Considering (14)-(16), the 3-

phase currents is computed by (17). Equations (19) and (20) can be used for torque computation in (12). It should be mentioned that the accuracy of the model depends on the value of Δt. In (14), R is the stator resistance matrix which is defined as:

$$R = diag[R_s]. \tag{21}$$

In which, R_s is the stator winding resistance. Also, in equations (14)-(17), $\lambda(t)$ and $v(t)$ are the stator flux and voltage vectors which are defined as:

$$\lambda = [\lambda_A \quad \lambda_B \quad \lambda_C]^T, v = [v_A \quad v_B \quad v_C]^T. \tag{22}$$

VII. RESULTED AND DISCUSSION

In this section, the torque ripple is calculated in various scenarios. At first, as in [1], a three-phase sinusoidal current source is applied to the motor with single-layer winding in skewed and un-skewed cases and the torque ripple is calculated. Then, for the same motor with single-layer winding, in both skewed and un-skewed cases, a three-phase sinusoidal voltage is applied. The results are compared with those in [1]. It is shown that different results are obtained in voltage-source case in comparison with the current-source case. Finally, the same calculations are done for the motor with double-layer winding.

Phase 'A' self-inductance and mutual inductance between phases 'A' and 'B' of the machine in both skewed and un-skewed cases for single and double-layer winding are shown in Fig. 6. There are two kinds of harmonic components in inductances due to slot openings and distributed winding which have high and low order components, respectively. It is seen in Fig. 6 that the high frequency components have been eliminated due to pole skewing. Moreover, the low frequency components are reduced in case of double-layer winding. In fact, the slot opening effects have been eliminated due to pole skewing which can reduce the produced torque ripple.

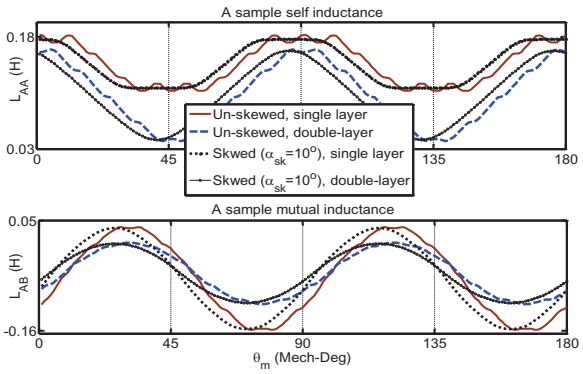

Fig. 6. The machine's inductances in single and double-layer winding, in skewed and un-skewed cases.

A. SynRM with single-layer windings

The machine with single-layer winding in skewed and un-skewed cases is simulated in this sub-section. The skewing angle is chosen $\alpha_{sk} = 10^\circ$ in skewed case and a 50 Hz three-phase 2A current source is applied to the motor:

$$\begin{aligned} i_A(t) &= 2\sqrt{2}\sin(2\pi f_s t - \varphi), \\ i_B(t) &= 2\sqrt{2}\sin(2\pi f_s t - \tfrac{2\pi}{3} - \varphi), \\ i_C(t) &= 2\sqrt{2}\sin(2\pi f_s t + \tfrac{2\pi}{3} - \varphi). \end{aligned} \tag{23}$$

The rotating speed is considered equal to synchronous speed which is 1500 RPM in 50 Hz power supply frequency. Moreover, the φ value is considered 45° to obtain the maximum average torque during simulation which is equal to 2.7 N.m. The output torque is calculated in both skewed and un-skewed cases. The results are illustrated in Fig. 7. It is seen that the torque has less ripple due to pole skewing. These calculations have been also carried out in [1] and [2] and the same results have been exactly obtained. Similar calculations have been done by applying the following three-phase voltages as input of the machine:

$$\begin{aligned} v_A(t) &= 95\sqrt{2}\cos(2\pi f_s t - \varphi), \\ v_B(t) &= 95\sqrt{2}\cos(2\pi f_s t - 2\pi/3 - \varphi), \\ v_C(t) &= 95\sqrt{2}\cos(2\pi f_s t + 2\pi/3 - \varphi). \end{aligned} \tag{24}$$

The machine torque in both skewed and un-skewed cases are illustrated in Fig. 8. It should be mentioned that the value of the voltage source is considered 95 V to obtain the average torque of 2.7 N.m. with tuned φ value. This causes the machine's performance to be similar to that with 2A current source power supply.

As it is seen in Fig. 8, the pole skewing has not considerable effect on the torque ripple in voltage source case. The current waveform is also shown in Fig. 8. It is clear that the current has some significant harmonic components because of non-sinusoidal winding function in single-layer case. In fact, the reason for this phenomenon is the limited slot numbers for winding distribution.

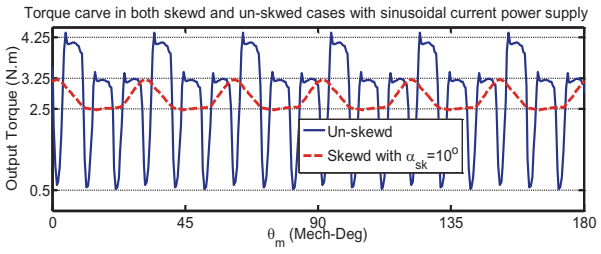

Fig. 7. Output torque in skewed and un-skewed cases with sinusoidal current source (single-layer winding).

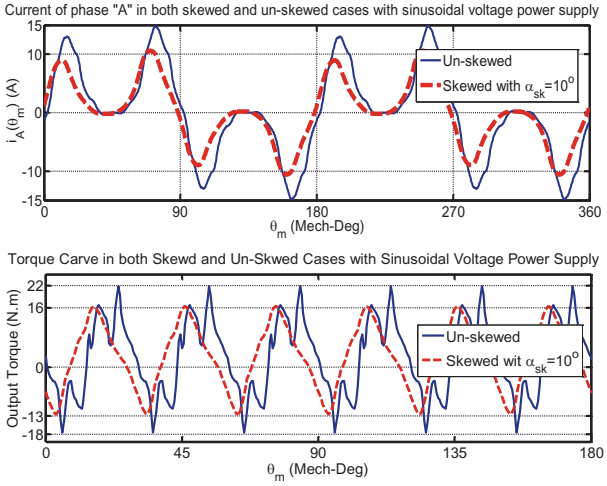

Fig. 8. Output torque and current waveform in skewed and un-skewed cases with sinusoidal voltage source (single-layer winding).

B. SynRM with double-layer winding

In this sub-section, the torque calculation for double-layer winding is performed. Figure 9 shows the output torque of machine with current source input.

In this case, a significant reduction is seen in the torque ripple. Exactly, the same results have been also reported in [1]. Comparing to Fig. 7, which has been obtained for single-layer winding, less torque ripple is produced in case of double-layer winding. Since, in reality, the voltage source power is usually supplied to the motor, (24) is considered as an input. The output torque and stator currents have been obtained for this case which is shown in Fig. 10. As it is seen in this figure, significant reduction in torque ripple is obtained in case of pole-skewed double-layer winding. This result has not been obtained in single-layer winding with voltage source power supply. As shown in Fig. 10, the machine's current has much less harmonic components than single-layer winding (see Fig. 8). In fact, the pole skewing is an effective tool for torque ripple reduction, only in cases that the machine currents have low harmonic components due to more slot numbers for each pole. In order to make better comparison, more results in different cases have been obtained which are listed in Table 2. As it is seen in the table, in current source case, the pole skewing has significant effect on the torque in both single and double-layer winding machine (about 80% reduction is seen in torque ripple); however, there is only 27.5% reduction in the torque ripple in voltage-fed single-layer winding machine. Also, in voltage-fed double-layer winding machine, the pole skewing reduces the torque ripple 84%.

Considering the results of Table 2, the effect of pole skewing on the torque ripple reduction can be summarized as follows:

- ✓ For sinusoidal current source-fed SynRM, the pole skewing significantly reduces the torque ripple in both single and double-layer winding cases. The ripple reductions in single and double-layer winding are 80.5% and 79%, respectively.
- ✓ For sinusoidal voltage source-fed SynRM, the pole arc skewing has not significant effect on the torque ripple reduction in single-layer winding case. This fact is due to generated harmonic components in the machine currents which are because of the produced space harmonics by the non-sinusoidal winding function. In this case, only 27.5% reduction is seen in the torque ripple.
- ✓ As an important result, the pole skewing improves the torque ripple just for the machines with sinusoidal winding function which can be obtained by multi-layer winding or more stator slot numbering.
- ✓ As another result, since in reality, the machine is supplied by voltage source, the pole arc skewing is an effective method for the SynRMs with the winding function having low harmonic components.

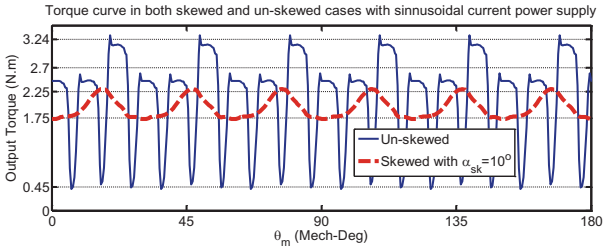

Fig. 9. Output torque in skewed and un-skewed cases with sinusoidal current source (double-layer winding).

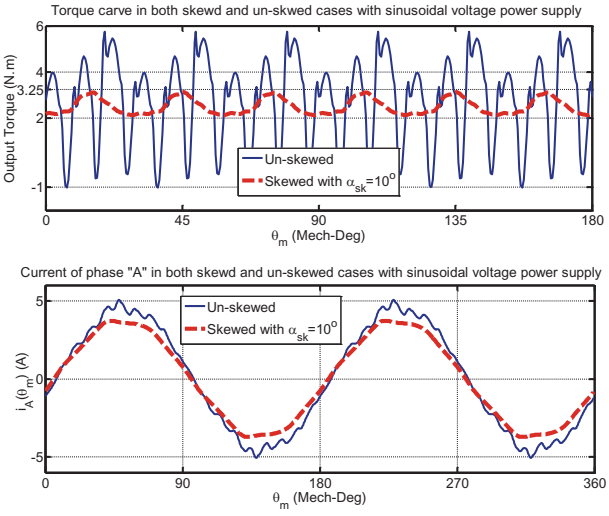

Fig. 10. Output torque and stator current in skewed and un-skewed cases with sinusoidal voltage source (double-layer winding).

Table 2: Torque ripple improvement due to pole skewing and double layer winding

	Current Source				Voltage Source			
Winding Layers	1	1	2	2	1	1	2	2
Average Torque (N.m)	2.8	2.8	2.1	2.1	2.8	2.8	2.5	2.5
Torque Ripple (%)	139	27.1	138	29.2	1428	1035	247	39.8
α_{sk}	0°	10°	0°	10°	0°	10°	0°	10°
Torque Ripple Reduction (%)	80.5		79		27.5		84	

VIII. VALIDATION OF THE RESULTS

As it is known, to analyze electrical machines, the finite element method (FEM) is an established method among researcher [1]-[4], [18]-[20]. In this section, a 3-D FEM is employed to evaluate the precision of the proposed method. The single-layer winding SynRM with un-skewed and 10° skewed poles is simulated in ANSOFT/Maxwell environment. φ value has been tuned to obtain average torque of 0 N.m for no-load condition in both FEM and proposed modeling method. It should be mentioned that the rotational speed has been considered as synchronous speed (1500 RPM) in simulations. The machine structure in Maxwell environment is shown in Fig. 11. The calculation of voltage-fed non-skewed SynRM torque in no-load condition has been done by the proposed method and compared with the results of the FEM. The results are presented in Fig. 12. The same calculations have been done for 10° skewed poles SynRM. The results are illustrated in Fig. 13. It is seen in these figures that the results obtained by the analytical calculations are close enough to the results of the FEM, validating the proposed method.

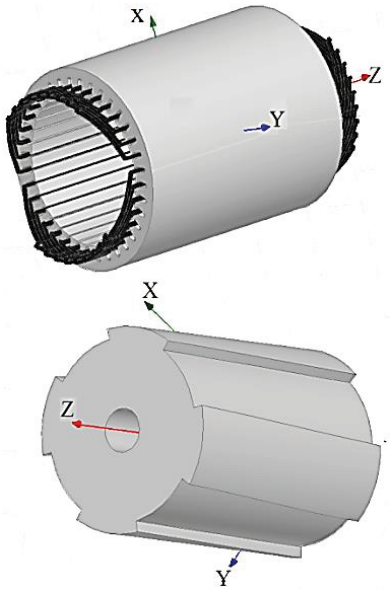

Fig. 11. Machine model in Maxwell environment.

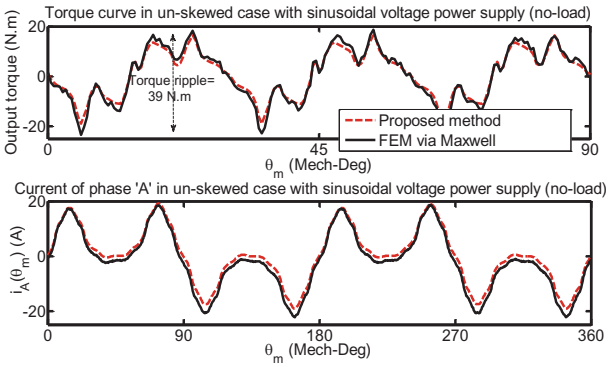

Fig. 12. Comparison of the proposed method with 3-D FEM for no-load voltage-fed machine in un-skewed case.

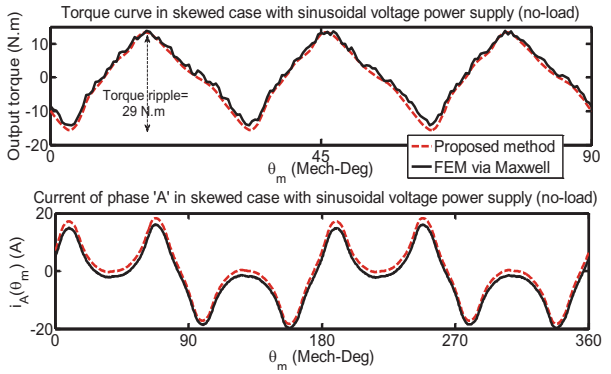

Fig. 13. Comparison of the proposed method with 3-D FEM for no-load voltage-fed machine in skewed case.

IX. CONCLUSION

In this paper, a numerical discrete-time method has been introduced to model SynRM in voltage-fed condition. An exact analytical method is proposed to calculate the currents and the torque of the motor. The proposed method has a simple procedure and can be applied to all other machines. According to the obtained results, it was shown that the pole skewing of SynRM has significant effect on the torque ripple reduction in double-layer winding machine which has lower harmonic components compared to single-layer winding. So, it is shown that the pole skewing is an

effective tool just in case that the winding function has low harmonic components which lead to semi-sinusoidal current. This case can be obtained by multi-layer windings or more slot numbers per pole. The machine has been simulated by 3-D FEM and the obtained results validate the accuracy of the proposed method.

REFERENCES

[1] T. Hamiti, T. Lubin, and A. Rezzoug, "A simple and efficient tool for design analysis of synchronous reluctance motor," *IEEE Trans. Magnetics*, vol. 44-12, pp. 4648-4652, 2008.

[2] T. Lubin, T. Hamiti, H. Razik, and A. Rezzoug, "Comparison between finite-element analysis and winding function theory for inductances and torque calculation of a synchronous reluctance machine," *IEEE Trans. Magnetics*, vol. 43-8, pp. 3406-3410, 2007.

[3] M. Jocsimovic, D. J. Penman, and N. Arthur, "Dynamic simulation of dynamic eccentricity in induction machine-winding function theory," *IEEE Trans*. *Energy Conversion*, vol. 15-2, pp. 143-148, 2000.

[4] J. Faiz and I. Tabatabaee, "Extension of winding function theory for non-uniform air gap in electrical machinery," *IEEE Trans. Magnetics*, vol. 38-6, pp. 3654-3657, 2002.

[5] I. Tabatabaee, J. Faiz, H. Lessani, and T. N. Razavi, "Modeling and simulation of a salient-pole synchronous generator with dynamic eccentricity using modified winding function theory," *IEEE Trans. Magnetics*, vol. 40-3, pp. 1550-1555, 2004.

[6] P. Ponomarev, P. Lindh, and J. Pyrhonen, "Effect of slot-poles combination on the leakage inductance and the performance of tooth-coil permanent-magnet synchronous machines," *IEEE Trans. Ind. Electronics*, vol. 60-10, pp. 4310-4317, 2013.

[7] T. C. Ilamparithi and S. Nandi, "Detection of eccentricity faults in three phase reluctance synchronous motor," *IEEE Trans. Ind. Applications*, vol. 48-4, pp. 1307-1377, 2012.

[8] T. Matsuo and T. A. Lipo, "Rotor design optimization of synchronous reluctance machine," *IEEE Trans. Energy Conversion*, vol. 9-2, pp. 359-365, 1994.

[9] H. Kiriyama, S. Kawano, Y. Honda, T. Higaki, S. Morimoto, and Y. Takeda, "High performance synchronous reluctance motor with multi-flux barrier for the appliance industry," in *Proc. IEEE Ind. Appl. Conf.*, vol. 1, pp. 111-117, Oct. 1998.

[10] Y. Inoue, S. Morimoto, and M. Sanada, "A novel control scheme for maximum power operation of synchronous reluctance motors including maximum torque per flux control," *IEEE Trans. Ind. Applications*, vol. 47-1, pp. 115-121, Jan./Feb. 2011.

[11] H. W. de Kock, A. J. Rix, and M. J. Kamper, "Optimal torque control of synchronous machines based on finite element analysis," *IEEE Trans. Ind. Electronics*, vol. 57-1, pp. 413-419, 2010.

[12] T. Ilamparithi and S. Nandi, "Comparison of results for eccentric cage induction motor using finite element method and modified winding function approach," *Joint Int. Conf. Power Electron., Drives, Energy Syst.*, pp. 1-7, Dec. 2010.

[13] C. Bruzzese, E. Santini, V. Benucci, and A. Millerani, "Model based eccentricity diagnosis for a ship brushless-generator exploiting the machine voltage signature analysis (MVSA)," *IEEE Int. Symp. Diag. Elect. Mach., Power Electron., Drives*, pp. 1-7, Aug./Sep. 2009.

[14] C. Bruzzese and G. Joksimovic, "Harmonic signatures of static eccentricities in the stator voltages and in the rotor current of no-load salient pole synchronous generators," *IEEE Trans. Ind. Electronics*, vol. 58-5, pp. 1606-1624, 2011.

[15] T. Ilamparithi and S. Nandi, "Analysis, modeling and simulation of static eccentric reluctance synchronous motor," *IEEE Int. Symp. Diag. Elect. Mach., Power Electron., Drives*, pp. 45-50, Sept. 2011.

[16] P. Neti and S. Nandi, "An improved strategy to detect stator inter-turn faults in synchronous reluctance motors using both negative sequence quantities and stored magnetic energy after supply disconnection," *IEEE IAS Annu. Meeting*, pp. 2234-2241, Sept. 2007.

[17] S. Saied, K. Abbaszadeh, and A. Tenconi, "Improvement to winding function theory for PM machine analysis," *Int. Conf. Power Eng., Energy and Electrical Drives*, pp. 1-6, May 2011.

[18] A. Shiri and A. Shoulaie, "Investigation of frequency effects on the performance of single-sided linear induction motor," *The Applied Computational Electromagnetics Society*, vol. 27, no. 6, 2012.

[19] E. Afjei and H. Torkaman, "Finite element analysis of switched reluctance generator under fault condition oriented towards diagnosis of eccentricity fault," *The Applied Computational Electromagnetics Society*, vol. 26, no. 1, 2011.

[20] E. Afjei, M. R. Tavakoli, and H. Torkaman, "Eccentricity compensation in switched reluctance machines via controlling winding turns/stator current: theory, modeling, and electromagnetic analysis," *The Applied Computational Electromagnetics Society*, vol. 28, no. 2, 2013.

Peyman Naderi was born in Ahvaz, Iran, in 1975. He received the B.S. degree in Electronic Engineering in 1998 and the M.S. degree in Power Engineering from Chamran University, Ahvaz, Iran in 2001. He has a Ph.D. degree in Power Engineering from K.N. Toosi University, Tehran, Iran. He is currently an Assistant Professor in Shahid Rajaee Teacher Training University of Tehran, Iran.

His interests are hybrid and electric vehicles, vehicles dynamic, power system transients and power system dynamics.

Abbas Shiri was born in Hashtrood, Iran in 1980. He received the B.Sc. degree from Tabriz University and the M.Sc. and Ph.D. degrees from Iran University of Science and Technology (IUST) in Electrical Engineering in 2004, 2006 and 2013, respectively. He is currently an Assistant Professor at Shahid Rajaee Teacher Training University, Tehran, Iran.

His areas of research interests include linear electric machines, electromagnetic systems and actuators, electrical machine design and modeling.

An Improved IEM2Mc Model for Surface Bistatic Scattering

Wenchao Zheng [1], Yi Leng [2], and Qingxia Li [1]

[1] Science and Technology on Multi-Spectral Information Processing Laboratory
School of Electronic Information and Communications
Huazhong University of Science and Technology, Wuhan, 430074, China
wenchaozheng@hust.edu.cn, qingxia_li@mail.hust.edu.cn

[2] Department of Information Counter
Air Force Early Warning Academy, Wuhan, 430019, China
lengyi119@aliyun.com (Corresponding author)

Abstract ─ In this paper, the IEM2Mc (integral equation model for second-order multiple s and complex-permittivity scattering media) model is modified in two aspects in bistatic scattering. Firstly, the full forms of the surface current terms in the Kirchhoff surface fields are reserved. Secondly, a transition function is used to estimate the Fresnel coefficients instead of the original expression. The simulating results of the improved IEM2Mc are compared with those of small perturbation method (SPM), Kirchhoff model (KA), and method of moment (MoM) for random rough surfaces scattering problems. It is shown that the improved IEM2Mc provides better predictions than the original form, especially for the large incident or scattering angle.

Index Terms ─ Bistatic scattering, IEM2M, IEM2Mc, KA, rough surface, SPM.

I. INTRODUCTION

IEM (integral equation model) is a widely used analytical model for the electromagnetic wave scattering in microwave remote sensing. The original IEM was proposed by Fung [1] based on the approximation for the integral equations described by Poggio and Miller. The further studies focus on removing the simplification in IEM to improve the accuracy. IEMM [2] comprises the multiple scattering effects by including the full form of the spectral representation of the Green's function (the effect of upward and downward waves on the surface fields). However, the IEMM doesn't handle the single scattering. Full form of the spectral representation of the gradient of the Green's function appears in the IEM2M model [3] and the advanced IEM model (AIEM) [4] for solving surface scattering problems.

However, both IEM2M and AIEM fail to deal with scattering from rough surface of complex-permittivity media. An error function related terms for the cross and complementary scattering coefficients are introduced by Du [5] to deal with scattering from rough surfaces of complex-permittivity media. Also, Alvarez-Perez [6] extends IEM2M to IEM2Mc for complex-permittivity scattering media based on a full 3D expansion of the outgoing spherical wave. Because of the full 3D expansion of the outgoing spherical wave, IEM2Mc in [6] is much simpler than the method in [5].

In the IEM2Mc, the expressions of the surface fields neglect the sum of horizontal and vertical Fresnel reflection coefficients. This neglection may bring about erroneous results at the bistatic configurations, particularly when the incident or scattering angle is large. Besides, in the emissivity calculations, this neglection may also produce unacceptable prediction, since the error will be accumulated by integrating all the scattering power over the half-space.

In this paper, the sum of horizontal and vertical Fresnel reflection coefficients in surface current expressions is added and a transition function is applied here to predict the Fresnel reflection. The newly derived IEM2Mc is verified by comparing the results with the SPM, KA, and MoM. The simulating is made on rough surfaces with small or moderate heights. In Section II, the scattered fields at the far zone, the scattered incoherent power and the scattering coefficients are specified. In Section III, the improved part of IEM2Mc is illustrated. Numerical simulations and comparisons with other methods are provided in Section IV. Finally, our conclusion is presented in Section V.

II. THE FORMULAS OF THE SCATTERING PROBLEM

Here we consider an incident plane wave impinging upon a rough surface from medium 1 to medium 2. The incident electric and magnetic fields

Submitted On: October 7, 2014
Accepted On: May 20, 2015

are:

$$\vec{E}^{\,i} = \hat{p}\, E_0 \exp[i(\vec{k}_1 \cdot \vec{r})] = \hat{p}\, E^i, \tag{1}$$

$$\vec{H}^{\,i} = \hat{k}_i \times (\hat{p}\, E^i)/\eta_1, \tag{2}$$

where $\hat{p}$ is the unit polarization vector; $\hat{k}_i$ is the unit vector in the incident direction; E_0 is the amplitude of the electric field; η_1 is the intrinsic impedance of medium 1; $\vec{k}_1 = \hat{k}_i k$, k is the wave number.

The equations for the surface tangential fields are:

$$\begin{aligned}\hat{n}'\times\vec{E}' &= 2\hat{n}'\times\vec{E}^{\,i} + \frac{1}{2\pi}\hat{n}'\times\int[ik\eta_1(\hat{n}''\times\vec{H}'')G_1 \\ &+ (\hat{n}''\times\vec{E}'')\times\nabla'' G_1 + (\hat{n}''\cdot\vec{E}'')\nabla'' G_1]ds'',\end{aligned} \tag{3}$$

$$\begin{aligned}\hat{n}'\times\vec{H}' &= 2\hat{n}'\times\vec{H}^{\,i} + \frac{1}{2\pi}\hat{n}'\times\int[-\frac{ik}{\eta_1}(\hat{n}''\times\vec{E}'')G_1 \\ &+ (\hat{n}''\times\vec{H}'')\times\nabla'' G_1 + (\hat{n}''\cdot\vec{H}'')\nabla'' G_1]ds'',\end{aligned} \tag{4}$$

where k $k = \omega\sqrt{\varepsilon_1\mu_1}$; G_1 is the Green function in medium 1; η_1 is the intrinsic impedance of medium 1; $\hat{n}'$ and $\hat{n}''$ are the unit normal vectors to the surface; $\hat{n}'\times\vec{E}'$ and $\hat{n}'\times\vec{H}'$ are the total tangential fields on surface in medium 1.

In IEM2Mc, a full 3D spectrum of the Green function is used instead of the Weyl representation of the Green function. The corresponding expression can be written as:

$$\begin{aligned}&G_m(\vec{r}',\vec{r}'') = \\ &\frac{1}{2\pi^2}\iiint_{R^3} e^{i[u(x'-x'')+v(y'-y'')]}\frac{e^{iw(z'-z'')}}{(w-q_m)(w+q_m)}dudvdw, \\ &q_m = \begin{cases}(k_m^2-u^2-v^2)^{1/2} & ,k_m^2 \ge u^2+v^2 \\ i(u^2+v^2-k_m^2)^{1/2} & ,k_m^2 \le u^2+v^2\end{cases}.\end{aligned} \tag{5}$$

The gradient of the Green function is given by:

$$\begin{aligned}&\nabla'' G_m(\vec{r}',\vec{r}'') = \frac{1}{2i\pi^2}\times \\ &\iiint_{R^3} e^{i[u(x'-x'')+v(y'-y'')+w(z'-z'')]}\frac{e^{iw(z'-z'')}}{(w-q_m)(w+q_m)}\vec{g}_m dudvdw, \\ &\vec{g}_m = u\hat{x}+v\hat{y}+w\hat{z}, \\ &m = \begin{cases}1, \ in \ \ medium\,1 \\ 2, \ in \ \ medium\,2\end{cases}.\end{aligned} \tag{6}$$

Because of the full 3D spectrum of the Green function, the damped waves originating inside a lossy medium or the evanescent waves in non-lossy medium can be evaluated.

The far-zone scattered fields are calculated in terms of surface fields. The far-zone scattered fields in the medium above the rough surface are derived according to the Stratton-Chu integral. It is divided into the Kirchhoff field and the complementary field:

$$E_{qp}^s = (E_{qp}^s)_k + (E_{qp}^s)_c. \tag{7}$$

In equation (7), the incident polarization is denoted by p and the receiving polarization by q. The incident polarization (p) could be horizontal polarization (h) or vertical polarization (v), and so is the receiving polarization (q):

$$\begin{aligned}E_{qp}^s &= K\int_s[(\hat{q}_s\times\hat{k}^s)\cdot(\hat{n}'\times\vec{E}_p'\,) + \eta_1\hat{q}_s\cdot(\hat{n}'\times\vec{H}_p'\,)]\times \\ &e^{-i\vec{k}^s\cdot\vec{r}'}D'dx'dy',\end{aligned} \tag{8}$$

where $K = ik_1 e^{ik_1R}/(4\pi R)$; $D' = \sqrt{1+Z_{x'}^2+Z_{y'}^2}$; $\hat{q}_s$ is the polarization vector.

The expression of the Kirchhoff field is:

$$(E_{qp}^s)_k = KE_0\int_s f_{qp}e^{-i[(\vec{k}^s-\vec{k}^i)\cdot\vec{r}']}dx'dy', \tag{9}$$

$$\begin{aligned}f_{qp} &= D'[(\hat{q}\times\hat{k}^s)\cdot(\hat{n}'\times\vec{E}_p'\,)_k \\ &+ \eta_1\hat{q}\cdot(\hat{n}'\times\vec{H}_p'\,)_k]/E^i.\end{aligned} \tag{10}$$

The Kirchhoff components will not be affected by the introduction of the full 3D Green function. The complementary field can be obtained in conjunction with a spectral representation for the Green's function and its gradient:

$$\begin{aligned}&(E_{qp}^s)_c = K\int_s[(\hat{q}_s\times\hat{k}^s)\cdot(\hat{n}'\times\vec{E}_p'\,)_c + \eta_1\hat{q}_s\cdot(\hat{n}'\times\vec{H}_p'\,)_c]\times \\ &\qquad e^{-i\vec{k}^s\cdot\vec{r}'}D'dx'dy' \\ &= \frac{KE_0}{8\pi^3}\{\int_{R^3}\int_{S^2}F_{qp}^1(\vec{k}^{\,i},\vec{k}^{\,s})\frac{e^{i[u(x'-x'')+v(y'-y'')+w(z'-z'')]}}{(w-q_1)(w+q_1)}\times \\ &e^{-i\vec{k}^s\cdot\vec{r}'}e^{i\vec{k}^i\cdot\vec{r}'}dx'dy'dx''dy''dudvdw + \\ &\int_{R^3}\int_{S^2}F_{qp}^2(\vec{k}^{\,i},\vec{k}^{\,s})\frac{e^{i[u(x'-x'')+v(y'-y'')+w(z'-z'')]}}{(w-q_2)(w+q_2)}\times \\ &e^{-i\vec{k}^s\cdot\vec{r}'}e^{i\vec{k}^i\cdot\vec{r}'}dx'dy'dx''dy''dudvdw\},\end{aligned} \tag{11}$$

$$F_{qp}^m = D'[(\hat{q}\times\hat{k}^s)\cdot(\hat{n}'\times\vec{E}_p'\,)_c^m + \eta_1\hat{q}\cdot(\hat{n}'\times\vec{H}_p'\,)_c^m]. \tag{12}$$

According to the new expression of the scattered field, the average incoherent power is obtained. In the original IEM2Mc, the Kirchhoff incoherent power is the same as that given in IEM2M. The cross incoherent power is:

$$\begin{aligned}&S_{qp}^{kc} = \mathrm{Re}\{1/\eta_1\}\,\mathrm{Re}\{\langle E_{qp}^{sc}E_{qp}^{sk*}\rangle - \langle E_{qp}^{sc}\rangle\langle E_{qp}^{sk*}\rangle\} \\ &= \frac{|KE_0|^2}{8\pi^2}\mathrm{Re}\{1/\eta_1\sum_{m=1,2}\mathrm{Re}\{f_{qp}^*\int_{R^3}dudvdw \\ &\int_{S^3}dx'dy'dx''dy''dx'''dy''' \\ &\times e^{i[u(x'-x'')+v(y'-y'')]}e^{-i[k_{sx}(x'-x''')+k_{sy}(y'-y''')]} \\ &\times e^{i[k_x(x''-x''')+k_y(y''-y''')]} \\ &\times[\langle e^{-ik_{sz}(z'-z''')}e^{ik_z(z''-z''')}e^{iw(z'-z'')}F_{qp}^m(\vec{k}^{\,i},\vec{k}^{\,s})\rangle \\ &-\langle e^{-ik_{sz}z'}e^{ik_z z''}e^{iw(z'-z'')}F_{qp}^m(\vec{k}^{\,i},\vec{k}^{\,s})\rangle\langle e^{i(k_{sz}-k_z)z'''}\rangle]\},\end{aligned} \tag{13}$$

if $\xi = x' - x''', \varsigma = y' - y''', \xi' = x'' - x''', \varsigma' = y'' - y'''$, then

$$\begin{aligned} S_{qp}^{kc} &= \mathrm{Re}\{1/\eta_1\}\,\mathrm{Re}\{\langle E_{qp}^{sc} E_{qp}^{sk\,*}\rangle - \langle E_{qp}^{sc}\rangle\langle E_{qp}^{sk\,*}\rangle\} \\ &= \frac{|KE_0|^2}{8\pi^2}\mathrm{Re}\{1/\eta_1 \sum_{m=1,2}\sum_{r=-1,1}\mathrm{Re}\{f_{qp}^{*}\int_{R^3} dudvdw \\ &\int d\xi d\varsigma d\xi' d\varsigma' e^{i[u(\xi-\xi')+v(\varsigma-\varsigma')]} e^{-i[k_{sx}\xi+k_{sy}\varsigma]} e^{i[k_x\xi'+k_y\varsigma']} \\ &\times e^{-\sigma^2[(k_{sz}-w)(k_z-w)(1-\rho_{12})]} F_{qp}^{m}(\vec{k}^{\,i},\vec{k}^{\,s}) \\ &\times [e^{-\sigma^2[(k_{sz}-w)(k_{sz}-k_z)(1-\rho_{13})]} e^{-\sigma^2[(w-k_z)(k_{sz}-k_z)(1-\rho_{23})]} \\ &- e^{-\sigma^2(k_{sz}-k_z)^2}]\}, \end{aligned} \tag{14}$$

where

$$\rho_{12} = \rho(\xi-\xi',\varsigma-\varsigma'); \quad \rho_{13} = \rho(\xi,\varsigma); \quad \rho_{23} = \rho(\xi',\varsigma').$$

The corresponding scattering coefficient is:

$$\begin{aligned} (\sigma^0)_{qp}^{kc} &= \frac{k_1^2}{2}\sum_{m=1,2}\mathrm{Re}\{f_{qp}^{*} e^{-\sigma^2[k_{sx}^2+k_{sz}^2-k_{sx}k_z]}\int_{R^2} dudv \\ &\times F_{qp}^{m}(\vec{k}^{\,i},\vec{k}^{\,s})\; e^{-\sigma^2[w^2-(k_{sz}+k_z)w]}[\sum_{n=1}^{\infty}\frac{[-\sigma^2(k_{sz}-w)(k_z-k_{sz})]^n}{n!} \\ &\times W_1^{(n)}(k_{sx}-u,k_{sy}-v)\delta(u-k_x)\delta(v) \\ &+\sum_{l=1}^{\infty}\frac{[\sigma^2(k_z-w)(k_z-k_{sz})]^l}{l!}W_1^{(l)}(u-k_x,v)\delta(k_{sx}-u) \\ &\times\delta(k_{sy}-v)+\frac{1}{2\pi}\sum_{n=1}^{\infty}\frac{[-\sigma^2(k_{sz}-w)(k_z-k_{sz})]^n}{n!}\times \\ &\sum_{l=1}^{\infty}\frac{[\sigma^2(k_z-w)(k_z-k_{sz})]^l}{l!}W_1^{(n)}(k_{sx}-u,k_{sy}-v) \\ &\times W_1^{(l)}(u-k_x,v)]\}. \end{aligned} \tag{15}$$

$W^{(n)}(\cdot)$ is the Fourier transform of the nth power of the normalized surface correlation function.

The complementary incoherent power is:

$$\begin{aligned} S_{qp}^{c} &= \frac{1}{2}\mathrm{Re}\{1/\eta_1\}\,\mathrm{Re}\{\langle E_{qp}^{sc} E_{qp}^{sc\,*}\rangle - \langle E_{qp}^{sc}\rangle\langle E_{qp}^{sc\,*}\rangle\} \\ &= \frac{|KE_0|^2}{2^7\pi^4}\mathrm{Re}\{1/\eta_1\}\times\sum_{m,n=1,2}\{\int_{R^6} dudvdwdu'dv'dw' \\ &\int_{s^4} dx'dy'dx''dy''dx'''dy'''dx^{v}dy^{v} \\ &\times e^{i[u(x'-x'')-u'(x'''-x^{v})+v(y-y'')-v'(y'''-y^{v})]} e^{-i[k_{sx}(x'-x''')+k_{sy}(y'-y''')]} \\ &e^{i[k_x(x''-x^{v})+k_y(y''-y^{v})]}[\langle e^{-ik_{sz}(z'-z''')} e^{ik_z(z''-z^{v})} e^{iw(z'-z'')} \\ &\times e^{-iw(z'''-z^{v})} F_{qp}^{m}(\vec{k}^{\,i},\vec{k}^{\,s}) F_{qp}^{n*}(\vec{k}^{\,i},\vec{k}^{\,s})\rangle \\ &-\langle e^{-i(k_{sz}z'+k_z z'')} e^{iw(z'-z'')} F_{qp}^{m}(\vec{k}^{\,i},\vec{k}^{\,s})\rangle\times \\ &\langle e^{i(k_{sz}z'''-k_z z^{v})} e^{-iw(z'''-z^{v})} F_{qp}^{n*}(\vec{k}^{\,i},\vec{k}^{\,s})\rangle]\}. \end{aligned} \tag{16}$$

The scattering coefficient of the complementary term is:

$$\begin{aligned} (\sigma^0)_{qp}^{c} &= \frac{k_1^2}{16}\sum_{m,n=1,2}\{e^{-\sigma^2(k_{sz}^2+k_z^2)}\int_{R^4} dudvdu'dv' F_{qp}^{m}(\vec{k}^{\,i},\vec{k}^{\,s}) \\ &F_{qp}^{n*}(\vec{k}^{\,i},\vec{k}^{\,s})\, e^{-\sigma^2[w_m^2+w_n^2-(k_{sz}+k_z)(w_m+w_n)]}[\sum_{h=1}^{\infty}\frac{[-\sigma^2(k_{sz}-w_m)(w_n-k_{sz})]^h}{h!} \\ &W_1^{(h)}(k_{sx}-u,k_{sy}-v)\delta(u-k_x)\delta(v)\delta(u-u')\delta(v-v')+ \\ &\sum_{l=1}^{\infty}\frac{[-\sigma^2(k_{sz}-w_m)(k_z-w_n)]^l}{l!}W_1^{(l)}(k_{sx}-u,k_{sy}-v)\delta(u-k_x)\delta(v) \\ &\times\delta(k_{sx}-u')\delta(k_{sy}-v')+\sum_{n=1}^{\infty}\frac{[-\sigma^2(k_z-w_m)(k_{sz}-w_n)]^n}{n!} \\ &\times W_1^{(n)}(u-k_x,v-k_y)\delta(k_{sx}-u)\delta(k_{sy}-v)\delta(u'-k_x)\delta(v) \\ &+\sum_{t=1}^{\infty}\frac{[-\sigma^2(k_z-w_m)(w_n-k_z)]^t}{t!}W_1^{(t)}(u-k_x,v-k_y)\delta(k_{sx}-u) \\ &\times\delta(k_{sy}-v)\delta(u-u')\delta(v-v')+\frac{1}{2\pi}\sum_{h=1}^{\infty}\frac{[-\sigma^2(k_{sz}-w_m)(w_n-k_{sz})]^h}{h!} \\ &\sum_{t=1}^{\infty}\frac{[-\sigma^2(k_z-w_m)(w_n-k_z)]^t}{t!}\times W_1^{(h)}(k_{sx}-u,k_{sy}-v) \\ &\times W_1^{(t)}(u-k_x,v-k_y)\delta(u-u')\delta(v-v')+ \\ &\frac{1}{2\pi}\sum_{l=1}^{\infty}\frac{[-\sigma^2(k_{sz}-w_m)(k_z-w_n)]^l}{l!}\sum_{n=1}^{\infty}\frac{[-\sigma^2(k_z-w_m)(k_{sz}-w_n)]^n}{n!} \\ &W_1^{(l)}(k_{sx}-u,k_{sy}-v)\times W_1^{(n)}(u-k_x,v-k_y)\delta(u+u'-k_{sx}-k_x) \\ &\times\delta(v+v'-k_{sy})]\}. \end{aligned} \tag{17}$$

The scattering coefficients are obtained by:

$$\sigma^0 = (\sigma^0)_{qp}^{k} + (\sigma^0)_{qp}^{kc} + (\sigma^0)_{qp}^{c}. \tag{18}$$

A more compact form is written as follows by extracting the single-scattering terms out of the cross and complementary terms and putting them together along with the Kirchhoff term:

$$\begin{aligned} (\sigma^o)_{qp}^{s} &= \frac{1}{2}k_1^2 e^{-\sigma^2(k_{sz}-k_z)^2}\times \\ &\sum_{n=1}^{\infty}\frac{\sigma^{2n}}{n!}|I_{qp}^{(n)}|^2 W_1^{(n)}(k_{sx}-k_x,k_{sy}-k_y), \end{aligned} \tag{19}$$

where

$$\begin{aligned} &W_1^{(n)}(k_{sx}-k_x,k_{sy}-k_y) \\ &= \frac{1}{2\pi}\int d\xi d\varsigma\,\rho^n(\xi,\varsigma)e^{-i[(k_{sx}-k_x)\xi+(k_{sy}-k_y)\varsigma]}, \end{aligned} \tag{20}$$

$$I_{qp}^{(n)} = (k_{sz}-k_z)^n f_{qp} + \frac{1}{4}\sum_{m=1}^{2}\sum_{r=1}^{2}\sum_{t=1}^{4}\gamma_m^{r,t}, \tag{21}$$

$$\gamma_m^{r,t} = \Gamma_m^{r,t} F_{qp}^{m,r,t}(\vec{k}^{\,i},\vec{k}^{\,s}), \tag{22}$$

$$\begin{aligned} \Gamma_m^{r,t} &= (-1)^{r(n-t)}\exp\{-\sigma^2 k_{sz}k_z\} \\ &\times\begin{cases} I^{(n-1)}(k_{sz}+k_z,q_m,a), & \text{if } t=1 \\ I^{(n)}(k_{sz}+k_z,q_m,a), & \text{if } t=2 \\ I_w^{(n-1)}(k_{sz}+k_z,q_m,a), & \text{if } t=3 \\ I_w^{(n)}(k_{sz}+k_z,q_m,a), & \text{if } t=4 \end{cases}, \end{aligned} \tag{23}$$

$$a=\begin{cases}k_{sz}, \text{ if } r=1\\ k_z, \text{ if } r=2\end{cases}, \tag{24}$$

$$I_0(k,q,a)=\exp\{-\sigma^2 k(a-\frac{k}{4})\}\times \frac{1}{q}[w(\sigma(\frac{k}{2}+q))+w(\sigma(-\frac{k}{2}+q))], \tag{25}$$

$$I^{(n)}(k,q,a)=\int_{-\infty}^{\infty}dw\frac{\exp\{-\sigma^2(w^2-kw)\}}{w^2-q^2}(w-a)^n =\frac{\exp\{\sigma^2 ka\}}{\sigma^{2n}}\frac{d^n I_0(k,q,a)}{dk^n}, \tag{26}$$

$$I_w^{(n)}(k,q,a)=\int_{-\infty}^{\infty}dw\frac{\exp\{-\sigma^2(w^2-kw)\}}{w^2-q^2}w(w-a)^n =\frac{1}{\sigma^2}\frac{dI^{(n)}(k,q,a)}{dk}. \tag{27}$$

III. IMPROVED PARTS FOR IEM2MC

In this section, new surface field coefficients are derived by keeping the full forms of the surface current terms in the Kirchhoff surface fields. Then, the transition function is applied to predict the Fresnel coefficients.

A. Surface field coefficients

The estimates of surface fields are the sum of the Kirchhoff and complementary fields. They are related to the scattering coefficients by f_{qp} and F_{qp} coefficients. In the original IEM2Mc, the terms of the surface fields neglect the sum of horizontal and vertical Fresnel reflection coefficients. Here, in the improved IEM2Mc, the complete form of the surface fields are applied to calculate f_{qp}. The f_{qp} coefficients with the sum of horizontal and vertical Fresnel reflection coefficients [7] are:

$$f_{vv}=-[(1-R_v)\hat{h}_s\cdot(\hat{n}'\times\hat{v})+(1+R_v)\hat{v}_s\cdot(\hat{n}'\times\hat{h})]D' -(R_v+R_h)(\hat{v}\cdot\hat{t})[(\hat{h}_s\cdot\hat{d})(\hat{n}'\cdot\hat{k}_i)-(\hat{n}'\cdot\hat{d})(\hat{h}_s\cdot\hat{k}_i) -(\hat{v}_s\cdot\hat{t})(\hat{n}'\cdot\hat{k}_i)]D', \tag{28}$$

$$f_{vh}=[(1-R_h)\hat{v}_s\cdot(\hat{n}'\times\hat{v})-(1+R_h)\hat{h}_s\cdot(\hat{n}'\times\hat{h})]D' -(R_v+R_h)(\hat{h}\cdot\hat{d})[(\hat{h}_s\cdot\hat{t})(\hat{n}'\cdot\hat{k}_i)-(\hat{n}'\cdot\hat{d})(\hat{v}_s\cdot\hat{k}_i) +(\hat{v}_s\cdot\hat{d})(\hat{n}'\cdot\hat{k}_i)]D', \tag{29}$$

$$f_{hv}=[(1-R_v)\hat{v}_s\cdot(\hat{n}'\times\hat{v})-(1+R_v)\hat{h}_s\cdot(\hat{n}'\times\hat{h})]D' -(R_v+R_h)(\hat{v}\cdot\hat{t})[(\hat{h}_s\cdot\hat{t})(\hat{n}'\cdot\hat{k}_i)-(\hat{n}'\cdot\hat{d})(\hat{v}_s\cdot\hat{k}_i) +(\hat{v}_s\cdot\hat{d})(\hat{n}'\cdot\hat{k}_i)]D', \tag{30}$$

$$f_{hh}=[(1+R_v)\hat{v}_s\cdot(\hat{n}'\times\hat{h})+(1-R_v)\hat{h}_s\cdot(\hat{n}'\times\hat{v})]D' -(R_v+R_h)(\hat{h}\cdot\hat{d})[(\hat{h}_s\cdot\hat{d})(\hat{n}'\cdot\hat{k}_i)-(\hat{n}'\cdot\hat{d})(\hat{h}_s\cdot\hat{k}_i) -(\hat{v}_s\cdot\hat{t})(\hat{n}'\cdot\hat{k}_i)]D'. \tag{31}$$

Substituting Equations (28)-(31) into (21), we obtain the newly derived $I_{qp}^{(n)}$. This modification is made on the Kirchhoff field and there will be no change with the complementary fields.

B. Transition function

In IEM2Mc, the Fresnel coefficient is chosen with a posteriori method:

$$R\rightarrow(R(\theta)+R(\theta_s))/2. \tag{32}$$

This means an approximation to the first mean-value theorem for integration together with the imposition of reciprocity on the scattered fields [6]. This approximation seems to work well in the IEM2M and IEM2Mc. However, when the Rv+Rh term is considered, the equation (32) may not derive good results.

Here, the transition function which was reported in [8] is applied instead of the original expression. The transition function links the two extremes for the $R(\theta_i)$ (Fresnel reflection evaluated at incident angle) and $R(\theta_{sp})$ (Fresnel reflection evaluated at specular angle). Thus, the Fresnel coefficients could be determined by a transition function as:

$$R_p=R_p(\theta_i)+(R_p(\theta_{sp})-R_p(\theta_i))(1-\frac{S_p}{S_p^0}), \tag{33}$$

where $S_p=\dfrac{\sigma_{pp}^{c}\mid_{R_p=R_p(0)}}{\sigma_{pp}^{0}\mid_{R_p=R_p(0)}}$; $S_p^0=\lim\limits_{k\sigma\to 0}\dfrac{\sigma_{pp}^{c}\mid_{R_p=R_p(0)}}{\sigma_{pp}^{0}\mid_{R_p=R_p(0)}}$;

$\lim\limits_{k\sigma\to 0}\sigma_{pp}^0=A+B+C;\ p=h,v.$

S_p is the ratio of the complementary term to the total scattering coefficients. Terms A, B, and C represent Kirchhoff, cross, and complementary terms, respectively.

IV. NUMERICAL SIMULATION

Since the improved model is applicable to the small to moderate rough surface scattering problems, the surface parameters for numerical simulation should be selected on this condition. To evaluate the scattering coefficients efficiently, a single-scattering expression (19) is applied. The single scattering coefficients have been widely used for surface scattering and its early version was already demonstrated by Macelloni's experiments [9] with a frequency range of 2-18 GHz. Besides, according to Tang's [10] observation, the reflected energy for single scattering is about 95% of the total reflected energy for smooth surfaces with $\sigma/l<0.25$ (σ is RMS height, l is the correlation length) and is still dominant (~65%) for surfaces with an intermediate roughness $\sigma/l<0.5$. Thus, if the value of the $k\sigma$ is determined in the simulation, the parameter l is limited to a range that σ/l is smaller than 0.25. We adopt some typical soil permittivity in the numerical simulation. For a real case, in order to match the radar

data, some semi-empirical calibration methods for IEM were required. For example, Baghdadi, et al. [11], replaced the measured correlation length by a calibration parameter corresponding to optimal correlation length, so that model simulations would closely agree with radar measurements. However, this is not what we consider here. In this section, the improved IEM2Mc was compared with the SPM, KA and MoM for rough surfaces in mono- and bistatic observation.

Figure 1 shows bistatic scattering coefficients calculated by four models for Gaussian rough surface ($k\sigma$ = 0.1, kl = 1.5) in small RMS height region. The incidence angle and scattering angle are θ_i = 30°, ϕ_i = 0°, ϕ_s = 30°. The simulating codes are programmed in Matlab and are implemented on a personal computer with an AMD Athlon II 3 GHz processor. The computation time of the original IEM2Mc and the improved IEM2Mc is 32.72 s and 32.92 s, respectively. Therefore, the computation efficiency of the improved IEM2Mc is almost the same as the original IEM2Mc. From the Fig. 1, when the scattering angle θ is larger than 60°, the bistatic scattering coefficients which are computed by SPM and original IEM2Mc drop much more quickly than those of the AIEM and improved IEM2Mc. The improved IEM2Mc are much closer to the AIEM.

Figure 2 is the comparing result in KA region with simulation parameters: f = 5 GHz, $k\sigma$ = 0.84, kl = 12.56, ε_r = 5.5+i2.2, θ_i = 40°, ϕ_i = 0°, ϕ_s = 0°, 180°. According to Fig. 2, the difference between the improved IEM2Mc and the original IEM2Mc becomes obvious when the scattering angle is large. This phenomenon verifies the conclusion by Wu [7], that the sum of horizontal and vertical Fresnel reflection coefficients is important for bistatic scattering when an accurate prediction is required. When the RMS height increases, Kirchhoff term will contribute more in the surface current expressions. Therefore, the improved IEM2Mc has a good agreement with KA in Fig. 2. In Fig. 3, the improved IEM2Mc is compared with the MoM [12] with $k\sigma$ = 1 and kl = 6. It shows that the bistatic scattering coefficients calculated by the improved IEM2Mc are closer to those by the MoM than the original IEM2Mc.

Next, we check the backscattering results between the improved IEM2Mc and the original IEM2Mc in Fig. 4. The MoM data is from Du [13]. The improved IEM2Mc agrees well with the MoM data than the original IEM2Mc, especially when the observation angle is large. However, both the original and improved IEM2Mc fail to match well with MoM at small angles of incidence.

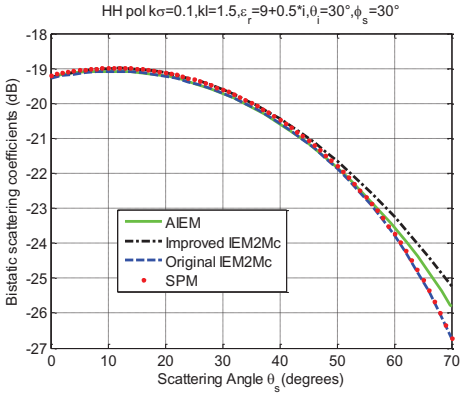

(a)

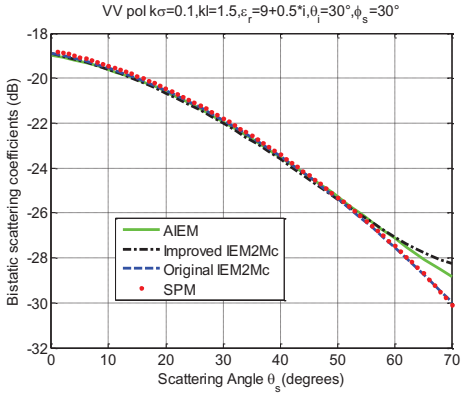

(b)

Fig. 1. The bistatic scattering coefficients obtained with SPM, the original IEM2Mc and the improved IEM2Mc at θ_i = 30°, ϕ_i = 0°, ϕ_s = 30°, with rough surface $k\sigma$ = 0.1, kl = 1.5: (a) co-polar horizontal polarization, and (b) co-polar vertical polarization.

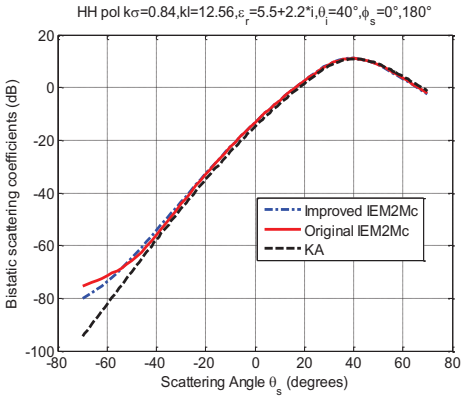

(a)

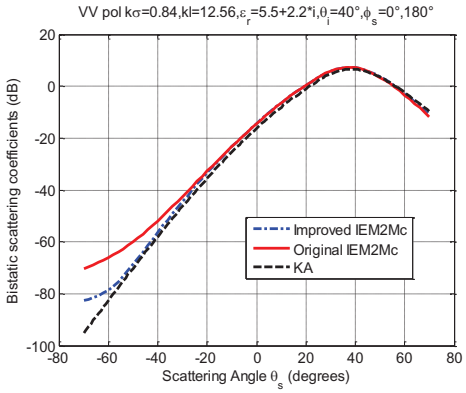

(b)

Fig. 2. Comparison of the bistatic scattering coefficients predicated by KA, the original IEM2Mc and the improved IEM2Mc at 5 GHz: (a) $\theta_i = 40°$ and co-polar horizontal polarization, and (b) $\theta_i = 40°$ and co-polar vertical polarization.

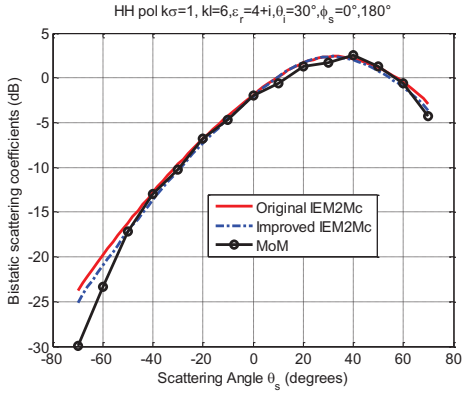

(a)

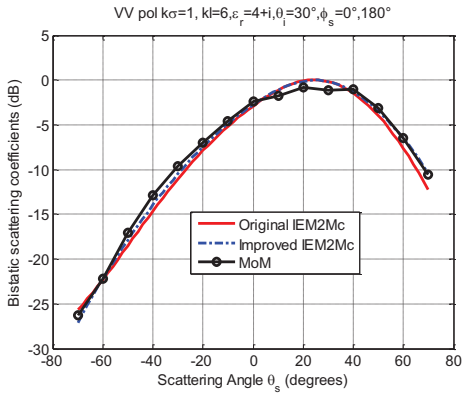

(b)

Fig. 3. Comparison of the bistatic scattering coefficients predicated by MoM, the original IEM2Mc and the improved IEM2Mc: (a) $\theta_i = 30°$ and co-polar horizontal polarization, and (b) $\theta_i = 30°$ and co-polar vertical polarization.

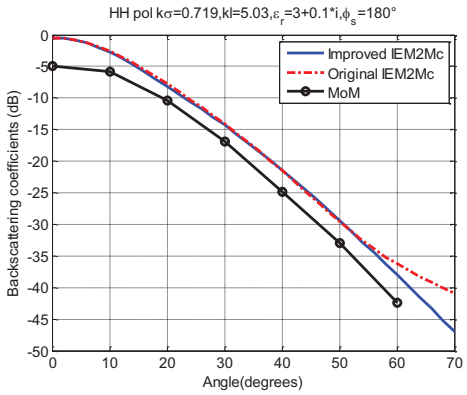

(a)

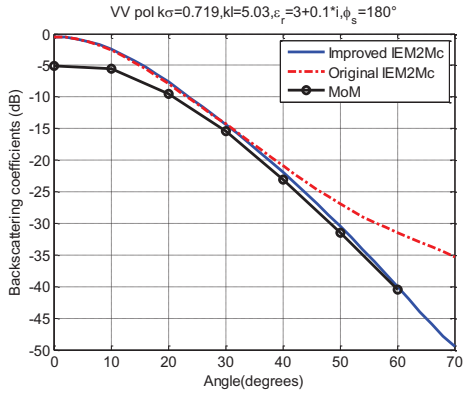

(b)

Fig. 4. The backscattering scattering coefficients obtained with MoM, the original IEM2Mc and the improved IEM2Mc with rough surface: (a) $k\sigma = 0.719$, $kl = 5.03$ and co-polar horizontal polarization, and (b) $k\sigma = 0.719$, $kl = 5.03$ and co-polar vertical polarization.

V. CONCLUSION

In this paper, an improved IEM2Mc model for surface bistatic scattering is derived with small or moderated RMS height. The full forms of the surface current terms in the Kirchhoff surface fields are reserved, so that the bistatic scattering coefficients are more accurate and more general. Besides, the physical-based approach with transition function to predict the Fresnel coefficients is proved to be better in the improved IEM2Mc than the posteriori method. The simulating results indicate that the improved IEM2Mc has better prediction than the original IEM2Mc, when comparing with SPM, KA, and MoM.

ACKNOWLEDGMENT

This work was supported in part by the National Natural Science Foundation of China under Grant

41176156, 41275032, and 61201123.

REFERENCES

[1] A. K. Fung, Z. Li, and K. S. Chen, "Backscattering from a randomly rough dielectric surface," *IEEE Trans. Geosci. Remote Sens*., vol. 30, no. 2, pp. 356-369, Mar. 1992.

[2] C. Y. Hsieh, A. K. Fung, G. Nesti, A. J. Sieber, and P. Coppo, "A further study of the IEM surface scattering model," *IEEE Trans. Geosci. Remote Sens*., vol. 35, no. 4, pp. 901-909, Jul. 1997.

[3] J. Alvarez-Perez, "An extension of the IEM/ IEMM surface scattering model," *Waves Random Media*, vol. 11, no. 3, pp. 307-329, Mar. 2001.

[4] K. S. Chen, T. D. Wu, L. Tsang, Q. Li, J. C. Shi, and A. K. Fung, "Emission of rough surfaces calculated by the integral equation method with comparison to three-dimensional moment method simulations," *IEEE Trans. Geosci. Remote Sens*., vol. 41, no. 1, pp. 90-101, Jan. 2003.

[5] Y. Du, "A new bistatic model for electromagnetic scattering from randomly rough surfaces," *Waves Random Media*, vol. 18, no. 1, pp. 109-128, Feb. 2008.

[6] J. Alvarez-Perez, "The IEM2M rough-surface scattering model for complex-permittivity scattering media," *Waves Random Media*, vol. 22, no. 2, pp. 207-233, May 2012.

[7] T. D. Wu, K. S. Chen, J. Shi, H. W. Lee, and A. K. Fung, "A study of an AIEM model for bistatic scattering from randomly rough surfaces," *IEEE Trans. Geosci. Remote Sens*., vol. 45, no. 9, pp. 2584-2598, Sep. 2008.

[8] T. D. Wu, K. S. Chen, J. Shi, and A. K. Fung, "A transition model for the reflection coefficient in surface scattering," *IEEE Trans. Geosci. Remote Sens*., vol. 39, no. 9, pp. 2040-2050, Sep. 2001.

[9] G. Macelloni, G. Nesti, P. Pampaloni, S. Sigismondi, D. Tarchi, and S. Lolli, "Experimental validation of surface scattering and emission models," *IEEE Trans. Geosci. Remote Sens*., vol. 38, no. 1, pp. 459-469, Jan. 2000.

[10] K. Tang and R. O. Buckius, "A statistical model of wave scattering from random rough surfaces," *International Journal of Heat and Mass Transfer*, vol. 44, pp. 4059-4073, 2001.

[11] N. Baghdadi, I. Gherboudj, M. Zribi, M. Sahebi, C. King, and F. Bonn, "Semi-empirical calibration of the IEM backscattering model using radar images and moisture and roughness field measurements," *International Journal of Remote Sens*., vol. 25, no. 18, pp. 3593-3623, Sep. 2004.

[12] F. Demontoux, C. Duffour, Y. Kerr, L. Kosolapova, H. Lawrence, V. Mironov, and J. P. Wigneron, "Coupling the temperature and mineralogy dependable soil dielectric model and a numerical model to compute scattering coefficient of complex multilayer soil structures," in *Proceedings of the Symposium on Remote Sensing of Natural Covers by Synthetic Aperture Radars*, Ulan-Ude, Russian Federation, pp. 330-343, 2010.

[13] Y. Du, J. A. Kong, W. Yan, Z. Wang, and L. Peng, "A statistical integral equation model for shadow-corrected EM scattering from a Gaussian rough surface," *IEEE Trans. Antennas Propag*., vol. 55, no. 6, pp. 1843-1855, Jun. 2007.

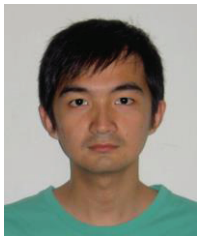

Wenchao Zheng received the B.S. degree in Electrical Engineering from Xi'an Institute of Posts and Telecommunications, Xi'an, China, in 2008 and the M.S. degree in Electrical Engineering from Wuhan Research Institute of Posts and Telecommunications, Wuhan, China in 2011.

He is currently pursuing the Ph.D. degree in Huazhong University of Science and Technology, Wuhan, China. His research interests include microwave remote sensing and multi-band antenna design.

Yi Leng (M'13) received the B.S. degree in Electronic Engineering from National University of Defense Technology, Changsha, China, in 1999, and the Ph.D. degree in Electronic Science and Technology from Huazhong University of Science and Technology, Wuhan, China, in 2008.

He is currently a Research Associate and Vice Director of Electromagnetic Engineering Research Center at Air Force Early Warning Academy, Wuhan, China. His current research interests include microwave antennas, wireless communication, and electromagnetic countermeasure.

Qingxia Li (M'08) received the B.S., M.S. and Ph.D. degrees in Electrical Engineering from Huazhong University of Science and Technology, Wuhan, China, in 1987, 1990, and 1999, respectively.

He is presently a Professor in Science and Technology on Multi-Spectral Information Processing Laboratory (School of Electronic Information and Communications), Huazhong University of Science and Technology,

Wuhan, China. His research interests include microwave remote sensing and deep space exploration, electromagnetic theory and application, antenna array and signal processing.

A Novel Slot Antenna with Reconfigurable Meander-Slot DGS for Cognitive Radio Applications

Mohammad M. Fakharian, Pejman Rezaei, and Ali A. Orouji

Department of Electrical and Computer Engineering
Semnan University, Semnan, 35131-19111, Iran
m_fakharian@semnan.ac.ir, prezaei@semnan.ac.ir, aliaorouji@semnan.ac.ir

Abstract ─ A new planar reconfigurable wideband slot antenna is proposed for cognitive radio (CR) applications in this paper. The wideband function is obtained by inserting a meander ε-shaped slot in the rectangular radiation patch. The reconfigurable characteristics with frequency diversity are achieved using four ideal switches integrated on the meander-slot defected ground structure (DGS) band stop filter embedded in the ground plane. The design procedures, impedance bandwidth, and radiation patterns are presented for explanation and examination of this antenna. The proposed reconfigurable slot CR antenna can work at three modes by controlling the switches at ON and OFF states. It operates over the frequency band between 1.52 GHz and 2.75 GHz (bandwidth of 57.6%), with two independent bands from 1.54 GHz to 2.28 GHz (38.7%) and 2.28 GHz to 2.85 GHz (22.2%). The measured results show that it has wide impedance bandwidth, multimode characteristics, and omnidirectional radiation patterns.

Index Terms ─ Cognitive radio (CR), defected ground structure (DGS), reconfigurable, reconfigurable meander-slot (RMS), slot antenna (SA).

I. INTRODUCTION

Recently, an increasing demand for antennas with multimode and cognitive radio (CR) operation in modern wireless applications with high-data-rate has drawn the very attention of researchers. The CR or software defined radio is directed to improve the spectral utilization by dynamically interacting with the RF surroundings. Sensing the surroundings may involve the measurement of the interference and communications traffic across a large part of the electromagnetic spectrum [1].

Dynamic control based on CR is usually achieved by incorporating switches in the antenna for reconfigurability. In other words, reconfigurable antennas with frequency diversity, which can scan the spectrum in a wideband mode and choose an available narrowband mode, provide the best solution for CRs. To this end, several CR antennas with complex single- and dual-port structure have been studied and investigated [2-7]. These references gave various methods for achieving frequency diversity using changing the structure of the antenna radiator or ground plane, defected microstrip structure bandpass filter, etc.

In recent years, a great trend towards the design and implementation of a reconfigurable defected ground structure (DGS) where the location of the transmission zeros can be controlled and tuned may be seen from a number of authors [8-9]. DGS is realized by etching a certain defected pattern or slot in the ground plane. The reconfigurable DGS can been used in many applications like antennas due to their interesting properties in terms of size miniaturization, arbitrary stopbands and suppression of surface waves [8, 10-12]. However, still not a large amount of work has been presented in this domain.

Several DGS have been proposed so far, such as dumbbell-shaped DGS, semicircle-shaped DGS, circle-shaped DGS, cross-shaped DGS, spiral DGS, arrow-head DGS, U-slot DGS, V-slot DGS, concentric ring DGS, MS-DGS and so on [10]. These DGSs are different from the quality factors (Q factors) and the band rejection characteristics [13]. Some of DGSs are already utilized in the letters as a switchable structure [8, 14]. In [8], a novel reconfigurable DGS unit cell on coplanar waveguide technology is presented. The presented DGS contains a number of PIN diodes on each side of the coplanar waveguide ground planes to give complete control of the number of transmission zeros obtained and their resonant frequencies. An UWB antenna with DGS and varactor for tuning the notch band has been studied in [14]. The varactor is loaded on the DGS to control the resonance frequency.

In this article, a new slot antenna with reconfigurable meander-slot (RMS) DGS, which was previously introduced in [13], and multimode performances for CRs is presented. In the proposed structure, wideband function is provided by etching a slot on the rectangular radiating stub, and a multi-resonance characteristic is obtained by using ideal

Submitted On: October 30, 2013
Accepted On: October 4, 2014

switches inside the MS-DGS. The reconfigurable characteristics by implementing ideal switches are already achieved in some articles [4, 15-16]. The MS-DGS using ideal switches in this paper is designed to achieve reconfigurability of several stop bands. This reconfigurable DGS, when integrated with a wideband antenna, results in a frequency-agile system with a wideband operation when the DGS is disconnected by placing switches in the ON/OFF states. Good return loss and radiation pattern characteristics are obtained in the frequency band of interest. Simulated and measured results are presented to validate the usefulness of the proposed antenna structure for wireless applications.

II. ANTENNA CONFIGURATION AND DESIGN

In this section, the proposed slot antenna integrated with MS-DGS for CR applications is illustrated in detail. Design procedures are separated into three sections. Firstly, we will introduce the MS-DGS and its reconfigurability which will be integrated into the new slot antenna. Secondly, the slot antenna with and without a new slot on the radiation patch will be studied. Finally, we will study the proposed antenna integrated with reconfigurable DGS. In this study, the ideal switches for reconfigurability are metal bridges. The presence of the metal bridge represents that the switch status is ON; in contrast, the absence of the metal bridge represents that the switch status is OFF. The simulated results are obtained by using Ansoft HFSS [17] based on finite element method.

A. Design and characteristic of RMS-DGS

In microwave and electromagnetic engineering, hairpin filters are widely used than parallel-coupled microstrip filters because of its good filterable property and compact structure. To this end, in [13], a novel DGS which the authors name as MS-DGS is presented. It is conceptually obtained by folding the multi long arm-slots outwards to the U-slot DGS. The typical MS-DGS is sketched in Fig. 1. Its defected pattern consisted of a U-shaped body and multi folding arms. In order to design a switchable DGS, four ideal switches are incorporated into the meander slot. The four switches are described as switch 1 (SW1), switch 2 (SW2), switch 3 (SW3) and switch 4 (SW4), as shown in Fig. 1. In general, horizontal slots of the MS provide inductance effects, while vertical slots exhibit capacitive characteristics [13]. Thus, the resonant frequency can be adjusted by controlling lengths of the meander slot. The dimension parameters of MS-DGS, including slot width c, w, central joint-slot length d, arm-slot length f, and side joint-slot length e are shown in Fig. 1. This MS-DGS is built on a FR4 substrate whose relative permittivity (ε_r) is 4.4 and thickness (h) is 0.8 mm. The microstrip line on the top layer is designed to be 50-Ω transmission line (its width is 1.16 mm under resonant frequency).

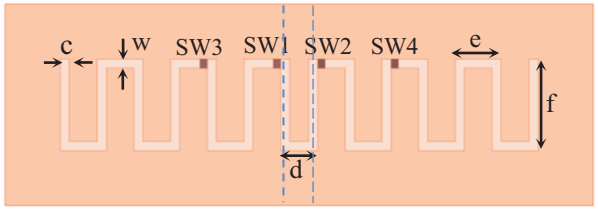

Fig. 1. Sketch view of MS-DGS with defected pattern dimensions.

The simulated reflection coefficient (S_{11}) and transmission coefficient (S_{21}) of the switching characteristics from DGS are illustrated in Fig. 2. In this simulation, the ideal switches are replaced with four metal strips with length 0.5 mm and width 0.4 mm. It is obvious that MS-DGS has four narrow stop bands with all switches OFF. The center frequency and number of these stop bands can be controlled by adjusting the MS lengths. When SW1, SW2 are ON and SW3, SW4 are OFF, the DGS has only one stop band which is near 8.6 GHz. For SW3, SW4 ON and SW1, SW2 OFF, the DGS has two stop bands with different center frequency compared to the previous situation. The DGS with longer length has narrower stop band than the DGS with shorter length at first center frequency. So, the switchable MS-DGS has tunable functions which can work in a stop band mode and multi stop band mode with different center frequency.

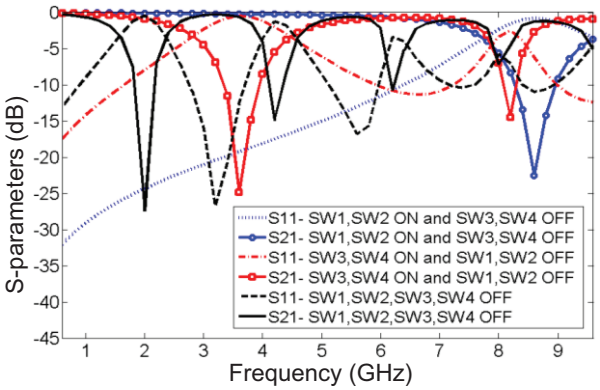

Fig. 2. Simulated S-parameters of the RMS-DGS.

B. Design of a novel slot antenna

The configuration of the rectangular slot antenna fed by a 50-Ω microstrip line is shown in Fig. 3 (a), which is etched on an FR4 substrate of permittivity 4.4 and thickness 0.8 mm. The basic antenna structure consists of a rectangular radiating stub with a 50-Ω microstrip feed line and a ground plane. The radiation patch and the feed line are printed on top of the

substrate, while the ground plane is printed on the bottom of the substrate.

In this study, to design a novel antenna, a meander ε-shaped slot has been added to the antenna structure. As illustrated in Fig. 3 (b), this slot is placed in the center of the radiating patch and is also symmetrical with respect to the longitudinal direction. The slot excites the resonant response and also acts as a half-wave resonant structure [18]. The meander ε-shaped slot creates an additional path for the surface current, which leads to an additional resonance, and consequently wider bandwidth can be produced [7].

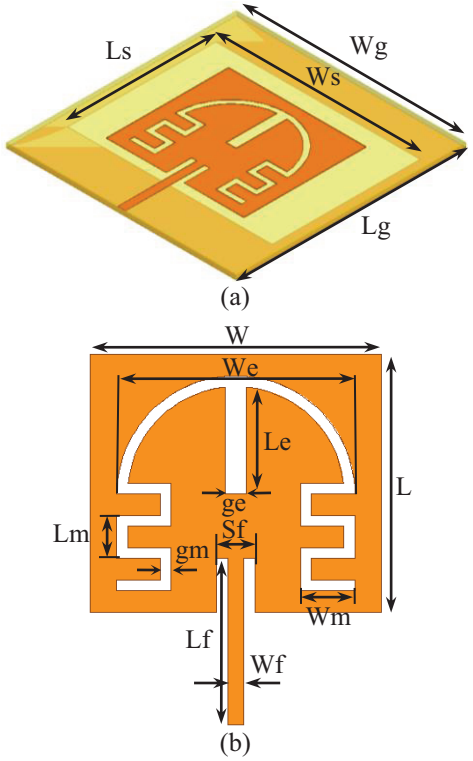

Fig. 3. Structure of the proposed slot microstrip antenna: (a) side view, and (b) modified radiating patch.

In this article, we start by choosing the aperture length Ls. We have a lot of pliability in choosing this parameter. The aperture length mostly affects the antenna bandwidth. As reduces, so does the antenna bandwidth, and vice versa. At the next step, we have to determine the aperture width Ws. The aperture width is approximately λs, where λs is the slot wavelength. λs depends on a number of parameters such as the slot width as well as the thickness and dielectric constant of the substrate on which the slot is designed. The last and final step in the design is to choose the length and width of the radiating patch L and W. A good starting point is to choose it to be equal to W=λm, where λm is the guided wavelength in the microstrip line.

Figure 4 shows the structure of the various antennas used for simulation studies. Return loss characteristics for an ordinary rectangular antenna [Fig. 4 (a)], with a slot in the ground plane [Fig. 4 (b)], and the antenna with meander ε-shaped slot in the radiating stub [Fig. 4 (c)] are compared in Fig. 5. It is found that by inserting slot in the ground plane, the antenna can create a wider bandwidth. Also as shown in Fig. 5, in this structure, the meander ε-shaped slot is used for the new resonance excitation function.

As shown in Fig. 5, the impedance bandwidth is effectively improved by the use of slot in the ground plane. In addition, by inserting the meander ε-shaped slot on the radiating patch, the lower-frequency bandwidth is significantly affected and the antenna can create the new resonant frequency at 1.57 GHz.

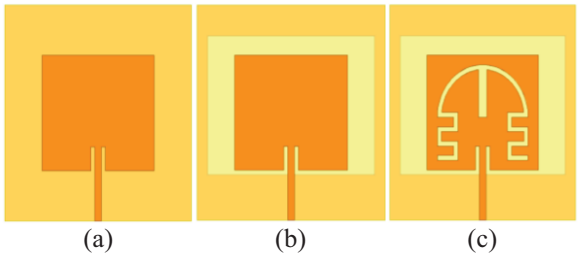

Fig. 4. (a) Ordinary antenna, (b) slot antenna, and (c) slot antenna with a new slot on radiating stub.

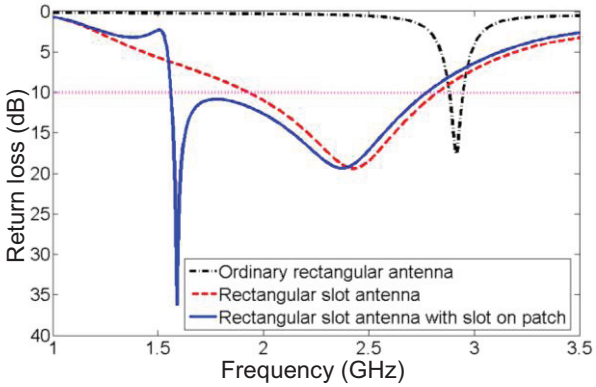

Fig. 5. Simulated antennas return loss shown in Fig. 4.

To design a novel wideband slot antenna, three modified slots are inserted in the radiating stub of the proposed slot antenna, as displayed in Fig. 6. Three such slots with different sizes are specified in as cases 1–3. Figure 6 also shows the effects of these slots with different values on the impedance matching. It is found that by cutting the multi MS of suitable dimensions at the follow of ε-shaped slot, additional resonances are excited and hence, wider impedance bandwidth with multi-resonance characteristics can be produced, especially at the lower band.

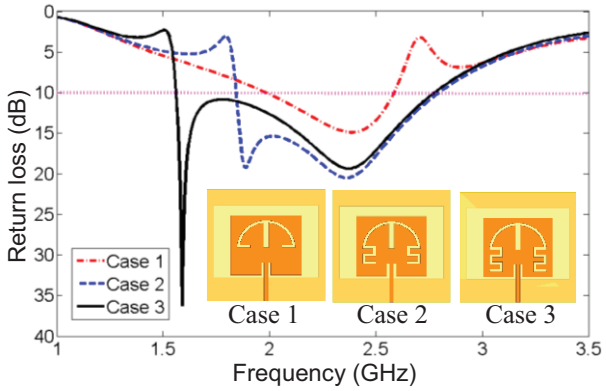

Fig. 6. Simulated return loss for the slot antenna at three cases with various slots on radiating patch.

C. Design of CR antenna with RMS-DGS

Based on the studies of RMS-DGS (Section A) and novel slot antenna (Section B), a CR antenna has been proposed numerically and experimentally.

The proposed antenna connected to a 50-Ω SMA connector is shown in Fig. 7. Firstly, a wideband slot antenna is designed. Secondly, a slot is etched in the radiation patch of the wideband slot antenna to produce wider band for covering UMTS 2100, PCS 1900, DCS 1800, 2.4 GHz WLAN 802/11 (b & g), 2.6 GHz WiMAX 802/16e, GPS, DMB, and DECT systems. Thirdly, a switchable MS-DGS is embedded in the proposed antenna ground plane to generate multiple frequency bands and controlling bandwidth for reducing or avoiding of systems.

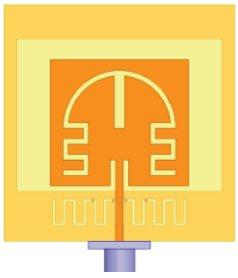

Fig. 7. Geometry of the proposed antenna.

The final dimensions of the proposed antenna are improved using an extensive parametric study and listed as follows: *L*g=45 mm, Wg=45 mm, Ls=29 mm, Ws=40 mm, L=24 mm, W=27 mm, Lf=15.5 mm, Wf=1.5 mm, Sf=3.5 mm, Le=9.9 mm, We=22 mm, ge=2 mm, Lm=4 mm, Wm=5 mm, and gm=1 mm. The dimensions of improved DGS of the antenna are f=5 mm, e=2.5 mm, d=2 mm, w=0.5 mm, and c=0.5 mm.

III. RESULTS AND DISCUSSIONS

To verify the above designs, the modified antenna is fabricated and measured. The four ideal switches, are also metal bridges which are replaced by a microstrip line in fabrication. In simulation and fabrication, the metal bridges with dimensions of 0.5×0.4 mm are used to approximate switches.

The improved antennas, as shown in Fig. 8, are measured using Agilent Network Analyzer. Measured and simulated results of return losses are compared in Fig. 9. The measured results almost agree with the simulated ones, which help to verify the accuracy of the simulation. The difference between the measured and simulated results may be due to a number of parameters such as the manufactured antenna dimensions as well as the thickness and dielectric constant of the substrate on which the antenna is fabricated.

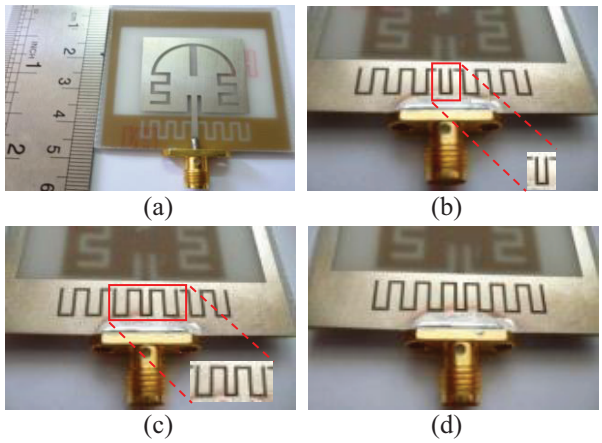

Fig. 8. Prototypes of improved antennas: (a) top view, (b) bottom view of proposed slot antenna with SW1, SW2 are ON, and SW3, SW4 are OFF (state 1), (c) with SW3, SW4 are ON, and SW1, SW2 are OFF (state 2), and (d) with all switches OFF (state 3).

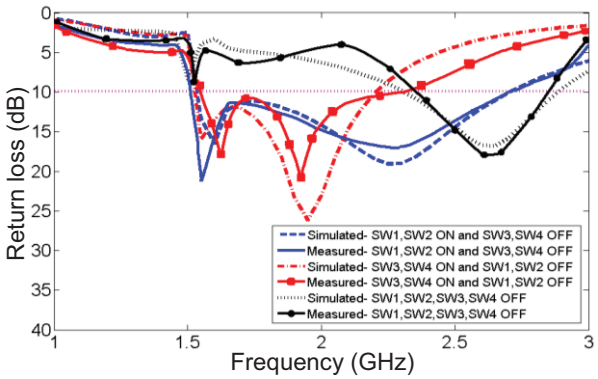

Fig. 9. Return losses of the antennas shown in Fig. 8.

It can be seen from Fig. 9, that CR antenna is a wideband antenna which has a wide bandwidth ranging from 1.52 GHz to 2.75 GHz with SW1, SW2 ON and SW3, SW4 OFF. In this state, antenna can be used in overlay mode for channel sensing. As for antenna with

SW3, SW4 ON and SW1, SW2 OFF, it is a wideband antenna with narrower band from 1.54 GHz to 2.28 GHz than previous state which can prevent from WLAN, WiMAX, and DMB systems. In this state, CR antenna can be used for underlay mode.

For the state of all switches OFF, proposed antenna has a narrower bandwidth from 2.28 GHz to 2.85 GHz compared with the previous two states, to expunge from UMTS 2100, PCS 1900, DCS 1800, GPS, and DECT systems. Thereby, we can control the switches ON and OFF to allow the proposed slot antenna to work in underlay and overlay modes for CR system. Also, the antennas can be used for multimode wireless systems by controlling the switches at ON and OFF states.

Figure 10 shows the measured radiation patterns including the co- and cross-polarization in the E- and H-planes at 1.57 GHz, 2.1 GHz, and 2.6 GHz for state 3 (with all switches OFF).

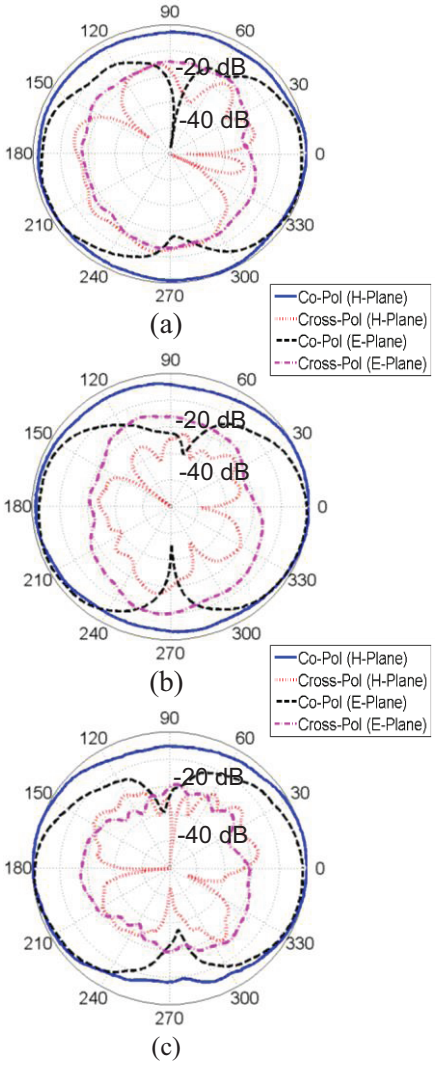

Fig. 10. Measured radiation patterns of antenna at: (a) 1.57 GHz, (b) 2.1 GHz, and (c) 2.6 GHz.

The radiation patterns are demonstrated that the antenna actually radiates over a wide frequency band. It can be seen that the radiation patterns in H-plane are nearly omnidirectional and dipole like in the E-plane for the three frequencies. It is found that the measured results of antenna using the RMS-DGS, the meander ε-shaped slot, and the ideal switches well satisfy the requirement of wideband CR applications.

IV. CONCLUSION

In this paper, a CR slot antenna integrated with RMS-DGS and the meander ε-shaped slot has been investigated. Reconfigurable DGS is analyzed and discussed before antenna design. The design procedures of CR antenna are illustrated in detail through analyzing antenna with and without slot and parametric studies. The reconfigurable functions are obtained using four ideal switches on MS-DGS. The switchable functions and bandwidth characteristics are investigated. By switching ON and OFF states of the four switches, CR slot antenna can work in three cases for underlay mode and overlay mode CR applications. The antenna with all switches ON and OFF is fabricated and measured. The impedance bandwidth and radiation patterns of the antenna are given and discussed. The proposed antenna can also be used as multimode antennas. As a result, they can well meet the wideband CR communication requirement and effectively change the modes.

ACKNOWLEDGMENT

The authors would like to thank the ITRC Antenna Lab members, especially Mr. Solat, Mr. Mirabdollahi and Mr. Akhlaghpasandi, for their cooperation.

REFERENCES

[1] S. K. Jayaweera, G. V. Vilar, and C. Mosquera, "Dynamic spectrum leasing: a new paradigm for spectrum sharing in cognitive radio networks," *IEEE Trans. Vehicular Tech.*, vol. 59, no. 5, pp. 2328-2339, 2010.

[2] Y. Tawk, J. Costantine, K. Avery, and C. G. Christodoulou, "Implementation of a cognitive radio front-end using rotatable controlled reconfigurable antennas," *IEEE Trans. Antennas Propagat.*, vol. 59, no. 5, pp. 1773-1778, 2011.

[3] E. Erfani, J. Nourinia, Ch. Ghobadi, M. NirooJazi, and T. A. Denidni, "Design and implementation of an integrated UWB/reconfigurable-slot antenna for cognitive radio applications," *IEEE Antennas Wireless Propagat. Lett.*, vol. 11, pp. 77-80, 2012.

[4] Y. Li, W. Li, and Q. Ye, "A reconfigurable triple-notch-band antenna integrated with defected microstrip structure band-stop filter for ultra-wideband cognitive radio applications," *Int. J. Antennas Propagat.*, pp. 1-13, 2013.

[5] V. Sharbati, P. Rezaei, A. Shahzadi, and M. M.

Fakharian, "A planar UWB antenna based on MB-OFDM applications with switchable dual band-notched for cognitive radio systems," *Int. J. Microwave Wireless Tech*., available on CJO2014. doi:10.1017/S1759078714001317.

[6] M. Al-Husseini, K. Y. Kabalan, A. El-Hajj, and C. G. Christodoulou, "Reconfigurable microstrip antennas for cognitive radio," Chapter 14 of *Advancement in Microstrip Antennas with Recent Applications*, Mar. 2013.

[7] A. Tariq and H. Ghafouri-Shiraz, "Frequency-reconfigurable monopole antennas," *IEEE Trans. Antennas Propagat*., vol. 60, no. 1, pp. 44-50, 2012.

[8] H. B. El-Shaarawy, F. Coccetti, R. Plana, M. El-Said, and E. A. Hashish, "Novel reconfigurable defected ground structure resonator on coplanar waveguide," *IEEE Trans. Antennas Propagat*., vol. 58, no. 11, pp. 3622-3628, 2010.

[9] A. M. E. Safwat, F. Podevin, P. Ferrari, and A. Vilcot, "Tunable bandstop defected ground structure resonator using reconfigurable dumbbell-shaped coplanar waveguide," *IEEE Trans. Microw. Theory Tech.*, vol. 54, no. 9, pp. 3559-3564, 2006.

[10] M. M. Fakharian and P. Rezaei, "Parametric study of UC-PBG structure in terms of simultaneous AMC and EBG properties and its applications in proximity-coupled fractal patch antenna," *Int. J. Engineering, Trans. A: Basics*, vol. 25, no. 4, pp. 389-396, 2012.

[11] M. M. Fakharian and P. Rezaei, "Numerical analysis of mushroom-like and uniplanar EBG structures utilizing spin sprayed Ni (–Zn)–Co ferrite films for planar antenna," *European J. of Scientific Research*, vol. 73, no. 1, pp. 41-51, 2012.

[12] M. M. Fakharian and P. Rezaei, "Very compact palmate leaf-shaped CPW-fed monopole antenna for UWB applications," *Microwave Opt. Tech. Lett.*, vol. 56, no. 7, pp. 1612-1616, Jul. 2014.

[13] Y. Zhu, X. Zhang, C. Li, F. Li, and G. Fang, "Novel compact meander-slot DGS with high quality factor," *Microwave Opt. Tech. Lett.*, vol. 50, no. 12, pp. 3164-3169, 2008.

[14] L. Sun Xiaolei, S. W. Cheung, and T. I. Yuk, "Generating a reconfigurable notch band for planar UWB monopole antennas," *Microwave Opt. Tech. Lett.*, vol. 55, pp. 2906-2910, 2013.

[15] Y. Li, W. Li, and Q. Ye, "A reconfigurable wide slot antenna integrated with sirs for UWB/ multiband communication applications," *Microw. Opt. Tech. Lett.*, vol. 55, no. 1, pp. 52-55, 2013.

[16] B. Li, J. Hong, and B. Z. Wang, "Switched band-notched UWB/dual-band WLAN slot antenna with inverted S-shapedd slots," *IEEE Antennas Wireless Propagat. Lett.*, vol. 11, pp. 572-575, 2012.

[17] Ansoft High Frequency Structure Simulator (HFSS), ver. 13, Ansoft Corporation, Canonsburg, PA, 2010.

[18] G.-P. Gao, M. Li, S.-F. Niu, X.-J. Li, B.-N. Li, and J.-S. Zhang, "Study of a novel wideband circular slot antenna having frequency band-notched function," *Progress in Electromagnetics Research*, vol. 96, pp. 141-154, 2009.

Mohammad M. Fakharian was born in Tehran, Iran, in 1987. He received the B.S. and M.S. degrees in Electrical Engineering from Semnan University, Semnan, Iran, in 2009 and 2012, respectively. Currently, he is working towards the Ph.D. degree in Communication Engineering from semnan University. His research interests include reconfigurable antennas and microwave circuit design.

Pejman Rezaei was born in Tehran, Iran, in 1977. He received the B.S. degree in Electrical Engineering from Communication Faculty, Tehran, Iran, in 2000, and the M.S. and Ph.D. degrees from Tarbiat Modarres University, Tehran, Iran, in 2002 and 2007, respectively. Currently, he is Assistant Professor in the Semnan University, Semnan, Iran. His current research interests are electromagnetics theory, antenna theory and design.

Ali A. Orouji was born in Neyshabour, Iran, in 1966. He received the B.S. and M.S. degrees in Electronic Engineering from Iran University of Science and Technology, Tehran, Iran, in 1989 and 1992, respectively, and the Ph.D. degree from the Indian Institute of Technology Delhi, Delhi, India, in 2006.

Since 1992, he has been a Faculty Member with Semnan University, Semnan, Iran. His research interests are in modeling of silicon-on-insulator metal–oxide–semiconductor field-effect transistors, antenna and novel device structures.

Design and Optimization of a CPW-Fed Tri-Band Patch Antenna Using Genetic Algorithms

K. Fertas [1], H. Kimouche [1], M. Challal [2], H. Aksas [1], R. Aksas [3], and A. Azrar [2]

[1] Microwave and Radar Laboratory
Ecole Militaire Polytechnique, Bordj El-Bahri, Algiers, 16000, Algeria
k.fertas@gmail.com

[2] Signals and Systems Laboratory, Dept. of Electronics, Institute of Electrical and Electronic Engineering
University of Boumerdes, Boumerdes, 35000, Algeria
mchallal@ieee.org

[3] Electronics Department
Ecole Nationale Polytechnique, Algiers, 16000, Algeria
rabia.aksas@gmail.com

Abstract ─ This paper investigates a compact tri-band patch antenna fed by a coplanar waveguide (CPW) line for the applications of WiFi, WiMAX and HiperLAN. The dimensions of the proposed antenna are optimized using genetic algorithms (GAs). The antenna is designed to function at three different resonant frequencies which are 2.46 GHz, 3.56 GHz and 5.5 GHz. Numerical results for the return loss, radiation pattern and gain of the antenna are presented. The antenna structure was fabricated, and the measured results have a good agreement with the full-wave simulated ones.

Index Terms ─ Coplanar waveguide (CPW), genetic algorithms (GAs), patch antenna, tri-band.

I. INTRODUCTION

In recent years, multiple service technology is broadly developed, especially in the radio frequency (RF) devices of the modern wireless communication systems such as high-speed wireless fidelity (WiFi), Bluetooth, worldwide interoperability for microwave access (WiMAX) and high performance radio local area network (HiperLAN) systems operating at frequencies between 2 GHz and 6 GHz. In order to accommodate this multi-band RF signal transmission and reception into a single RF transceiver, dual or more bands devices are required to incorporate circuits working in different bands into a single unit so that size, cost and device number can be reduced. To meet this demand, several multi-band antennas with a variety of services have been carried out [1]-[4]. However, it is still a big challenge to design this type of antenna with suitably compact circuit size, high gain and more design feasibility.

In this paper, we propose a novel compact tri-band patch antenna fed by a coplanar waveguide (CPW) line for WiFi at 2.46 GHz, WiMAX at 3.56 GHz and HiperLAN at 5.5 GHz. The antenna structure is simple, compact and has controllable topology where its dimensions are optimized using internal genetic algorithms (GAs). The substrate material used for the design is an epoxy glass type with a thickness of 1.6 mm and a relative permittivity of 4.4. Two different electromagnetic (EM) simulators and measurements are used to validate the results obtained for the return loss response. The simulation results show a good agreement to the measurement ones.

II. THE PROPOSED ANTENNA GEOMETRY

The geometry and parameters of the proposed antenna fed by a CPW line is shown in Fig. 1. The patch antenna is printed on a dielectric substrate of a height equal to 1.6 mm and a relative permittivity of 4.4. The width of the 50 Ω microstrip fed line is 3 mm. The choice of the radiating element shape depends on diverse factors such as radiated power, polarization type, multi-band operation, gain and bandwidth of the radiator. The parameters for optimal antenna design which are selected to achieve the compact dimensions and possible best features such as high radiation efficiency, etc., are presented in the next section. The antenna was simulated and its prototype was fabricated

Submitted On: January 1, 2015
Accepted On: May 20, 2015

and measured.

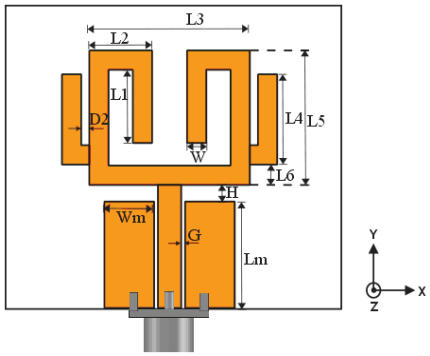

Fig. 1. The proposed antenna.

III. OPTIMIZATION AND SIMULATION: RESULTS AND DISCUSSIONS

The optimization objective of the proposed structure consists of finding the best values of geometrical parameters which are close to the objective function of GAs. The literature has reported some works about the application of GAs for general electromagnetic (EM) problems [5]-[9] and particularly for the design and optimization of antennas arrays [10]-[11]. The GAs are a class of search techniques that employ the mechanics of natural selection and genetics to conduct a global search of a solution space. The search objective is to find a good solution to the given problem. To start the optimization, the GA selects a set of designs, almost always at random. This set is called the population, just as in biology. The GA evaluates the performance of each member of the population using a simulator or analytic expression, and then applies a cost function. This function compares individual performance to the desired or ideal performance. It then returns a single number as a measure of its fitness to the GA. Table 1 illustrates the variation intervals of the antenna geometrical parameters.

Table 1: Geometrical parameters interval of the antenna

Parameters (mm)	Interval
W	[1 5]
Wm	[1 15]
Lm	[5 20]
H	[0.5 5]
G	[0.2 1]
L1	[0.1 15]
L2	[2 15]
L3	[5 30]
L4	[0 15]
L5	[5 20]
L6	[0 10]
D2	[0 5]

The aim of this part is to minimize the average value of the S_{11} module (in dB) in the three bands of ([2.4 2.48] GHz, [3.5 3.7] GHz, [5.15 5.8] GHz) frequencies which correspond to WiFi, WiMAX and HiperLAN standards respectively. The cost function is computed for each individual as the sum of return losses at desired frequencies, given by Eq. (1), and the fitness is to minimize the cost:

$$\cos t = \frac{1}{N_b}\sum_{n_b=1}^{N_b}\left(\frac{\sum_{n_i=1}^{N_i}\left|S_{11}(n_i)\right|_{dB}}{N_i}\right), \quad (1)$$

where $\left|S_{11}(n_i)\right|_{dB}$ is the magnitude of the reflection coefficient, N_i is the number of desired frequency band and N_b is the number of frequency points in the desired frequency band.

In this case, the multi-objective optimization function of the reflection coefficient must meet the following requirements:

$S_{11} \leq$ -15 dB for 2.4 GHz $\leq$ f $\leq$ 2.48 GHz,
$S_{11} \leq$ -15 dB for 3.5 GHz $\leq$ f $\leq$ 3.7 GHz,
$S_{11} \leq$ -15 dB for 5.15 GHz $\leq$ f $\leq$ 5.8 GHz,

and the GA, used in the optimization, has the following properties:

- Number of population members: 60,
- Number of generations: 30,
- Mutation rate: 0.01.

The optimization time for the antenna optimization took 2 days 03 hours and 21 minutes with HP I5 CPU 2.5 GHz and RAM = 6 Go.

The results obtained by a GA optimization are illustrated in Table 2, whereas the reflection coefficient simulation versus frequency of the proposed antenna is shown in Fig. 2. Figure 2 shows the presence of three diverse resonant frequencies which are 2.46 GHz, 3.56 GHz and 5.5 GHz, in which a good matching is satisfied.

Table 2: Optimized dimensions of the antenna

Parameters (mm)	Optimized Value
W	2.43
Wm	6.26
Lm	13.33
H	2.06
G	0.476
L1	9.19
L2	7.91
L3	20.22
L4	11.29
L5	16.83
L6	2.55
D2	1.01

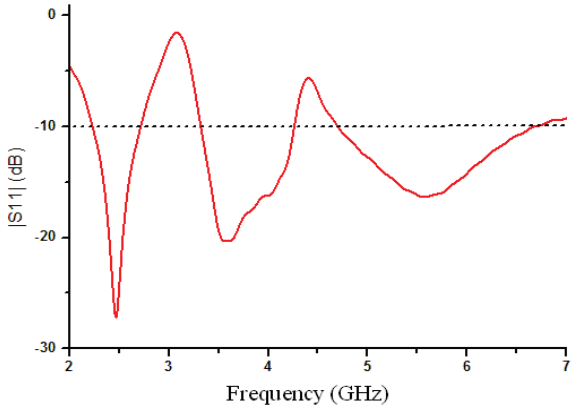

Fig. 2. The input reflection coefficient versus frequency.

The current distribution of the structure is shown in Fig. 3 for diverse resonant frequencies values. It is clear the current circulation is concentrated on the feeding line and in diverse regions of the radiated element.

Figure 4 shows the 3D radiation patterns variation for various resonant frequencies values, whereas Fig. 5 shows the 2D radiation patterns at three distinct frequencies in the plans: (a) $\theta = 90°$, (b) $\varphi = 90°$, and (c) $\varphi = 0°$. In the E-plane ($\varphi = 90°$) and H-plane ($\varphi = 0°$), Fig. 5 (b and c), the radiation pattern is bidirectional oriented towards the angles $\theta = 0°$ and $\theta = 180°$ for the three resonant frequencies. Consequently, the proposed antenna pattern looks like to that of a dipole.

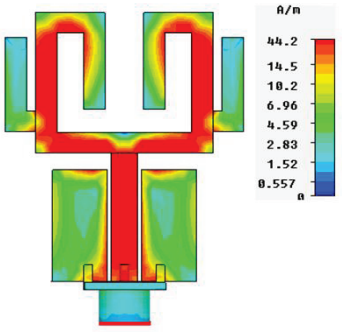

(a)

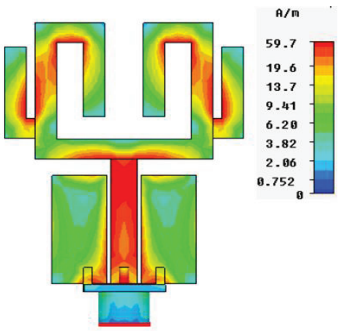

(b)

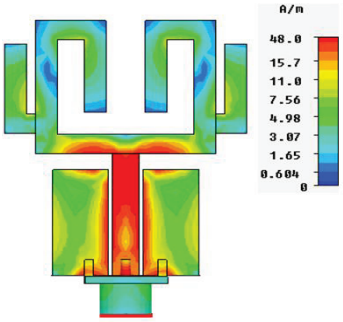

(c)

Fig. 3. Current distribution at three distinct frequencies: (a) f = 2.46 GHz, (b) f = 3.56 GHz, and (c) f = 5.5 GHz.

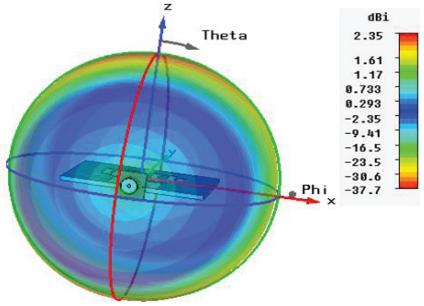

(a)

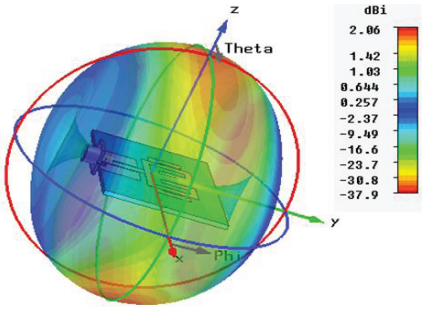

(b)

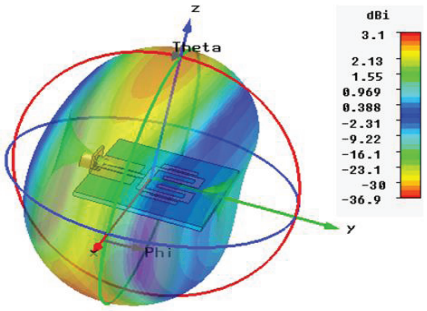

(c)

Fig. 4. 3-D radiation patterns at three distinct frequencies: (a) f = 2.46 GHz, (b) f = 3.56 GHz, and (c) f = 5.5 GHz.

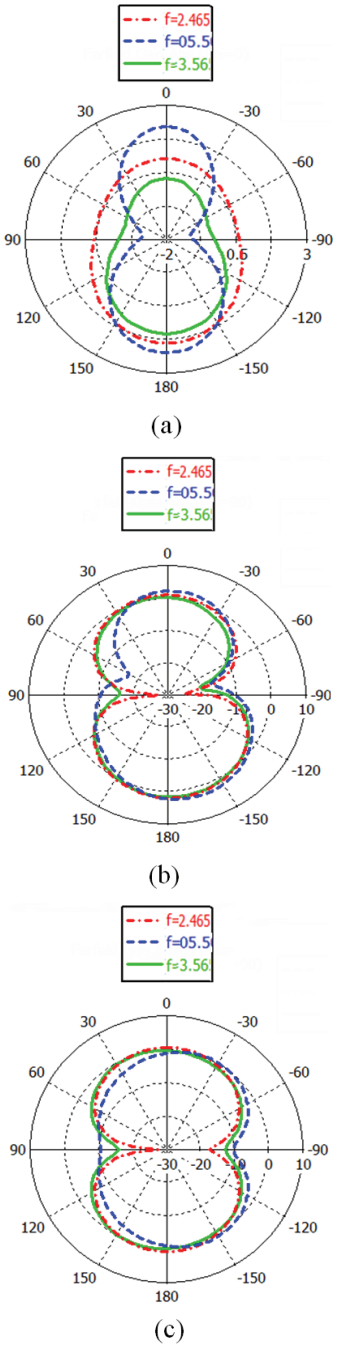

Fig. 5. 2-D radiation patterns at three distinct frequencies in the plans: (a) θ = 90°, (b) φ = 90°, and (c) φ = 0°.

For the frequency 2.46 GHz, the maximum gain is around 2.15 dBi in the direction φ = 90° and θ = 180° with a -3 dB aperture of 83.6°. For the frequency 3.56 GHz, the maximum gain is approximately 1.7 dBi in the direction φ = 90° and θ = 179° with a -3 dB aperture of 80.6°. For the frequency 5.5 GHz, the maximum gain is approximately 2.8 dBi in the direction φ = 90° and θ = -165° with a -3 dB aperture of 68.9°.

Figure 6 shows the simulated maximum gain of the proposed antenna in the three bands. It is shown that this antenna has a good gain, varies between 2.1 dBi and 2.3 dBi inside the first frequency band, between 1.4 dBi and 2.4 dBi inside the second frequency band, and between 2.6 dBi and 3.4 dBi inside the third frequency band.

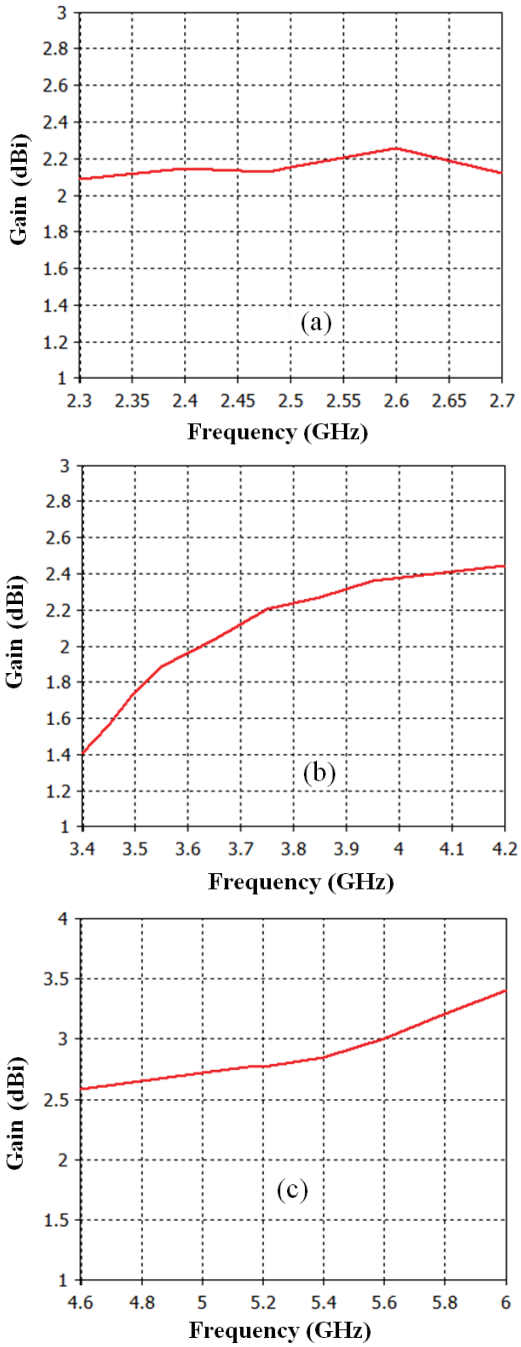

Fig. 6. Maximum gains versus frequency in the three bands.

IV. IMPLEMENTATION AND MEASUREMENT

The proposed antenna with small in size of 27.1x32.22 mm^2 is fabricated as shown in Fig. 7.

From Fig. 8, an acceptable agreement between the measured and simulated return losses is achieved. Moreover, these results show three diverse resonant frequencies with a small shifting toward high frequencies. The small deviations between the simulated and measured results may most probably be caused by the usual connectors and manufacturing errors. Moreover, the limitation of the EM simulator's may lead to discrepancy between the simulated and measured results. Usually, such discrepancies may be attributed to the dielectric material that should be characterized before realization since its properties deviates from those set in the software simulator.

The measured results are compared with some of the efficient and related antennas existing in literature and summarized in Table 3. The measured results indicate that the proposed antenna can meet the bandwidth requirements of WiFi/WiMAX/HiperLAN standards. It provides good performance in terms of better matching, larger bandwidth and smaller in size than those published works.

Figure 8 shows the measured and simulated input reflection coefficient. The antenna characteristics were measured with an HP8719ES VNA.

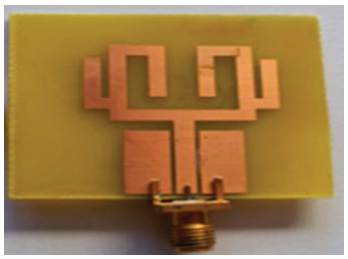

Fig. 7. Photograph of the fabricated compact tri-band antenna.

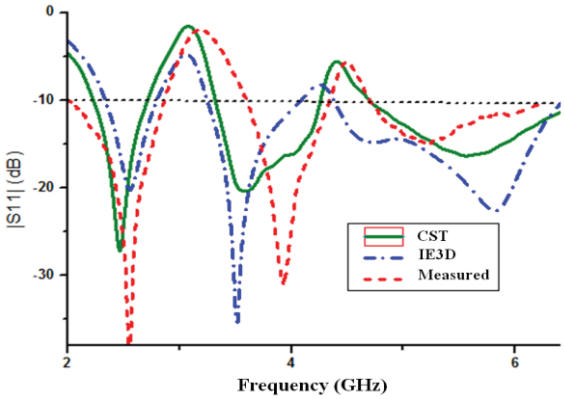

Fig. 8. Comparison between simulation and measurements of the input reflection coefficient.

Table 3: Comparison of the proposed CPW-fed tri-band antenna with other reported antennas

	Substrate Material (ε_r/h)	Size (mm^2)	Resonant Frequencies (GHz)	Max $\|S_{11}\|$ (dB)	Measured Impedance Bandwidths (GHz)	Max Gain (dB)
Ref. [2]	4.4/1.6	30x42	2.50/3.50/5.50	-26/-16/-14	0.41/0.44/1.00	< 2
Ref. [3]	2.2/1.588	36.56x43.42	2.40/3.50/5.70	-32/-17/-22	0.12/0.15/0.20	-
This work	4.4/1.6	27.1x32.22	2.46/3.56/5.50	-40/-32/-15	0.94/0.82/1.60	2.15/1.7/2.8

V. CONCLUSION

In this paper, a novel compact tri-band antenna fed by a CPW line for WiFi, WiMAX and HiperLAN has been introduced and investigated. The proposed antenna dimensions have been optimized using genetic algorithms (GAs). The obtained results by this algorithm are acceptable and show the importance of using a GA in the field of antennas synthesis. The results achieved by simulation as well as measurement show tri-bands behavior with a good matching for all resonant frequencies.

REFERENCES

[1] M. Pokorný, J. Horák, and Z. Raida, "Planar tri-band antenna design," *Radioengineering*, vol. 17, pp. 28-36, 2008.

[2] J. Chen, S. T. Fan, W. Hu, and C. H. Liang, "Design of tri-band printed monopole antenna for WLAN and WIMAX applications," *Progress In Electromagnetics Research C*, vol. 23, pp. 265-275, 2011.

[3] G. Sami, M. Mohanna, and M. L. Rabeh, "Tri-band microstrip antenna design for wireless communication applications," *NRIAG Journal of Astronomy and Geophysics*, vol. 2, pp. 39-44, 2013.

[4] S. B. Chen, Y. C. Jiao, W. Wang, and F. S. Zhang, "Modified T-shaped planar monopole antennas for multiband operation," *IEEE Trans. Mi-crow. Theory Tech.*, vol. 54, no. 8, pp. 3267-3270, 2006.

[5] Y. R. Samii and E. Michielssen, *Electromagnetic Optimization by Genetic Algorithms*, John Wiley & Sons, Inc., 1999.

[6] R. L. Haupt and S. E. Haupt, *Practical Genetic Algorithm*, Second edition, John Wiley & Sons, Inc., 2004.

[7] D. A. Coley, *An Introduction to Genetic*

Algorithms for Scientists and Engineers, World Scientific, 1999.

[8] C. A. Balanis, *Antenna Theory: Analysis and Design*, Third edition, John Wiley & Sons, Inc., 2005.

[9] D. S. Weile and E. Michielssen, "Genetic algorithm optimization applied to electromagnetics: a review," *IEEE Trans. Antennas Propag*., vol. 45, no. 3, Mar. 1997.

[10] F. J. Ares-Pena, J. A. Rodrigues-Gonzalez, E. Villanueva-Lopez, and S. R. Rengarajan, "Genetic algorithms in the design and optimization of antenna array patterns," *IEEE Antennas and Propag. Mag.*, vol. 47, no. 3, pp. 506-510, Mar. 1999.

[11] D. Marcano and F. Duran, "Synthesis of antenna arrays using genetic algorithms," *IEEE Antennas and Propag. Mag*., vol. 42, pp. 12-20, Jun. 2000.

Khelil Fertas was born on April 25, 1983, in Blida, Algeria. He received the Engineer degree in June of 2006 from The University of M'sila, Algeria, and the M.S. degree in January of 2014 from Ecole Militaire Polytechnique, Algiers, Algeria. His fields of interest include Propagation and Antennas.

Hocine Kimouche was born in 1965, in Algiers, Algeria. He received the Engineer degree in 1990 from Ecole Militaire Polytechnique (EMP) of Algiers, Algeria, and the M.S. and Doctorate degrees from the University of Limoges, France, respectively in 1994 and 1998. Currently, he is an Associate Professor with the Ecole Militaire Polytechnique, Algiers, Algeria. His main researches of interest include Microwaves, Propagation and Antennas.

Mouloud Challal was born on March 6, 1976, in Algiers, Algeria. He received the Engineer degree in April off 1999 from the University of Bab-Ezzouar, Algiers, Algeria, the M.S. degree in December of 2001 from National Polytechnic School of Algiers, Algeria, and the Doctorate degree in March of 2012 from the University of Boumerdes, Boumerdes, Algeria. Currently, he is an Associate Professor with the Institute of Electrical and Electronic Engineering of Boumerdes University. His research interests include RF/Microwave Circuits, Electromagnetic Field Theory, Propagation and Antennas.

Challal is a Member of IEEE and European Microwave Association (EuMA), and is a Reviewer of several international refereed journals and conferences.

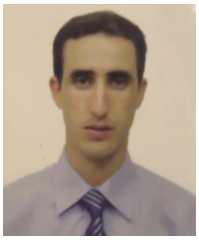

Hamza Aksas was born on September 21, 1981, in Algiers, Algeria. He received the Engineer degree in June of 2005 from National Polytechnic School of Algiers, Algeria, and the M.S. degree in February of 2014 from Ecole Militaire Polytechnique, Algiers, Algeria. His fields of interest include Propagation and Antennas.

Rabia Aksas was born in 1950, in Algeria. He received the M.S. and Doctorate degrees in Electronics from National Polytechnic School (presently ENSP) of El-Harrach, Algiers, Algeria, respectively in 1982 and 1995. Currently, he is a Senior Professor in the Electronics Department at National Polytechnic School of Algiers. Throughout his long career, he has been teaching various courses such as Telecommunication Systems, Vibrations and Waves, Electromagnetic Field, Radio Wave Propagation and Antennas. In addition to his teaching load, he worked in various projects in the antennas field as a Research Director. His research interests are in the areas of Electromagnetic Field Theory, Microwaves, Propagation and Antennas.

Aksas has published over 44 scientific papers in international refereed journals and conferences.

Arab Azrar was born in Takerboust, Bouira, Algeria, on August 2, 1971. He received the B.S. degree in Electrical and Electronic Engineering form National Institute of Electricity and Electronics of Boumerdes Algeria in 1995 and the M.S. and Doctorate degrees from National Polytechnic School of El-Harrach, Algeria respectively in 1998 and 2004. Currently, he is a Lecturer in the Institute of Electrical and Electronic Engineering of Boumerdes University and his fields of interest include Antennas, Propagation and Microwaves.

Narrow Band, Sharp Roll-Off Rejection Frequency Selective Surface Based on Substrate Integrated Waveguide

Mehran Shamaei Samani, Reza Sarraf Shirazi, and Gholamreza Moradi

Department of Electrical Engineering
Amirkabir University of Technology, Tehran, Iran
Mehranshamaey@aut.ac.ir, Sarraf@aut.ac.ir, Ghmoradi@aut.ac.ir

Abstract ─ In this paper, a novel frequency selective surface which has a narrower passband and sharper roll-off rejection than the other single layer designs, is presented. Also, it has better independency from angle and polarization of incident plane wave. In this design a ring loop is placed on a cylindrical cavity of substrate integrated waveguide (SIW). Because of the most compatibility between loop and the electric fields of cylindrical cavity, minimum insertion loss and narrow passband are achieved.

Index Terms ─ Cylindrical cavity, frequency selective surface (FSS), ring loop, substrate integrated waveguide (SIW).

I. INTRODUCTION

The frequency selective surfaces are recognized as spatial filters which pass or stop some frequency bands [1-3]. This filtering can be used in RCS controlling, radomes, sub-reflectors, anti-interfering walls, and so on.

In designing FSS's, like in other filters, obtaining the appropriate frequency characteristics, such as low insertion loss in passband, sharp roll-off and high rejection in out of bands, is one of the greatest challenges. More important than this, is making the frequency characteristics independent from the angle and polarization of incident plane wave [4]. There are so many attempts to improve these two factors such as dielectric loading [5], different periodic elements [4], close coupled FSS [6], and super dense stacked patches [7]. All above methods improve some characteristics of FSS but some of them by increasing the cost. As all improving methods work in the microstrip layout, no increment in Q-factor achieved and need for increasing Q-factor is sensible [8]. In recent years, with introducing SIW technology [9-10] and implementation of FSS on the cavity of SIW, brilliant results are obtained such as sharp roll-off rejection, stability of response about angle and polarization of incidence [11-13].

All recent FSS's are implemented on square SIW cavity and with resonators compatible with square cavity like square loop, cross slot. But we know for the same size, cylindrical cavity has more Q-factor than square cavity [14], so cylindrical SIW cavity can be used to achieve better characteristics than conventional FSS implemented with square SIW cavities (SIWC). In this paper, a FSS structure with circular loop placed on cylindrical SIW cavity is presented, which has a narrower passband and sharper roll-off rejection than available FSS-SIWs

II. DESIGN

One of the important facts in stability of FSS's response is geometrical symmetry [15]. It seems that using a more symmetrical resonator such as circular loop instead of square loop or cross slot, improves this independency. Also keep in mind that circular cavity, for the same dimension, has more Q-factor than square cavity. So it is obvious that a FSS structure which is implemented with circular loop placed on cylindrical SIW cavity has better frequency characteristics and incident independency than conventional SIW FSSs. According to above descriptions, one cell of FSS structure is shown in Figs. 1 and 2, and the geometrical parameters are listed in Table 1.

Via diameter and via spacing come from these inequalities:

$$0.05 < p/\lambda < .025,$$

$$1 < p/d < 2,$$

which p is via diameter and d is via spacing. Other parameters and how they are determined will be described in the next section in which two formulas for the resonance of structure will be mentioned.

Submitted On: February 6, 2014
Accepted On: May 26, 2015

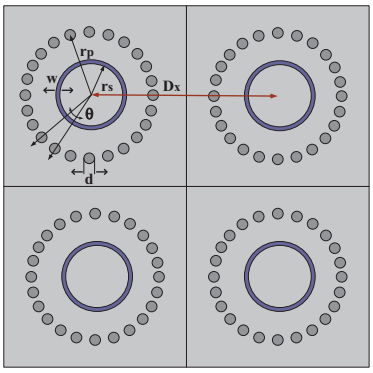

Fig. 1. Geometry of FSS with cylindrical cavity.

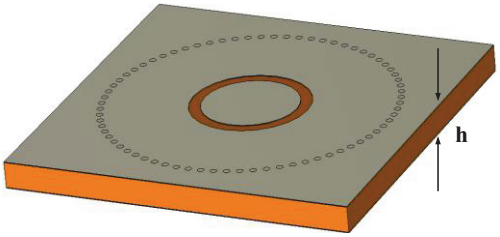

Fig. 2. One cell of SIWC-FSS simulated in CST software.

III. FORMULATION

In SIW-FSS structures, because of SIW cavity resonant mode, there is one more resonating mode than conventional FSS structures. Cavity resonant mode in our design is TE_{010} (for which there is no variation in the z axis because of thin substrate height [14]). The resonant frequency of this structure is calculated:

$$f_{cav} = \frac{c}{2\pi\sqrt{\varepsilon_r}}\left(\frac{A \cdot p'_{01}}{r_{eff}}\right), \tag{1}$$

$$r_{eff} = r_p - B \cdot \frac{d}{2}, \tag{2}$$

p'_{01} is the first root of the derivative of Bessel function of kind 1 with $n=0$ and that is equal to 3.832. A and B are empirical constants derived from numerical methods and for X-band frequency is 0.927 and 0.73. Also, the resonance frequency of circular loop is:

$$f_{slot} = \frac{c}{2\pi C(r_s + \frac{w}{2})\sqrt{\varepsilon_{eff}}}, \tag{3}$$

C is another empirical constant and here is 0.926.

Suppose that a FSS in 12 GHz with 350 MHz bandwidths (f_1 to f_2) should be designed. f_{cav} and f_{slot} in equations (1) and (3) are selected equal to f_1 and f_2. By solving these equations, r_s and $(r_p+w/2)$ are obtained. The spacing between cells should be less than $\lambda/2$. These are the rough parameters and after some optimization the final parameters can be achieved.

IV. SIMULATION RESULTS

For analysis and simulation of FSS structures, according to type of the design, there are some methods such as FDTD [16], FDFD, MoM [17], spectral domain approach, variational method [18], point matching method [19], mutual impedance method [5]-[20], modal matching method [21-22], multimode equivalent network method [23] and equivalent circuit method [24].

In this paper as our novelty is in the design, no numerical methods have been used directly. So powerful full-wave simulator, CST, which is applying finite integral equation, was utilized and following results were obtained.

Figure 3 shows the transmission and reflection of SIW-FSS for normal incident. It is obvious that there is a sharp roll-off in 12.18 GHz because of SIW cavity.

Figures 4 and 5 show transmission, and Figs. 6 and 7 show reflection of SIW-FSS for some different angle of incident and two polarizations. It is clear that for all incident angles until 30° and two polarizations, there is a stable frequency response for this SIW-FSS.

A comparison between the results obtained from this SIW cylindrical cavity FSS and one which is presented in [8], shows the narrowness of this design.

The configuration of FSS rectangular SIW cavity is illustrated in Fig. 8. Transmission and reflection response of these two designs shows in Figs. 9 and 10.

This narrow band property is about the essence of circular loop in comparison with the square loop. The other fact is the compatibility between resonant mode of circular loop and cylindrical cavity.

Field contours of TE_{01} for cylindrical SIW is shown in Fig. 11. If the circular loop cuts the field contours, a compatible mode matching happens and electromagnetic wave suck in the cavity, for the other side of cavity, this procedure happens inversely.

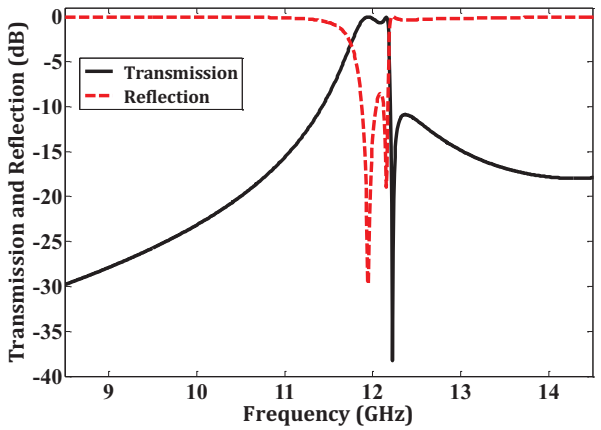

Fig. 3. Frequency response of SIWC-FSS (reflection and transmission).

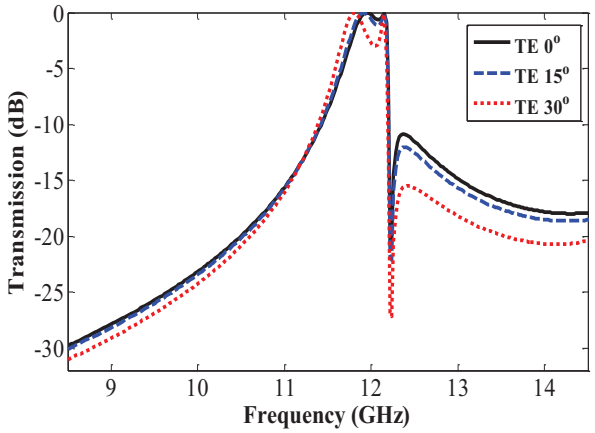

Fig. 4. Transmission response versus angle of incidence for TE polarization.

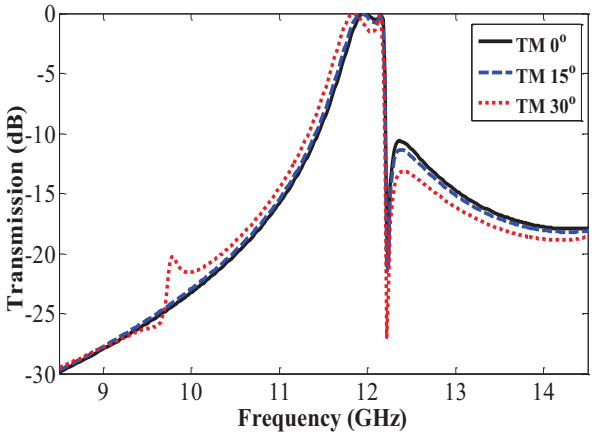

Fig. 5. Transmission response versus angle of incidence for TM polarization.

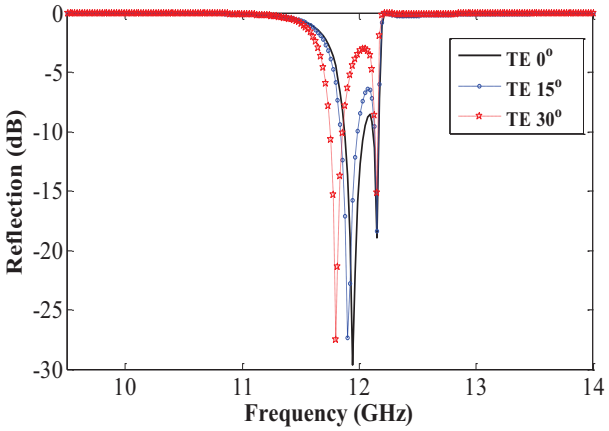

Fig. 6. Reflection response versus angle of incidence for TE polarization.

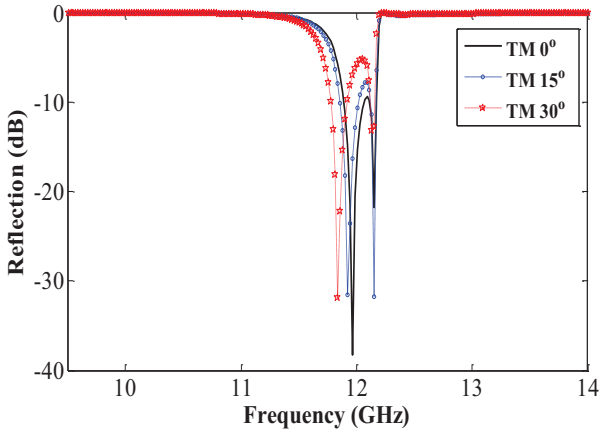

Fig. 7. Reflection response versus angle of incidence for TM polarization.

Table 2: Geometrical parameters for SIW square cavity FSS in simulation

Parameter	Value	Parameter	Value
D_x	14 (mm)	D_y	14 (mm)
L_1	8 (mm)	L_2	8 (mm)
W_1	1 (mm)	W_2	1 (mm)
d_1	3 (mm)	d_W	3 (mm)
d	1 (mm)	d_p	3 (mm)
h	1 (mm)	ε_r	2.65

The resonance which appears in 16 GHz in proposed design is related to circular patch existing in the centre of the shape. In narrow-band application, most of the time, sharp roll-off rejection is more important than beyond out of band behavior.

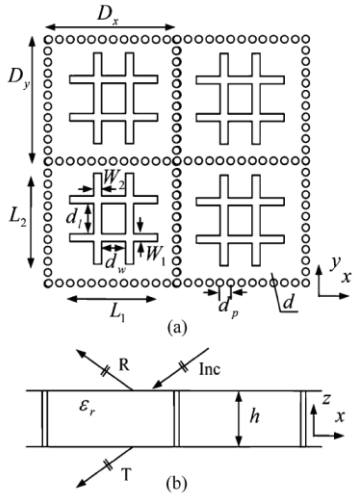

Fig. 8. Configuration of SIW square cavity FSS which is compared with proposed SIWC-FSS.

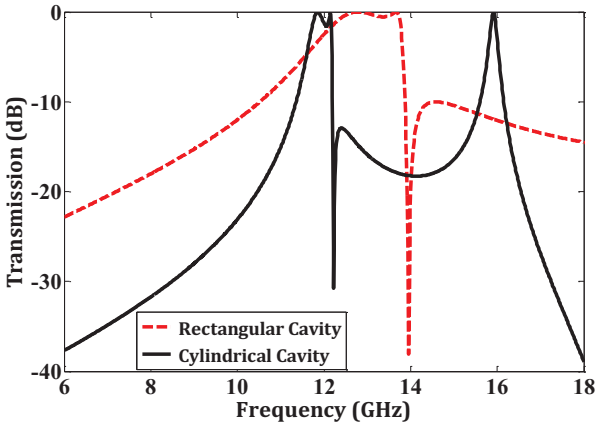

Fig. 9. Comparison between transmission response of SIW square cavity FSS and proposed SIWC-FSS.

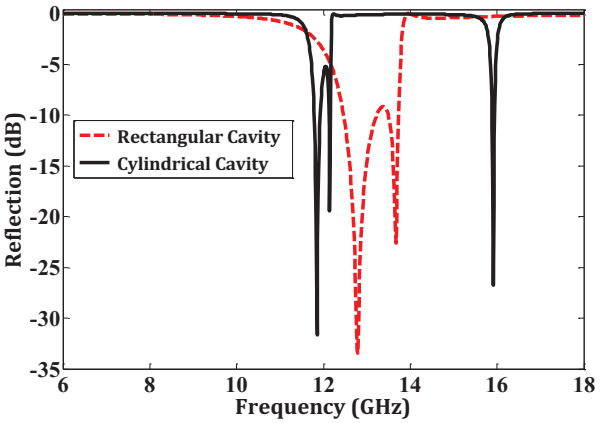

Fig. 10. Comparison between reflection response of SIW square cavity FSS and proposed SIWC-FSS.

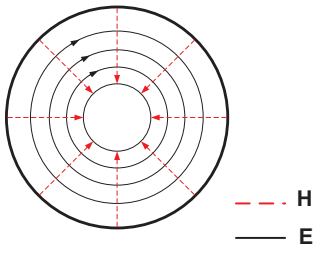

Fig. 11. Electromagnetic fields of TE_{01} for cylindrical SIW and conventional waveguide.

V. CONCLUSION

A FSS design with narrow passband and sharp roll-off rejection in a single layer format was presented. These features are related to use of SIW cylindrical cavity and circular loop mounted on it. As shown in the previous sections, the most compatibility between resonant modes of cylindrical cavity and circular loop, cause to these features. Also, because of extremely symmetrical shape, the maximum independency from angle and polarization of incident plane wave obtained.

REFERENCES

[1] B. A. Munk, *Frequency Selective Surfaces: Theory and Design*, John Wiley & Sons, New York, 2000.

[2] R. Drupp, J. Smith, T. Mayer, L. Li, D. Werner, and J. Bossard, "The synthesis of frequency selective surfaces for infrared filters," *ACES Conference Paper*, vol. Nanoscale Frequency Selective Surfaces, 2006.

[3] L. Latrach, N. Sboui, A. Gharsallah, A. Gharbi, and H. Baudrand, "Analysis and design of a planar multilayered FSS with arbitrary incidence," *ACES Journal*, vol. 23, no. 2, 2008.

[4] J. Shaker and L. Shafai, "Removing the angular sensitivity of FSS structures using novel double-layer structures," *IEEE Microw. Guided Wave. Lett.*, vol. 5, no. 10, pp. 324-325, Oct. 1995.

[5] R. J. Luebbers and B. A. Munk, "Some effects of dielectric loading on periodic slot arrays," *IEEE Trans. Antennas Propag.*, vol. 26, no. 4, Jul. 1978.

[6] J. C. Vardaxoglou and D. S. Lockyer, "Modified FSS response from two sided and closely coupled arrays," *Electron. Lett.*, vol. 30, no. 22, 1994.

[7] S. B. Savia and E. A. Parker, "Superdense FSS with wide reflection band and rapid roll-off," *Electron. Lett.*, vol. 38, no. 25, Dec. 2002.

[8] G. Q. Luo, et al., "Theory and experiment of novel frequency selective surface based on substrate integrated waveguide technology," *IEEE Trans. Antennas and Propage.*, vol. 53, no. 12, Dec. 2005.

[9] E. Mehrshahi and M. Salehi, "A simple technique for propagation characteristics of substrate integrated waveguide," *ACES Journal*, vol. 25, no. 8, 2010.

[10] G. Di Massa, L. Boccia, G. Amendola, and E. Arnieri, "Full wave analysis of substrate integrated waveguide," *ACES Conference Paper*, vol. Advances in Computer-Aided Design of Electromagnetic Structures and Devices, 2006.

[11] G. Q. Luo, et al., "High performance frequency selective surface using cascading substrate integrated waveguide cavities," *IEEE Microw. and Wireless Comp. Letters*, vol. 16, no. 12, Dec. 2006.

[12] G. Q. Luo, et al., "Frequency-selective surfaces with two sharp sidebands realized by cascading and shunting substrate integrated waveguide cavities," *IET Microw. Antennas Propag.*, 2008.

[13] R-R. Xu, Z-Y. Zong, and W. Wu, "Single-layer miniaturized loaded frequency selective surfaces with enhanced bandwidth," *8th International Symposium on Antennas, Propagation and EM*

Theory, ISAPE, Nov. 2008.

[14] D. M. Pozar, *Microwave Engineering*, 3rd edition, John Wiley and Sons, New York, 2005.

[15] E. A Parker and S. M. A. Hamdy, "Rings as elements for frequency selective surfaces," *Electronics Letters*, 1981.

[16] M. K. Karkkainen and P. M. T. Ikonen, "Finite-difference time-domain modeling of frequency selective surfaces using impedance sheet conditions," *IEEE Trans. Antennas Propagat*., vol. 53, no. 9, Sept. 2005.

[17] R. Mitra, C. H. Chan, and T. Cwik, "Techniques for analyzing frequency selective surfaces - a review," *Proceedings of the IEEE*, vol. 76, no. 12, Dec. 1988.

[18] R. B. Kieburtz and A. Ishimaru, "Scattering by a periodically aperture conducting screen," *IRE Trans. Antennas Propag.*, vol. 9, Nov. 1961.

[19] R. H. Ott, R. G. Kouyoumjian, and L. Peters Jr., "Scattering by a two dimensional periodic array of narrow plates," *Radio Sci.*, vol. 2, no. 11, pp. 1347-1359, Nov. 1967.

[20] R. J. Luebbers and B. A. Munk, "Mode matching analysis of biplanar slot arrays," *IEEE Trans. Antennas Propag*., vol. 273, no. 3, May 1979.

[21] C. C. Chen, "Scattering by a two-dimensional periodic array of conducting plates," *IEEE Trans. Antennas Propag*., vol. 18, no. 5, Sept. 1970.

[22] C. C. Chen, "Transmission through a conducting screen perforated periodically with apertures," *IEEE Trans. Microw. Theory Tech*., vol. 18, no. 9, Sept. 1970.

[23] M. Guglielmi and A. A. Oliner, "Multimode network description of a planar periodic metal-strip grating at a dielectric interface-part 1: rigorous network formulations," *IEEE Trans. Microw. Theory Tech*., vol. 37, no. 3, Mar. 1989.

[24] F. Costa, A. Monorchio, and G. Manara, "An overview of equivalent circuit modeling techniques of frequency of frequency selective surfaces and metasurfaces," *ACES Journal Paper*, vol. 29, no. 12, 2014.

Mehran Shamaei was born in 1984 and received the B.S. and M.S. degrees from the Amirkabir University of Technology (Tehran Polytechnic), Tehran, Iran, in 2008 and 2010, respectively; all in Electrical Engineering. He is currently working towards the Ph.D. degree at same university. His research interests include frequency selective surfaces and reflect array antennas.

Reza Sarraf Shirazi was born in Yazd, Iran in 1958. He received the Ph.D. degrees in Electrical Engineering from Amirkabir University of Technology (Tehran Polytechnic), Tehran, Iran in 2006. His main research interests are numerical Electromagnetics and radio wave propagation. He is currently an Assistant Professor with the Electrical Engineering Department, Amirkabir University of Technology. He has published several papers in the refereed journals and international conferences.

Gholamrreza Moradi was born in Shahriar, Iran in 1966. He received the Ph.D. degree in Electrical engineering from Amirkabir University of Technology (Tehran Polytechnic), Tehran, Iran in 2002. His main research interests are numerical Electromagnetics, antennas, active microwave and mm-wave circuits and systems. He is currently an Associate Professor with the Electrical Engineering Department, Amirkabir University of Technology. He has published several papers in the refereed journals and international conferences.

Hybrid MLFMA/MLACA for Analysis of Electromagnetic Scattering from Inhomogeneous High-Contrast Objects

Y. L. Hu, Z. H. Fan, D. Z. Ding, and R. S. Chen

Department of Communication Engineering
Nanjing University of Science and Technology, Nanjing, 210094, China
eerschen@njust.edu.cn

Abstract ─ An efficient hybrid method is proposed to analyze the electromagnetic scattering from the composite structures comprising PEC and inhomogeneous high-contrast dielectric materials with the volume-surface integral equation (VSIE) approach, which uses the main framework of the multilevel fast multipole algorithm (MLFMA) but adopts the multilevel adaptive cross approximation algorithm (MLACA) and the equivalent dipole-moment (EDM) to deal with part of the "strong" interaction of MLFMA. Numerical results are presented to demonstrate the accuracy and efficiency of the proposed scheme.

Index Terms ─ Equivalent dipole-moment, multilevel adaptive cross approximation algorithm, multilevel fast multipole algorithm, volume-surface integral equation.

I. INTRODUCTION

A lot of attentions have been paid for the analysis of electromagnetic scattering from the composite structures comprising PEC and inhomogeneous high-contrast dielectric materials for its wide range of applications, such as PEC targets coated with multilevel dielectric radar absorbing materials, the near space hypersonic vehicle coated with inhomogeneous plasma and so on. Some numerical methods can be used to deal with inhomogeneous composite objects, such as PMCHWT [1-2], Müller [3], JMCFIE [4-5], etc.; but they are effective only for the piecewise inhomogeneous dielectric and the efficiency will be decreased with the number of the subdomains increasing.

VSIE [6-7] can handle composite structures with arbitrarily inhomogeneous dielectric materials conveniently. However the number of unknowns N is large for an electrically large size problem, which brings the difficulty for solving matrix equation due to the computational complexity, $O(N^2)$ for iterative solver and $O(N^3)$ for direct solver.

MLFMA [8-14] is a widely used fast algorithm and it can be used to reduce the computational complexity both for memory and CPU time. However the computational resources of the "strong" interactions are still large for the composite objects comprising high-contrast dielectric since the finest level size should be larger than 0.2 λ_0, where λ_0 is the free space wavelength. MLACA [15-18] is another popular fast technique to analyze the electromagnetic problems. Compared with MLFMA, MLACA is purely algebraic and not limited by the forms of Green's function.

Although MLFMA and MLACA can be applied to accelerate the solving progress, the process of matrix filling is still time-consuming, especially for the dielectric part with high-contrast. EDM [19-21] is an arising method which can accelerate the computation of impedance matrix. In this paper, MLACA and EDM are used to speed up the computation for the "strong" interactions, and the threshold values for different parts of VSIE matrix are analyzed. Several numerical tests are given to validate the efficiency to analyze the electromagnetic scattering from the composite structures comprising PEC and inhomogeneous high-contrast dielectric materials.

It is well known that MLFMA, MLACA, EDM and some kinds of their combinations have been used in scattering analysis for several years, while they are first used together on VSIE. The hybrid scheme is a very useful and efficient method for the analysis of electromagnetic scattering from these composite objects. We find a special application area to make the three algorithms play better roles. In our proposed hybrid method, the respective advantages of three fast algorithms are played to remedy above problems tactfully. These advantages are verified in numerical results accordingly.

This paper is organized as follows. The theory and formulations of VSIE are demonstrated in part A of Section II, and the introductions of hybrid fast algorithms are mentioned in part B. Numerical results are shown and analyzed in Section III, and the conclusions are included in Section IV.

Submitted On: November 27, 2014
Accepted On: May 26, 2015

II. THEROY AND FORMULATIONS

A. Volume-surface electric field integral equations

Consider an arbitrarily shaped composite structure illuminated by a plane wave $\mathbf{E}^{inc}$ in free space, the geometry of composite structures is shown in Fig. 1.

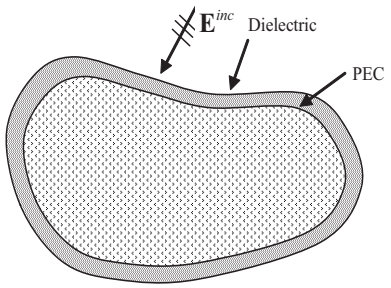

Fig. 1. Geometry of composite structure.

The PEC part of the composite structures is denoted by S, and the dielectric part is denoted by V. Where the relative permeability is all 1 and the permittivity $\varepsilon(\mathbf{r})$ is a position function in the space. Based on the boundary conditions of the total electric field, VSIE can be written as the following formats:

$$\mathbf{E}^{inc}(\mathbf{r}) = \mathbf{D}(\mathbf{r})/\varepsilon(\mathbf{r}) + j\omega\mathbf{A}_V(\mathbf{r}) + \nabla\Phi_V(\mathbf{r}) + j\omega\mathbf{A}_S(\mathbf{r}) + \nabla\Phi_S(\mathbf{r}) \quad \mathbf{r}\in V, \tag{1}$$

$$\mathbf{E}^{inc}_{\tan}(\mathbf{r}) = [j\omega\mathbf{A}_V(\mathbf{r}) + \nabla\Phi_V(\mathbf{r}) + j\omega\mathbf{A}_S(\mathbf{r}) + \nabla\Phi_S(\mathbf{r})]_{\tan} \quad \mathbf{r}\in S. \tag{2}$$

In equations (1) and (2), $\mathbf{E}^{inc}$ is the incident electric field, "tan" represents the tangential component, $\mathbf{D}(\mathbf{r})$ is the electric flux density. $\mathbf{A}_V(\mathbf{r})$, $\Phi_V(\mathbf{r})$, $\mathbf{A}_S(\mathbf{r})$ and $\Phi_S(\mathbf{r})$ are the vector magnetic potentials and scalar electric potentials produced by the volume and surface currents, respectively. The electric flux densities $\mathbf{D}(\mathbf{r})$ are represented by the SWG [22] basis functions. At the same time, the surface currents $\mathbf{J}_S(\mathbf{r})$ are represented by the RWG [23] basis functions. After the Galerkin's test, equations (1) and (2) can be converted to the following matrix equations:

$$\begin{bmatrix} \mathbf{Z}^{DD} & \mathbf{Z}^{DM} \\ \mathbf{Z}^{MD} & \mathbf{Z}^{MM} \end{bmatrix} \begin{bmatrix} \mathbf{I}^{D} \\ \mathbf{I}^{M} \end{bmatrix} = \begin{bmatrix} \mathbf{V}^{D} \\ \mathbf{V}^{M} \end{bmatrix}. \tag{3}$$

The four parts of impedance matrix $\mathbf{Z}^{DD}$, $\mathbf{Z}^{DM}$, $\mathbf{Z}^{MD}$ and $\mathbf{Z}^{MM}$ are represent volume basis test volume integral equation, volume basis test surface integral equation, surface basis test volume integral equation and surface basis test surface integral equation, respectively.

B. Hybrid fast algorithm applied for VSIE

In order to reduce the filling time of MoM, EDM is introduced for impedance matrix generation. Using EDM method, the scattered filed produced by the surface and volume currents can be relapced by the approximation of the radiated field produced by a very small diopole with equivalent moment. The interaction between the source and testing basis functions can be computed directly without double integrals when their distance is larger than the threshold value. In this paper, the threshold value in $\mathbf{Z}^{DD}$ part for dielectric is assigned as $0.15\,\lambda_D$ and $0.15\,\lambda_0$ for the other parts, where λ_D is the wavelength in dielectric.

Although the time of impedance matrix evaluating is reduced, the memory consumption and time of matrix-vector product (MVP) are unchanged. MLFMA can be utilized to accelerate electromagnetic scattering calculation, which is based on the addition theorem for the scalar Green's function. In the frame of MLFMA, the near and far interaction parts are constituted for the MVP, the near parts are still the same with MoM/EDM approach, the far parts are accelerated by MLFMA and not computed explicitly.

Though MLFMA is an efficient method for solving the 3D electrically large problems, the phenomenon of "low frequency breakdown" should be attentioned when the finest box size of MLFMA is less than 0.2 λ_0. For the high-contrast dielectric materials, the consumptions of "near" region interactions in the frame of MLFMA are still unacceptable due to the relatively fine discretization. Therefore, MLACA is used in the "near" region to remedy the shortages mentioned above. The same octal-tree structure is employed in MLACA as in MLFMA, and the finest box size can be assigned as $0.15\,\lambda_D$, which is smaller than that used in MLFMA. Therefore the pressure of the "strong" interaction portion in MLFMA can be reduced by MLACA. During the procedure of MLACA, the impedance matrix can be split into two classes sub-matrix blocks. The blocks in the first class are the diagonal blocks built by the self-group or two adjacent groups interactions, which are calculated by MoM/EDM approach. The blocks in the second class represent the interactions of well-separated groups, which are numerically rank-deficient, and they can efficiently be compressed with MLACA. Therefore the second class blocks can be written as $[\mathbf{Z}_{m\times n}] \approx [\mathbf{U}_{m\times r}]\times[\mathbf{V}_{n\times r}]^H$ to approximate the interactions of two well-separated groups in MLACA, where r is its rank, m and n represent the number of the basis functions in the observation and source boxes, respectively. With moderately grouping in the scheme, r is often much smaller than m and n. The singular value decomposition (SVD) algorithm can be used to further remove the redundancies in the matrices generated by MLACA.

In this paper, the hybrid MLFMA/MLACA algorithm is proposed to analyze the electromagnetic scattering from composite structures comprising PEC and inhomogeneous high-contrast dielectric materials. The impedance matrix can be written as:

$$[\mathbf{Z}]=[\mathbf{Z}_0]+[\mathbf{Z}_1]+[\mathbf{Z}_2]. \quad (4)$$

$[\mathbf{Z}_0]$ is the "near" part computed by MoM/EDM, $[\mathbf{Z}_1]$ is the "middle" part compressed by MLACA, and $[\mathbf{Z}_2]$ is the "far" part accelerated by MLFMA. In order to demonstrate our proposed scheme clearly, the impedance matrix can be described by the figure format as shown in Fig. 2.

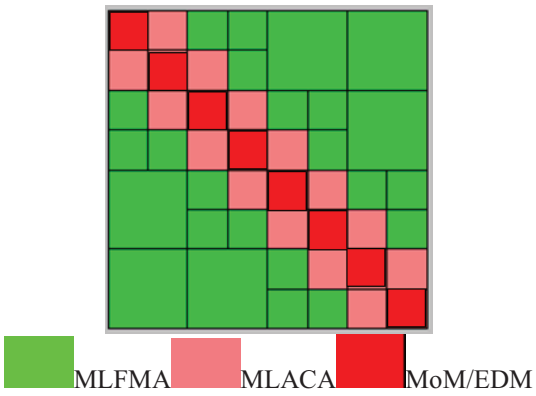

Fig. 2. The distribution of sub-matrix blocks.

III. NUMRICAL RESULTS

In this section, four numerical examples are presented to show the accuracy and efficiency of this scheme. The first and last three examples are performed on the server with same 2.67 GHz CPU, different RAM of 512 GB and 48 GB, respectively. The tolerance of MLACA in these examples is chosen as 5e-3. The multi-frontal sparse direct solver Mumps [24] is used as a preconditioner to accelerate the convergence.

Firstly, the electromagnetic scattering from a series of coated spheres are computed to test the accuracy of the proposed method and the ability to analyze the object with the increasing unknowns. The radius of PEC sphere is 0.8 m, and the thickness of coated layer is 0.1 m. The relative permittivity of dielectric layer is 4. It is illuminated by the vertical polarization plane wave traveling along Z direction at four kinds of incident frequencies 150 MHz, 300 MHz, 600 MHz and 1.2 GHz. The unknown numbers are 16768, 115616, 850816 and 6510080 for the different cases, respectively. 40 cores are used for the parallel computation. The curves of the bistatic RCS for different cases are shown in Fig. 3. It is observed that there are good agreements between the proposed method and Mie series results. The requirements of memory and CPU time are shown in Table 1.

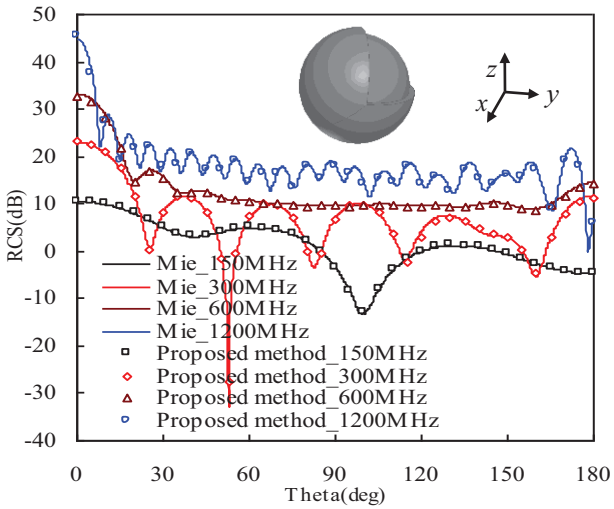

Fig. 3. The bistatic RCS of coated sphere with different frequencies (phi=0).

Table 1: Requirements of memory and CPU time

Frequency (MHz)	150	300	600	1200
Memory (GB)	0.28	3.9	47.9	459.6
CPU time (s)	82	1292	7998	45989

Next, in order to demonstrate the effect of the proposed method with different relative permittivities, three PEC cylinders with different coating materials are considered. Here, all of the coated PEC cylinder have same dimensions with the height 1.6 m and radius 0.1 m, the thickness of coating material is 0.07 m. They are illuminated by a vertical polarization plane wave traveling along Z direction at the frequency of 0.3 GHz. The relative permittivity of them are ε_r=2,4,16, and the unknowns are 5787, 12726, 96404 for the three cases, respectively. Here, the choices of EDM threshold value are discussed in detail according to the results of second model. The parameters of MLFMA and MLACA are unchanged. The value of relative root mean square (RRMS) error is defined as $\sqrt{(1/n)\sum_{i=1}^{n}|a_i-b_i|^2/|b_i|^2}$, where a_i and b_i are the values of bistatic RCS for the test results and VSIE method with only MLFAM and MLACA, n denotes the number of observation. Now, except for $\mathbf{Z}^{DD}$ part, the calculations of impedance matrix for the other three parts are accelerated by EDM with different threshold values. Then only the calculation of $\mathbf{Z}^{DD}$ part is combined with EDM, the curves of RRMS error are shown in Fig. 4. From the curves, it can be found that the RRMS error is acceptable when the threshold value in $\mathbf{Z}^{DD}$ part is assigned as $0.15\lambda_D$ and $0.15\lambda_0$ for the other parts. The curves of the bistatic RCS for three

different relative permittivities are shown in Fig. 5. It is observed that there are good agreements between them when compared with FEKO results (based on MoM/MLFMA with surface equivalence principle). As listed in Table 2, their memory requirement and CPU time are compared to show the efficiency of the proposed method, when 8 cores are used for the parallel computation. It can be found that memory requirement of "strong" interaction portion and CPU time can be reduced as high as 75% and 88% for the proposed method.

In the third example, the effect comparisons of proposed hybrid method with dielectric materials and PEC are demonstrated. A X33 scale model is considered, which is shown as Fig. 6. It is illuminated by a vertical polarization plane wave traveling along $-X$ direction at the frequency of 0.3 GHz. The PEC and high-contrast carbon fiber medium are considered to use as the fuselage material, respectively. Their unknowns are 12948, 235940, respectively. The thickness of carbon fiber is 0.01 m, the relative permittivity is 40 and the conductivity is 1e-3. The curves of the bistatic RCS are shown in Fig. 7 for both MLFMA+MLACA+EDM and MLFMA. It can be found the accuracy of the hybrid method is acceptable when compared with MLFMA. As listed in Table 3, their memory requirement and CPU time are compared to show the efficiency of the proposed method, when 40 cores are used for the parallel computation. For the high-contrast material, there are bigger advantages for memory requirement of "strong" interaction portion and CPU time than PEC material.

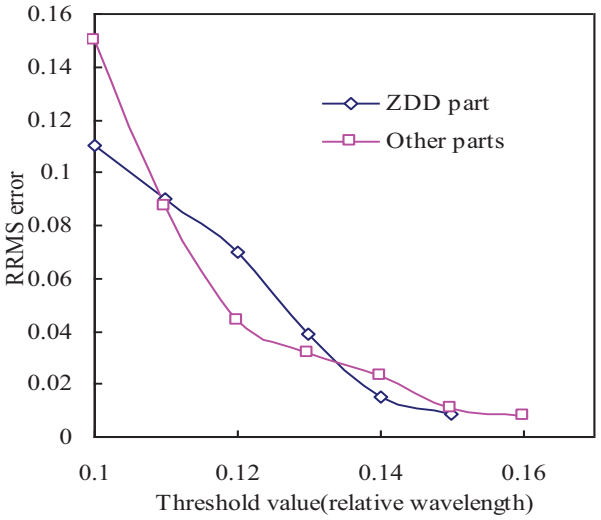

Fig. 4. The analysis of EDM threshold values with different relative wavelengths (λ_D for $\mathbf{Z}^{DD}$ part, λ_0 for the other parts).

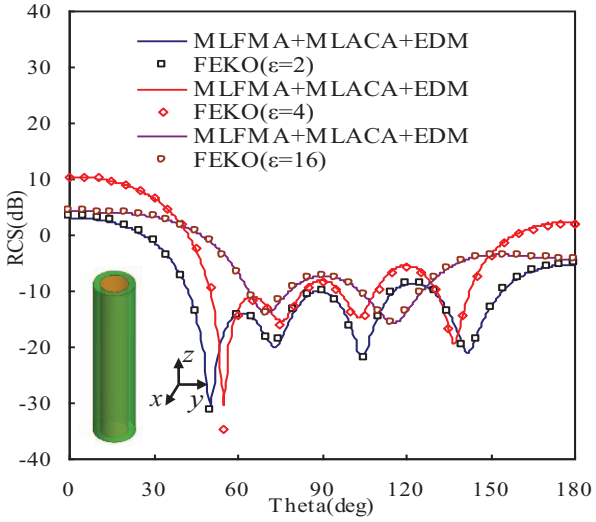

Fig. 5. The bistatic RCS of coated cylinder with different cases (phi=0).

Table 2: Comparison of the cost and performance

	MLFMA			MLFMA+MLACA		
Relative permittivity	2	4	16	2	4	16
Number of levels	2			2+1	2+2	2+3
CPU time for each MVP (s)	1.8	5.9	109	0.7	1.5	9
Total time (s) (MoM)	45	539	17984	28	121	2436
Total time (s) (MoM/EDM)	41	505	15237	25	96	2208
Near part cost (MB)	116	545	13239	80	211	3245
Memory saving ratio (%)				31	61	75
Time saving ratio (%)				44	82	88

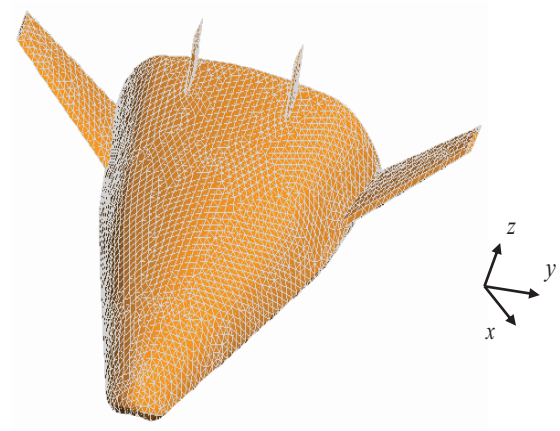

Fig. 6. The geometry of the X33.

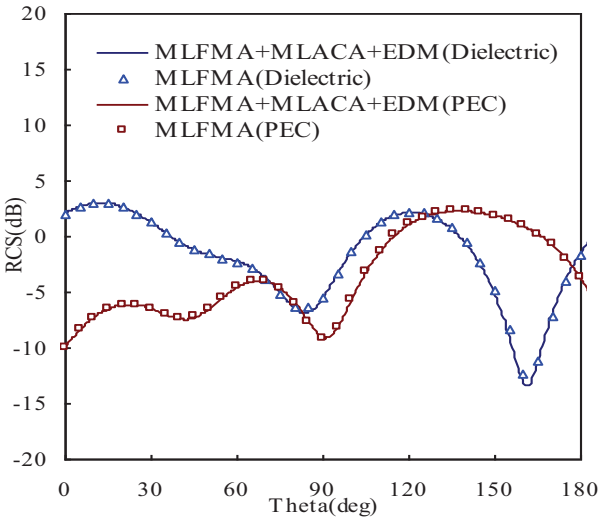

Fig. 7. The bistatic RCS of different materials (phi=0).

Table 3: Comparison of the cost and performance

	MLFMA		MLFMA+MLACA	
Material	Dielectric	PEC	Dielectric	PEC
Number of levels	2	2	2+3	2+1
CPU time for each MVP (s)	102	0.7	12.1	0.61
Total time (s) (MoM)	11457	37.5	5275	78.5
Total time (s) (MoM/EDM)	9897	29.6	4519	70.9
Near part cost (GB)	26.8	0.27	4.9	0.19
Memory saving ratio (%)			82%	29%
Time saving ratio (%)			61%	--

In order to demonstrate the advantage of VSIE to analyze the inhomogeneous composite object, an inhomogeneous composite body of revolution is considered as the last example, which is illuminated by a vertical polarization plane wave traveling along $-X$ direction at the frequency of 2 GHz and the unknown is 221621. Its relative permittivity in XoY plane is shown in Fig. 8. The curves of the bistatic RCS are shown in Fig. 9 for MLACA+MLFMA+EDM and the MLFMA. It can be found that there is a good agreement between them when compared with the MLFMA. As listed in Table 4, their memory requirement and CPU time are compared to show the efficiency of the proposed method, when 40 cores are used for the parallel computation. It can be found that memory requirement of "strong" interaction portion and CPU time can be reduced 59% and 57% for the proposed method.

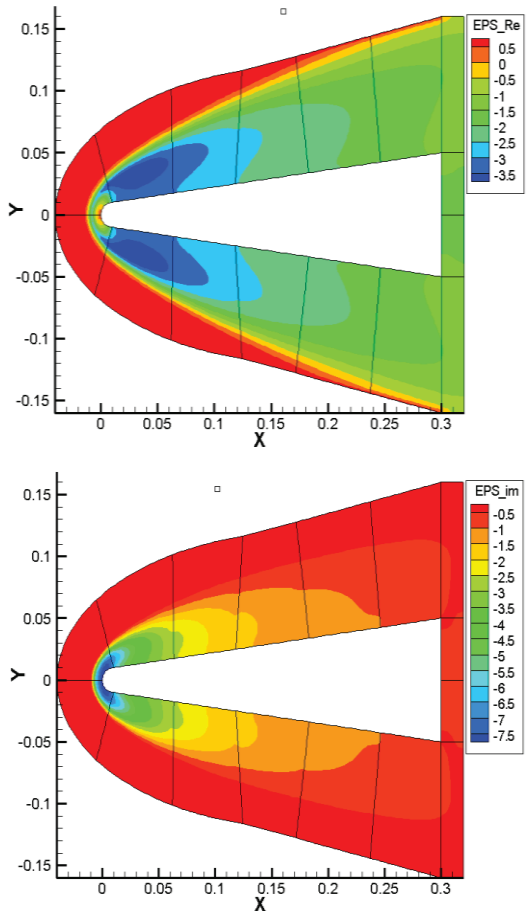

Fig. 8. The distribution of relative permittivity (real and imagine part).

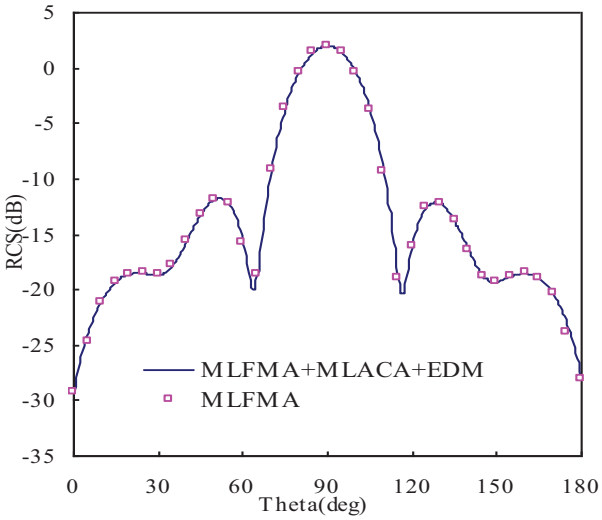

Fig. 9. The bistatic RCS of the inhomogeneous composite body (phi=0).

Table 4: Comparison of the cost and performance

	MLFMA	MLFMA+MLACA
Number of levels	2	2+2
CPU time for each MVP (s)	27.3	9.9
Total time (s) (MoM)	3115	1578
Total time (s) (MoM/EDM)	2691	1325
Near part cost (GB)	31.6	12.9
Memory saving ratio (%)		59%
Time saving ratio (%)		57%

IV. CONCLUSION

In this paper, the combination of MLACA and EDM is introduced to further accelerate MLFMA in the VSIE to efficiently analyze the electromagnetic scattering from composite structures comprising PEC and inhomogeneous high-contrast dielectric materials. Its memory requirements of "strong" interaction portion and CPU time have been reduced effectively when compared with MLFMA.

REFERENCES

[1] P. L. Huddleston, L. N. Medgyesi-Mitschang, and J. M. Putnam, "Combined field integral equation formulation for scattering by dielectrically coated conducting bodies," *IEEE Trans. Antennas Propag*., vol. 34, no. 4, pp. 510-520, Apr. 1986.

[2] K. C. Donepudi, J.-M. Jin, and W. C. Chew, "A higher order multilevel fast multipole algorithm for scattering from mixed conducting/dielectric bodies," *IEEE Trans. Antennas Propag*., vol. 51, no. 10, pp. 2814-2821,Oct. 2003.

[3] P. Yla-Oijala and M. Taskinen, "Well-conditioned Muller formulation for electromagnetic scattering by dielectric objects," *IEEE Trans. Antennas Propag*., vol. 53, no. 10, pp. 3316-3323, 2005.

[4] P. Yla-Oijala and M. Taskinen, "Application of combined field integral equation for electromagnetic scattering by dielectric and composite objects," *IEEE Trans. Antennas Propag*., vol. 53, no. 3, pp. 1168-1173, 2005.

[5] P. Ylä-Oijala, M. Taskinen, and J. Sarvas, "Multilayered media Green's functions for MPIE with general electric and magnetic sources by the Hertz potential approach," *Progress In Electromagnetics Research*, vol. 33, pp. 141-165, 2001.

[6] C. C. Lu and W. C. Chew, "A coupled surface-volume integral equation approach for the calculation of electromagnetic scattering from composite metallic and material targets," *IEEE Transactions on Antennas Propagation*, vol. 48, no. 12, pp. 1866-1868, Dec. 2000.

[7] C. Luo and C.-C. Lu, "Electromagnetic scattering computation using a hybrid surface and volume integral equation formulation," *Applied Computational Electromagnetics Society (ACES) Journal*, vol. 22, no. 3, pp. 340-349, 2007.

[8] R. Coifman, V. Rokhlin, and S. Wandzura, "The fast multipole method for the wave equation: a pedestrian prescription," *IEEE Magazine on Antennas and Propagation*, vol. 35, no. 3, pp. 7-12, 1993.

[9] J. M. Song and W. C. Chew, "Fast multipole method solution using parametric geometry," *Microwave and Optical Technology Letter S*, vol. 7, no. 16, pp. 760-765, 1994.

[10] H. Fangjing, N. Zaiping, and H. Jun, "An efficient parallel multilevel fast multipole algorithm for large-scale scattering problems," *Applied Computational Electromagnetics Society (ACES) Journal*, vol. 25, no. 4, pp. 381-387, 2010.

[11] J. M. Song, C.-C. Lu, and W. C. Chew, "Multilevel fast multipole algorithm for electromagnetic scattering by large complex objects," *IEEE Transactions on Antennas Propagation*, vol. 45, no. 10, pp. 1488-1493, 1997.

[12] M. Chen, R. Chen, Z. Fan, and D. Ding, "Accelerating the multilevel fast multipole method with parallel preconditioner for large-scale scattering problems," *Applied Computational Electromagnetics Society (ACES) Journal*, vol. 26, no. 10, pp. 815-822, 2011.

[13] B. Dembart and E. Yip, "The accuracy of fast multipole methods for Maxwell's equations," *IEEE Comput. Sci. Eng*., vol. 5, no. 3, pp. 48-56, 1998.

[14] D. Ding, S. Tao, and R. Chen, "Fast analysis of finite and curved frequency- selective surfaces using the VSIE with MLFMA," *International Journal of Numerical Modelling: Electronic Networks, Devices and Fields*, vol. 24, no. 5, pp. 425-436, 2011.

[15] M. Bebendorf, "Approximation of boundary element matrices," *Numerische Mathematik*, vol. 86, no. 4, pp. 565-589, 2000.

[16] K. Zhao, M. N. Vouvakis, and J. F. Lee, "The adaptive cross approximation algorithm for accelerated method of moments computations of EMC problems," *IEEE Transactions on Electromagnetic Compatibility*, vol. 47, no. 4, pp. 763-773, 2005.

[17] J. M. Tamayo, A. Heldring, and J. M. Rius, "Multilevel adaptive cross approximation (MLACA)," *IEEE Transactions on Antennas Propagation*, vol. 59, no. 12, pp. 4600-4608, Feb. 2011.

[18] Z. N. Jiang, R. S. Chen, Z. H. Fan, Y. Y. An, M. M. Zhu, and K. W. Leung, "Modified adaptive

cross approximation algorithm for analysis of electromagnetic problems," *Applied Computational Electromagnetics Society (ACES) Journal*, vol. 26, no. 2, pp. 160-169, 2011.

[19] J. Yuan, Z. Niu, Z. Li, and C. Gu, "Electromagnetic scattering by arbitrarily shaped PEC targets coated with anisotropic media using equivalent dipole-moment method," *Journal of Infrared Millimeter, and Terahertz Waves*, vol. 31, no. 6, pp. 744-752, 2010.

[20] J. Yuan and K. Su, "Electromagnetic radiation from arbitrarily shaped microstrip antenna using the equivalent dipole-moment method," *International Journal of Antennas and Propagation*, vol. 2012, Article ID 181235, 2012.

[21] X. Chen, C. Gu, J. Ding, X. Deng, Z. Niu, and Z. Li, "An equivalent dipole-moment method based multilevel fast multipole algorithm for dielectric objects," *Applied Computational Electromagnetics Society (ACES) Journal*, vol. 27, no. 5, pp. 408-412, 2012.

[22] S. M. Rao and D. R. Wilton, "Transient scattering by conducting surfaces of arbitrary shape," *IEEE Transactions on Antennas Propagation*, vol. 39, no. 1, pp. 56-61, Jan. 1991.

[23] S. M. Rao and T. K. Sarkar, "Numerical solution of time domain integral equations for arbitrarily shaped conductor/dielectric composite bodies," *IEEE Trans. Antennas Propag*., vol. 50, no. 12, pp. 1831-1837, 2002.

[24] P. R. Amestoy, I. S. Duff, J. Koster, and J.-Y. L'Excellent, "A fully asynchronous multifrontal solver using distributed dynamic scheduling," *SIAM Journal on Matrix Analysis and Applications*, vol. 23, pp. 15-41, 2001.

Yanlong Hu received the B.Sc. degree in Information and Computing Sciences from Nanjing University of Information Science & Technology, Nanjing, China, in 2011.

He is currently working towards the Ph.D. degree in Electromagnetic Fields and Microwave Technology at the School of Electrical Engineering and Optical Technique, Nanjing University of Science and Technology. His current research interests include computational electromagnetics, antennas, electromagnetic scattering and propagation.

Zhenhong Fan was born in Jiangsu, China, in 1978. He received the M.Sc. and Ph.D. degrees in Electromagnetic Field and Microwave Technique from Nanjing University of Science and Technology (NJUST), Nanjing, China, in 2003 and 2007, respectively.

During 2006, he was with the Center of wireless Communication in the City University of Hong Kong, Kowloon, as a Research Assistant. He is currently an Associate Professor with the Electronic Engineering of NJUST. He is the author or co-author of over 20 technical papers. His current research interests include computational electromagnetics, electromagnetic scattering and radiation.

Dazhi Ding was born in Jiangsu, China, in 1979. He received the B.S. and Ph.D. degrees in Electromagnetic Field and Microwave Technique from Nanjing University of Science and Technology (NUST), Nanjing, China, in 2002 and 2007, respectively.

During 2005, he was with the Center of Wireless Communication in the City University of Hong Kong, Kowloon, as a Research Assistant. He is currently an Associate Professor with the Electronic Engineering of NJUST. He is the author or co-author of over 30 technical papers. His current research interests include computational electromagnetics, electromagnetic scattering, and radiation.

Rushan Chen (M'01) was born in Jiangsu, China. He received the B.Sc. and M.Sc. degrees from the Department of Radio Engineering, Southeast University, China, in 1987 and 1990, respectively, and the Ph.D. degree from the Department of Electronic Engineering, City University of Hong Kong, in 2001.

He joined the Department of Electrical Engineering, Nanjing University of Science and Technology (NJUST), China, where he became a Teaching Assistant in 1990 and a Lecturer in 1992. Since September 1996, he has been a Visiting Scholar with the Department of Electronic Engineering, City University of Hong Kong, first as Research Associate, then as a Senior Research Associate in July 1997, a Research Fellow in April 1998, and a Senior Research

Fellow in 1999. From June to September 1999, he was also a Visiting Scholar at Montreal University, Canada. In September 1999, he was promoted to Full Professor and Associate Director of the Microwave and Communication Research Center in NJUST, and in 2007, he was appointed Head of the Department of Communication Engineering, NJUST. He was appointed as the Dean in the School of Communication and Information Engineering, Nanjing Post and Communications University in 2009. And in 2011, he was appointed as Vice Dean of the School of Electrical Engineering and Optical Technique, Nanjing University of Science and Technology. His research interests mainly include microwave/millimeter-wave systems, measurements, antenna, RF-integrated circuits, and computational electromagnetics. He has authored or co-authored more than 200 papers, including over 140 papers in international journals.

Chen received the 1992 Third-Class Science and Technology Advance Prize given by the National Military Industry Department of China, the 1993 Third-Class Science and Technology Advance Prize given by the National Education Committee of China, the 1996 Second-Class Science and Technology Advance Prize given by the National Education Committee of China, and the 1999 First-Class Science and Technology Advance Prize given by Jiangsu Province, as well as the 2001 Second-Class Science and Technology Advance Prize. He is the recipient of the Foundation for China Distinguished Young Investigators presented by the National Science Foundation (NSF) of China in 2003. In 2008, he became a Chang-Jiang Professor under the Cheung Kong Scholar Program awarded by the Ministry of Education, China. Besides, he was selected as a Member of Electronic Science and Technology Group by Academic Degree Commission of the State Council in 2009. Chen is a Senior Member of the Chinese Institute of Electronics (CIE), Vice-Presidents of Microwave Society of CIE and IEEE MTT/APS/EMC Nanjing Chapter. He serves as the Reviewer for many technical journals such as IEEE Trans. on AP and MTT, Chinese Physics etc., and now serves as an Associate Editor for the International Journal of Electronics.

Octave-Band Monopole Antenna with a Horseshoe Ground Plane for Wireless Communications

M. M. Abdollahi [1], N. Ojaroudi [2], M. Mehranpour [1], and F. Ghiasvand [1]

[1] Department of Electrical Engineering
Imam Khomeini International University, Qazvin
farhood_abdollahi@yahoo.com, mehranpour.mehdi@gmail.com, fazel_piol@yahoo.com

[2] Young Researchers and Elite Club
Ardabil Branch, Islamic Azad University, Ardabil, Iran
n.ojaroudi@yahoo.com

Abstract ─ In this manuscript, a new design of octave-band monopole antenna with multi-resonance characteristic is presented .The antenna consists of a fork-shaped radiating patch with three pairs of teeth, a feed-line and a horseshoe ground plane. Simulated and measured results show that the antenna design exhibits an operating bandwidth (VSWR<2) from 2 to 20 GHz, which provides a wide usable fractional bandwidth of more than 160%. The proposed antenna has a symmetrical structure, therefore displays a good omnidirectional radiation pattern even at higher frequencies. The designed antenna has a very small size of 15×17 mm^2 and the impedance bandwidth of the designed antenna is higher than the other antennas reported in the literature to date. The proposed antenna configuration is simple, easy to fabricate and can be integrated into UWB systems.

Index Terms ─ Bandwidth enhancement, horseshoe ground plane, octave-band antenna, UWB applications.

I. INTRODUCTION

After allocation of the frequency band from 3.1 to 10.6 GHz for the commercial use of ultra-wideband (UWB) systems by the Federal Communication Commission (FCC) [1], ultra wideband systems have received phenomenal gravitation in wireless communication. Designing an antenna to operate in the UWB band is quite a challenge because it has to satisfy the requirements such as ultra wide impedance bandwidth, omnidirectional radiation pattern, constant gain, high radiation efficiency, constant group delay, low profile, easy manufacturing, etc. [2]. In UWB communication systems, one of key issues is the design of a compact antenna while providing wideband characteristic over the whole operating band. Consequently, a number of microstrip antennas with different geometries have been experimentally characterized [3-6].

Three new small wideband printed monopole antennas using rotated T-shaped slot and parasitic structures, sprocket-shaped ground plane in the upper edge of ground plane, and fractal structure to achieve the maximum impedance bandwidth were proposed in [7-9]. Some methods are used to obtain the multi-resonance function in the literature [8-12].

In this paper, a different design is proposed to obtain the very wide bandwidth for the compact monopole antenna which provides a wide usable fractional bandwidth of more than 160%. Good VSWR and radiation pattern characteristics are obtained in the frequency band of interest. The proposed antenna is successfully implemented and the simulation results show reasonable agreement with the measurement results. The designed antenna has a small dimension and the impedance bandwidth of the designed antenna is higher than the UWB antennas reported recently [3-13].

II. ANTENNA DESIGN

The structure of proposed monopole antenna fed by a microstrip line is shown in Fig. 1. The dielectric substance (*FR4*) with thickness of 1 mm with relative permittivity of 4.4 and loss tangent 0.018 is chosen as substrate to facilitate printed circuit board integration. The basic monopole antenna structure consists of a fork-shaped radiating patch, a feed line, and a semi-circular ground plane. The proposed antenna is connected to a 50-Ω SMA connector for signal transmission. Final values of the presented antenna design parameters are specified in Table 1.

The three essential parameters for the design of a rectangular microstrip monopole antenna are operation frequency (f_0); as the ultra-wideband (UWB) uses the

Submitted On: November 30, 2013
Accepted On: December 11, 2014

frequency range from 3.1-10.6 GHz. Hence, the antenna designed must be able to operate in this frequency range. The resonant frequency selected for antenna design is 3 GHz (lower resonance frequency). The dielectric material selected for antenna design is FR4 which has a dielectric constant of the substrate (ε_r) of 4.4. A substrate with a high dielectric constant has been selected since it reduces the dimensions of the antenna, height of dielectric (h). Hence, the essential parameters for the design are: f_0 = 3 GHz, ε_r = 4.4 and h = 1.6 mm. The dimensions of the patch along its length have now been extended on each end by a distance ΔL, which is given empirically by:

$$\Delta L = 0.412h\frac{(\varepsilon_{eff}+0.3)}{(\varepsilon_{eff}-0.258)}\frac{\frac{W_{sub}}{h_{sub}}+0.264}{\frac{W_{sub}}{h_{sub}}+0.8}, \quad (1)$$

where h_{sub} is the height of dielectric, W_{sub} is the width of the microstrip monopole antenna and ε_{reff} is the effective dielectric constant. Then, the effective length (L_{eff}) of the patch can be calculated as follows:

$$L_{eff} = L + 2\Delta L. \quad (2)$$

For a given resonant frequency f_0, the effective length is given as:

$$L_{eff} = \frac{C}{2f_o\sqrt{\varepsilon_{reff}}}. \quad (3)$$

For a rectangular microstrip antenna, the resonance frequency for any TM_{mn} mode is given by as:

$$\varepsilon_{eff} = \frac{(\varepsilon_r+1)}{2}\frac{(\varepsilon_r-1)}{2}\frac{1}{(1+12\frac{h}{w})^{\frac{1}{2}}}. \quad (4)$$

The width W_{sub} of microstrip antenna is given by:

$$W = \frac{C}{2f_0\sqrt{\frac{(\varepsilon_r+1)}{2}}}. \quad (5)$$

The design steps for the proposed UWB microstrip and calculations are given as follows:

Step 1: Calculation of the width (W_{sub}): the width of the microstrip monopole antenna is given by Eq. (5) by substituting $c = 3\times10^8$ m/s, ε_r = 4.4 and f = 3 GHz, we get: W_{sub} = 15 mm.

Step 2: Calculation of effective dielectric constant (ε_{reff}): Eq. (4) gives the effective dielectric constant by substituting ε_r = 4.4, W = 15 mm and h = 1.6 mm, we get: ε_{reff} = 4.2703.

Step 3: Calculation of the effective length (L_{eff}): Eq. (3) gives the effective length by substituting ε_r = 4.4, C = 3e8 m/s and f_0 = 3 GHz, we get: L_{eff} = 10.3696 mm.

Step 4: Calculation of the length extension (ΔL): Eq. 1 gives the length extension by substituting ε_{reff} = 4.2703, W = 15 mm and h = 1.6 mm, we get: ΔL = 0.0190 mm.

Step 5: Calculation of actual length of patch (L_{sub}): the actual length is obtained by Eq. 2 as, substituting L_{eff} = 10.369 mm and ΔL = 0.0190, we get: L_{sub} = 10.3316 mm which is fixed in L_{sub} = 10 mm.

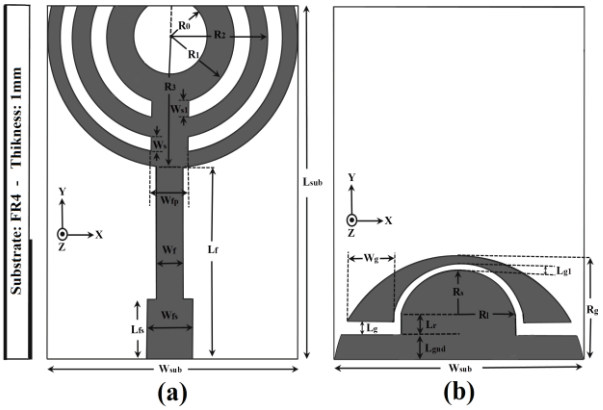

Fig. 1. Structure of the proposed antenna: (a) top layer, and (b) bottom layer.

Table 1: Final parameters values of the antenna

Param.	mm	Param.	mm	Param.	mm
W_{sub}	15	L_{sub}	17	R_g	5.5
W_{fs}	1.6	L_{fs}	2.6	W_f	0.7
L_f	7	W_{fp}	1	W_s	0.6
W_{s1}	0.6	R_3	7.5	R_2	6.2
R_1	4.7	R_0	3.2	W_g	2.7
L_g	0.6	L_{gnd}	1.6	L_r	1.4
R_s	2.13	R_1	4	L_{g1}	0.19

Regarding defected ground structures (DGS) theory, creating slits in the ground plane provide additional current paths. Moreover, these structures change the inductance and capacitance of the input impedance, which in turn leads to change the bandwidth [3-5]. Therefore, by converting a semi-circular ground plane to the horseshoe structure, much enhanced impedance bandwidth can be achieved. In addition, based on electromagnetic coupling theory (ECT), by increasing the teeth of fork-shaped radiating patch, additional coupling is introduced between the patch and the ground plane and impedance bandwidth of the antenna is improved without any cost of size or expense [7].

III. RESULTS AND DISCUSSIONS

In this section, the microstrip monopole antenna with various design parameters was constructed, and the numerical and experimental results of the input

impedance and radiation characteristics are presented and discussed. The analysis and performance of the proposed antenna is explored by using Ansoft simulation software high-frequency structure simulator (HFSS) [14], for better impedance matching.

The structure of the various antennas used for simulation studies were shown in Fig. 2. VSWR characteristics for the fork-shaped antenna with a semi-circular ground plane (Fig. 2 (a)), the antenna with a horseshoe ground plane (Fig. 2 (b)), and the proposed antenna (Fig. 2 (c)) structures are compared in Fig. 3.

As shown in Fig. 3, by using a horseshoe ground plane additional resonances at 11 and 16.7 GHz can be achieved. In addition, by increasing the teeth of fork-shaped radiating patch new resonance at 12.5 GHz is generated. By using these structures, the antenna exhibits an operating bandwidth from 2 to 20 GHz. Also, the input impedance of the proposed antenna on a Smith-Chart is shown in Fig. 4.

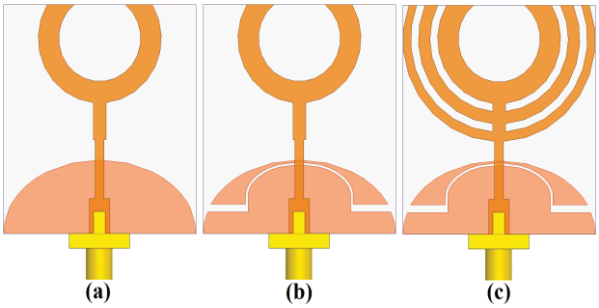

Fig. 2. (a) Fork-shaped antenna with a semi-circular ground plane, (b) the antenna with a horseshoe ground plane, and (c) the proposed antenna structure.

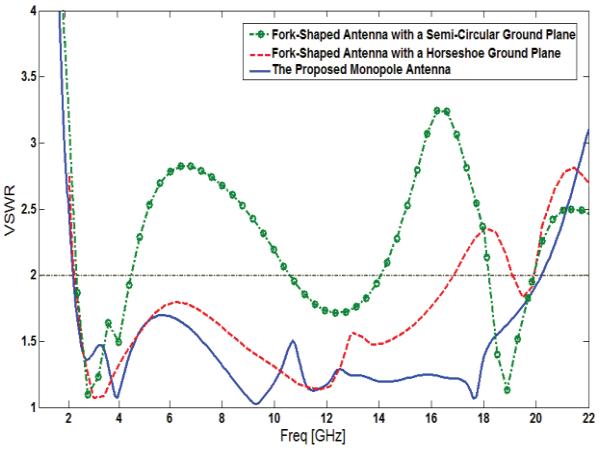

Fig. 3. Simulated VSWR characteristics for the various structures shown in Fig. 2.

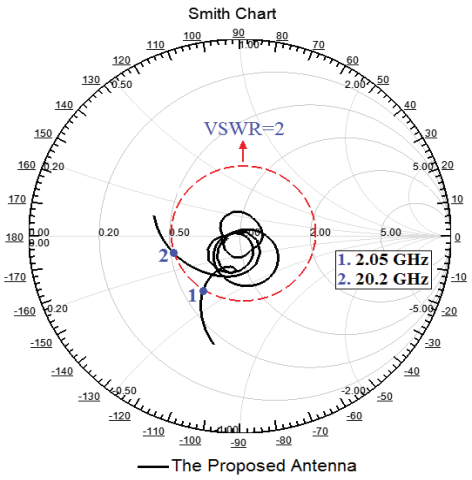

Fig. 4. Simulated input impedance on a Smith-Chart for the proposed antenna.

The simulated current distributions for the proposed antenna at the additional resonances frequencies are presented in Fig. 5. It can be observed in Fig. 5 (a) and 5 (b), that the directions of surface currents are reversed in compared to each other, which the antenna impedance changes at 4 and 12 GHz due to the resonant properties of the horseshoe ground plane structure. Also, the simulated current distribution at the middle resonance frequency (10 GHz) is presented in Fig. 5 (c). As shown in Fig. 5 (c), the current concentrated on the edges of the interior and exterior of the teeth of fork-shaped radiating patch at 10 GHz [15-18].

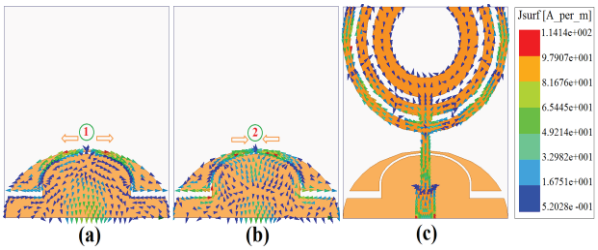

Fig. 5. Simulated surface current distributions for the proposed antenna; (a) 4 GHz, (b) 12.5 GHz, and (c) 17.5 GHz.

As illustrated in Fig. 6, the proposed antenna was designed and fabricated. Figure 7 shows the measured and simulated VSWR characteristics of the proposed antenna. The fabricated antenna has the frequency band of 2 GHz to over 20 GHz.

However, as seen, there exists a discrepancy

between measured data and the simulated results. This discrepancy is mostly due to a number of parameters such as the fabricated antenna dimensions as well as the thickness and dielectric constant of the substrate on which the antenna is fabricated, the wide range of simulation frequencies. In a physical network analyzer measurement, the feeding mechanism of the proposed antenna is composed of a SMA connector and a microstrip line (the microstrip feed-line is excited by a SMA connector); whereas, the simulated results are obtained using the Ansoft simulation software (HFSS), that in HFSS by default, the antenna is excited by a wave port that it is renormalized to a 50-Ohm full port impedance at all frequencies. In order to confirm the accurate return loss characteristics for the designed antenna, it is recommended that the manufacturing and measurement processes need to be performed carefully. Moreover, SMA soldering accuracy and FR4 substrate quality need to be taken into consideration [19-22].

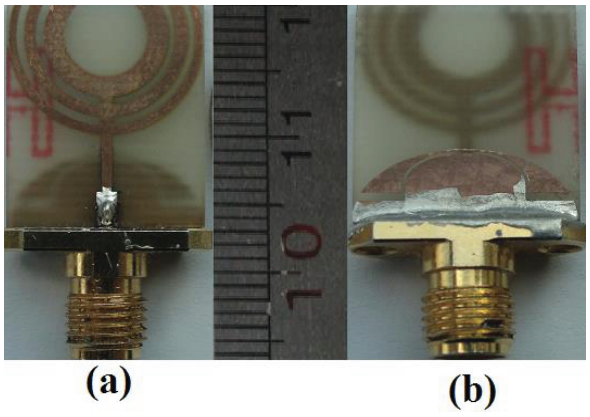

Fig. 6. Photograph of the fabricated antenna: (a) top view, and (b) bottom view.

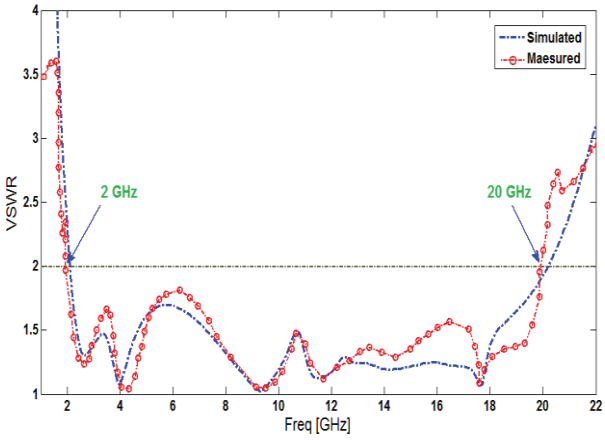

Fig. 7. Measured and simulated VSWR characteristics of the proposed antenna.

Figure 8 depicts the simulated radiation patterns including the co-polarization and cross-polarization in the H-plane (x-z plane) and E-plane (y-z plane). It can be seen that nearly omnidirectional radiation pattern with low cross-polarization level can be observed on x-z plane. The radiation patterns on the y-z plane are like a small electric dipole leading to bidirectional patterns in a very wide frequency band. With the increase of frequency, the radiation patterns become worse because of the increasing effects of the cross-polarization [23-30].

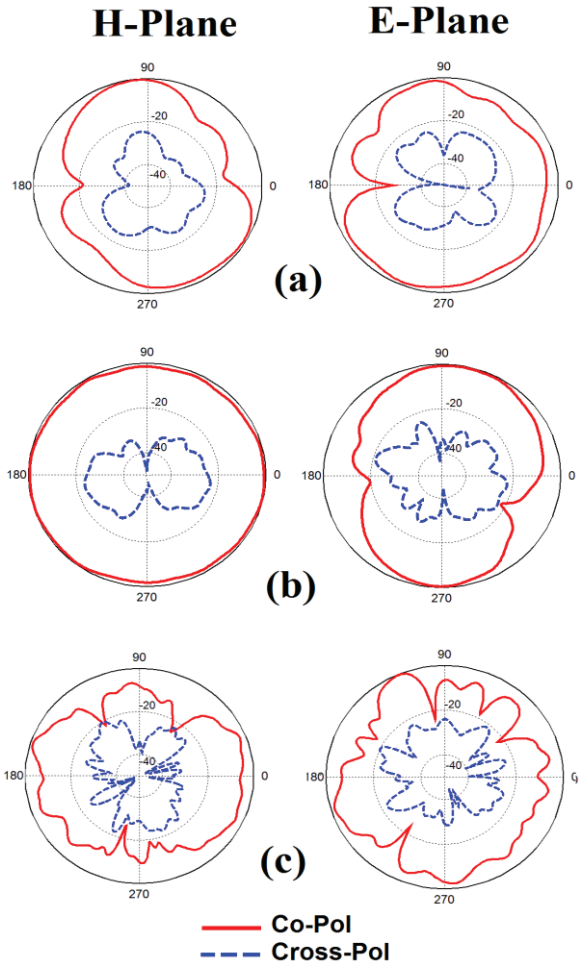

Fig. 8. Simulated radiation patterns for the proposed antenna at: (a) 4 GHz, (b) 12.5 GHz, (c) 14 GHz, and (d) 17.5 GHz.

IV. CONCLUSION

In this paper, a new design of microstrip monopole antenna with simple configuration is proposed which provides a very wide bandwidth for various UWB applications. The presented antenna consists of a fork-shaped radiating patch with three pairs of teeth, a feed-

line and a horseshoe ground plane. The fabricated antenna has the frequency band of 2 to over 20 GHz. Good VSWR and radiation pattern characteristics are obtained in the frequency band of interest.

REFERENCES

[1] FCC News Release, FCC NEWS (FCC 02-48), Feb. 14, 2002.

[2] D. Cheng, *Compact Ultra Wideband Microstrip Resonating Antenna*, US Patent7872606, Jan. 2011.

[3] M. R. Ghaderi and F. Mohajeri, "A compact hexagonal wide slot antenna with microstrip-fed for UWB application," *IEEE Antennas and Wireless Propag. Lett*., vol. 10, pp. 682-685, 2011.

[4] Z. N. Chen, "Impedance characteristics of planar bow-tie-like monopole antennas," *Electronics Letters*, vol. 36, pp. 1100-1101, Jun. 2000.

[5] N. Ojaroudi, M. Ojaroudi, and N. Ghadimi, "UWB omnidirectional square monopole antenna for use in circular cylindrical microwave imaging systems," *IEEE Antennas Wireless Propag. Lett*., vol. 11, pp. 1350-1353, 2012.

[6] J. Liang, C. C. Chiau, X. Chen, and C. G. Parini, "Study of a printed circular disc monopole antenna for UWB systems," *IEEE Trans. Antennas Propag.*, vol. 53, pp. 3500-3504, 2005. DOI: 10.1109/TAP.2005.858598.

[7] N. Ojaroudi, "Design of small reconfigurable microstrip antenna for UWB-CR applications," *19th International Symposium on Antenna and Propagation,* ISAP2014, Kaohsiung, Taiwan, Dec. 2-5, 2014.

[8] A. Azari, "A new fractal antenna for super wideband applications," *Progress in Electromagnetics Research Symposium*, Cambridge, MA, USA, pp. 885-888, Jul. 2010.

[9] K. Chung, T. Yun, and J. Choi, "Wideband CPW-fed monopole antenna with parasitic elements and slots," *Electron. Lett*., vol. 40, pp. 1038-1040, 2004.

[10] M. Mehranpour, H. Boudaghi, M. Ghiamy, and J. Nourinia, "A very compact monopole antenna with variable frequency band-notch for ultra-wideband applications," *International Symposium on Telecommunication, IST2012*, Tehran, Iran, 2012.

[11] N. Ojaroudi, M. Ojaroudi, N. Ghadimi, and M. Mehranpour, "UWB omni-directional square monopole antenna for use in circular cylindrical microwave imaging systems," *Applied Computational Electromagnetics Society (ACES) Journal*, vol. 28, no. 2, pp. 123-7129, Feb. 2013.

[12] A. J. Kerkhoff, R. L. Rogers, and H. Ling, "Design and analysis of planar monopole antennas using a genetic algorithm approach," *IEEE Trans. Antennas Propag*., vol. 2, pp. 1768-1771, 2004.

[13] Ansoft High Frequency Structure Simulator (HFSS), ver. 13, Ansoft Corporation, Pittsburgh, PA, 2010.

[14] J. Y. Sze and K. L. Wong, "Bandwidth enhancement of a microstrip line-fed printed wide-slot antenna," *IEEE Trans. Antennas Propag*., vol. 49, pp. 1020-1024, 2001.

[15] C.-Y. Huang, S.-A. Huang, and C.-F. Yang, "Band-notched ultra-wideband circular slot antenna with inverted C-shaped parasitic strip," *Electron. Lett.*, vol. 44, no. 15, pp. 891-892, Jul. 2008.

[16] M. Ojaroudi, S. Bashiri, N. Ojaroudi, and M. T. Partovi, "Octave-band, multi-resonance CPW-fed small slot antenna for UWB applications," *Electron. Lett.*, vol. 48, no. 16, pp. 980-982, 2012.

[17] P. H. Rao, "CPW-fed octave band slot antenna," *Microw. Opt. Technol. Lett*., vol. 48, pp. 2405-2408, 2006.

[18] V. Rodríguez, "A multi-octave, open-boundary, quad-ridge horn antenna for use in S- to KU-bands," *Microwave Journal*, vol. 49, pp. 84-92.5, 2006.

[19] A. Sutinjo, M. Okoniewski, and R. H. Johnston, "An octave band switched parasitic beam-steering array," *IEEE Antenna and Wireless Propagation Letters*, vol. 6, pp. 211-214, 2007.

[20] E. Lier, D. H. Werner, P. S. Clinton, Q. We, and A. J. Bossard, "An octave-bandwidth negligible-loss radiofrequency metamaterial," *Nature Publishing Group*, vol. 10, pp. 216-222, 2011.

[21] N. Ojaroudi, "New design of multi-band PIFA for wireless communication systems," *19th International Symposium on Antenna and Propagation, ISAP2014*, Kaohsiung, Taiwan, Dec. 2-5, 2014.

[22] A. Raghunathan, N. U. Shankar, and R. Subrahmanyan, *An Octave Bandwidth Frequency Independent Dipole Antenna*, US Patent, arXiv: 1304.2919v1, 2013.

[23] A. Raghunathan, N. U. Shankar, and R. Subrahmanyan, "A monolayer multi-octave bandwidth log-periodic microstrip antenna," *Progress In Electromagnetics Research Letters*, vol. 41, pp. 97-104, 2013.

[24] N. Ojaroudi, M. Mehranpour, Y. Ojaroudi, and S. Ojaroudi, "Investigation and FDTD analysis of UWB microstrip antenna with dual narrow band-notched characteristic," *Applied Computational Electromagnetics Society (ACES) Journal*, vol. 29, no. 10, pp. 784-792, Oct. 2014.

[25] N. Ojaroudi, M. Ojaroudi, N. Ghadimi, and M. Mehranpour, "UWB omni-directional square

monopole antenna for use in circular cylindrical microwave imaging systems," *Applied Computational Electromagnetics Society (ACES) Journal*, vol. 28, no. 2, pp. 123-7129, 2013.

[26] N. Ojaroudi, M. Mehranpour, S. Ojaroudi, and Y. Ojaroudi, "Application of the protruded structures to design an UWB slot antenna with band-notched characteristic," *Applied Computational Electromagnetics Society (ACES) Journal*, vol. 29, no. 2, pp. 184-189, 2014.

[27] N. Ojaroudi, "Application of protruded Γ-shaped strips at the feed-line of UWB microstrip antenna to create dual notched bands," *International Journal of Wireless Communications, Networking and Mobile Computing*, vol. 1, no. 1, pp. 8-13, 2014.

[28] N. Ojaroudi, "Bandwidth improvement of monopole antenna using π-shaped slot and conductor-backed plane," *International Journal of Wireless Communications, Networking and Mobile Computing*, vol. 1, no. 2, pp. 14-19, 2014.

[29] N. Ojaroudi, "A modified compact microstrip-fed slot antenna with desired WLAN band-notched characteristic," *American Journal of Computation, Communication and Control*, vol. 1, no. 3, pp. 56-60, 2014.

[30] N. Ojaroudi, "An UWB microstrip antenna with dual band-stop performance using a meander-line resonator," in *Proceedings of the 22nd International Conference on Software, Telecommunications and Computer Networks (SoftCOM)*, Split, Croatia, Sept. 17-19, 2014.

Compact Wideband Bandpass Filter Using Improved Triple-Mode Resonator with Broad Upper Stopband

Daotong Li [1], Yonghong Zhang [1], Kaida Xu [2], Kaijun Song [1], and Joshua Le-Wei Li [3]

[1] EHF Key Lab of Science
University of Electronic Science and Technology of China (UESTC), Chengdu 611731, China
bzxy06@gmail.com, zhangyhh@uestc.edu.cn, ksong@uestc.edu.cn

[2] Institute of Electromagnetics and Acoustics, Department of Electronic Science
Xiamen University, Xiamen 361005, China
xukaida25@gmail.com

[3] Institute of Electromagnetics, School of Electronic Engineering
University of Electronic Science and Technology of China (UESTC), Chengdu 611731, China
lwli@uestc.edu.cn

Abstract ─ A triple-mode microstrip square ring short stub-loaded stepped impedance resonator (SIR) is proposed for the design of bandpass filters (BPFs). The resonator possesses three resonances over the wide frequency band, which can be employed to implement a BPF with flat response. This kind of the filter is able to control spurious response by changing the structure of the resonator. For validation, a triple-mode BPF with central frequency of 2.55 GHz has been designed, fabricated and measured. Good agreement is observed between measured and simulated results.

Index Terms ─ Triple-mode resonator, wideband bandpass filter, wide stopband response.

I. INTRODUCTION

With the rapid development of modern mobile and wireless communication systems, the filters with compact size and high performance are increasingly essential. Many ways have been developed to make the filters more compact. An effective one is to modify the traditional resonator to generate additional modes, thus the resonator can be treated as multiple resonators in electrical [1]. Among them, dual-mode filter is the most common multiple-mode filter, which has been analyzed deeply and comprehensively in many reports with various configurations, including circular loop [2], square loop [3], hexagonal loop [4], circular patch [5], defected ground structure [6], and triangular patch [7]. Triple-mode characteristics can be achieved by loading a stub to a resonator [8]. The $\lambda/2$ transmission line resonator with a pair of center loaded stubs is used to design the triple-mode filters [9-10].

In this paper, we will present a different type of triple-mode filter by using a novel improved tri-section stepped impedance multiple-mode resonator. The multiple-mode resonator is developed from a conventional SIR dual-mode resonator [11]. By introducing a short stub and a square ring stub loaded in the center of the SIR, a compact triple-mode BPF with wideband response, wide stopband, low insertion loss, and high selectivity is realized. The proposed BPF has been simulated, implemented, and measured. Good agreement is observed between simulated results and measured results.

II. ANALYSIS AND DESIGN OF PROPOSED WIDEBAND BANDPASS FILTER

A. Characteristic of the triple-mode resonator

The proposed triple-mode resonator shown in Fig. 1 is excited via capacitive couplings by input/output port. It consists of a square ring, short stub and a SIR resonator, and the parameters are indicated in Fig. 1. Mode decomposition provides a deeper insight to the operation of the resonator, where the corresponding even- and odd-mode resonators are illustrated in Fig. 2.

The symmetrical plane in Fig. 1 will behave as an electric wall (EW) or a magnetic wall (MW) under the odd-mode or the even-mode excitation, respectively. The resonator equivalent circuits are depicted in Fig. 2, where Y_{ineven} and Y_{inodd} represent the input admittances of the odd-mode equivalent circuit and the even-mode equivalent circuit, respectively.

Submitted On: April 8, 2014
Accepted On: May 25, 2015

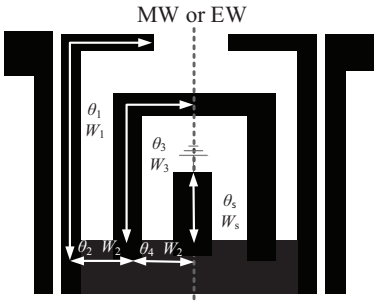

Fig. 1. Layout of proposed triple-mode resonator.

For even-mode excitation, the equivalent circuit is shown in Fig. 2 (a), which contains two resonant circuits: a tri-section quarter-wavelength resonator with one short end and a tri-section quarter-wavelength resonator with open end, as shown in Figs. 2 (c) and (e). The input impedance of the two even-mode equivalent circuits $Y_{\text{ineven\_1}}$ and $Y_{\text{ineven\_2}}$ can be deduced as:

$$Y_{ineven\_1} = \frac{Z_1 Z_2 - Z_1 Z_3 \tan(\theta_3)\tan(\theta_2)}{j(Z_1 Z_2 Z_3 \tan(\theta_3) + Z_1^2 Z_2 \tan(\theta_2)} \quad (1.1)$$

$$\frac{-Z_2 Z_3 \tan(\theta_1)\tan(\theta_3) - Z_2^2 \text{an}(\theta_2)\tan(\theta_1)}{+Z_1 Z_2^2 \tan(\theta_1) - Z_1^2 Z_3 \tan(\theta_1)\tan(\theta_2)\tan(\theta_3))},$$

$$Y_{ineven\_2} = \frac{-jZ_1 Z_2 Z_3 \cot\theta_1 + jZ_2^2 Z_3 \tan\theta_2}{Z_2 Z_3 + Z_1 Z_3 \cot\theta_1 \tan\theta_2} \quad (1.2)$$

$$\frac{+Z_2 jZ_3^2 \tan\theta_3 + jZ_1 Z_3^2 \cot\theta_1 \tan\theta_3 \tan\theta_2}{+Z_1 Z_2 \cot\theta_1 \tan\theta_3 - Z_2^2 \tan\theta_2 \tan\theta_3},$$

where θ_i (i=1,2,3 and s) is the electrical length for the section of the triple-mode resonator shown in Fig. 2.

The two even-mode resonance condition can be derived by setting $Y_{\text{ineven\_1}} = 0$ and $Y_{\text{ineven\_2}} = 0$. Figure 2 (c) shows the Path I of even-mode equivalent circuit. The resonant frequencies of $f_{\text{even\_2}}$ can be extracted as follows:

$$\frac{Z_3}{Z_2}\tan(\theta_2)\tan(\theta_3) + \frac{Z_3}{Z_1}\tan(\theta_1)\tan(\theta_3) + \frac{Z_2}{Z_1}\tan(\theta_1)\tan(\theta_2) = 1. \quad (1.3)$$

For the simplicity of analysis, keep the condition of $\theta_1=\theta_2=\theta_3=\theta$, and set $K_1=Z_1/Z_2$, $K_2=Z_2/Z_3$, then (1.3) can be rewritten as:

$$\left(\frac{1}{K_2} + \frac{1}{K_1 K_2} + \frac{1}{K_1}\right)\tan^2(\theta) = 1. \quad (1.4)$$

Therefore, the condition for the fundamental resonance of a symmetrical tri-section SIR with equal section lengths can be derives as [12-13]:

$$\theta = \tan^{-1}\left(\sqrt{\frac{K_1 K_2}{K_1 + K_2 + 1}}\right). \quad (1.5)$$

Similarly for the resonant frequencies of $f_{\text{even\_1}}$, Fig. 2 (e) shows the Path II of even-mode equivalent circuit. When $\theta_1=(\theta_2+\theta_4)=\theta_s=\theta$ and $K_3=Z_2/Z_s$, the fundamental resonant frequency $f_{\text{even\_1}}$ occurs at:

$$\theta = \tan^{-1}\left(\sqrt{\frac{K_1 + K_1 K_3 + 1}{K_3}}\right). \quad (1.6)$$

For odd-mode excitation, its equivalent circuit shown in Fig. 2 (b) can be decomposed into two resonant circuits: a tri-section stepped-impedance resonators and a quarter-wavelength SIR, which are shown in Figs. 2 (d) and (e), respectively. The required odd-mode resonant frequency $f_{\text{odd\_1}}$ is introduced by the typical quarter-wavelength SIR. The input impedance of the two odd-mode equivalent circuit $Y_{\text{inodd\_1}}$ can be deduced as:

$$Y_{inodd\_1} = \frac{Z_2 - Z_1 \tan(\theta_1)\tan(\theta_2 + \theta_4)}{jZ_2((Z_1 \tan(\theta_1) + Z_2 \tan(\theta_2 + \theta_4))}. \quad (1.7)$$

The resonance condition can be derived by setting $Y_{\text{inodd\_1}} = 0$. The fundamental resonant frequency $f_{\text{odd\_1}}$ occurs at:

$$\tan(\theta_1)\tan(\theta_2 + \theta_4) = K_1. \quad (1.8)$$

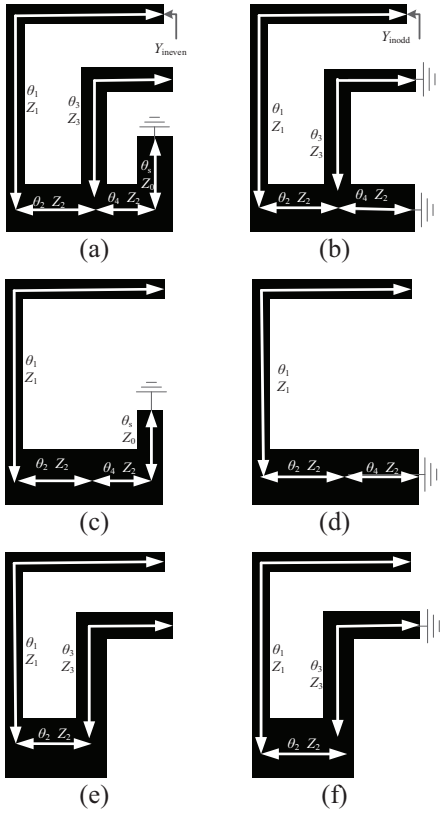

Fig. 2. Equivalent circuits of the triple-mode resonator: (a) even-mode, (b) odd-mode, (c) Path I of even-mode equivalent circuit, (d) Path I of odd-mode equivalent circuit, (e) Path II of even-mode equivalent circuit, and (f) Path II of odd-mode equivalent circuit.

Figure 3 shows the EM simulated frequency responses of the triple-mode resonator under the weak coupling, where f_i (i=1, 2and 3) corresponds to the ith resonant frequency of triple-mode resonator and f_{zi} (i=1 and 2) are the frequency locations of the transmission zeros. We can see that there are three resonances in the passband of the filter and two transmission zeros near the passband edges.

Figure 4 shows the simulated even- and odd-mode normalized resonant frequencies f_r/f_0, where f_0 is set to 2.35 GHz. It is obvious to see from Figs. 4 (a), (b) that the resonant frequency f_{odd_1} receives little influence from the introduced square ring and short-stub, whereas f_{even_1} and f_{even_2} can be varied separately by changing the length θ_s and L_3 of the short-stub and square ring, respectively. As shown in Fig 4 (a), by changing the short-stub length θ_s, the first resonant frequency f_{even_1} can be shifted within a wide range, while the f_{odd_1} is fixed and f_{even_2} varies slightly. Figure 4 (b) shows the distribution of resonant frequencies for cases of different length of θ_3, it is clear that the third resonant frequency f_{even_2} can be shifted within a wide range, while f_{even_1} and f_{odd_1} are nearly unchanged.

According to the curves in Fig. 5, the variation of resonant frequencies can be controlled by changing the impedance ratios of the tri-section SIR. As shown in Fig. 5 (a), the resonant frequency f_{even_1} can be changed widely by altering the impedance ratio of K_3, and the resonance frequencies f_{odd_1} and f_{even_2} varies slightly. It also can be seen from Fig. 5 (b), the resonant frequency f_{even_2} can be shifted within a wide range versus different impedance ratio of K_2, with the resonant frequencies f_{even_1} and f_{odd_1} having almost no change. Figure 5 (c) shows the variation of resonant frequencies f_{even_1}, f_{odd_1} and f_{even_2} versus the impedance ratio of K_1, which have a common trend, but the change of resonant frequency f_{odd_1} is more intense.

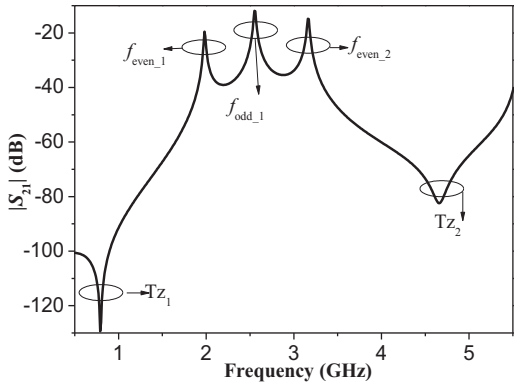

Fig. 3. Simulation transmission response of the wideband filter with weak coupling.

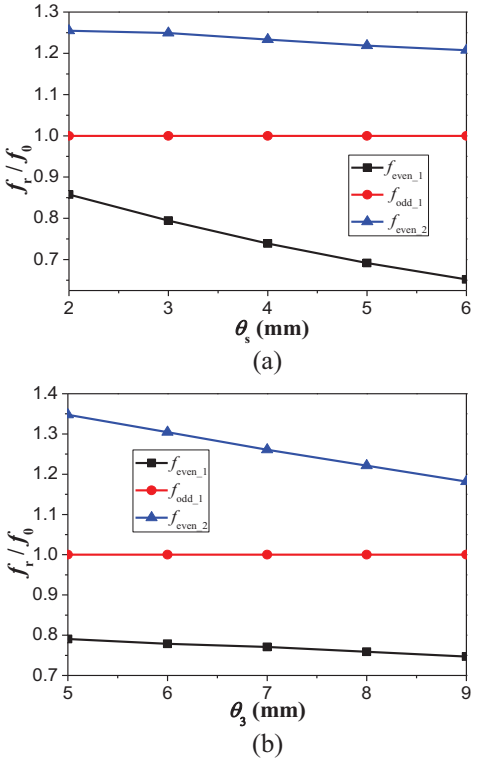

Fig. 4. (a) Analysis of resonator frequencies versus θ_s, and (b) analysis of resonator frequencies versus θ_3.

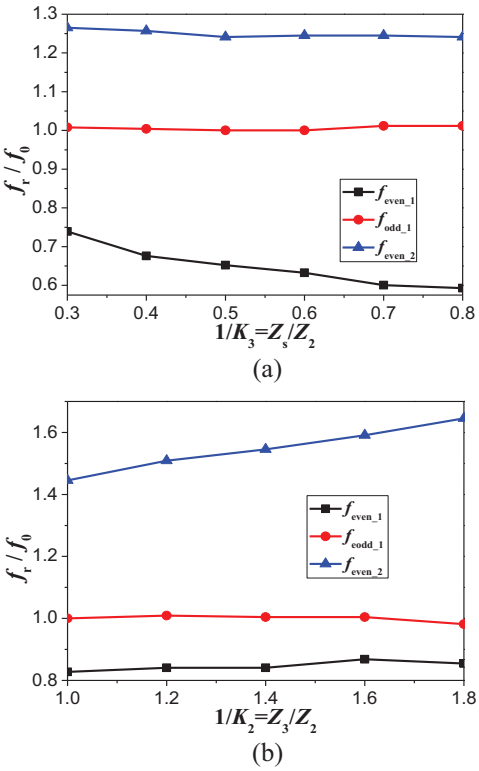

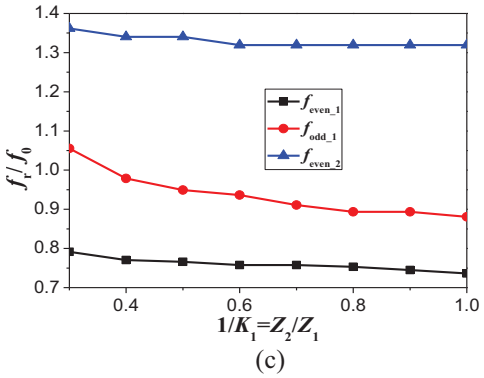

(c)

Fig. 5. Variation of resonant frequencies versus impedance ratio. Analysis of resonator frequencies versus impedance ratio of: (a) K_3, (b) K_2, and (c) K_1.

Based on the above analysis, the resonant frequencies of the proposed triple-mode resonator could be controlled by tuning the length of θ_1, θ_2, θ_3 and θ_s and the impedance ratio K_1, K_2 and K_3. There is more freedom in design compared with traditional triple-mode resonator.

B. Filter design

The coupling scheme of the triple-mode filter is presented in Fig. 6. The dark circles and the white circles indicate resonant modes of resonators and source/load, respectively. These modes are all directly coupled to both the source and the load. The coupling between microstrip resonator and source/load can be modified by changing their distance and overlap length. The coupling between the even mode of the triple-mode resonator and input or output are both positive and the coupling between the odd mode and source is positive, while the coupling between this mode and load is negative. The dashed line indicates the coupling between source and load that is determined by the gap between input and output microstrip line. Therefore, the corresponding coupling matrix of the coupling scheme is given by:

$$M = \begin{bmatrix} 0 & M_{S1} & M_{S2} & M_{S3} & M_{SL} \\ M_{1S} & M_{11} & 0 & 0 & M_{1L} \\ M_{2S} & 0 & M_{22} & 0 & M_{2L} \\ M_{3S} & 0 & 0 & M_{33} & M_{3L} \\ M_{LS} & M_{L1} & M_{L2} & M_{L3} & 0 \end{bmatrix} \quad (1.9)$$

Due to symmetrical geometry of the proposed filter, the coupling coefficients agree with $M_{S1}=M_{L1}$, $M_{S2}=M_{L2}$, and $M_{S3}=-M_{L3}$. So two inherent transmission zeros of the resonator and a transmission zero introduced by the source-load coupling can be achieved, which improve the selectivity of the proposed BPF. Therefore, the generalized coupling matrix for the proposed BPF with central frequency of 2.55 GHz can be obtained on the basis of the approach of synthesis in [14] as follows:

$$M = \begin{bmatrix} 0 & -0.6042 & -0.4861 & 0.8205 & 0.0186 \\ -0.6042 & 1.5887 & 0 & 0 & 0.6035 \\ -0.4861 & 0 & -1.4814 & 0 & 0.4854 \\ 0.8205 & 0 & 0 & -0.2436 & 0.8199 \\ 0.0186 & 0.6035 & 0.4854 & 0.8199 & 0 \end{bmatrix}.$$

The scattering characteristic of the proposed filter shown in Fig. 7 was synthesized. Three transmission poles are clearly observed in the passband of the filter. In addition, three transmission zeros are created which improve the selectivity in the transition band and rejection in the stopband.

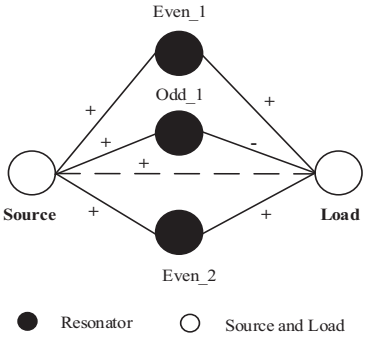

Fig. 6. The coupling scheme of proposed triple-mode BPF.

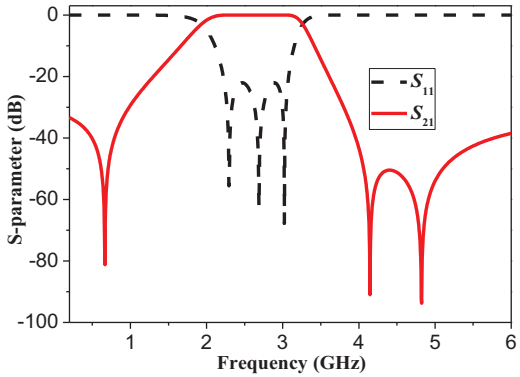

Fig. 7. Synthesized theory result of triple-mode BPF.

III. SIMULATION AND EXPERIMENT

Based on the triple-mode resonator, a wide-band BPF has been designed and fabricated on Taconic RF-35 substrate with relative dielectric constant of ε_r=3.5 and thickness of h=0.508 mm. The geometry of the proposed filter is shown in Fig. 8. It consists of one triple-mode resonator and a pair of parallel-coupled quarter wavelength feedlines. The dimensions of the proposed wideband BPF shown in Fig. 8.

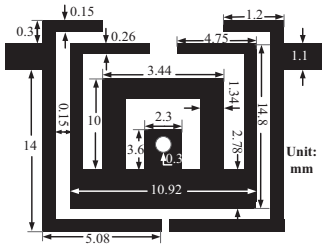

Fig. 8. Layout of the proposed filter.

The photograph of the fabricated filter is presented in Fig. 9 (a). The measurement is accomplished by using Agilent 8757D network analyzer. The simulated and measured frequency responses are compared in Fig. 9 (b). Dotted lines and solid lines indicate the simulated and measured results, respectively. The 3-dB passband of the proposed filter is from 1.8 to 3.3 GHz, and its passband return loss is larger than 15.6 dB. Five transmission poles are clearly observed at 1.99, 2.18, 2.55, 2.97, and 3.23 GHz in the passband of the filter, three of them are due to the triple-mode resonator, and the other two are yielded by the $\lambda/4$ coupled feedlines. Three transmission zeros are generated at 0.42, 4.28, and 4.64 GHz. The locations of the transmission zeros were affected in the stopband due to the dynamic range of measurement instruments. The minimum insertion loss in the stopband is greater than 20 dB. The simulated and measured maximum insertion losses in the passband are 0.06 and 0.55 dB, respectively. Measured results agree well with the simulated ones. The designed filter circuit occupies the overall size of about 30 mm × 15 mm.

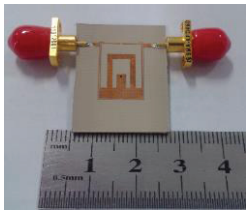

(a)

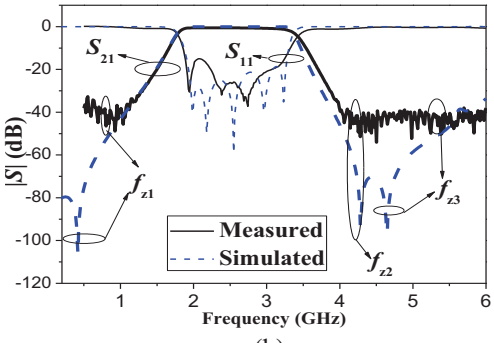

(b)

Fig. 9. (a) Photograph of the fabricated filter, and (b) measured and simulated response.

IV. CONCLUSIONS

In this paper, a BPF using triple-mode square ring short stub loaded stepped impedance resonator has been proposed and fabricated. With the analysis of even- and odd-mode resonances, the characteristics of the triple-mode resonator were investigated. When the triple-mode resonator is employed to implement a wideband BPF, the triple resonant frequencies along with the three attenuation poles close to the edges of the passband on either side, essentially give rise to a flat passband and a wide upper stopband response. The coupling matrix of proposed structure is established to further explain the proposed design. The measured results exhibit good agreement with the simulation, verifying the proposed structure and design methodology.

ACKNOWLEDGMENT

The work for this grant was supported in part by National Key Scientific Instrument and Equipment Development Projects (Grant No: 2013YQ200503), by National Natural Science Foundation of China (Grant No: 61271026), by the Program for New Century Excellent Talents in University (Grant No: NCET-11-0066).

REFERENCES

[1] K. Ma, K. S. Yeo, and Q. Sun, "A novel planar multimode bandpass filter with radial perturbation," *Microw. Opt. Technol. Lett*., vol. 51, pp. 964-966, 2009.

[2] I. Wolff, "Microstrip bandpass filter using degenerate modes of a microstrip ring resonator," *Electron. Lett*., vol. 8, pp. 302-303, 1972.

[3] J. S. Hong and M. J. Lancaster, "Bandpass characteristics of new dual-mode microstrip square loop resonators," *Electron. Lett*., vol. 31, pp. 891-892, 1995.

[4] R. J. Mao and X. H. Tang, "Novel dual-mode bandpass filters using hexagonal loop resonators," *IEEE Trans. Microw. Theory Tech*., vol. 54, pp. 3526-3533, 2006.

[5] B. T. Tan, S. T. Chew, M. S. Leong, and B. L. Ooi, "A modified microstrip circular patch resonator filter," *IEEE Microw. Wireless Compon. Lett*., vol. 12, pp. 252-254, 2002.

[6] M. Al-Sharkawy, A. Boutejdar, F. Alhefnawi, and O. Luxor, "Improvement of compactness of lowpass/bandpass filter using a new electromagnetic coupled crescent defected ground structure (DGS) resonators," *The Applied Computational Electromagnetics Society (ACES) Journal*, vol. 25, no. 9, Jul. 2010.

[7] J. S. Hong and S. Li, "Theory and experiment of dual-mode microstrip triangular patch resonators and filters," *IEEE Trans. Microw. Theory Tech*.,

vol. 52, pp. 1237-1243, 2004.

[8] J. S. Hong and H. Shaman, "Dual-mode microstrip open-loop resonators and filters," *IEEE Trans. Microw. Theory Tech*., vol. 55, pp. 2099-2109, 1996.

[9] L. Zhu and W. Menzel, "Compact microstrip bandpass filter with two transmission zeros using a stub-tapped half wavelength line resonator," *IEEE Microw. Wireless Compon. Lett*., vol. 13, pp. 16-18, 2003.

[10] L. Li, Z.-F. Li, and Q.-F. Wei, "A quasi-elliptic wideband bandpass filter using a novel multiple-mode resonator constructed by an asymmetric compact microstrip resonant cell," *Microw. Opt. Technol. Lett*., vol. 51, pp. 713-714, 2009.

[11] M. Makimoto and S. Yamashita, "Bandpass filters using parallel coupled stripline stepped impedance resonators," *IEEE Trans. Microw. Theory Tech*., vol. 28, pp. 1413-1417, 1980.

[12] D. Packiaraj, M. Ramesh, and A. T. Kalghatgi, "Design of a tri-section folded SIR filter," *IEEE Microw. Wireless Compon. Lett*., vol. 16, pp. 317-319, 2006.

[13] A. Eroglu and R. Smith, "Triple band bandpass filter design and implementation using SIRs," *26th Annual Review of Progress in Applied Computational Electromagnetics (ACES)*, pp. 862-865, Tampere, Finland, Apr. 2010.

[14] S. Amari, U. Rosenberg, and J. Bornemann, "Adaptive synthesis and design of resonator filters with source/load-multiresonator coupling," *IEEE Trans. Microw. Theory Tech*., vol. 50, pp. 1969-1978, 2002.

Dao Tong Li received the B.S. degree in Electronic Information Science and Technology from Binzhou University, Binzhou, China, in 2010. He is currently working toward the Ph.D. degree in the School of Electronic Engineering, University of Electronic Science and Technology of China (UESTC), Chengdu, China. His research interests include RF/microwave and mm-wave devices, circuits and systems.

Yong Hong Zhang received the B.S., M.S. and Ph.D. degrees from the University of Electronic Science and Technology of China (UESTC), Chengdu, China, in 1992, 1995, and 2001, respectively. He is currently a Full Professor in the School of Electronic Engineering, University of Electronic Science and Technology of China. His research interests are in the area of microwave and millimeter wave technology and applications.

Kai Da Xu received the B.S. and Ph.D. degrees in Electromagnetic Field and Microwave Technology from the University of Electronic Science and Technology of China (UESTC), Chengdu, China, in 2009 and 2015, respectively. He is now an Assistant Professor with the Institute of Electromagnetics and Acoustics, and Department of Electronic Science, Xiamen University, Xiamen, China. His research interests include RF/microwave and mm-wave circuits, antennas, and nanoscale memristors.

Kai Jun Song received the M.S. degree in Radio Physics and the Ph.D. degree in Electromagnetic Field and Microwave Technology from the University of Electronic Science and Technology of China (UESTC), Chengdu, China, in 2005 and 2007, respectively. Since 2007, he has been with the EHF Key Laboratory of Science, School of Electronic Engineering, UESTC, where he is currently a Full Professor. His current research fields include microwave and millimeter-wave/THz power-combining technology; UWB circuits and technologies; microwave/millimeter-wave devices, circuits and systems; and microwave remote sensing technologies.

Joshua Le-Wei Li received his Ph.D. degree in Electrical Engineering from Monash University, Melbourne, Australia, in 1992. In 2010, he was invited to join the School of Electronic Engineering at the University of Electronic Science and Technology of China (UESTC), Chengdu, China. His research interests include electromagnetic theory computational electromagnetics, radio wave propagation and scattering in various media, microwave propagation and scattering in tropical environment, and analysis and design of various antennas.

A Parallel Implementation for the Time-Domain Analysis of a Rectangular Reflector Antenna Using OpenMP

Ghada M. Sami [1, 3] and Khaled Ragab [2,3]

[1] Mathematics Department, College of Science
King Faisal University, Saudi Arabia
gsami@kfu.edu.sa

[2] College of Computer Sciences and Information Technology
King Faisal University, Saudi Arabia
kabdultawab@kfu.edu.sa

[3] Mathematics Department, Faculty of Science
Ain Shams University, Cairo, Egypt

Abstract ─ This paper presents and evaluates a parallel time domain analysis of a rectangular reflector on multicores machine. Rectangular reflector antennas have motivated the time-domain analysis of electromagnetic scattering problems. The asymptotic time domain physical-optics (TDPO) is applied to the analysis of a rectangular reflector illuminated by a Gaussian-impulse. It is a numerical technique used in computational electrodynamics. The effects of time-delayed mutual coupling between points on the surface will be ignored to avoid the numerical limitations found in other conventional time-domain techniques such as interpolation error, numerical dispersion error, etc. As a result, the scattered signals at the specular reflection point, at the edges, and at the corners can be clearly distinguished. Furthermore, this paper evaluates and compares the performance of the sequential time-domain analysis against the parallel time-domain analysis on multicores machine.

Index Terms ─ Electromagnetic scattering, parallel computing, rectangular reflector, time domain.

I. INTRODUCTION

Reflector antennas are intensively applied in the radars, communication, and guidance, etc. Nowadays, the problems of electromagnetic (EM) scattering have been widely applied in fields of remote sensing, target identification, radar detection, and so on. The interest in the transient analysis of EM phenomena has been growing in recent years. This is due to the advance of ultra-wide band (UWB) radars and their associated antennas, various antennas have been proposed for UWB application [1], with mobile radio channels by means of their response to pulsed excitation [2]. There are several methods that are used to analysis the EM scattering that will be explored in next section. They have inherent difficulties with numerical instability, interpolation errors, and need of extensive computer memory and CPU time to solve problems involving large scatterers. It is more efficient to deal with the transient analysis directly in the time domain. The time domain physical-optics (TDPO) [5-6] is an alternative method that requires relatively small amounts of computer memory and CPU time.

Consequently, this paper will focus on implementing the TDPO approximation method on parallel computer system. However, this section will discuss several computational electromagnetic (CEM) numerical methods either implemented in sequential or in parallel as follows.

Physical-optics (PO) approximation is one of these techniques. It has been widely used and considered as a good approximation of the far field electromagnetic scattering [16]. Starting from the Stratton-Chu integral equations, the PO expressions can be obtained for the PO scattered magnetic field in frequency domain [17]. The PO approximation is initially applied in the frequency-domain with the inverse Fourier transform [9] and [10]. Those equations are obtained directly from *Maxwell's equations* by applying *Green's theorem* in its vector form [17-18]. The PO requires integration over the illuminated surface of the scatterer. Due to the complex exponential term, the integrand of the PO integral is a very oscillatory function, especially at high frequencies. Therefore, it is very expensive to compute these kinds of integrals by simple numerical integration techniques such as Levin's integration method [19]. For large scatterer, the PO approximation is an efficient method in the frequency domain [7-8]. To accelerate the computing

Submitted On: February 8, 2015
Accepted On: June 6, 2015

of the PO, there are some researches that handle PO in parallel based shared memory [28] and distributed memory [29-30].

Moreover, there exist several analytical and numerical techniques for obtaining the response of scattering problems directly in the time domain, which is the most natural approach to be used, such as the finite-difference time-domain method (FDTD) [3, 11-13]. Recently, the FDTD method is being used to solve a wide variety of practical problems, because it can be competitive with the FEM in terms of versatility and solve time, even on a single PC or laptop computer loaded with a 2 GB memory. However, the main advantage of the FDTD becomes increasingly apparent when it is run either on multi-core processors or MPI protocol with low-cost high speed networks, because it can be parallelized more efficiently than FEM [21-25]. Several works [26-27] present a hybrid FDTD numerical algorithm which has been successfully developed and validated. They employ distributed and shared memory thorough of *MPI* and *OpenMP* [14].

II. THEORY AND FORMULATION

The TDPO integral is evaluated over the illuminated surface of the scatterer with a closed-form expression based on Gaussian-impulse. The formula of the TDPO is derived with the inverse Fourier transform. The scattered field of the TDPO is obtained as follows [20]:

$$\bar{e}^{TDPO}(\bar{r},t) = -\eta_o \iint_{S} \frac{1}{4\pi\left|\bar{r}-\bar{r}`\right|} \frac{\partial \bar{j}_{st}^{PO}(\bar{r}`,\tau(t,\bar{r}`))}{\partial\, t}\, ds`, \quad (1)$$

where $\bar{j}_{st}^{PO}$ is given as:

$$\bar{j}_{st}^{PO}(\bar{r}`,\tau(t,\bar{r}`)) = \bar{j}_{s}^{PO}(\bar{r}`,\tau(t,\bar{r}`)) - [(\bar{j}_{s}^{PO}(\bar{r}`,\tau(t,\bar{r}`)))\cdot\hat{r}]\cdot\hat{r}, \quad (2)$$

$$\bar{j}_{s}^{PO}(\bar{r}`,\tau(t,\bar{r}`)) = 2\,\hat{n}\times\bar{h}^{inc}(\bar{r}`,\tau(t,\bar{r}`)), \quad (3)$$

where the vector ***r`*** locates the integration point on the scatterer surface, ***r*** is the distance between the observing point *P* and the origin *O* as shown in Fig. 1, ***c*** is the velocity of the light and is $\eta_o$ the intrinsic free space impedance, $\bar{j}_{s}^{PO}(\bar{r}`,\tau(t,\bar{r}`))$ is the surface-current distribution in the time domain and $\bar{h}^{inc}(\bar{r}`,\tau(t,\bar{r}`))$ is the time-domain magnetic field incident on the surface.

The delay time of the propagation is given by:

$$\tau(t,\bar{r}`) = t - \frac{\left|\bar{r}-\bar{r}`\right|}{c}. \quad (4)$$

Based on Eq. (1), the surface-current density does not need to be solved. Consequently, minimum computer memory is required and no interpolation evaluation needs to be carried out because the incident fields are known for all positions and times. This benefit makes this approach suitable for limited computer-memory requirement (e.g., personal computer). Figure 1 shows the geometry of a rectangular reflector illuminated by an incident wave. We assume that incident wave is bandpass Gaussian-pulse transmit from x-polarized small dipole point source, which has the following form:

$$\bar{h}^{inc}(\bar{r}_k`,t) = \frac{B}{\sqrt{2\pi}\,\left|\bar{r}_k`\right|\,\sigma}\,\mathrm{Exp}[-((t-\frac{\left|\bar{r}_k`\right|}{c})/\sigma)^2]\,[2\,\mathrm{Cos}[\omega_o\,(t-\frac{\left|\bar{r}_k`\right|}{c})]]\,\mathrm{Sin}[\theta_x]\,\hat{\varphi}_x. \quad (5)$$

σ is the standard deviation of Gaussian envelope, *B* is the magnitude parameter of impulse, and ω_o is the angular frequency. From Eq. (5), we can form the time – domain representation ***v(t)***:

$$\boldsymbol{v(t)} = \mathrm{Exp}[-((t-\frac{\left|\bar{r}_k`\right|}{c})/\sigma)^2]\,[\,\mathrm{Cos}[\omega_o\,(t-\frac{\left|\bar{r}_k`\right|}{c})]], \quad (6)$$

as a real signal, we can write ***v(t)*** as:

$$\boldsymbol{v(t)} = \mathrm{Re}\,[\mathrm{Exp}[-((t-\frac{\left|\bar{r}_k`\right|}{c})/\sigma)^2]\,[\mathrm{Exp}[j\,\omega_o\,(t-\frac{\left|\bar{r}_k`\right|}{c})]]] = \mathrm{Re}[F\,(t)\,\mathrm{Exp}\,(j\,\omega_o\,t)], \quad (7)$$

where ***F(t)*** is analytic low pass input signal:

$$\boldsymbol{F(t)} = I - j\,Q,$$

where

$$I = \mathrm{Exp}[-((t-\frac{\left|\bar{r}_k`\right|}{c})/\sigma)^2]\,\mathrm{Cos}[\omega_o\,\frac{\left|\bar{r}_k`\right|}{c}],$$

and

$$Q = \mathrm{Exp}[-((t-\frac{\left|\bar{r}_k`\right|}{c})/\sigma)^2]\,\mathrm{Sin}[\omega_o\,\frac{\left|\bar{r}_k`\right|}{c}],$$

where ***I*** and ***Q*** are the *In-phase* and *Quadrate* parts. ***F(t)*** corresponds to the complex envelope of ***v(t)*** and is useful to know the intensity of the scattered wave in time domain.

The next step is show how such a bandpass system can be given an equivalent baseband representation at the center frequency, as:

$$U(t) = \frac{1}{2\pi\,T}\int_{t-\frac{T}{2}}^{t+\frac{T}{2}} u(\tau)\,\mathrm{Exp}[-j\,\omega_o\tau]\,d\tau. \quad (8)$$

The baseband output is the sum over each path, of the delayed replicas of the baseband input. When we get the U (t), it is possible to draw dB plot, as shown in Fig. 3 (b).

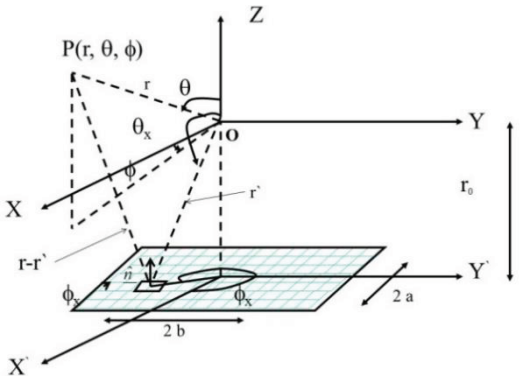

Fig. 1. Geometry of a rectangular reflector.

III. PARALLEL IMPLEMENTATIONS OF THE TDPO

In this paper, the *OpenMP* [14] programming interface was employed to parallelize the computations of the EM based on the TDPO method. It was developed on the multicore central processing unit (CPU) in multiple precisions arithmetic. *OpenMP* has been used to parallelize the code and memory-hierarchy-based optimization techniques to reduce the computer time of the code. Using these techniques, the computer time can be reduced in a factor close to the number of cores of the CPU [33]. While acceleration of the computational electromagnetic methods on graphics processing units (GPUs) has recently become a hot topic of investigations, multicore CPU still remains a source of significant computational power comparable to the GPU throughput for specific algorithms [15]. To the best of our knowledge, accurate computation of scattered field of the TDPO over rectangular reflector illuminated by a Gaussian-impulse for rectangular requires the multiple precision arithmetic, which has not been implemented as a library on GPUs yet. Therefore, it can be anticipated, that the proposed parallel CPU implementation will open the door to the implementation of the TDPO method on heterogeneous computing systems simultaneously deploying the computational power of multicore CPUs and GPUs for the tasks best suited for each.

In this paper, the authors implemented their computing solution on parallel using *OpenMP* as follows. It begins with a single thread of control, called the *master thread*, which exists for the duration of the program. The set of variables available to any particular thread is called the *thread's execution context*. During execution, the master thread may encounter parallel regions, at which the master thread will fork new threads, each with its own stack and execution context. At the end of the parallel region, the forked threads will terminate, and the master thread continues execution.

The master thread performs the following steps to compute scattered field of the TDPO:

- The geometry parameters of the rectangular reflector antennas are input to master thread. In addition, it initializes the constant values using Eq. (5) that calculates the incident wave $\bar{h}^{inc}(\bar{r}_k^{`},t)$.
- Calculate the scattered field of the TDPO equation $\bar{e}^{TDPO}(\bar{r},t)$ by transforming the integral in equation 1 into sum of scatter fields over *M x N* small rectangular reflectors. The master thread creates NTHREADS worker threads where each one calculates the sum over a small rectangle reflector.

The computing of the scattered field of the TDPO over rectangular reflector is obtained by Eq. 1. The rectangular reflector can be divided into *M x N* small rectangular reflectors as shown in Fig. 1, where $M=2a/0.1\lambda$, $N=2b/0.1\lambda$, and λ denotes the wavelength. Consequently, the integration in Eq. 1 can be expressed as the summation of scattered fields over these *M x N* small rectangular reflectors. Therefore, it is time-consuming calculations that are needed to be performed in parallel. At this time, the code has been parallelized by distributing the *M* vectors of rectangular reflectors into NTHREADS threads. Each thread calculates the sum of the scattered field over *N* rectangular reflectors. The total sum of all the scatter fields by *M x N* small rectangular reflectors constitutes the scattered field by the target as follows:

```
#pragma omp parallel shared () private () {
        #pragma omp for schedule (static)
  for (i=-M; i<=M; i++)
    for (j=-N; j<=N; j++)
        sum = sum + Compute_ScatteredField (i, j);
    }
```

The main problem that appears in using *OpenMP* is the order of the loops. If the directions of the observation points are used as outer loop, then each core can compute the scattered field created by all the rectangular in one direction, and at the end, it should store the result in a position of the output vector. But if the index of the rectangular reflector is used as the outer loop, then each core must compute the scatter field over this small rectangular and then use the reduction method to add all the results. Unfortunately, the reduction method is not well implemented for vectors in *OpenMP*, and each core must wait for the others to write their results.

IV. NUMERICAL RESULTS AND DISCUSSION

To explore the effectiveness of the used parallel technique, this paper implemented and carried out sequential and parallel experiments to examine the processing time needed to compute of the scattered field of the TDPO over rectangular reflector.

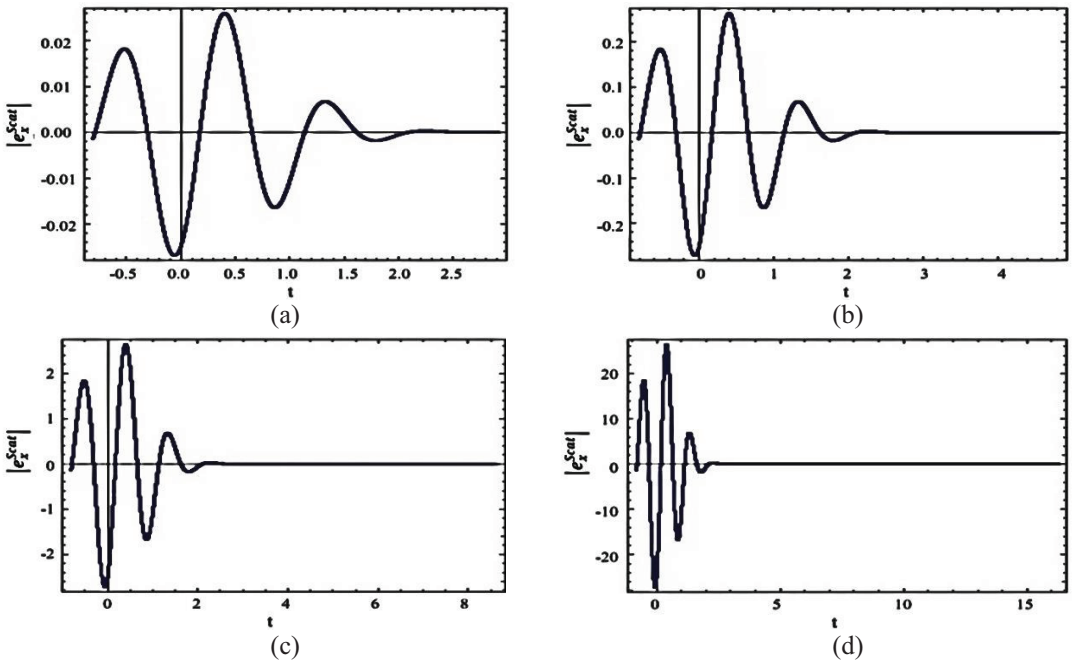

Fig. 2. (a-d). Scattered field rectangular reflector with Gaussian-impulse excitation TDPO with reflector diameters, *d*, *2 d*, *4 d* and *8 d*, respectively.

A. Setup

These computing algorithms were implemented by C++ programming language using *Microsoft Visual Studio Professional 2012* on a *HP* server (*ProLiant* ML350p Gen8) with two *Intel Xeon (R)* processors (*E5-2620 @ 2.00 GHz*), each processor has *6* cores and *32* GB RAM. The total number of physical cores is *12*. Hence, it is capable of running *12* threads simultaneously. The multicore CPU implementation was performed using the *OpenMP* programming model as in [14,31]. For the purpose of comparison, we have used *Mathematica* version 9.0.

B. Numerical results

Numerical results were obtained for a variety of configurations. As a target, we use a PEC rectangular plate as shown in Fig. 1, where λ is the wave length, σ is the standard deviation of Gaussian-impulse and $\tau = \frac{t - t_o}{\sigma}$ and $d = c\sigma$ is the reflector diameter.

Figure 2 (a)-(d) shows the numerical solution of the scattered field of the TDPO. The three scattering components shall be distinct, i.e., specular reflection at the center of rectangle, edge diffraction at the center of the edge, and corner diffraction at the corners were shown in Fig. 2 (a)-(d), respectively. In Fig. 2 (a)-(d), the reflectors diameters are *d, 2 d*, *4 d* and *8 d*, respectively. The scattered field TDPO increases as a result of increasing the reflectors diameter *d* by factors 2, 4, and 8. The results appear to be more accurate and stable faster than those obtained by frequency domain physical optics [20]. For greater reflector size, the time domain solution requires considerably more computing power consequently we implemented it in parallel. Figure 3 (a) shows that the observation point is very close to the reflector shadow boundary associated with upper diffraction point and Gaussian-impulse excitation with coordinates r = 100 m, $\theta = 65^o, \phi = 0^o$. Radiation pattern for Gaussian-impulse excitation, based in the peak response at the three scattering components is plotted in Fig. 3 (b). To compute the scattered field of the TDPO over rectangular reflector with diameter *10 d* the single-threaded code requires *177.422* seconds. While the multi-threaded code with *12* threads requires *19.73* seconds. The merits of the parallel computing are speedup S_l and efficiency E_l using *l* parallel threads that can be computed as follows [32]: $S_l = T_{sequential}/T_l$ and $E_l = T_{sequntial}/(l.\ T_l)$, where $T_{sequential}$ is the computing time in sequential, T_l is the computing time using *l* threads and $1 \leq S_l \leq l$. However, the computing overhead is determined as follows: $O(l) = T_l\,(1-E_l) = T_l - (T_{sequential}/l)$. This experiment shows that with *12* threads the computing is speedup by 8.99x and efficiency is 75%. Figure 4 (a) shows the plot that presents the speedup as a function of reflector diameters (*d, 2 d, 4 d, 6 d* and *8 d* respectively). Moreover, it verifies that *Mathematica* runs between 1.65 and 1.72 times slower than *OpenMP* C++ implementation. The multi-thread code achieves an excellent speedup when executed on multiple cores. Figure 4 (b) demonstrates the required computing time

according to different reflector diameters along with increasing the number of parallel threads. This figure shows that for small wavelength the effect of parallel has less significant, however it shows significant impact as the reflector; s diameter is increasing. Moreover, we extend our experiments to reflector diameter 25 *d* and then we are able to calculate the scatter field in sequential within *12* hours and *14* minutes however it take one hour and *35* minutes and *20* seconds with carrying out *12* threads per *12* cores. This experiment shows that with *12* threads the computing is speedup by 8.02x and efficiency around 65%.

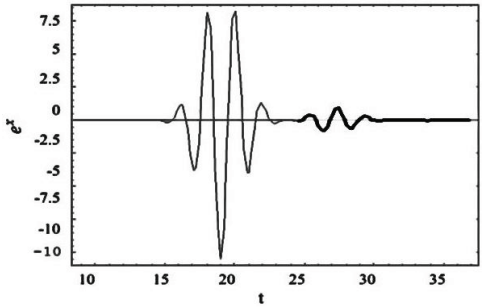

(a)

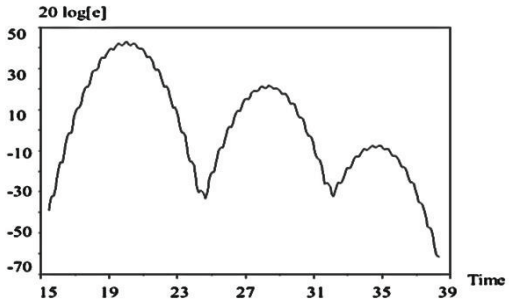

(b)

Fig. 3. (a) Scattered field of a rectangular reflector with Gaussian-impulse excitation at r = 100 m, $\theta = 65^o, \phi = 0^o$, and (b) radiation pattern for Gaussian-impulse excitation.

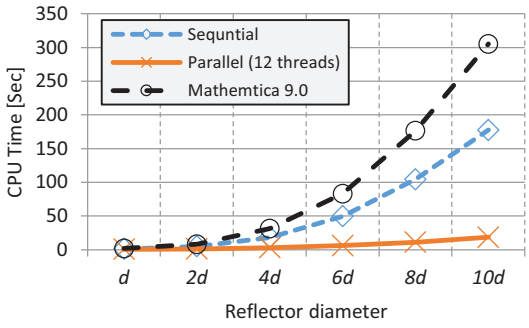

(a)

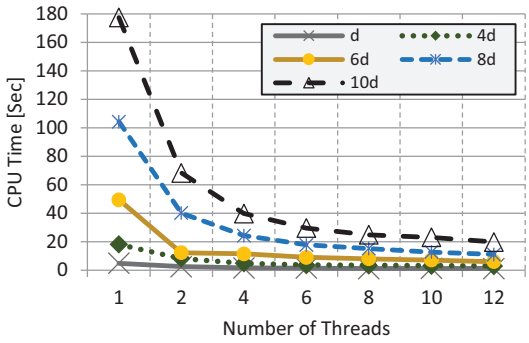

(b)

Fig. 4. Speeding up the computing of the scattered field of the TDPO over rectangular reflector.

IV. CONCLUSION

To determine the analysis of a rectangular reflector illuminated by a Gaussian-impulse considering the UWB radar application, this work extends the concept of the frequency-domain physical optics approximation to time-domain. The scattered field of the TDPO is obtained by performing the inverse Fourier transform over the frequency-domain scattered field that is obtained by calculating the integral over the illuminated surface using the free space *Green's* function.

The numerical results show the applicability of TDPO, as the scattered signals at the specular reflection point, edge diffraction and corner diffraction. Figure 2 (a)-(d) shows comparisons of the TDPO results based on a frequency domain physical optics. The frequency domain physical optics solution requires considerably more computer time and becomes inherently unstable. Moreover, the TDPO can reduce CPU time drastically. The parallel implementation of the TDPO is developed over multicores using *OpenMP*. The parallel performance of the parallel TDPO program is measured. Finally, the results show that the speed up ratio is approximately equal to *8.99x* with *12* threads.

REFERENCES

[1] C. E. Baum and E. G. Farr, *Impulse Radiating Antennas, Ultra-wideband Short-pulse Electro-magnetic*, book edited by H. Bertoni, et al., Plenum Press, 1993.

[2] W. Zhang, "A wind-band propagation model based on UTD for cellular mobile communication," *IEEE Transaction on Antennas and Propagation*, vol. 45, pp. 1669-1678, 1997.

[3] A. Tirkas and A. Balanis, "Finite-difference time-domain method for antenna radiation," *IEEE Trans. on Antenna and Propagation*, vol. 40, no. 3, 1992.

[4] P. R. Rosseau and P. U. Phatak, "Time-domain uniform geometrical theory of diffraction for a curved wedge," *IEEE Transactions on Antennas and Propagation*, vol. 43, pp. 1375-1382, Dec. 1995.

[5] G. Cassis Rego, et. al., "Time-domain analysis of a reflector antenna illuminated by a Gaussian pulse," *Journal of Microwave and Optoelectronic*, vol. 1, no. 4, 1999.

[6] L. Yang, D. Ge, and B. Wei, "FDTD/TDPO hybrid approach for analysis of the EM scattering of combinative objects," *Progress In Electromagnetics Research, PIER*, vol. 76, pp. 275-284, 2007.

[7] W. Rusch and P. Potter, *Analysis of Reflector Antenna*, New York: Academic, pp. 46-49, 1970.

[8] R. F. Harrington, *Time-Harmonic Electro-magnetic Fields*, New York: McGraw-Hill, pp. 127, 1961.

[9] E. Kennaugh and R. Cosgriff, "The use of impulse response in electromagnetic scattering problems," *IRE Natl. Conv. Rec*., pt. 1, pp. 72-77, 1958.

[10] E. Kennaugh and D. Moffatt, "Transient and impulse response approximation, *Proc. IEEE*, pp. 893-901, 1965.

[11] K. Vee, "Numerical solution of initial boundary value problems involving Maxwell's equations in isotropic media," *IEEE Transactions on Antennas and Propagation*, vol. 14, no. 5, pp. 302-307, 1966.

[12] A. Taflove and S. Hagness, *Computational Electromagnetics: The Finite-Difference Time Domain Method*, 3rd ed., Artech House, Norwood, MA, 2005.

[13] W. Yu, Raj Mittra, Tao Su, Yongjun Liu, and Xiaoling Yang, *Parallel Finite Difference Time Domain Method*, Artech House, Norwood, MA, 2006.

[14] OpenMP Architecture Review Board, OpenMP application Program Interface (ver. 3.1), 2011.

[15] V. W. Lee, et al., "Debunking the 100X GPU vs. CPU myth: an evaluation of throughput computing on CPU and GPU," *Proc. 37th Annu. Int. Symp. Comput. Archit*., pp. 451-460, 2010.

[16] J. S. Asvestas, "The physical optics method in electromagnetic scattering," *Journal of Math. Phys.*, vol. 21, no. 2, pp. 290-299, 1980.

[17] J. A. Stratton, *Electromagnetic Theory*, McGraw-Hill, 1941.

[18] R. Mittra, *Computer Techniques of Electro-magnetics*, Pergamon Press, 1973.

[19] A. Durgun and M. Kuzuoglu, "Computation of physical optics integral by LEVIN'S integration algorithm," *Progress In Electromagnetics Research M*, vol. 6, pp. 59-74, 2009.

[20] E.-Y. Sun and W. V. T. Rusch, "Time-domain physical-optics, " *IEEE Transactions on Antennas and Propagation*, vol. 42, no. 1, pp. 9-15, 1994.

[21] A. Taflove and S. Hagness, *Computational Electromagnetics: The Finite-Difference Time Domain Method*, 3rd ed., Artech House, Norwood, MA, 2005.

[22] W. Yu, R. Mittra, T. Su, Y. Liu, and X. Yang, *Parallel Finite Difference Time Domain Method*, Artech House, Norwood, MA, 2006.

[23] W. Yu, X. Yang, Y. Liu, L.-C. Ma, T. Su, N. Huang, and R. Mittra, "New direction in computational electromagnetics solving large problems using the parallel FDTD on the BlueGene/L supercomputer yielding teraflop-level performance," *IEEE Antennas and Propagation Magazine*, vol. 50, no. 23, pp. 20-42, 2008.

[24] W. Yu, R. Mittra, X. Yang, and Y. Liu, "Performance analysis of parallel FDTD algorithm on different hardware platforms," *IEEE Antennas and Propagation Society Int. Symposium*, pp. 1-4, 2009.

[25] T. P. Stefański, "Fast implementation of FDTD-compatible Green's function on multicore processor," *IEEE Antennas and Wireless Propagation Letters*, vol. 11, pp. 81-82, 2012.

[26] L. Adhianto and B. Chapman, "Performance modeling of communication and computation in hybrid MPI and OpenMP applications," *IEEE 12th Int. Conf. on Parallel and Distributed Systems (ICPADS'06)*, 2006.

[27] R. Rosenberg, et. al., "Modeling pulse propagation and scattering in a dispersive medium: performance of MPI/OpenMP hybrid code," *IEEE Conference (SC'06)*, 2006.

[28] M. Arias-Acuña, et. al., "Fast far field computation of single and dual reflector antennas," *Journal of Engineering*, *Hindawi Publishing*, vol. (2013), pp. 1-11, 2013.

[29] W. A. Imbriale and T. Cwik, "A simple physical optics algorithm perfect for parallel computing architecture," In *10th Annual Review of Progress in Appl. Comp. Electromagnetic*, pp. 434-441, 1994.

[30] C. Parrot, et. al., "A distributed memory multilevel fast physical optics algorithm," *The 3rd European Conf. on Antennas and Propagation*, 2009.

[31] P. Pacheco, *An Introduction to Parallel Programming*, Morgan Kaufmann, 1st ed., 2011.

[32] C. P. Kruskal, et. al., "A complexity theory of efficient parallel algorithms," *Automata, Languages and Programming Lecture Notes in Computer Science*, vol. 317, pp. 333-346, 1988.

[33] M. D. Hill and M. R. Marty, "Amdahl's law in the

multicore era," *IEEE Computer*, Jul. 2008.

G. Sami is an Assistant Professor at the Department of Mathematics and Statistics, College of Sciences, King Faisal University, Saudi Arabia. Moreover, she is on Leave Assistant Professor at Department of Mathematic, Ain Shams University, Cairo, Egypt. She received her B.Sc., M.Sc., Ph.D. degrees in Applied Mathematics from Ain Shams University, Cairo, Egypt in 1991, 1996 and 2001 respectively. She acted as a Visiting Researcher at Tokyo Institute of Technology in 2003. Her research interests include electromagnetic fields, time-domain physical optics, scattering, etc.

K. Ragab is an Associate Professor at the Department of Computer Science, College of Computer and Information Technology, King Faisal University, Saudi Arabia. Moreover, he is on Leave Assistant Professor of Computer Science at Department of Mathematic, Computer Science Division, Ain Shams University. He joined the Department of Computer Science, Tokyo University in 2005 as Postdoctoral position. He was born in 1968 and received his B.Sc. and M.Sc. degrees in Computer Science from Ain Shams University, Cairo, Egypt in 1990, 1999, respectively, and Ph.D. degree in Computer Science from Tokyo Institute of Technology in 2004. He has worked in Ain Shams University, Cairo Egypt in 1990-1999 as Assistant Lecturer. He has worked as Research Scientist in the Computer Science Dept., Technical University of Chemnitz, Germany in 1999-2001. His research interests include parallel and distributed computing, Image processing, Peer-to-Peer Systems, and Overlay Networks.

A New Design of Cell Phone Body for the SAR Reduction in the Human Head

M. I. Hossain [1], M. R. I. Faruque [1*], and M. T. Islam [2]

[1] Space Science Center (ANGKASA)
[2] Department of Electrical, Electronic and Systems Engineering
Universiti Kebangsaan Malaysia, 43600- Bangi, Selangor, Malaysia
ipk_eee@yahoo.com, rashedgen@yahoo.com, tariqul@ukm.edu.my

Abstract ─ In this paper, a new design of cell phone body is presented to reduce the specific absorption rate (SAR) in the human head. The SAR in the human head and total absorbed power by the cell phone user are calculated along with antenna performances in terms of radiation efficiency and directivity to validate the effects of cell phone body. It is found that the SAR in the head is reduced significantly for both the lower and upper global systems for mobile (GSM) frequency band. The new mobile body provides 63.8% reduction in the SAR at 900 MHz and 69.2% reduction at 1800 MHz in comparison of without mobile cover configuration. Moreover, the mobile casing improves the radiation efficiency 6% and 7% in the lower and the upper GSM frequency band respectively.

Index Terms ─ Antenna, FDTD method, human hand model, human head model, mobile body, SAR.

I. INTRODUCTION

The health hazard of emitted electromagnetic (EM) radiation from the cellular phone has become a point of open deliberation as the use of mobile handset is increasing exponentially. For the protection of the human body from EM exposure, international authoritative bodies have defined exposure guidelines [1, 2]. The EM energy absorbed by human body tissues can be evaluated by the specific absorption rate (SAR) [3]. The safety limit of SAR averaging 1 g of tissues (SAR1g) is set to 1.6 W/Kg by Federal Communication Commission (FCC) [4] and 2 W/Kg for 10 g of tissues by IEEE [5]. Therefore, the reduction of the SAR is an essential issue for the cell phones and many researchers are working on this aspect. The simplest and easiest method for SAR reduction is to increase the spacing between human head and cell phone antenna because the SAR values are inversely proportional to this distance [6]. In addition, conducting material closed to the human body processes significant effects on the SAR values, which highly depends on the position and size of conducting material [7,8]. In [9], a conducting material was used as a protection attachment between the handset antenna and the human head. Moreover, radio frequency (RF) shielding using ferrite sheet has proved to be an attractive way of reducing the SAR in the human head [10]. In [11], a ferrite loaded short mono-pole antenna was proposed to reduce the SAR. Numerical results showed that the proposed arrangement can enhance antenna performance and reduce the SAR in the head for the frequency 1800 MHz and higher. On the other hand, a ferrite sheet with PIFA antenna was investigated in [12]. The considerable amount of SAR reduction was observed at 900 MHz.

The SAR values can also be reduced by using artificial magnetic conductor (AMC), electromagnetic band gap (EBG) and photonic band gap (PBG) surfaces. In [13], two patch EBG structure was used in the ground plane of the antenna. The results revealed the reduction in total dispersed power and SAR toward the head. In [14], a study on the effects of EBG structure on the SAR and the radiation characteristics of dipole antenna has been presented. The outcomes indicated that EBG structure can improve the radiation efficiency and reduce the SAR at 3.5 GHz. Recently, metamaterials have been proposed for the SAR reduction of cell phone as they process extraordinary physical properties. The metamaterials are artificially constructed structure having negative permittivity, negative permeability or both simultaneously [15]. In [16], the designed square split ring resonator (SSRR) using metamaterial was used to degrade the SAR values. This investigation has achieved the SAR reduction at 900 MHz. In [17], the proposed metamaterial provided the moderate amount of reduction in SAR values for dual GSM frequency bands.

However, the cell phone casing processes significant effects on the SAR values. In [8], a study of materials to reduce the SAR values has been presented. The numerical results showed that the cell phone case box made of materials with higher conductivity produces higher pick SAR in the human head. In this paper, a new design of mobile casing for PIFA antenna is used for the reduction of EM absorption for both GSM lower and upper frequency bands at 900 MHz and at 1800 MHz respectively. The antenna performances are also

Submitted On: May 19, 2014
Accepted On: May 25, 2015

evaluated to clarify the effectiveness of the new cell phone body.

II. MODELS AND METHODS

In this investigation, the study of SAR reduction using cell phone body was conducted by the finite-difference time-domain (FDTD) method to lossy Drude model [18-19]. The major simulation tool used in this study, was Computer Simulation Technology Microwave Studio (CST MWS) based on the FDTD method [20]. A dual band PIFA was used in experimental set-up. The antenna elements were made of PEC comprising patches, ground plane, feed, and shorting wall. Additionally, FR-4 circuit board and electrical circuits were used along with antenna to take effect on the real cell phone. The dimensions of the circuit board are 80 mm × 40 mm × 1.6 mm. Figure 1 and 2 shows the return loss characteristics and the geometry of the antenna with circuit board respectively. A body of the mobile phone was modeled using two different materials. The body of the mobile phone was modeled using plastic with dimensions 82 mm × 42 mm × 10 mm. The thickness of plastic sheet is 0.5 mm with 2.9 relative permittivity. The LCD, dimensions 60 mm × 38 mm × 2.2 mm, of the cell phone was considered as a part of handset body. An additional double-layer sheet of thickness 2 mm was placed below the LCD monitor which contributed to reduce the SAR values considerably. The additional sheet consists of silicon (1 mm) and PEC (1 mm). The permittivity and tangent loss of silicon sheet are 11.9 and 0.00025 respectively. Figure 3 (a) indicates the cell phone model with proposed body structure. The dimensions and properties of handset components were set to comply with industry standard. The specific anthropomorphic mannequin (SAM) phantom was used as a head model which consists of SAM shell and SAM liquid. A hand model was also utilized in this study. The dielectric properties of head and hand model have been listed in Table 1. Figure 3 (b) represents the simulation setup of handset model with head and hand phantom. In this lossy-Drude simulation model, domain was 128 × 128 × 128 cells with cell sizes $dx = dy = dx = 3$ mm. The evaluation of SAR is defined as SAR = $\sigma E^2/2\rho$, where σ, ρ and E represent the conductivity of the tissue, the density of the tissue and induced electric field strength in the human head respectively. The peak SAR values were averaged over 1 g of tissue.

Table 1: Properties of head and hand models

Materials	Relative Permittivity, ε_r		Conductivity, σ (S/m)	
	900 MHz	1800 MHz	900 MHz	1800 MHz
SAM shell	3.7	3.5	0.0016	0.0016
SAM liquid	40.5	40	0.97	1.42
Hand	36.2	32.6	0.79	1.26

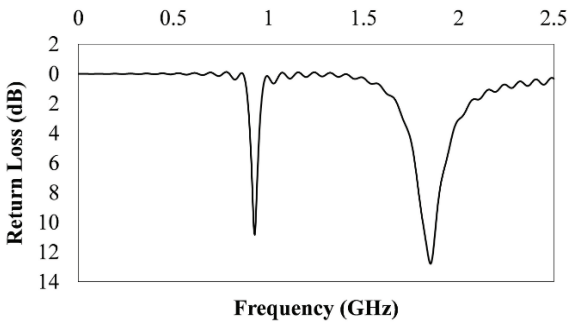

Fig. 1. Return loss characteristics of the PIFA.

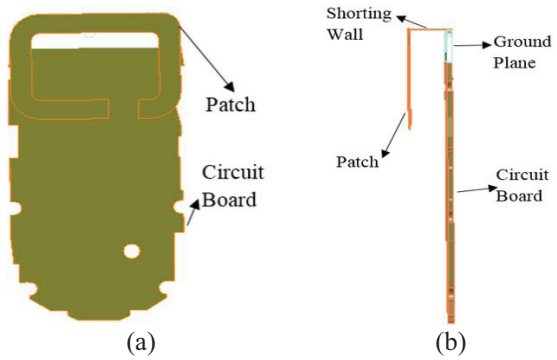

Fig. 2. PIFA with circuit board: (a) front view, and (b) side view.

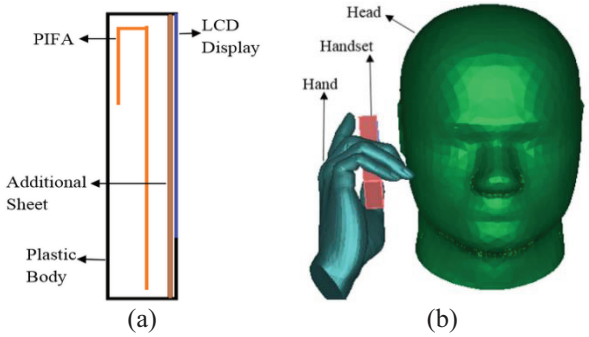

Fig. 3. (a) Handset model, and (b) head and hand model in talk position.

III. RESULTS AND DISCUSSIONS

In this paper, a mobile body with an additional sheet has been proposed to reduce the peak SAR in the human head. The additional sheet was double layer. Additionally, single layer sheets of aluminum, silicon and PEC with mobile casing was also investigated. The investigation results may be classified into three broad categories:

A. Without additional sheet configurations;
B. Single-layer additional sheet configurations;
C. Double-layer additional sheet configuration.

A. Without additional sheet configurations

In this section, plastic mobile casing without additional sheet is used. Figure 4 represents the values of SAR and total absorbed power off with and without cell phone body configurations. The body is made of plastic materials with 1 mm thickness. The plastic cell phone body leads to reduce the SAR 57.9% at the lower frequency band and increase the SAR 3.6% at the upper frequency band as compared to without casing configuration. Moreover, the total absorbed power is reduced 53.7% at 900 MHz and increased 4.6% at 1800 MHz due to the plastic body. It is clear from the obtained results that the plastic body affects the EM absorption greatly at the lower frequency band and slightly at the upper frequency band.

However, this plastic body can reduce the SAR at the lower frequency band considerably, but increases the SAR at the upper frequency band. Moreover, the plastic cell phone body increases radiation efficiency 12% at 900 MHz and decreases 1% at 1800 MHz as indicated in Fig. 5. The directivity of antenna is not affected greatly due to the plastic body for both frequency bands.

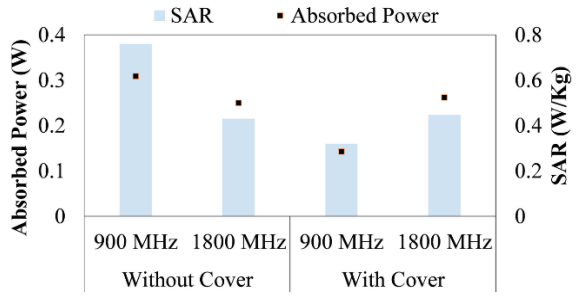

Fig. 4. SAR values and absorbed powers considering with and without phone body.

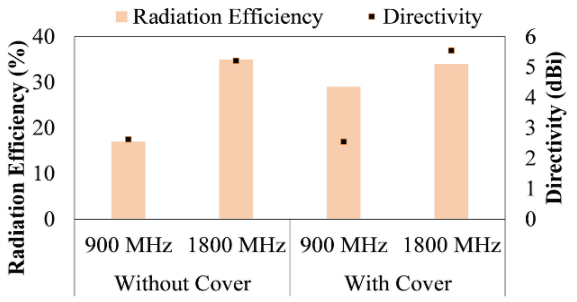

Fig. 5. Radiation efficiency and directivity considering with and without phone body.

B. Single-layer additional sheet configurations

A single layer of silicon sheet was used as an additional sheet with plastic mobile body. The SAR values and absorbed power are plotted in Fig. 6. The results indicate that the mobile body with 1 mm additional silicon sheet provides 68.4% SAR reduction at 900 MHz and 2.4% SAR at 1800 MHz as compared to without casing configuration. Sequentially, 1 mm additional aluminum sheet lead to 68.3% SAR reduction at the lower frequency band and 4.22% increment at the upper frequency band as shown in Fig. 7. The PEC sheet of 1 mm reduces the SAR 59.2% at 900 MHz and 66.1% at 1800 MHz (as indicated in Fig. 8). The reduction in total absorbed power is 68.3%, 67.96% and 58.9% for 1 mm silicon, aluminum and PEC additional sheet respectively in the lower frequency band. At the upper frequency band, 3.85%, 3.85% and 14.4% increment in total power absorption are observed after using additional silicon, aluminum and PEC sheet respectively. The additional sheet (silicon, aluminum and PEC) thickness of 2 mm provides a further little bit lower the SAR values and total adsorbed powers. The PEC sheet can reduce the peak SAR sufficiently rather than total absorbed power.

At 900 MHz, mobile cover with silicon and aluminum additional sheet of thickness 1 mm improve the radiation efficiency 11% (as shown in Figs. 9 and 10) and PEC leads to increase 6.5% (as indicated in Fig. 11) compared to without casing configuration. On the other hand, 1 mm silicon and aluminum sheet provide 1% degradation of radiation efficiency and 1 mm PEC leads to degrade 3% at the upper frequency band. The results of antenna directivity do not change considerably after using a mobile body with additional sheet.

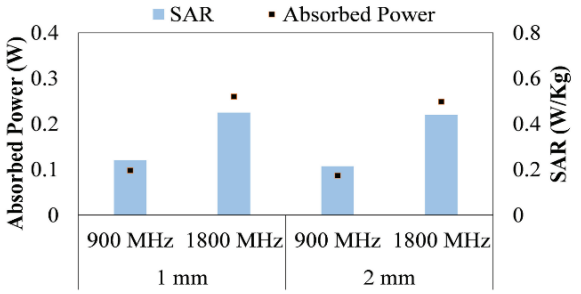

Fig. 6. SAR value and absorbed power for plastic mobile body with additional silicon sheet.

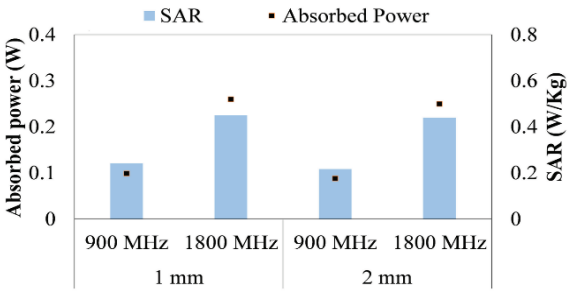

Fig. 7. SAR values and absorbed powers for plastic phone body with additional aluminum sheet.

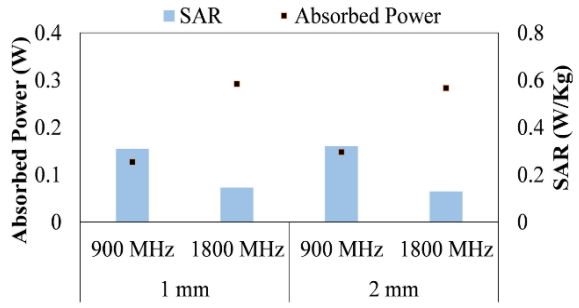

Fig. 8. SAR values and absorbed powers plastic phone body with additional PEC sheet.

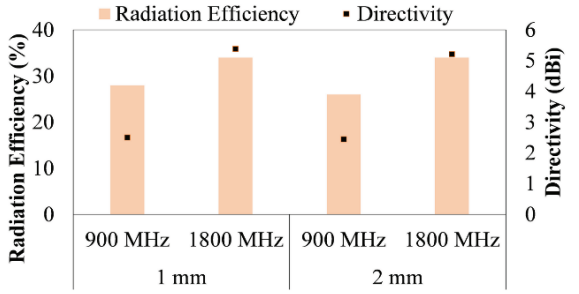

Fig. 9. Radiation efficiency and directivity of plastic cell phone body with additional silicon sheet.

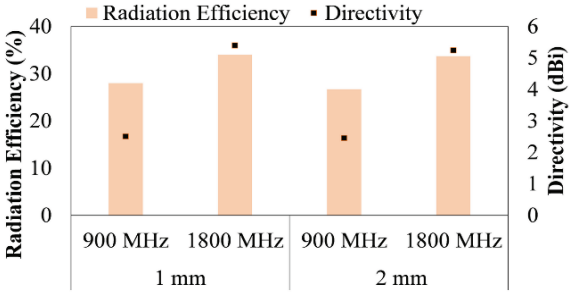

Fig. 10. Radiation efficiency and directivity considering plastic body with additional aluminum sheet.

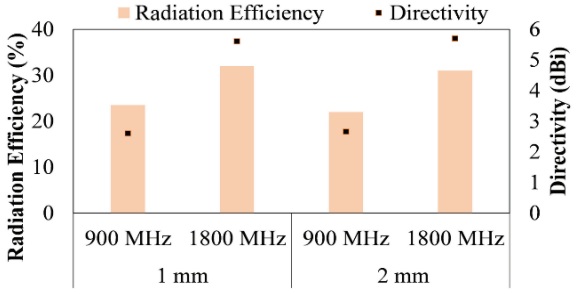

Fig. 11. Radiation efficiency and directivity for plastic phone body with additional PEC sheet.

C. Double-layer additional sheet configuration

From the results of single layer additional sheet, it is clear that the cell phone body with silicon and aluminum additional sheet decreases the SAR at the lower frequency band significantly and PEC sheet degrades the SAR highly at the upper frequency band. The body with silicon-PEC double-layer additional sheet can affect both frequency bands. Figure 12 shows the SAR values and absorbed powers in case of mobile body with double-layer and without casing configuration.

The 3D distribution of the SAR values is shown in Table 2. Comprising with without body configuration, the proposed cell phone casing with double-layer sheet can reduce the SAR 63.8% and 69.2% at 900 MHz and 1800 MHz respectively. Similarly, 45% and 14% reduction in total absorbed power can be achieved at the lower and upper frequency band respectively, due to the cell phone casing with double-layer additional sheet. Moreover, the proposed cell phone body leads to improve radiation efficiency 6% at 900 MHz and 7% at 1800 MHz (as shown in Fig. 13). Figure 14 represents the curves theta versus directivity with constant phi (φ=90). The antenna directivity is not affected significantly for both frequency bands.

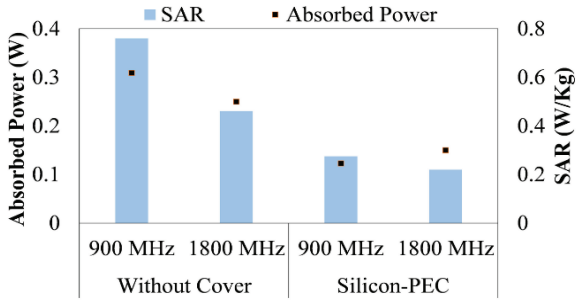

Fig. 12. SAR values and absorbed powers in case of plastic mobile body with additional silicon-PEC double-layer sheet.

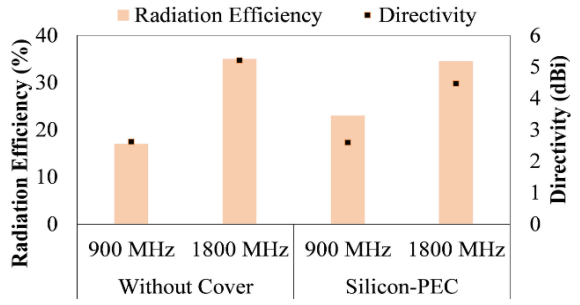

Fig. 13. Radiation efficiency and directivity for plastic phone body with additional silicon-PEC double-layer sheet.

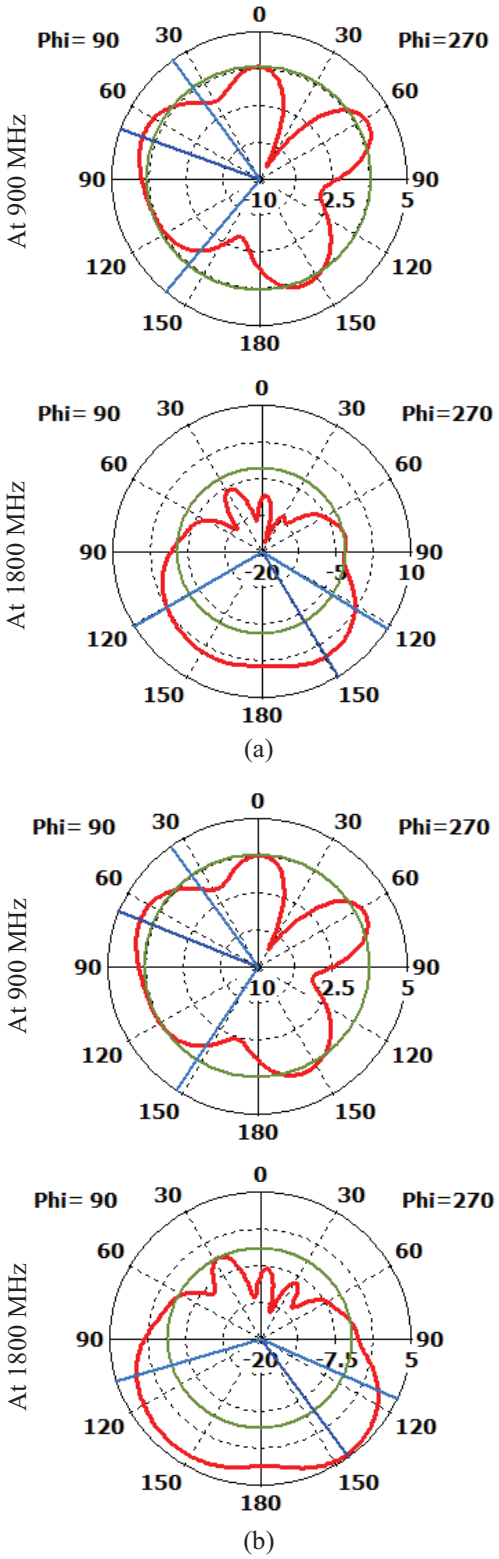

Fig. 14. Theta (degree) vs. directivity (dBi) curves xz-plane for: (a) without casing, and (b) new body configurations.

Table 2: 3D distribution of SAR values of without body and body with silicon-PEC double-layer sheet

	At 900 MHz	Scale	At 1800 MHz
Without casing	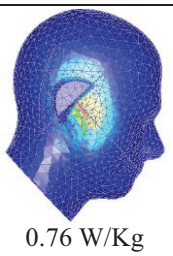 0.76 W/Kg	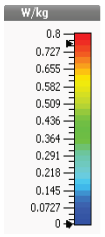	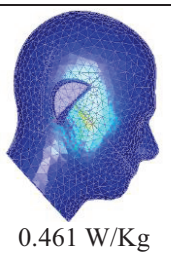 0.461 W/Kg
Casing with silicon-PEC sheet	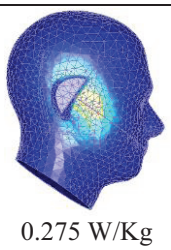 0.275 W/Kg	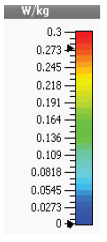	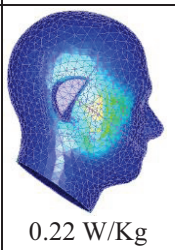 0.22 W/Kg

IV. CONCLUSION

In this paper, a new design of cell phone body has been proposed for the reduction of EM absorption in the human head. The mobile body consists of plastic and a double-layer silicon-PEC additional sheet. The numerical results show that the proposed casing provides significant reduction of EM absorption towards the human head as well as improve radiation efficiency for both lower and upper GSM frequency bands. The silicon layer of additional sheet provides SAR reduction, particularly for the lower frequency band and PEC layer for the upper frequency band. Although the proposed design increases the cell phone thickness about 10%, it reduces the SAR 63.8% and 69.2% for the lower and upper frequency band of PIFA respectively. In case of total absorbed power by the user, 45% and 14% reduction are achieved. Moreover, the presented cell phone body improves the radiation efficiency 6% and 7% at 900 MHz and 1800 MHz respectively. It can be concluded that the proposed cell phone casing may process significant role to protect cell phone user from health risk of EM radiation.

REFERENCES

[1] I. Guideline, "Guidelines for limiting exposure to time-varying electric, magnetic, and electromagnetic fields (up to 300 GHz)," *Health Phys.*, vol. 74, pp. 494-522, 1998.

[2] M. I. Hossain, M. R. I. Faruque, M. T. Islam, and N. H. M. Hanafi, "Application of auxiliary antenna elements for SAR reduction in the human head," *Advanced Materials Research*, vol. 974, pp. 288-292, 2014.

[3] M. R. I. Faruque, N. A. Husni, M. I. Hossain, M. T. Islam, and N. Misran, "Effects of mobile phone radiation onto human head with variation of holding cheek and tilt positions," *Journal of Applied Research and Technology*, vol. 12, no. 5, pp. 871-876, 2014.

[4] Federal Communications Commission, Evaluating Compliance with FCC Guidelines for Human Exposure to Radiofrequency Electromagnetic Field, 2001.

[5] IEEE Standard for Safety Levels with Respect to Human Exposure to Radio Frequency Electromagnetic Fields, 3 kHz to 300 GHz - Amendment 1: Specifies ceiling limits for induced and contact current, clarifies distinctions between localized exposure and spatial peak power density, IEEE Std. C95.1a-2010 (Amendment to IEEE Std. C95.1-2005), pp. C1-9, 2010.

[6] O. Kivekas, J. Ollikainen, T. Lehtiniemi, and P. Vainikainen, "Bandwidth, SAR, and efficiency of internal mobile phone antennas," *Electromagnetic Compatibility, IEEE Transactions on*, vol. 46, pp. 71-86, 2004.

[7] K. Yanase and A. Hirata, "Effective resistance of grounded humans for whole-body averaged SAR estimation at resonance frequencies," *Progress In Electromagnetics Research B*, vol. 35, 2011.

[8] H. Y. Chen and W. Y. Chiou, "Material studies on cellular phones for reducing SAR in a human head model," in *Antennas and Propagation Society International Symposium, 2002. IEEE*, pp. 448-451, 2002.

[9] K. Chan, K. Chow, L. Fung, and S. Leung, "Effects of using conductive materials for SAR reduction in mobile phones," *Microwave and Optical Technology Letters*, vol. 44, pp. 140-144, 2005.

[10] J. Pretorius, "Design and manufacture of a ferrimagnetic wave absorber for cellular phone radiations," in *Electron. Devices for Microwave and Optoelectronic Applications, 2004 EDMO 2004, 12th International Symposium on*, pp. 119-123, 2004.

[11] M. I. Kitra, C. J. Panagamuwa, P. McEvoy, J. Vardaxoglou, and J. R. James, "Low SAR ferrite handset antenna design," *Antennas and Propagation, IEEE Transactions on*, vol. 55, pp. 1155-1164, 2007.

[12] M. T. Islam, M. R. I. Faruque, and N. Misran, "Design analysis of ferrite sheet attachment for SAR reduction in human head," *Progress In Electromagnetics Research*, vol. 98, pp. 191-205, 2009.

[13] S. il Kwak, D. U. Sim, J. H. Kwon, and H. Do Choi, "Comparison of the SAR in the human head using the EBG structures applied to a mobile handset," in *Microwave Conference, 2007, European*, pp. 937-940, 2007.

[14] R. Ikeuchi, K. H. Chan, and A. Hirata, "SAR and radiation characteristics of a dipole antenna above different finite EBG substrates in the presence of a realistic head model in the 3.5 GHz band," *Progress In Electromagnetics Research B*, vol. 44, pp. 53-70, 2012.

[15] M. I. Hossain, M. R. I. Faruque, M. T. Islam, and M. H. Ullah, "A new wide-band double-negative metamaterial for C- and S-band applications," *Materials*, vol. 8, no. 1, pp. 57-71, 2014.

[16] M. R. I. Faruque, M. Islam, and M. Ali, "A new design of metamaterials for SAR reduction," *Measurement Science Review*, vol. 13, pp. 70-74, 2013.

[17] G. F. Pedersen and J. B. Andersen, "Integrated antennas for hand-held telephones with low absorption," in *Vehicular Technology Conference, 1994 IEEE 44th*, pp. 1537-1541, 1994.

[18] J.-N. Hwang and F.-C. Chen, "Reduction of the peak SAR in the human head with metamaterials," *Antennas and Propagation, IEEE Transactions on*, vol. 54, pp. 3763-3770, 2006.

[19] C. H. Li, E. Ofli, N. Chavannes, and N. Kuster, "Effects of hand phantom on mobile phone antenna performance," *Antennas and Propagation, IEEE Transactions on*, vol. 57, pp. 2763-2770, 2009.

[20] CST Microwave Studio, 3D EM Simulation Software [Online], available: https://www.cst.com/Products/CSTMWS.[Accessed:01-Nov-2014].

MD Ikbal Hossain was born in Naogaon, Bangladesh, in 1986. He received the B.Sc.Eng. (Hons) of Electrical and Electronic Engineering from the Rajshahi University of Engineering and Technology (RUET), Bangladesh in 2010. From October 2010 to October 2013, he worked as a Lecturer at International Islamic University Chittagong, Chittagong, Bangladesh. Currently pursuing his second degree at the Universiti Kebangsaan Malaysia (UKM), Malaysia. His recent research has focused on communication engineering, which scrutinizes in analyzing the electromagnetic wave absorption towards human.

Mohammad Rashed Iqbal Faruque was born in Chittagong, Bangladesh in 1974. He received the B.Sc. and M.Sc. degrees in Physics from the University of Chittagong, Chittagong, Bangladesh in 1998 and 1999, respectively, and a Ph.D. degree in Telecommunication Engineering from the Universiti Kebangsaan Malaysia (UKM) in 2012. From July 2000 to until 2007, he worked as a Lecturer at Chittagong University of Engineering and Technology (CUET), Chittagong, From June 2007 to November 2008, he was an Assistant Professor at the University of Information Technology and Sciences (UITS), Chittagong. He has authored or co-authored approximately 6 book chapters, 90 referred journals and 40 conference papers. He is currently a Senior Lecturer of Space Science Centre (ANGKASA), UKM, Malaysia. His research interests include the RF, electromagnetic field and propagation, FDTD analysis, electromagnetic radiation, metamaterials applications and electromagnetic compatibility.

Mohammad Tariqul Islam is a Professor at the Institute of Space Science of the Universiti Kebangsaan Malaysia (UKM). He is also the Group Leader of Radio Astronomy Informatics Group at UKM. Prior to joining UKM, he was a Lecturer in Multimedia University, Malaysia. He is a Senior Member of the IEEE. He is serving as the Editor-in-Chief of the International Journal of Electronics & Informatics (*IJEI*). He has been very promising as a Researcher, with the achievement of several International Gold Medal awards, a Best Invention in Telecommunication Award and a Special Award from Vietnam for his research and innovation. He has been awarded "Best Researcher Award" in 2010 and 2011 at UKM. His professorial interests include the areas of communication antenna design, radio astronomy antennas, satellite antennas, and electromagnetic radiation analysis. He has published over 200 journal papers and a few book chapters on various topics related to antennas, microwaves and electromagnetic radiation analysis. He also has filed 6 patent applications on communication antennas. Thus far, his publications have been cited 1748 times, and the H-index is 25 (Source: Scopus). He is now handling many research projects from the Ministry of Science, Technology and Innovation (MOSTI), Ministry of Higher Education Malaysia (MOHE) and some International research grants from Japan.

A New Multifractal Geometry for Design of Frequency Selective Surfaces with Dual Band Response

Erico C. Braz [1] and Antonio L. P. S. Campos [2]

[1] Academic Department
Federal Institute of Education, Science and Technology of Rio Grande do Norte (IFRN)
Campus Natal – Zona Norte, Rua Brusque, 2926, Conjunto Santa Catarina, Potengi, Natal-RN, CEP: 59112-490
erico.braz@ifrn.edu.br

[2] Department of Communication Engineering
Federal University of Rio Grande do Norte (UFRN)
Av. Senador Salgado Filho, 3000, Natal, RN, Brazil, CEP: 59072-970
antonio.luiz@pq.cnpq.br

Abstract ─ In this paper, we proposed a new multifractal geometry for design of frequency selective surfaces (FSS) with dual band response. The proposed new geometry is called Ericampos. The main advantage of the proposed geometry is to design dual band FSS and makes it flexible in terms of controlling resonance and bandwidth. In addition, the proposed structure is easy to implement. The validation of the proposed structure was initially verified through simulations in a commercial software and then the structure was built and experimental results were obtained. A good agreement between numerical and experimental results is observed. The structure shows angular stability and polarization independence.

Index Terms ─ Angular stability, FSS, multifractal Ericampos geometry, polarization independence.

I. INTRODUCTION

The technological development in recent decades in the construction of planar structures has performed a key role in the implementation of devices with low weight, small volume and low cost, making these structures attractive for applications in aerospace systems and wireless communications, such as WLAN, Bluetooth, WMAN, among others.

In literature, there is a large number of works with frequency selective surfaces (FSS) and may be noted that the application of fractal geometry in FSS is increasing.

The study of fractal geometry is not something recent. In fact, it began in 1974, with the mathematician Benoît Mandelbrot using the word "fractal" to indicate objects whose complex geometry could not be characterized as an integral dimension. His examples included galaxies, coastal areas, snowflakes and the Cantor set.

Several researchers have focused on studies with multiband FSS response lately. This is because various applications such as mobile communications and wireless computer networks need multiband operation with resonance frequencies closed. Fractal geometry is a good solution for this problem. These structures are recognized by their properties of self-similarity and fractional dimension [1].

Fractal curves are based on a mathematical concept geometry [2]. The FSS fractal geometric shape has a large effective length, which may be designed in various ways. Fractal shapes has some interesting properties such as the ability to obtain an arbitrarily large electrical length confined to a finite volume.

The use of fractal elements in FSS design allows the development of compact spatial filters with better performance compared with conventional structures [3]. Several iterations in fractals can be used to design FSS with multiband frequency response associated with self-similarity structure contained in [4].

Many studies on the FSS with fractal elements were performed by analyzing only monofractal geometry structures, where the proportion of the adjacent resonance frequencies is approximately equal to the fractal dimension [5]-[7]. However, these structures cannot be used in multiband designs with different ratios of resonance frequencies.

In this work, an analysis of FSS with a new type of multifractal geometry, which is named Ericampos, is performed. This structure optimize the design of multiband FSS structures and allows construction of structures with different proportions of multiband frequency resonances.

Submitted On: July 24, 2014
Accepted On: May 26, 2015

II. MULTIFRACTAL GEOMETRY

The proposed multifractal geometry is a new multifractal geometry, developed by the authors of this paper. Its geometric construction starts with a square as initiator element, Q_0, and the generator element, Q_1, is a combination of a square element with mass probability p_1 and four square elements with mass probability p_2, each. This process is repeated *ad infinitum* obtained for each element. Therefore, after m iterations we have $5m$ elements, where $m = 0, 1, 2, \ldots, \infty$ and Q_n is the *nth* fractal element. The ratio ρ is defined as:

$$\rho = \frac{p_1}{p_2}, \tag{1}$$

Thus, be μ_n the probability measure of the *nth* level fractal, then, if I is an interval of Q_n we have:

$$\mu_n(I) = p_1^k p_2^{n-k}, \tag{2}$$

where, by construction of I, the element with probability p_1 is taken k times and the elements with probability p_2 are taken $n - k$ times. For example, for Q_1, $k = 1$ and $n = 4$.

Now, generalizing the above definition for all elements, it has $Q_n(y)$ as the set that contains the subintervals of length δ_n, then the local dimension is defined as:

$$y = \frac{\log(\mu_n(I))}{\log(\delta_n)}. \tag{3}$$

Also, $N_{\delta n}$ is the number of elements with length δ_n contained in $Q_n(y)$, then:

$$N_{\delta_n} = 4^k \frac{n!}{k!(n-k)!}. \tag{4}$$

If we consider only the y values greater than zero, we define a function $f(y)$, or multifractal dimension, as:

$$f_n(y) = \frac{\log(N_{\delta_n})}{\log(\delta_n)}. \tag{5}$$

The proposed geometry is shown in Fig. 1. Figure 1 (a) has a monofractal geometry. Figure 1 (b) has the multifractal geometry. So, as you can see, the fractal dimension of the geometry is changed independently. This provides greater design flexibility.

In Fig. 2 is shown a spectral diagram for the proposed structure. It can be seen that the multifractal spectrum has a maximum value of the fractal dimension of monofractal, or $\rho = 1$ and the area occupied by the conducting patches is highly concentrated. It is observed that reducing ρ the multifractality of the system increases and favors the spreading of the area occupied by the conducting patches.

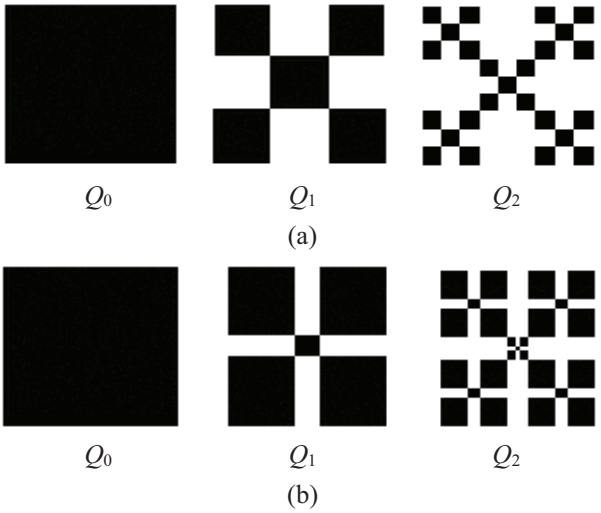

Fig. 1. Proposed geometry: (a) monofractal, and (b) multifractal.

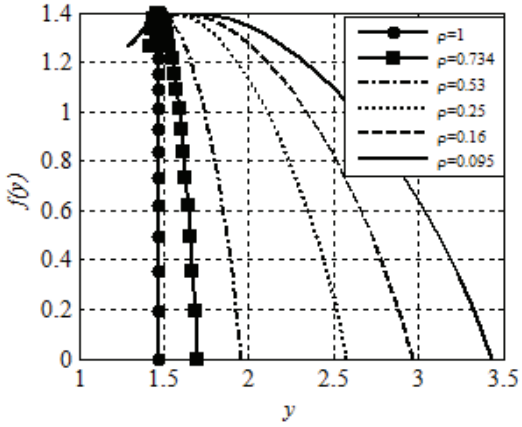

Fig. 2. Multifractal spectrum for different ratios fractality.

To analyze the effect of multifractality, simulations of the transmittance were performed for different values of ρ and for vertical and horizontal polarizations. In Fig. 3, we can observe the coefficient of transmission for different simulation scenarios and vertical polarization. It appears that the increased multifractality enables a reduction in the resonance frequency and increased bandwidth, which does not occur for monofractal geometries. In monofractal case, there is a reduction in the frequency and bandwidth. In Fig. 4, we observe the same behavior for horizontal polarization. Thus, it can be seen that the structure has the independence of polarization.

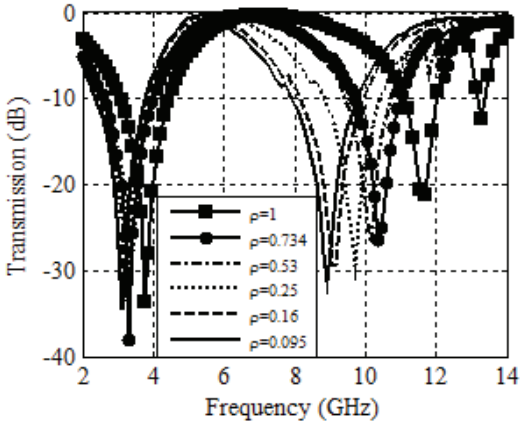

Fig. 3. Transmission coefficient for various ratios of fractality and vertical polarization.

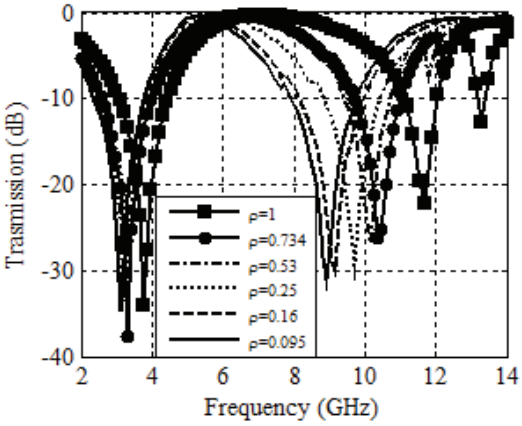

Fig. 4. Transmission coefficient for various ratios of fractality and horizontal polarization.

After previous simulations, was designed a FSS with multifractal geometry Ericampos level 2. The geometry was obtained from an initiator element (squared patch) with 15 mm of side. The individual cell has periodicity of 15.5 mm in the x and y directions. Probabilities p_1 and p_2 equal to 0.0178 and 0.1878, respectively, were used, giving a ratio $\rho = 0.095$.

In Fig. 5, we can see the frequency response of the FSS designed for different angles of incidence and vertical polarization. It may be noted that there is no degradation in resonance frequency or bandwidth. This shows that the geometry is stable in terms of incidence angles. In the simulations, the angles of incidence for an incident plane wave were changed from 0º to 45º. This range covers almost all applications of interesting for FSS.

In Fig. 6, we can see the frequency response of the FSS designed for different angles of incidence and horizontal polarization. It may be noted that, as in the case of vertical polarization, no degradation in resonance frequency or bandwidth. This shows that the structure has the independence of polarization.

It can be seen that the designed structure has possible applications in the S- and X-band.

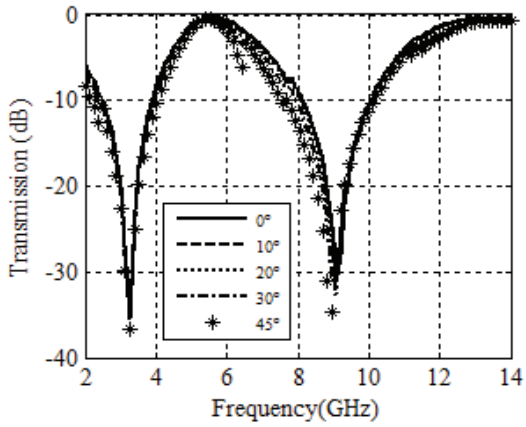

Fig. 5. Transmission coefficient of the FSS designed for different angles of incidence and vertical polarization.

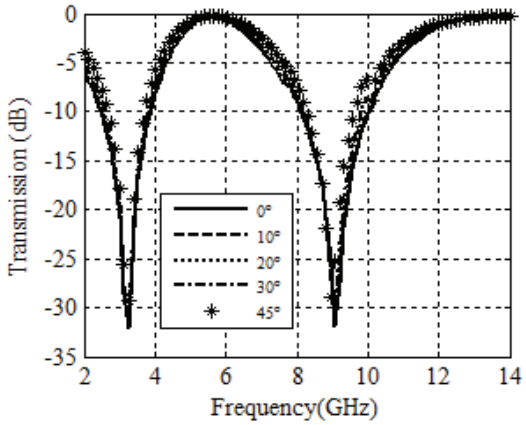

Fig. 6. Transmission coefficient of the FSS designed for different angles of incidence and horizontal polarization.

III. EXPERIMENTAL RESULTS

To validate the analysis performed, a prototype FSS was designed and built, and experimental characterizations were performed. Thus, we could compare the simulated results with measurements. The measurements were carried out using a vector network analyzer from Rohde & Schwarz (ZVB-14), which operates at 14 MHz to 10 GHz, and two horn antennas operating in the band from 700 MHz to 18 GHz with 16 dBi gain. A photograph of the measurement setup is shown in Fig. 7. Bulkhead on which is fixed the FSS is circulated by absorbers to avoid diffraction at the edges and lined with metal to ensure that the signal passes only through the FSS window.

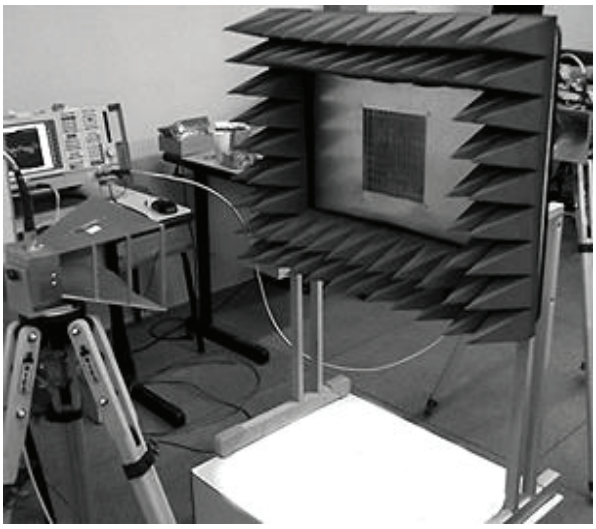

Fig. 7. Photograph of the measurement setup.

In Fig. 8, can be seen a comparison between numerical and measured results for cascaded FSS for normal incidence. The measured and simulated results show good agreement. At the second resonance, a little difference at the resonance frequency can be noted. This may be occuring because the FSS was built with a milling machine table and this may have slightly reduced the thickness of the dielectric, which would be more critical at higher frequencies. This would explain the small difference between the simulated and measured results, at the second resonance.

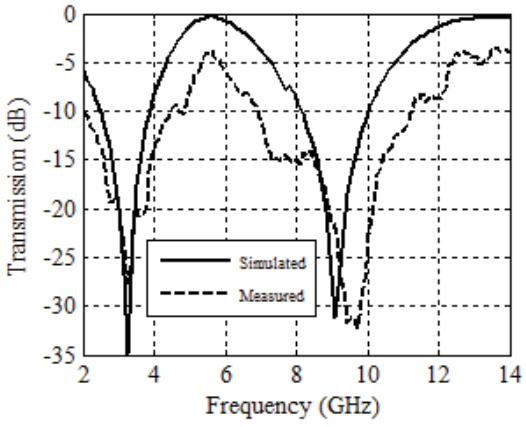

Fig. 8. Comparison between simulated and measured results of the normal incidence transmission coefficient of the FSS designed.

In Figd. 9 and 10, we can see measured results of vertical and horizontal polarizations, respectively, with oblique incidence. The angles of incidence ranging from 0 to 30 degrees. The measured results show that the bandwidth does not suffer degradation in both cases, for different incidence angles, confirming the stability angle and polarization independent. The angles of incidence were changed from 0º to 30º because we have limitations at the measurement setup.

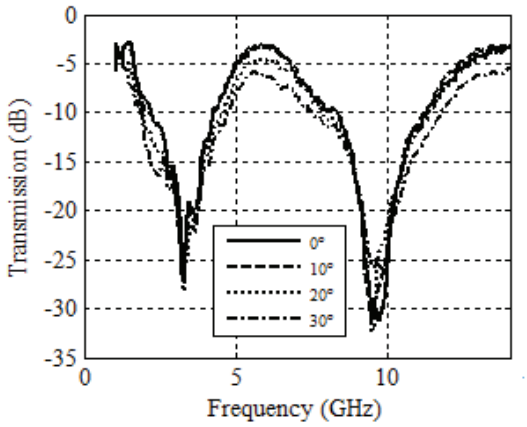

Fig. 9. Transmittance measured FSS designed for different angles of incidence and vertical polarization.

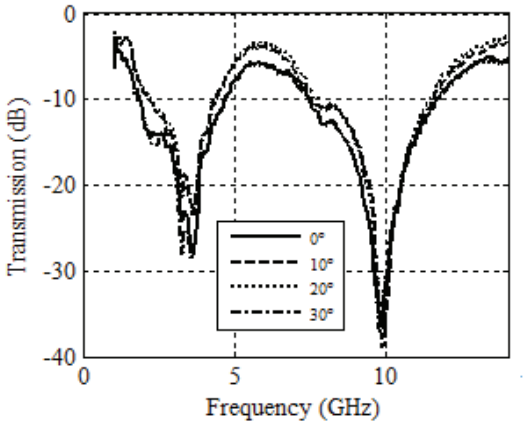

Fig. 10. Transmittance measured FSS designed for different angles of incidence and horizontal polarization.

IV. CONCLUSION

In this paper, we presented a new multifractal geometry for design of dual band FSS. The new geometry was named Ericampos and the FSS presented potential for applications in S- and X-band. The main advantage of the proposed structure is to design multiband FSS with multiple frequency ratios between the adjacent bands and a facility to build the designed structures. In addition, the proposed structure increases the degree of freedom in design of multiband structure according to the number of fractal iterations. The validation of the proposed structure was initially verified through simulations in a commercial software and then with measurements. A good agreement

between simulated and measured results was obtained. The structure shows angular stability and polarization independence.

ACKNOWLEDGMENT

The authors thank the National Council for Scientific and Technological Development - CNPq for partial support of the research through project 301365/2011-3.

REFERENCES

[1] K. Falconer, *Fractal Geometry Mathematical Foundations and Applications*, John Willey and Sons, New York, 1990.

[2] B. Mandelbrot, *The Fractal Geometry of Nature*, Freeman and Company, New York, 1983.

[3] J. Romeu and Y. Rahmat-Samii, "Fractal FSS: a novel dual-band frequency selective surface," *IEEE Transaction on Antennas and Propagation*, vol. 48, no. 7, pp. 1097-1105, 2000.

[4] E. E. C. Oliveira, A. L. P. S. Campos, and P. H. F. Silva, "Miniaturization of frequency selective surfaces using fractal Koch curves," *Microwave and Optical Technology Letters*, vol. 51, no. 8, pp. 1983-1986, 2009.

[5] J. Kaur, S. Singh, and A. Kansal, "Multiband behavior of Sierpinski fractal antenna," *Research Journal of Information and Technology*, vol. 3, no. 9, pp. 263-268, 1994.

[6] S. N. Sinha and M. Jain, "A self-affine fractal multiband antenna," *IEEE Antennas and Wireless Propagation Letters*, vol. 6, pp. 110-112, 2007.

[7] D. Rathee and J. Ashraf, "CPW-fed Sierpinski fractal monopole antenna with varying scale factor," *International Journal of Electronics Engineering*, vol. 3, no. 1, pp. 77-80, 2011.

Erico C. Braz graduated (2006) and MA (2010) in Electrical Engineering by Federal University of Rio Grande do Norte. He has experience in the use of Adaptive Systems with Variable Structure, power electronics and control applications in electrical machines (current, speed, torque, etc.). He currently teaches the basics, tech and technology education at the Federal Institute of Education, Science and Technology of Rio Grande do Norte.

Antonio L. P. S. Campos obtained Bachelors and Masters in Electrical Engineering in 1996 and 1999, respectively, from the Federal University of Rio Grande do Norte. The Ph.D. in Electrical Engineering was obtained at the Federal University of Paraíba, in 2002. He is currently a Professor at the Federal University of Rio Grande do Norte, where he teaches in the undergraduate courses in Electrical Engineering and Telecommunications Engineering. He is also a professor of graduate studies in Electrical and Computer Engineering of the Federal University of Rio Grande do Norte (PPgEEC/UFRN), which guides students in masters, doctorate and teaches courses in the field of Telecommunications program. He is Fellow of CNPq Research Productivity, Level 1-D.

Analysis of Edge Terminated Wide Band Biconical Antenna

C. Subba Rao [1] and A. Sudhakar [2]

[1] Department of Electronics and Communication Engineering
Prasad V Potluri Siddhartha Institute of Technology, Vijayawada, A.P., 520004, India
csr949@gmail.com

[2] Department of Electronics and Communication Engineering
RVR & JC College of Engineering, Chowdavaram, Guntur, A.P., 522019, India
alapati_sudhakar@yahoo.com

Abstract ─ A finite length biconical antenna has standing waves existing due to its abrupt discontinuity at the terminals and results in band width limitation. An appropriate termination of these terminals can enhance its bandwidth to a considerable extent and make it truly wide band. A finite biconical antenna with its edges terminated in thick loop (circular) is proposed and its radiation characteristics are analyzed for different values of 'βr'. Where 'β' is the wave number and 'r' is the length of the antenna. Compact antennas for ultra wide band (UWB) and above are in demand for modern communications and the proposed antenna meets the wide band requirement at UWB and above such as X, Ku, K bands with very low return loss.

Index Terms ─ Biconical, discontinuity, loop, return loss, termination.

I. INTRODUCTION

The research paper proposes, investigates and analyzes a biconical antenna with its edges terminated in circular metal loop. The antenna provides wide band width and is appropriate for the use in present day wireless communication applications. The addition of metallic loop of appropriate radius at the terminals makes the edges smoothly curved. It minimizes reflections and results in enhanced bandwidth and reduced return loss. Biconical antenna was first analyzed by S. A. Schelkunoff who stated that the cones are enclosed in a sphere with its center coinciding with the apex of the biconical antenna. Input impedance of small angle biconical antenna has been presented and is the basis for further investigations of the element. A spherical boundary surface has been used for calculation of fields [1-2]. Smith [3], Tai [4-6], Papas, King [7-8] have proposed spherically capped biconical antenna. Badii and Tomiyama have reported the numerical analysis of biconical antenna in transmitting mode and obtained solutions to near and far fields. Normalized complex power for electrically long biconical antenna is presented [9]. S. S. Sandler and King [10], in recent times S. N. Samaddar and E. L. Mokole [11], D. Ghosh and T. K.Sarkar [12], have proposed and investigated the wide angle spherically capped biconical antenna. Radiation characteristics such as pattern, input impedance, return losses and transient response of the element are established with formulations. A small biconical antenna using shorting pins has been designed by Amert and Whites that operates up to UWB [13]. Lu, et al., have presented top-loaded biconical antenna for UWB indoor base station applications. But this antenna is complex to fabricate and is heavy. Radiation pattern and return loss characteristics exhibit oscillations [14]. Jacobs and others presented a truncated asymmetric conical dipole for wide band applications up to 17 GHz [15].

Smith [3] is the first researcher to propose enhancement of band width in wide angle conical antennas with the edges terminated properly. He has considered cones with angles 61.8° and 101.2° with reduced length. Tai has presented the analysis of biconical antennas with small cone angles and also the E.M.F method of analysis for the spherically capped conical antennas.

King and Papas have reported the determination of input impedance and expression for the radiation from spherically capped conical antenna fed by coaxial line.

Sandler and King have proposed biconical antennas of different lengths for operation from 20 MHz to 1 GHz. Samaddar and Mokole have reported the analysis of a 20 inches wide angle cones up to 10 GHz [10]. They have also established the direction of maximum radiation in cones with unequal angles.

Ghosh and Sarkar have extended the analysis of wide-angle (106.2° and 140°) spherically capped biconical antennas. The height of each cone is 56 mm. The spherical cap termination at the end of each cone minimizes the reflections due to sudden discontinuity at

Submitted On: September 30, 2014
Accepted On: June 4, 2015

the ends of the cone and enhances the band width of the antenna. The spherical cap termination widens its band width, but it is limited by poor efficiency for $\beta r << 1$. For electrically large structure such as $\beta r >> 1$, the radiation pattern breaks in to smaller lobes and loses its directivity and shape. The proposed element is satisfactory around $\beta r \approx 1$.

Analysis of spherically capped wide angle biconical antenna has been widely reported by researchers. These elements which are terminated at the ends by spherical cap are large in height and are widely flared with cone angles above 100°. Their limitations are also presented in the corresponding results.

The paper presents a new technique of termination of cone edges. The cone angle of the proposed radiator is 90° and is small in length as compared to those proposed so far. Each cone of this small antenna is terminated at its ends by a thick circular conductor with a diameter of 1 mm, made of the same material. The cones are not totally covered by spherical cap and this reduces the weight of the antenna considerably. The curved conductor at each point on the edge of the cone provides appropriate matching. This reduces the reflections from the termination.

The antenna is modeled and simulated in CST and HFSS from 1 to 40 GHz frequency range. The research work is analyzed for $\beta r = 0.524, 3.14, 5.2, 10.47, 15.7, 21$.

II. ANTENNA STRUCTURE

An infinite biconical antenna is non-resonant and standing waves do not exist, which results in wide band performance. A finite biconical antenna is not perfectly non-resonant, due to its sudden discontinuity at the ends that causes band width limitation and high return loss.

An appropriate termination of the ends of the cones enhances its band width. It is established that the spherical cap acts as a sink for the surface current and provides a smooth transition for current flow from the cone edges. Biconical antennas of different heights and varying cone angles have been proposed for wide band operation. The authors have proposed a biconical antenna with ends terminated in circular loop of appropriate radius that is of relatively small in height compared to those reported earlier. The proposed ring terminated biconical antenna is shown in Fig. 1.

Total length of the proposed antenna is 25 mm. Length of each cone is 12.5 mm. Separation between the cones is 1 mm. Radius of the cone at the apex is 0.9 mm. Dimensions of the loop have to be carefully considered and the upper radius of the cone and outer radius of the loop should be the same. The outer diameter of the loop is 25 mm and its inner diameter is 22 mm for good termination of the cone. Diameter of loop conductor is 1.5mm. Optimum return loss is realized for 1-2 mm radius of the loop conductor. When the outer radius of the loop is greater than the cone top radius then it results in low return loss and distorted radiation pattern.

The loop is correctly fused on the outer edge of the cone. This converts the sharp and abrupt discontinuity of the top end of the cone in to a smooth curved termination for the current flow. The biconical antenna is modeled in method of moment based CST and HFSS soft wares and simulated using both to obtain its performance for optimization. Time domain solver is used for simulation which is faster and takes less time as compared to frequency domain solver and is good for wideband structures. The solver generates field results for many frequencies with one simulation run. There is no restriction on mesh configurations. The volume of occupancy of this element is very small which is on par with those of microstrip antennas. All the design parameters are listed in Table 1.

Fig. 1. Antenna structure - biconical antenna with ring.

Table 1: Design parameters of the antenna

Parameter Name	Dimensions (mm)
Upper radius of top cone	12.5
Bottom radius of top cone	0.9
Upper radius of bottom cone	0.9
Bottom radius of bottom cone	12.5
Length of each cone	12.5
Separation between the cones	1
Outer radius of the terminating loop	12.5
Inner radius of the terminating loop	11
Diameter of termination loop	1.5
Position of termination loop	±13
Volume of the structure	4.0625 cm^3
Cone angle	90°

III. SIMULATION

The proposed design is simulated in CST and HFSS from 1 to 40 GHz. In CST the far-field monitor of field monitor window is used for the radiation pattern generation. In HFSS the far-field radiation sphere is used for the pattern. Hexahedral mesh configuration with minimum mesh step of 0.45 and maximum of 1.259 is used. The results are analyzed by optimizing the design parameters of the element such as

the radius, position of the loop and the separation between the cones at the apex. Design parameters listed in Table 1 are selected for obtaining optimum results.

Antenna simulation results with and without termination at 6 and 40 GHz are presented in Figs. 2-5. Comparing the current distribution on the cones at the corresponding frequencies of the element with and without termination reveals that the current density is uniform on the surface of the cone with ring termination. The current density reduces gradually with maximum at the apex or feed point towards the end. Each circular contour on the cone shows equal current density points.

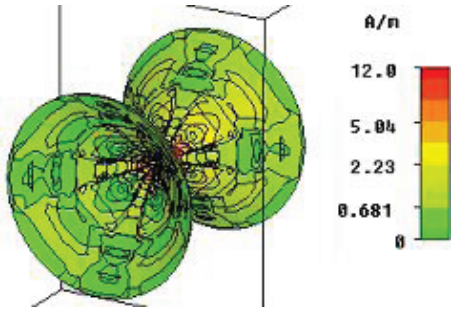

Fig. 2. Surface current distribution on cone without ring at 6 GHz.

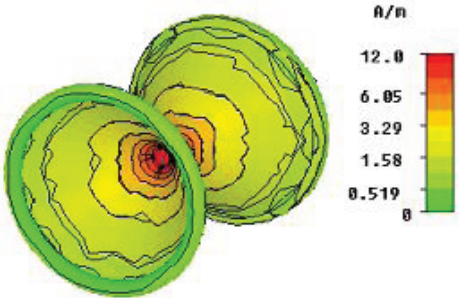

Fig. 3. Surface current distribution on cone with ring at 6 GHz.

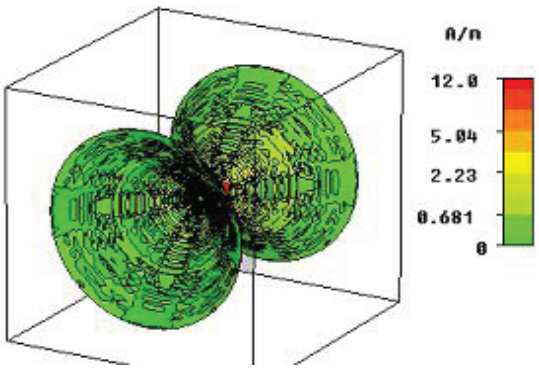

Fig. 4. Surface current distribution on cone without ring at 40 GHz.

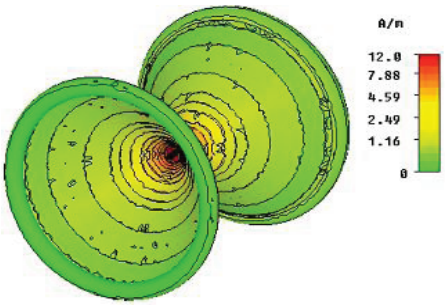

Fig. 5. Surface current distribution on cone with ring at 40 GHz.

At the joint where the cone end meets the loop, the current density is smooth and continuous around the neck and on the loop as well. The contour lines show equal current density points. Hence, there's an improvement in the band width and return loss. The current density on the cones without termination in Fig. 2 and Fig. 4 is non-uniform. It appears like small patches on the surface of the cones.

The simulation results show that the terminated cones have uniform current distribution as depicted in Fig. 3 and Fig. 5. The ring with its gradual curvature at the end provides smooth transition at each point on the edge of the cone. The spherical cap termination is not as smooth at the joint as the proposed loop discussed in this paper. Termination with loop is simple and reduces weight and volume as compared to that of a spherical cap. Analysis was done using current distribution on the cones at two frequencies (6 & 40 GHz). The same current distribution is observed at other frequencies also.

IV. RADIATION PATTERNS

The far zone broad side normalized electric field in E-plane is presented in Eq. (1). For a biconical antenna the radiation pattern is independent in azimuth direction. This equation depicts E-field of the biconical antenna that has no standing waves and represents radiation at low and high frequencies as well for cone angles greater than 40 degrees. The formula cannot be used for cones with small angles.

$$R(\theta,\omega)=\frac{E_\theta^{rad}(r,\theta,\omega)}{E_\theta^{rad}\left(r,\pi/2,\omega\right)}=\frac{\sum_{n=1}^{\infty}\frac{i^{n-1}(2n+1)}{2n(n+1)}\frac{p^1(\cos\theta)g_n(\mu_1,\mu_2)}{h_{n-1}^{(2)}(ka)-\frac{n}{ka}h_n^{(2)}(ka)}}{\sum_{n=1}^{\infty}\frac{i^{n-1}(2n+1)}{2n(n+1)}\frac{p^1(0)g_n(\mu_1,\mu_2)}{h_{n-1}^{(2)}(ka)-\frac{n}{ka}h_n^{(2)}(ka)}}. \quad (1)$$

The omnidirectional pattern with maximum of the main beam is perpendicular to the axis of the cone and the radiation is confined between the two cones. Radiation patterns in vertical plane are shown and are omitted in horizontal plane for brevity. Elevation plane patterns at βr = 0.524, 3.142, 5.24, 10.47, 15.7 & 21 are

shown in Figs. 6-11 respectively. These patterns are smooth without ripples, side lobes and grating lobes. The low frequency patterns for βr = 0.524 are perfectly omnidirectional. Radiation patterns at specific frequencies are obtained in dB and normalized in both CST and HFSS, and are superimposed. Radiation patterns for βr = 15.7 and 21 are depicted in Fig. 10 and Fig. 11 respectively shows ripples or oscillations in the main beam and is not as smooth as those of βr < 10.47.

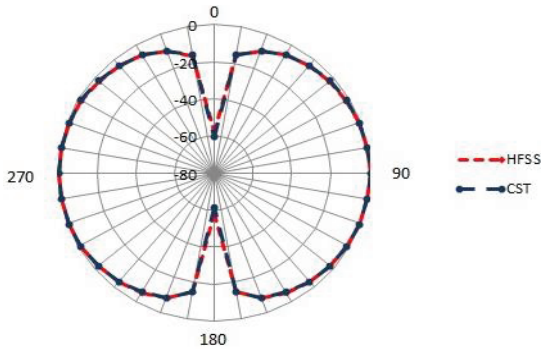

Fig. 6. Radiation pattern at 1 GHz (βr = 0.524).

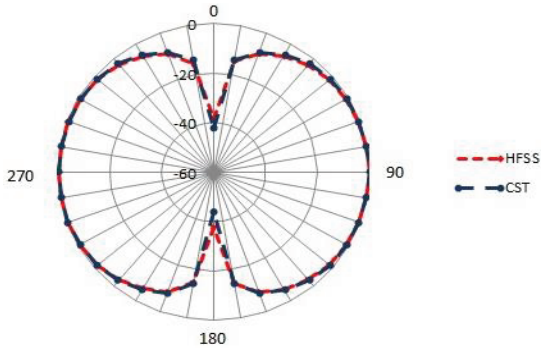

Fig. 7. Radiation pattern at 6 GHz (βr = 3.142).

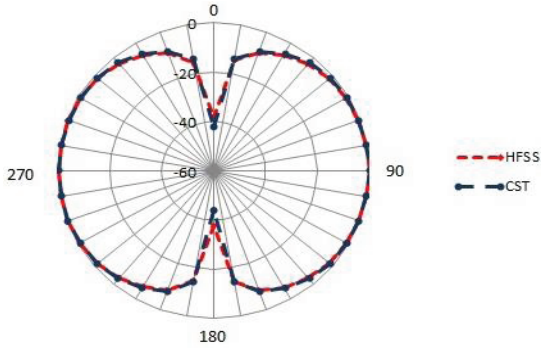

Fig. 8. Radiation pattern at 10 GHz (βr = 5.24).

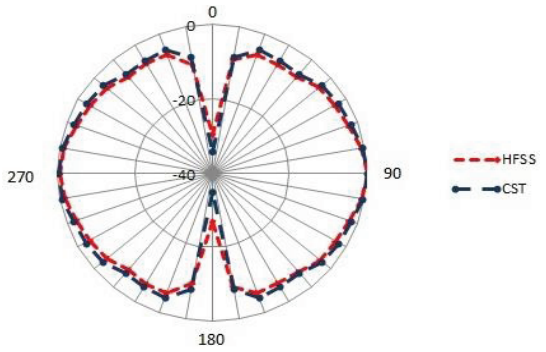

Fig. 9. Radiation pattern at 20 GHz (βr = 10.47).

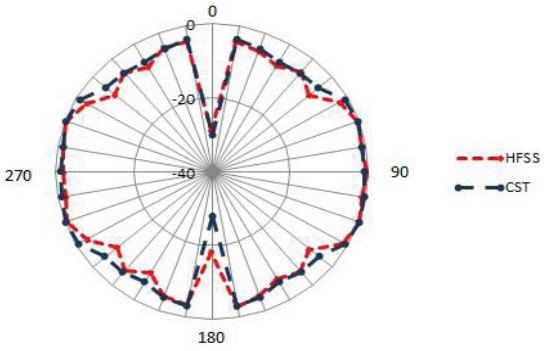

Fig. 10. Radiation pattern at 30 GHz (βr = 15.7).

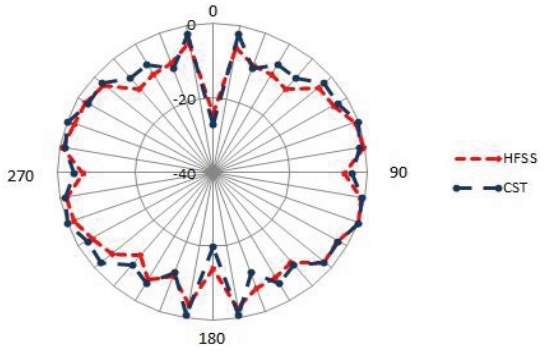

Fig. 11. Radiation pattern at 40 GHz (βr = 21).

V. RETURN LOSS

Another important parameter that shows considerable improvement is the return loss. The return loss is the negative of the reflection coefficient (S_{11}) when expressed in decibels. The S-parameter (input reflection coefficient) S_{11} for antenna without and with termination is shown in Fig. 12 and Fig. 13, respectively. Return loss for cone without termination is less than that of ring termination for most of the

frequency range. The parameters of the cone and the loop are optimized to get best value of return loss, i.e., 10 dB and more from 7.5 to 25 GHz. This frequency range covers X, Ku and K bands which are important for modern wireless applications. In the low frequency range 1-7.5 GHz and at high frequency range, i.e., 25-40 GHz the return loss is varying up to 5 dB and is omitted for brevity. It can be used as receiving antenna for short distance communication in the above mentioned ranges. The input impedance of biconical antenna involves resistance and reactance. As 'βr' increases the resistance and reactance of the conical antenna oscillates around its characteristic values and these oscillations cause fluctuations in the reflection coefficient. Papas and King [7] reported that the input resistance and reactance of biconical antenna with cone angles greater than 40° vary with frequency over wide frequency ranges. Consequently, the reflection coefficient also exhibits similar variations with frequency. Reflection coefficient of the antenna without termination shows dip at 9 & 17 GHz, whereas the element with edge termination shows similar oscillations at much reduced levels. The return loss of the terminated cone at each frequency has increased nearly by 5 dB. The inner circumference of the loop is 69.12 mm.

For large loops the circumference C = wavelength (λ):

$C = \lambda = 2*\pi*r = 69.12$ mm ~ 4.5 GHz,

$C/2 = \lambda/2 = 34.55$ mm ~ 9 GHz,

$C/4 = \lambda/4 = 17.28$ mm ~ 17 GHz.

The antenna is resonant at half wavelength intervals and causes a dip at these frequencies which is characteristic of the loop. Table 2 shows the values of gain and return loss at different values of 'βr' for both terminated and non-terminated cones.

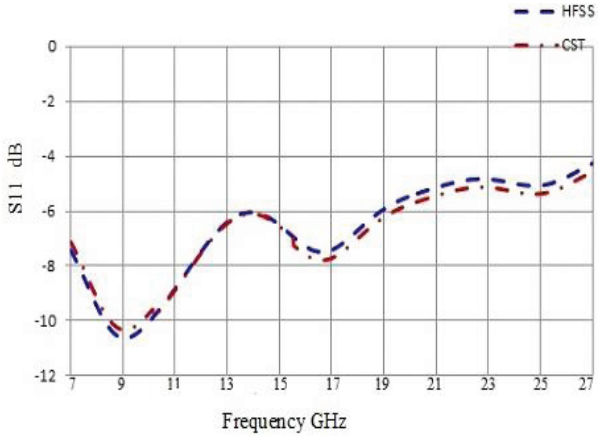

Fig. 12. S_{11} vs. frequency - without edge termination.

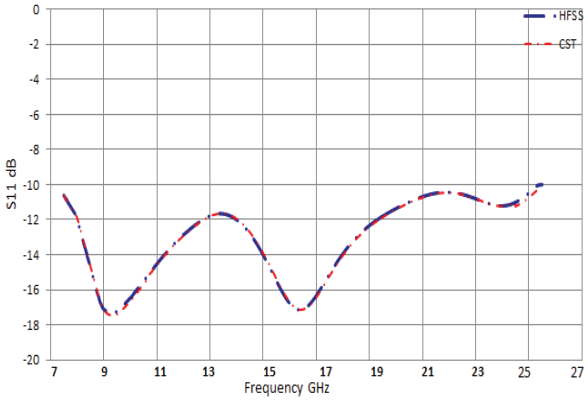

Fig. 13. S_{11} vs. frequency - with edge termination.

Table 2: Gain and return loss

βr	Gain		Return Loss	
	Without Ring	With Terminating Ring	Without Ring (dB)	With Terminating Ring (dB)
0.524	-0.825	0.37	0.2	1
3.142	-0.4033	0.9	6	8
5.24	0.0625	0.6	10	17
10.47	0.6912	0.8	5.5	11.5
15.7	0.2127	1.21	5	7.5
21	1.44	1.532	3.5	4

All the results have been obtained by using two Hi-end EM simulation soft wares CST and HFSS. These results are superimposed to analyze their similarities and deviations. Radiation patterns from 1 GHz to 10 GHz are perfectly omnidirectional at all the angles without any deviation. Above 10 GHz there are slight deviations at certain angles such as 0° and 180°, values in HFSS shows some increase in minima as compared to that of CST and this is negligible.

The S_{11} values in both simulators closely follow at each frequency. Radiation results shown using both solvers are in close agreement at each frequency. This establishes that the proposed design parameters are optimum.

VI. CONCLUSION

The proposed wide band biconical antenna with ring termination is novel and hasn't been reported previously. It is presented that the curved conductor at the top edge of the cone provides smooth transition for current flow and provides an appropriate termination for the current. This causes smooth and uniform current density on the terminated cone surface preventing reflections from the edge of the cone. A uniform current distribution is realized from the feed to the open end. It

results in improvement of the return loss of the proposed antenna in the mid frequency range covering three major frequency bands X, Ku and K. It is also observed by the authors that at low and high frequencies the return loss varies up to 5 dB, whereas the radiation pattern is perfectly omnidirectional from 1 to 40 GHz in the region between the cones. Hence, the proposed technique has enhanced the band width of the finite biconical antenna considerably.

REFERENCES

[1] S. A. Schelkunoff, "Theory of antennas of arbitrary size and shape," *Proceedings of I.R.E.*, pp. 1165-1190, Sept. 1941.

[2] S. A. Shelkunoff, "Principal and complementary waves in antennas," *Proceedings of I.R.E.*, pp. 23-32, Jan. 1946.

[3] P. D. P.Smith, "The conical dipole of wide angle," *Journal of Applied Physics*, vol. 19, pp. 11-23, Jan. 1948.

[4] C. T. Tai, "On the theory of biconical antennas," *Journal of Applied Physics*, vol. 19, pp. 1155-1160, Dec. 1948.

[5] C. T. Tai, "A study of the E.M.F. method," *Journal of Applied Physics*, vol. 20, pp. 717-723, Jul. 1949.

[6] C. T. Tai, "Application of variational principle to biconical antennas," *Journal of Applied Physics*, vol. 20, pp. 1076-1084, Nov. 1949.

[7] C. H. Papas and R. King, "Input impedance of wide-angle conical antennas fed by a coaxial line," *Proceedings of I.R.E.*, vol. 37, pp. 1269-1271, Nov. 1949.

[8] C. H. Papas and R. King, "Radiation from wide-angle conical antennas fed by a coaxial line," *Proceedings of I.R.E.*, vol. 39, pp. 49-51, Jan. 1951.

[9] V. Badii, K. Tomiyama, and D. M. Grimes, "Biconical transmitting antennas, a numerical analysis," *Journal of Applied Computational Electromagnetics Society*, vol. 5, no. 1, pp. 62-92, 1990.

[10] S. S. Sandler and R. W. P. King, "Compact conical antennas for wide-band coverage," *IEEE Transactions on Antennas and Propagation*, vol. 42, pp. 436-439, Mar. 1994.

[11] S. N. Samaddar and E. L. Mokole, "Biconical antennas with unequal cone angles," *IEEE Transactions on Antennas and Propagation*, vol. 46, no. 2, pp. 181-193, Feb. 1998.

[12] D. Ghosh and T. K. Sarkar, "Design of a wide-angle biconical antennas for wide band communication," *Progress in Electromagnetics Research B*, vol. 16, pp. 229-245, 2009.

[13] A. K. Amert and K. W. Whites, "Miniaturization of the biconical antenna for ultra wideband applications," *IEEE Transactions on Antennas and Propagation*, vol. 57, no. 12, Dec. 2009.

[14] W. J. Lu, Y. F. Weng, S. W. Cheung, and H. B. Zhu, "Compact top-loaded ultra wide band biconical antenna for indoor base-station applications," *Microwave and Optical Technology Letters*, vol. 52, no. 11, pp. 2594-2598, Nov. 2010.

[15] O. B. Jacobs, J. W. Odendaal, and J. Joubert, "Analysis and design of a wide band omnidirectional antenna," *Microwave and Optical Technology Letters*, vol. 53, no. 6, pp. 1352-1356, Jun. 2011.

C. Subba Rao received his Ph.D. from Jawaharlal Nehru Technological University, Hyderabad, A.P., India. He's published research papers in national and international journals and conferences. He is currently serving as Associate Professor in the Dept. of E.C.E., Prasad V. Potluri Siddhartha Institute of Technology, Vijayawada-520007, A.P., India.

A. Sudhakar received his M.E. degree in 1985 from Jadavpur University, Calcutta and received his Ph.D. at the Andhra University, Visakhapatnam. He worked as an Associate Professor at AIMST, Malaysia, during (2003-2005). He has over 30 years of teaching and research experience in the field of Electronics and Communication Engineering. He's published several papers in various national and international journals and has co-authored several books. He is presently working as Principal, R.V.R & J.C. College of Engineering, Guntur, A.P., India.